Experimental study on the Capture/Desorption of gaseous iodine (I2, CH3I) on environmental aerosols

Hanaa Houjeij

THÈSE PRÉSENTÉE

POUR OBTENIR LE GRADE DE

DOCTEUR DE

L'UNIVERSITÉ DE BORDEAUX

Sciences Chimiques

Chimie Analytique et Environnementale

Hanaa HOUJEIJ

Etude expérimentale des réactions de capture/désorption des iodes gazeux (I$_2$, CH$_3$I) sur des aérosols environnementaux

Sous la direction de : Dr. Sophie SOBANSKA
Encadrante : Dr. Anne Cécile GREGOIRE

Soutenue le 13 Novembre 2020

Membres du jury:

Mme. MASCETTI Joëlle	Directeur de recherche, CNRS	Présidente
Mme TOUBIN Céline	Professeure, Université de Lille	Rapporteur
M. WORTHAM Henri	Professeur, Aix-Marseille Université	Rapporteur
M. LOUIS Florent	Maître de Conférences, Université de Lille	Examinateur
M. MASSON Olivier	Ingénieur de recherche, IRSN	Examinateur
M. VILLENAVE Eric	Professeur, Université de Bordeaux	Examinateur
M. COUSSAN Stéphane	Chargé de recherche, CNRS	Invité

Titre : Etude expérimentale des réactions de capture/désorption des iodes gazeux (I₂, CH₃I) sur des aérosols environnementaux

_____

Résumé

Lors d'un grave accident de centrale nucléaire l'iode gazeux I^{131}, émit principalement sous les formes I$_2$ ou CH$_3$I, peut affecter la santé humaine et l'environnement lors de son rejet dans l'atmosphère. Les modèles de dispersion de l'iode ne tiennent pas compte de la réactivité de l'iode avec les espèces gazeuses ou les aérosols atmosphériques. Cependant, la modification de la spéciation chimique et/ou la forme physique des composés de l'iode n'est pas sans conséquence sur leur dispersion et leurs impacts sanitaires. Dans le cadre de l'amélioration des outils de simulation de la dispersion atmosphérique de l'iode radioactif, ce travail vise à contribuer à l'état actuel des connaissances sur la chimie de l'iode par une approche expérimentale permettant la compréhension des processus d'interaction entre CH$_3$I gazeux, les aérosols et l'eau.

L'interaction entre CH$_3$I et l'eau a été étudiée à l'échelle moléculaire par des expériences en matrice cryogénique appuyées par des calculs théoriques. Un excès d'eau en regard de CH$_3$I, a été utilisé pour simuler les conditions atmosphériques. Les dimères et trimères de CH$_3$I sont observés malgré la quantité élevée d'eau ainsi que la formation d'agrégats mixtes de CH$_3$I et de polymères d'eau. Ceci peut s'expliquer par la faible affinité du CH$_3$I pour l'eau. Dans l'atmosphère, CH$_3$I et H$_2$O gazeux formeront probablement des agrégats d'eau et des polymères de CH$_3$I au lieu d'hétéro complexes de type (CH$_3$I)$_m$-(H$_2$O)n. L'interaction entre CH$_3$I et la glace amorphe en tant que modèle de glace atmosphérique a fait l'objet d'une étude préliminaire. L'adsorption de CH$_3$I sur la glace amorphe et sa désorption complète au-delà de 47 K ont été observés.

L'étude expérimentale des processus d'interactions entre CH$_3$I et le NaCl sec et humide comme modèle des sels marins a été réalisée en utilisant la Spectroscopie Infrarouge à Transformée de Fourier par Réflexion Diffuse (DRIFTS). Les spectres DRIFTS de NaCl mettent en évidence CH$_3$I adsorbé sur la surface de NaCl. Les spectres FTIR montrent de nouvelles bandes d'absorption, qui ont été attribuées à une nouvelle géométrie d'interaction de CH$_3$I avec NaCl. Le processus d'adsorption de CH$_3$I sur NaCl est probablement une chimisorption puisqu'aucune désorption n'a été observée. Nous avons démontré que l'adsorption du CH$_3$I n'atteint pas la saturation même après 5 heures d'exposition. Ce processus présente une cinétique d'ordre 1 par rapport à la concentration de CH$_3$I en phase gazeuse. Les coefficients

d'absorption sont de l'ordre de 10^{-11}, avec une énergie globale d'absorption de -38 kJ.mol^{-1}. Ces résultats montrent une faible probabilité de capture des molécules de CH_3I par la surface de NaCl. La présence d'eau à la surface de NaCl ne semble pas modifier l'interaction entre CH_3I et NaCl, ce qui est cohérent avec sa faible affinité pour l'eau.

Les interactions de CH_3I avec divers solides inorganiques et organiques comme modèles pour les aérosols atmosphériques ont été étudiées à l'aide d'un réacteur statique couplé à la chromatographie en phase gazeuse permettant de suivre la phase gazeuse. Nous avons montré une faible interaction entre CH_3I et les aérosols étudiés indiquant sa faible affinité pour les surfaces des aérosols quelle que soit leur composition. Nous émettons l'hypothèse que la teneur en eau en surface de l'aérosol est un paramètre clé. Ainsi, lorsqu'il est libéré dans l'atmosphère, CH_3I interagit très peu avec la surface des aérosols et reste en phase gazeuse. Cependant, bien qu'en faible teneur, CH_3I est irréversiblement adsorbé à la surface des sels d'halogénures, ce qui pourrait être pris en compte dans le modèle de dispersion pour en évaluer l'impact.

_____

Title: Experimental study on the Capture/Desorption of gaseous iodine (I$_2$, CH$_3$I) on environmental aerosols

_____

Abstract

Gaseous iodine I^{131} mainly under I$_2$ or CH$_3$I forms, when released into the atmosphere during a severe nuclear power plant accident may affect both human health and environment. The atmospheric dispersion models of iodine do not take into account the potential reactivity of iodine with atmospheric gas or particles species. However, the modification of the chemical speciation and/or the physical form of iodine compounds is not without consequences on the transport of iodine in the atmosphere and its health effects. Within the framework of improving the atmospheric dispersion tools of radioactive iodine, this work aims to contribute to the actual state of knowledge of atmospheric iodine chemistry by experimental approaches focusing on understanding the CH$_3$I-aerosols and CH$_3$I-water interaction processes.

The interaction between CH$_3$I and water at the molecular scale has been investigated using cryogenic matrix experiments supported by theoretical DFT calculations. A large excess of water regarding CH$_3$I was used in order to mimic atmospheric conditions. Dimers and trimers of CH$_3$I are observed despite the high water amount in the initial mixture together with mixed aggregates between CH$_3$I and water polymers. This may be explained by the low affinity of CH$_3$I with water. This result highlights that, in the atmosphere, gaseous CH$_3$I and H$_2$O will likely form aggregates of water and CH$_3$I polymers instead of (CH$_3$I)$_m$-(H$_2$O)$_n$ hetero complexes. Further, the interaction between CH$_3$I and amorphous ice as a model of atmospheric ice have been preliminary investigated. The adsorption of CH$_3$I on amorphous has been observed but with a complete desorption of CH$_3$I above 47 K.

Experimental study of interaction processes between gaseous iodine (CH$_3$I) and both dry and wet NaCl as surrogate of sea salt aerosols has been carried out using Diffuse Reflectance Infrared Fourier Transformed Spectroscopy (DRIFTS). The DRIFTS spectra of NaCl surface clearly evidenced adsorbed CH$_3$I on the NaCl surface particles. The FTIR spectra revealed new absorption bands that have been attributed to a new adsorption geometry. The adsorption process of CH$_3$I on NaCl is likely a chemisorption since no desorption was observed. We have demonstrated that the adsorption of CH$_3$I on NaCl did not reach saturation even after 5 hours of continuous flow of CH$_3$I. CH$_3$I capture at the NaCl surface presents a 1st order kinetics relative to its gas phase concentration. The uptake coefficients were determined to be in the order of 10^{-11}, with a global adsorption energy of about -38 kJ.mol^{-1}. These results show a low

probability of CH₃I molecules to be captured by NaCl surface. The presence of water on the surface of NaCl seems to have no effect on the interaction between CH₃I and NaCl, which is consistent with the low affinity of CH₃I for water.

The interactions of CH₃I with various inorganic and organic powdered solids as models for atmospheric aerosols have been investigated using static reactor coupled with gas chromatography (GC) allowing the monitoring of the gas phase. We have highlighted a weak interaction between CH₃I and inorganic and organic aerosols indicating a low affinity of CH₃I whatever the aerosol surface composition. We hypothesis that the water content at the aerosol surface is a key parameter. So that, when released in the atmosphere, CH₃I will interact very little with the surface of the aerosols and will stay in the gaseous phase. However, although in low content, a part of CH₃I is irreversibly adsorbed on the surface of the halide salts that could be considered in the atmospheric iodine model to estimate potential impact.

_____

Keywords

Spectroscopy, iodine chemistry, reactivity, aerosol, nuclear safety, atmospheric chemistry

_____

Unité de recherche

[Institut des Sciences Moléculaires, UMR 5255, 351 Cours de la Libération, 33405 Talence]

[Laboratoire expérimentation environnement et chimie, IRSN/PSN-RES/SEREX, 13115 Saint Paul Lez Durance Cedex]

To my parents,

To Rabih Maatouk,

To my brother and sister.

Acknowledgment

Glossary

FPs: Fission Products

PWR: Pressurized Water Reactor

TED: Thyroid Equivalent Dose

PA: Proton Acceptor

PD: Proton Donor

nmr: non rotating monomer

DRIFTS: Diffuse Reflectance Fourier Transform Infrared Spectroscopy

ICP-MS: Inductively Coupled Plasma- Mass Spectrometery

GC: Gas Chromatography

MIS: Matrix Isolation Spectroscopy

FTIR: Fourier Transform Infrared Spectroscopy

Table of content

Table of Figures

Table of Tables

23

Executive summary in French

L'énergie nucléaire est une source de production d'électricité pilotable et à très faible émission de carbone (4 g/KWh) (1). En France, le parc de réacteurs nucléaires électrogènes comporte 56 unités réparties dans 18 centrales et contribue à hauteur de 70% (2019) à la production d'électricité au niveau national [2,3]. Ce parc est caractérisé par un très haut niveau de sûreté assuré par l'exploitant (EDF) et contrôlé par un organisme indépendant - l'autorité de sureté nucléaire (ASN). Bien que sa probabilité d'occurrence soit très faible (<10^{-5} réacteur/an), la survenue d'un accident avec un relâchement de produits de fission à l'atmosphère n'est pas à exclure – comme lors de l'accident de Fukushima Daiichi survenu le 11 mars 2011– suite au séisme et surtout au tsunami majeur qui ont affecté la côte ouest du Japon.

Lors d'une telle situation accidentelle, de l'iode (I^{131}) peut être rejeté dans l'atmosphère principalement sous les formes gazeuses I_2 ou CH_3I et sous forme aérosol. Si les modèles de dispersion de l'iode actuellement utilisé à l'IRSN (Institut de Radioprotection et de Sûreté Nucléaire) prennent en compte ces différentes espèces lors de leur émission, en revanche leur évolution lors de leur transport dans le compartiment atmosphérique n'est pas encore à ce stade modélisé [4]. La modification de la spéciation chimique et/ou la forme physique des composés de l'iode – notamment gazeux – n'est pas sans conséquence du fait de sa radio toxicité. Récemment, l'IRSN a récemment engagé des travaux visant à mieux prendre en compte cette réactivité dans les modèles de dispersion [4, 5].

La compréhension de la réactivité de l'iode en phase gazeuse dans la troposphère a beaucoup progressé ces quarante dernières années permettant de mieux décrire les propriétés oxydante et photochimique des composés halogénés et leur rôle dans le cycle de l'ozone. Un mécanisme décrivant la réactivité de l'iode en phase gazeuse ainsi que les interactions avec les autres composés troposphériques d'importance (ozone, composés organiques volatils, oxydes d'azote…) ont pu être établis [6] et est en cours d'intégration dans les outils de modélisation développés par l'IRSN [4, 5]. Cependant, à ce jour, la réactivité des composés iodés avec les aérosols atmosphériques est encore très peu documentée. Seules quelques études ont porté sur la réactivité de composés iodés avec des sels d'halogénure représentatifs de sels marins [7-9] ou bien avec des particules de suie [10,11]. Le comportement des composés iodés avec l'eau atmosphérique (un des principaux constituants de l'atmosphère) ou avec des particules de glace n'est également que très peu documentée [12-19].

Dans ce contexte, les travaux présentés ici ont eu pour objet de faire progresser la connaissance sur la réactivité de l'iode dans l'atmosphère d'une part avec la vapeur d'eau et la glace, et d'autre part, avec les principales classes de particules atmosphériques (sels marin, aérosols inorganiques secondaire, aérosols organiques). Ces travaux ont porté plus particulièrement sur l'iodure de méthyle. Cette espèce iodée gazeuse bien que présente en trace dans la troposphère (jusqu'à 1830 ppt volumique en zone côtière [20]) est un des composés majeurs qui pourrait être relâché en situation accidentelle d'une installation nucléaire et présenter, à proximité du point de rejet, des concentrations bien supérieures à celles observées naturellement. En outre sa longue persistance dans la troposphère (5-11 jours [6,21]) fait que cette espèce peut potentiellement interagir avec de nombreux types de particules en suspension. L'objectif est de pouvoir (i) identifier la nature des interactions entre l'iodure de méthyle et les autres composés atmosphériques : micro-hydratation dans le cas de la vapeur d'eau atmosphérique, adsorption ou absorption à la surface des particules solides ; (ii) déterminer les paramètres principaux qui régissent ce processus d'interaction (température, humidité dans une première approche) (iii) de quantifier ces interactions en déterminant les coefficients de capture apparents.

La formation d'agrégats de CH_3I ainsi que l'interaction entre CH_3I et l'eau ont été étudiées à l'échelle moléculaire grâce à la technique des matrices cryogéniques couplée à la Spectroscopie Infrarouge à Transformée de Fourier. La technique des matrices cryogéniques permet d'isoler des espèces instables à température ambiante (telles que les intermédiaires réactionnels, les isomères présentant un puit de potentiel très plat …) et par ce biais d'étudier les premiers stades de l'hydratation d'une molécule dans son état fondamental. Effectivement à des températures comprises entre 4 et 10 K, seuls les états fondamentaux sont peuplés. Le piégeage cryogénique est généralement réalisé dans des gaz rares ou neutres (Ar, Ne, Xe, N_2 …) pour éviter toute réaction chimique entre la matrice et les dopants. A ces températures, les mouvements des molécules d'intérêt dans la matrice sont très limités offrant une très bonne résolution spectrale et permettant l'étude des liaisons inter et intra moléculaires d'espèces piégées dans une même cage matricielle. Les conditions d'observation dans une matrice cryogénique sont éloignées des conditions atmosphériques classiques ; cependant, du fait de la très faible concentration en iodure de méthyle dans le mélange gazeux initial (CH_3I/Argon : 1 /1000 ou CH_3I/H_2O/Argon : 1 /24 /1500), les édifices moléculaires observés sont très probablement formés en phase gazeuse. En effet, l'atome d'iode est un atome lourd et permet une diffusion à longue distance très limitée de CH_3I dans la matrice d'argon. Aussi, les dimères et les trimères de CH_3I sont probablement formés en phase gazeuse, et piégés en tant que tels dans la matrice ou séparés dans la même cage matricielle lors de leur dépôt. Ceci

est confirmé par les expériences de réchauffement progressif de la matrice de 10K à 35K, qui montrent une augmentation de la proportion de dimères et trimères avec la température au détriment de la proportion de monomères, laissant supposer que ceux-ci sont suffisamment proches pour reformer des clusters dès que la diffusion à courte distance est favorisée.

L'étude des interactions à l'échelle moléculaire permet de mieux comprendre l'étape initiale d'association entre les molécules et donc la formation des premiers agrégats. Dans une application atmosphérique, les mécanismes de formation de ces premiers agrégats peuvent s'assimiler aux premières étapes des processus de nucléation des molécules gazeuses. L'interprétation des spectres IR a nécessité le support de calculs de chimie théorique afin de déterminer les paramètres géométriques, énergétiques et spectroscopiques des édifices moléculaires attendus (dimère et trimère de CH_3I et complexes de types $(CH_3I)_n$-$(H_2O)_m$. Ces calculs ont été réalisés par les outils utilisant la théorie de la fonctionnelle de la densité (DFT) au niveau ωB97X-D avec les bases étendues aug-cc-pVTZ pour H, C et O et aug-cc-PP pour l'iode.

Pour les mélanges CH_3I/Ar 1 :1000, les spectres IR obtenus en matrice Ar ont permis d'identifier sans ambiguïté la présence du monomère, de dimères et trimères $(CH_3I)_n$ (avec n = 1,2 et 3). Ces résultats complètent ceux de la littérature [22] et démontrent que dans ces conditions de concentration en CH_3I la formation de dimères et trimères est favorisée et se produit en phase gaz avant le piégeage des molécules dans la cage matricielle. Nous n'avons pas observé de clusters de plus haut degré $((CH_3I)_n$ n> 3).

Dans le cas de la microhydratation de CH_3I, un excès d'eau en regard de CH_3I a été utilisé afin de simuler l'environnement des molécules de CH_3I en conditions atmosphériques. Les monomères, dimères et trimères de CH_3I sont toujours observés malgré la quantité élevée d'eau. Ces agrégats de CH_3I interagissent également avec les agrégats d'eau. La perturbation des agrégats d'eau par les monomères et clusters de CH_3I est plus favorablement observée et se traduit par un décalage en fréquence des bandes d'absorption caractéristiques de H_2O. La complexité des spectres FTIR dans les régions spectrales des modes de vibration caractéristiques de H_2O et CH_3I ne permet pas une identification complète des espèces en présence. En effet, les nombreuses structures stables $(CH_3I)_n$-$(H_2O)_m$ prédites par les calculs de chimie théorique présentent des spectres proches avec de faibles décalages en fréquence. Quatre complexes ont pu être identifiés sans ambiguïté : un complexe de type CH_3I-H_2O (1 :1), un complexe de type CH_3I-$2H_2O$ (1 :2), et deux complexes de type CH_3I-$3H_2O$ (1 :3). En

revanche, les autres complexes candidats (2 :1 ou 2 :2) n'ont pu être identifiés avec certitude, ce qui n'exclut pas leur présence.

Ces observations indiquent que dans l'atmosphère, CH_3I et H_2O gazeux formeront probablement des agrégats d'eau et des clusters de CH_3I préférentiellement aux hétéro complexes de type $(CH_3I)_n$-$(H_2O)_m$. Ceci peut s'expliquer par la faible affinité du CH_3I pour l'eau. Ces données confortent et complètent significativement les travaux antérieurs [12,22] portant sur la formation de ces édifices en phase gazeuse.

L'interaction entre CH_3I et la glace amorphe en tant que modèle de glace atmosphérique a fait l'objet d'une étude préliminaire. L'adsorption de CH_3I sur la glace amorphe à très basse température (4K) et la perturbation des modes dH de la surface de la glace amorphe, puis la désorption complète au-delà de 47 K des molécules de CH_3I ont été observés. Cependant ces processus d'adsorption et de désorption ne sont pas systématiques, ce qui démontrerait des processus de surface plus complexes. Ces expériences nécessitent une étude plus approfondie afin de rendre compte de l'influence de la cinétique d'injection sur la capture de CH_3I par la surface.

Par ailleurs il serait intéressant de comprendre :
(1) Comment le CH_3I est-il adsorbé sur la surface de glace amorphe pure ? Y a-t-il une liaison $CH_3I...H_2O$ ou une formation de complexe ? Y a-t-il une formation de polymère CH_3I en surface ?
(2) Est-il possible de désorber le CH_3I en utilisant uniquement l'énergie cinétique d'un flux gazeux ?
(3) Est-il possible de désorber le CH_3I en irradiant sélectivement le mode dH ?
(4) Qu'en est-il du comportement photochimique de CH_3I en surface de la glace amorphe?

L'étude expérimentale des processus d'interactions entre CH_3I gazeux et le NaCl solide sec et humide comme modèle des sels marins a été réalisée en utilisant la Spectroscopie Infrarouge à Transformée de Fourier par Réflexion Diffuse (DRIFTS). Cette technique permet de suivre l'évolution de la surface d'une phase solide exposée à un gaz en temps réel et est bien adaptée aux solides transparents au rayonnement infrarouge [23]. Un traitement mathématique approprié des spectres, permet d'obtenir des informations quantitatives à partir des intensités des bandes [24]. L'interprétation en termes de nombre de molécules de CH_3I adsorbées par le solide a nécessité une calibration externe par une technique analytique complémentaire (analyse par ICP-MS de la teneur en iode du sel exposé à CH_3I). Cette

calibration suppose que la quantité totale d'iode analysée est sous forme CH₃I. Cette étude a été menée dans des conditions expérimentales au plus proche de situations atmosphériques en condition nocturne (23°C, pression atmosphérique, sel sec, réacteur non éclairé). Seule la concentration en iodure de méthyle, comprise entre 200 et 1000 ppm, utilisée dans nos expériences, est très supérieure aux valeurs mesurées dans l'atmosphère et n'est pas réaliste. Toutefois, ceci permet dans une première approche, d'étudier les processus d'interactions gaz-solide les plus probants [20].

L'analyse des spectres d'absorption FTIR a porté sur l'évolution des bandes vibrationnelles caractéristiques de CH₃I (3200-700 cm⁻¹). Les bandes vibrationnelles typiques de la liaison C-I n'ont pu être observées, leur fréquence étant inférieure à la fréquence de coupure imposée par le matériau de la fenêtre de la cellule DRIFT (ZnSe - 600 cm⁻¹).

Les spectres obtenus mettent en évidence la présence de CH₃I adsorbé sur la surface de NaCl, pour toutes les concentrations étudiées. Cette adsorption est clairement observée par le déplacement en fréquence du mode vibrationnel de déformation symétrique de CH₃, qui, par rapport à sa fréquence centrée à 1262 cm⁻¹ en phase gazeuse [25], se présente sous forme d'une bande large déplacée vers le rouge (1244 cm⁻¹) et dont l'intensité croît avec la durée d'exposition [26]. La décomposition spectrale de cette bande (en utilisant un modèle Gaussien de description des bandes d'absorption) a permis d'identifier cinq bandes dont quatre peuvent être attribuées à CH₃I adsorbé (1275, 1244, 1220, 1183 cm⁻¹) à la surface de NaCl et la dernière à CH₃I en phase gazeuse en surface du solide diffusant (1262 cm⁻¹). Bien que moins intenses, les bandes liées aux modes vibrationnels d'élongation de CH₃ (2900-3000 cm⁻¹) sont aussi observées. La présence de plusieurs bandes pour le même mode de vibration peut être attribuée aux différentes orientations géométriques possibles des molécules de CH₃I adsorbées à la surface des particules de NaCl.

Les spectres FTIR montrent en outre de nouvelles bandes d'absorption IR intenses à 1024 et 1073 cm⁻¹ qui évoluent en fonction du temps d'exposition à CH₃I gazeux. Ces deux bandes sont systématiquement observées lors de l'exposition d'un sel d'halogénure (NaCl, NaI et KBr) à CH₃I et ne sont pas décrites dans des travaux précédents concernant l'adsorption du CH₃I sur des aluminosilicates poreux ou des surfaces métalliques [27-31]. Les fréquences de ces bandes sont similaires à celles observées sur les spectres de CH₃Cl, CH₃OH et CH₂I₂ adsorbés sur une surface et reportées dans la littérature [26, 32-37]. Cependant, les conditions de formation de telles espèces décrites dans ces précédents travaux, sont très différentes de nos conditions expérimentales et la formation de ces espèces à la surface de NaCl suite à l'interaction avec

CH$_3$I est hautement improbable. Ces nouvelles bandes qui sont caractéristiques des modes vibrationnels de déformation des liaisons CH sont directement corrélées aux bandes observées à 1275, 1244, 1220 et 1183 cm^{-1} et caractéristiques de l'adsorption de CH$_3$I. Ces deux bandes à 1024 et 1073 cm^{-1} sont fortement décalées vers le rouge par rapport à la bande de déformation de CH$_3$ libre (1262cm^{-1}) ce qui suggère une forte interaction de CH$_3$I avec la surface de NaCl. Le calcul DFT du monomère de CH$_3$I, montre une orientation du moment dipolaire de CH$_3$I vers l'atome de carbone, ce qui conduit à une charge de Mulliken partiellement négative pour l'atome d'iode et partiellement positive pour les atomes d'hydrogène. Si nous supposons que CH$_3$I est adsorbé sur NaCl avec une configuration C$_3$v, alors nous pouvons attendre une attraction des atomes d'hydrogène vers les atomes de chlorure de NaCl en raison de la différence de charge. Ce type d'orientation, non décrite dans la littérature, peut expliquer un fort déplacement des fréquences des bandes de déformation de CH$_3$I vers le rouge. L'observation de deux bandes pour cette configuration reflète la non équivalence des atomes d'hydrogène de CH3I en surface de NaCl.

Le processus d'adsorption de CH$_3$I sur NaCl est probablement une chimisorption puisqu'aucune désorption n'est observée, qu'elle soit spontanée, induite par un flux d'argon ou par activation thermique. Nous avons démontré que l'adsorption du CH$_3$I n'atteint pas la saturation même après 5 heures d'exposition. Cependant, il n'a pas été possible de déterminer le mécanisme réactionnel d'interaction de CH$_3$I à la surface de NaCl à partir des seules analyses spectrales. De ce fait, ce processus ne peut être considéré que d'un point de vue macroscopique – reflétant un mécanisme plus complexe à l'échelle microscopique. Ce processus présente une cinétique d'ordre 1 par rapport à la concentration de CH$_3$I en phase gazeuse. La vitesse d'adsorption diminue si la température croît (dans la gamme de température explorée 25-150°C).

Le coefficient de capture moyen (γ_{ss}) de CH$_3$I est très faible de l'ordre de 10^{-11}. Ces résultats montrent une faible probabilité de piégeage des molécules de CH$_3$I par la surface de NaCl, piégeage qui est néanmoins irréversible. L'interaction de CH$_3$I sur les sels d'halogénure est d'autant plus forte que l'anion est moins électronégatif (dans l'ordre d'interaction croissante : NaCl<KBr<NaI). La teneur en eau en surface de l'aérosol pourrait être un paramètre influant sur le comportement de CH$_3$I dans l'atmosphère. Toutefois, les expériences d'adsorption de CH$_3$I sur des poudres humidifiées ne montrent pas un comportement très différent de celui du solide sec. La présence d'eau à la surface de NaCl ne semble pas modifier l'interaction entre CH$_3$I et NaCl, ce qui serait cohérent avec la faible affinité de CH$_3$I pour l'eau.

Les interactions de CH₃I avec divers solides comme modèles pour les aérosols atmosphériques ont été étudiées à l'aide d'un réacteur statique couplé à la chromatographie en phase gazeuse. Cette technique analytique permet de déterminer la concentration de CH₃I de la phase gazeuse après exposition aux particules solides. Ces solides ont été choisis comme étant représentatifs de quelques aérosols inorganiques (bicarbonate de sodium, nitrate de sodium, sulfate de sodium, nitrate d'ammonium) et aérosols organiques tels que des acides carboxyliques (acide malonique, acide citrique, acide oxalique et leur sels de sodium) et des acides gras (acide palmitique). Compte de tenu de la faible interaction attendue entre CH₃I et les solides, les paramètres d'étude ont été choisis de telle sorte à favoriser cette interaction : temps de séjour long dans le lit de particules (0.8 s et 16 s) et faible concentration initiale de CH₃I (entre 1 et 100 ppb). Quelles que soient les conditions expérimentales, aucune interaction avec CH₃I n'a pu être mise en évidence indiquant sa faible affinité pour les surfaces des aérosols quelle que soit leur composition.

Ainsi, dans les conditions expérimentales qui ont été explorées, CH₃I interagit très peu avec la surface des aérosols solides. Dans l'atmosphere, il resterait principalement en phase gazeuse. De ce fait, comme mentionné dans la littérature, les processus photochimiques en phase gazeuse sont vraisemblablement la voie réactive principale impliquant l'iodure de méthyle. Toutefois, bien qu'en faible proportion, nous avons montré que CH₃I est irréversiblement adsorbé à la surface des sels d'halogénures, ce qui ne serait pas sans conséquence d'une part, sur la dispersion atmosphérique de l'iode notamment en cas de relâchement accidentel d'iode radioactif et d'autre part, sur sa photoréactivité.

Les données acquises lors de ces travaux vont permettre de compléter la compréhension du cycle atmosphérique de l'iode et *in fine* de mieux modéliser la dispersion atmosphérique d'un rejet accidentel et donc de mieux anticiper les possibles conséquences sanitaires.

Ces travaux ouvrent de nombreuses perspectives dans le domaine de la réactivité des composés iodés organiques en conditions atmosphérique. En phase gazeuse, si les processus photochimiques sont bien documentés, l'influence de la microhydratation sur la photoréactivité des iodes organiques n'a pas été investiguée à notre connaissance, et encore moins les effets catalytiques potentiels des aérosols qui pourraient modifier les processus photochimiques. L'interaction avec la glace est également un champ à explorer.

L'organisation des molécules de CH₃I à la surface des sels d'halogénure ainsi que leur dynamique reste à confirmer. Les calculs de chimie théorique et des expériences en matrice

réalisées avec des espèces deutérées telles que CD_3I, CD_2HI, etc. permettrait de conforter l'attribution des bandes observées à 1073 et 1024 cm^{-1} et de proposer un modèle d'interaction CH_3I-surface. Le rôle de l'eau sur l'interaction avec les sels marins reste également à clarifier par des études théoriques ou expérimentales en utilisant d'autres techniques d'analyse de surface. Des études avec des concentrations en CH_3I représentatives de celles de l'atmosphere ($[CH_3I]_g$ maximum=2000 ppt) sont nécessaires pour pouvoir transposer nos résultats de laboratoire à des processus atmosphériques.

Enfin, des travaux similaires concernant l'iode moléculaire (I_2), qui est l'autre composé iodé gazeux d'importance susceptible d'être rejeté dans l'atmosphère en cas d'accident nucléaire, sont nécessaires pour compléter les modèles de dispersion.

References

[1] EDF "CO_2 emissions". https://www.edf.fr/en/edf/co-sub-2-sub-emissions [Citation in April 2020].

[2] Operational & Long-Term Shutdown Reactors, (2020). https://pris.iaea.org/PRIS/World Statistics/ [Citation in April 2020].

[3] Le nucléaire en chiffres, Source RTE- Billan Électrique 2017- Électricité Fr., (2017). https://www.edf.fr/groupe-edf/espaces-dedies/l-energie-de-a-a-z/toutsurlenergie/produire-de-l-electricite/le-nucleaire-en-chiffres   [Citation in April 2020].

[4] J. Trincal, Thèse de Doctorat Modélisation du comportement de l'iode dans l'atmosphère, 2015, Lille University.

[5] C. Fortin, V. Fèvre-Nollet, F. Cousin, P. Lebègue, F. Louis, Box modelling of gas-phase atmospheric iodine chemical reactivity in case of a nuclear accident, Atmos. Environ., 214 (2019) 116838/1-116838/24. https://doi.org/10.1016/j.atmosenv.2019.116838.

[6] A. Saiz-Lopez, J.M.C. Plane, A.R. Baker, L.J. Carpenter, R. Von Glasow, C.G. Juan, G. McFiggans, R.W. Saunders, Atmospheric Chemistry of Iodine, Chem. Rev. 112 (2012) 1773–1804. https://doi.org/10.1021/cr200029u.

[7] J.C. Mossinger, R.A. Cox, Heterogeneous Reaction of HOI with Sodium Halide Salts, Phys. Chem. Chem. Phys., 105 (2001) 5165–5177. https://doi.org/10.1021/cr020507n.

[8] A. Allanic, M.J. Rossi, Heterogeneous reactions of HOI on substrates of atmospheric importance, Geophys. Res. Lett., 104 (1999) 18689–18696. https://doi.org/10.1029/1999JD 900285.

[9] N.S. Holmes, J.W. Adams, J.N. Crowley, Uptake and reaction of HOI and $IONO_2$ on frozen and dry $NaCl/NaBr$ surfaces and H_2SO_4, Phys. Chem. Chem. Phys., 3 (2001) 1679–1687. https://doi.org/10.1039/b100247n.

[10] W. Wang, M. Ge, Y. Tian, L. Yao, A flow tube study of methyl iodine uptake on soot surface, Chem. Phys. Lett., 440 (2007) 348–351. https://doi.org/10.1016/j.cplett.2007.04.053

[11] Y. Shi, W. Weigang, G. MaoFa, The uptake of ethyl iodide on black carbon surface, Chinese Sci. Bull., 53 (2008) 733–738. https://doi.org/10.1007/s11434-007-0488-2.

[12] F. Ito, Infrared studies of the CH_3I-H_2O complex and large CH_3I clusters in Ar matrices, J. Mol. Struct., 1035 (2013) 54–60. https://doi.org/10.1016/j.molstruc.2012.09.027.

[13] S. Taamalli, D. Khiri, S. Suliman, S. Khanniche, C. Ivan, L. Cantrel, M. Ribaucour, F. Louis, Unraveling the Tropospheric Microhydration Processes of Iodous Acid HOIO, ACS Earth Sp. Chem., 4 (2020) 92–100. https://doi.org/10.1021/acsearthspacechem.9b00257.

[14] S. Khanniche, F. Louis, L. Cantrel, I. Černušák, A theoretical study of the microhydration of iodic acid ($HOIO_2$), Comput. Theor. Chem., 1094 (2016) 98–107. https://doi.org/10.1016/j.comptc.2016.09.010.

[15] A. Allanic, R. Oppliger, H. van den Bergh, M.J. Rossi, The Heterogeneous Kinetics of the Reactions $ClONO_2$ + HX/ice (X = Br, I), $BrONO_2$ + HI/ice and the Reactivity of the Interhalogens BrCl, ICl and IBr with HX/ice (X = Cl, Br, I) in the Temperature Range 180 to 205 K, Zeitschrift fur Phys. Chemie, 214 (2000) 1479–1500. https://doi.org/ 10.1524/zpch.2000.214.11.1479.

[16] B. Fluckiger, A. Thielmann, L. Gutzwiller, M.J. Rossi, Real Time Kinetics and Thermochemistry of the Uptake of HCl , HBr and HI on Water Ice in the Temperature Range 190 to 210 K, Berichte der Bunsen-gesellschaft-physical Chem. Chem. Phys., 928 (1998) 915–928. https://doi.org/10.1002/BBPC.19981020704.

[17] S.B. Barone, M.A. Zondlo, M.A. Tolbert, Investigation of the Heterogeneous Reactivity of HCl , HBr , and HI on Ice Surfaces, Phys. Chem. A, 103 (1999) 9717–9730. https://doi.org/ 10.1021/jp990400c.

[18] L.T. Chu, L. Chu, Uptake and Interaction of HI on Ice Films, Phys. Chem. B, 101 (1997) 6271–6275. https://doi.org/10.1021/jp963185y.

[19] C.J. Percival, J.C. Mo, R.A. Cox, The uptake of HI and HBr on ice, Phys. Chem. Chem. Phys., 1 (1999) 4565–4570. https://doi.org/10.1039/A904651H.

[20] C. Peters, S. Pechtl, J. Stutz, K. Hebestreit, G. Hönninger, K.G. Heumann, A. Schwarz, J. Winterlik, U. Platt, Reactive and organic halogen species in three different European coastal environments, Atmos. Chem. Phys. 5 (2005) 3357–3375. https://doi.org/10.5194/acp-5-3357-2005.

[21] F.C. Kupper, C.J. Carrano, Key aspects of the iodine metabolism in brown algae : a brief critical review, R. Soc. Chem., Metallomics. 11 (2019) 756–764. https://doi.org/10.1039/c8mt00327k.

[22] F. Ito, T. Nakanaga, Y. Futami, S. Kudoh, M. Takayanagi, M. Nakata, Isomeric structures of CH_3I dimers in a supersonic jet studied by matrix-isolation infrared spectroscopy and ab initio calculation, Chem. Phys. Lett., 343 (2001) 185–191. https://doi.org/ 10.1016/S0009-2614(01)00688-1.

[23] R. Vogt, B.J. Finlayson-Pitts, A Diffuse Reflectance Infrared Fourier Transform Spectroscopic (DRIFTS) study of the surface reaction of NaCl with gaseous NO_2 and HNO_3, J. Phys. Chem. 98 (1994) 3747–3755. https://doi.org/ 10.1021/j100065a033.

[24] J. Sirita, S. Phanichphant, F.C. Meunier, Quantitative analysis of adsorbate concentrations by diffuse reflectance FT-IR, Anal. Chem. 79 (2007) 3912–3918. https://doi.org/10.1021/ac0702802.

[25] C. Su, J.C. Yeh, C.C. Chen, J.C. Lin, J.L. Lin, Study of adsorption and reactions of methyl iodide on TiO_2, J. Catal. 194 (2000) 45–54. https://doi.org/ 10.1006/jcat.2000.2909.

[26] M. Chebbi, B. Azambre, L. Cantrel, A. Koch, A Combined DRIFTS and DR-UV-Vis Spectroscopic in Situ Study on the Trapping of CH_3I by Silver-Exchanged Faujasite Zeolite, J. Phys. Chem. C. 120 (2016) 18694–18706. https://doi.org/ 10.1021/acs.jpcc.6b07112.

[27] M.L. Colaianni, P.J. Chen, H. Gutleben, J.T. Yates, Vibrational studies of CH_3I on Si(100)-(2×1): adsorption and decomposition of the methyl species, Chem. Phys. Lett. 191 (1992) 561–568. https://doi.org/ 10.1016/0009-2614(92)85589-3.

[28] F. Solymosi, G. Klivényi, HREELS study of CH_3I and CH_3 adsorbed on Rh(111) surface, J. Electron Spectros. Relat. Phenomena. 64/65 (1993) 499–506. https://doi.org/ 10.1016/0368-2048(93)80115-3.

[39] J. Lin, B.E. Bent, Iodomethane dissociation on Cu(111): Bonding and chemistry of adsorbed methyl groups, J. Vac. Sci. Technol. A Vacuum, Surfaces, Film. 10 (1992) 2202–2209. https://doi.org/ 10.1116/1.578005.

[30] C.J. Jenks, B.E. Bent, N. Bernstein, F. Zaera, The Chemistry of Alkyl Iodides on Copper Surfaces. 1. Adsorption Geometry, Phys. Chem. B. 104 (2000) 3008–3016. https://doi.org/ 10.1021/jp993021s.

[31] M.A. Henderson, G.E. Mitchell, J.M. White, The chemisorption of methyl halides (Cl, Br and I) on Pt (111), Surf. Sci. Lett. 184 (1987) 325–331. https://doi.org/ 10.1016/0167-2584(87)90754-7.

[32] T. Makino, S. Zulaehah, J.S. Gueriba, W.A. Diño, M. Okada, CH_3Cl/Cu (410): Interaction and Adsorption Geometry, J. Phys. Chem. C. 122 (2018) 11825–11831. https://doi.org/ 10.1021/acs.jpcc.8b01296.

[33] J. Cserenyi, L. Ovari, T. Bansagi, F.Solymosi, Adsorption and reactions of CH_3Cl on Mo C based catalyst, J. Mol. Catal. A Chem. 162 (2000) 335–352. https://doi.org/10.1016/S1381-1169(00)00301-0.

[34] J.Rakso, J.Bontovics, F.Solymosi, Infrared Spectroscopic Study of the Adsorption and Dissociation of Methyl Halides on Silica-Supported Pd, J. Catal. 143 (1993) 138–148. https://doi.org/10.1006/JCAT.1993.1260.

[35] F. Zaera, H. Hoffmann, P.R. Griffiths, Determination of molecular chemisorption geometries using reflection-absorption infrared spectroscopy: alkyl halides on Pt (111), J. Electron Spectros. Relat. Phenomena. 54–55 (1990) 705–715. https://doi.org/ 10.1016/0368-2048(90)80263-A.

[36] G. Klivényi, F. Solymosi, Generation of CH_2 species: thermal and photo-induced dissociation of CH_2I_2 on Rh(111) surface, Surf. Sci. 342 (1995) 168–184. https://doi.org/10.1016/0039-6028(95)00767-9.

[37] M.K. Weldon, C.M. Friend, Spectroscopic characterization of surface methylene on Mo(110), Surf. Sci. 321 (1994) L202-L208. https://doi.org/10.1016/0039-6028(94)90175-9.

General Introduction

Nuclear energy is one of different sources of energy used to produce electricity by chain reaction. It is well known that nuclear energy provides efficient and reliable electricity with producing very low greenhouse gas emissions during operation. U.S., China and France are the three leading nuclear countries in the world. Indeed, France has the highest density of nuclear power plants. More than 70% of its electricity has been generated by nuclear power on 2017 [1], [2] with CO_2 emissions of 4g/KWh from nuclear stream [3]. The nuclear power plants currently in operation in France comprise a total of 56 Pressurized Water Reactors (PWRs) at 18 nuclear facility sites [4]. Even though nuclear sites are secured and the probability of having severe nuclear accident is low due to safety measures, the risk of having a severe nuclear accident to occur such as the accident at Three Mile Island (USA, 1978), Chernobyl (Ukraine, 1986), and more recently Fukushima (Japan, 2011) still exists. These accidents have different harmful consequences due to the important release of fission products. Among them, Iodine (^{131}I) present a particular interest because it is a highly volatile radiotoxic radionuclide. Indeed, iodine can be released in gaseous form (essentially I_2 and RI – R = alkyl group/chain type CH_3I) despite the presence of filtration devices. However, the release of iodine products into the atmosphere can be highly reactive and can interact with other species present in the atmosphere (gas or particles) to evolve in gaseous or particulate form. These interactions can take place in the near field (typically around 11 km with respect to the point of emission [5]) and at longer distance, which plays an important role on the dispersion of iodine in the atmosphere. Further, it can impact both human health and environment.

Over the past 25 years, IRSN (Institut de Radioprotection et de Sûreté Nucléaire) has developed the integral Accident Source Term Evaluation Code (ASTEC) [6] which is used to simulate an accidental sequence of a PWR and predict fission products source term and in particular, the radioiodine source term. Iodine atmospheric dispersion is then modelled by C^3X operational tool [7] also developed by IRSN but without considering the iodine physical/chemical evolution in the atmosphere, i.e. the gas phase evolution or interaction with atmospheric aerosols. This is worrisome because the simulated atmospheric dispersion of radioiodine may be quite different from the actual ones due to the different possible fates of iodine within the Earth's atmosphere that may drive different chemical forms (gas or particles). Forthwith, the radiological consequences (thyroid equivalent dose) are predicted without considering the actual forms of the dispersed iodine. This prediction is indeed

dependent on the chemical form of iodine released and can be improved by assuming the iodine physical/ chemical evolution in the atmosphere.

Recently, the iodine speciation and gas phase chemistry during its atmospheric dispersion following a severe accident has been a topic for Ph.D. works at IRSN [8, 9]. These studies have developed a complete reaction mechanism of iodine reactivity in gas phase. However, to date, very few experimental or theoretical studies have been carried out that look at the iodine-aerosol interactions under severe accident conditions of nuclear safety interest. Even though, due to the potential involvement of iodine species in tropospheric ozone loss, only few atmospheric studies have studied the interactions of iodine-containing species with particulate matters such as with sodium halides solids [10-12], ice and soot surface [13, 14]. Additionally, the behavior of iodine compounds when exposed to water vapor (one of the most abundant atmospheric agent) [15- 17] or iced particles is parsley documented [18-21].

Within this framework, the goal of this Ph.D. work is to improve the actual state of knowledge of atmospheric iodine chemistry focusing on the gaseous iodine - atmospheric aerosols interaction by experimental works. The objective is to provide reliable data for IRSN in order to improve the atmospheric dispersion tool of radioactive iodine. Further, it will help to better predict land contamination and human exposure as well as to optimize counter-measures. Thus, this thesis focuses on laboratory experiments dealing with the heterogeneous chemical interactions between modelled atmospheric aerosols and iodine-based gaseous species (CH_3I) under dry and humid conditions. The interaction between CH_3I and water vapor or CH_3I and amorphous ice have been also investigated. If these experiments show that there are some interactions occurring between gaseous iodine (CH_3I) and atmospheric aerosols or water vapor, many preliminary questions will therefore be raised:

1. What is the type of interaction between gaseous iodine and atmospheric aerosols (physisorption, chemisorption…)?
2. What is the quantity of gaseous iodine taken up by the atmospheric aerosols?
3. What is the influence of temperature and humidity on the interaction?
4. Does gaseous iodine undergo micro hydration process in the atmosphere?

In this context, the 1st purpose of this thesis is to bring knowledge to the field of CH_3I reactivity with water (and ice). This reactivity was investigated at cryogenic temperatures using cryogenic experimental devices. Theoretical calculations have been performed on a set of methyl iodide species to support the observed formed species.

The 2nd purpose is to understand the influence of atmospheric aerosols on the transport of gaseous iodine (CH_3I). The first experimental study has been focused on the evolution of NaCl as model of atmospheric sea salt aerosols when exposed to CH_3I under dry/humid gas conditions, at room temperature using DRIFTS (Diffuse Reflectance Infrared Fourier Transform Spectroscopy) technique. The second experimental study focused on the capture of gaseous CH_3I when it is in contact with models of inorganic and organic aerosols under dry conditions and at room temperature using static reactor coupled with gas chromatography.

The manuscript is organized as follows:

Chapter 1 describes the context of the thesis. This chapter briefly presents the general operation of the Pressurized Water Reactor (PWR) and describes a typical nuclear severe nuclear scenario and its consequences. Additionally, the iodine dispersion issue in the atmosphere when a nuclear accident occurs is discussed.

Chapter 2 is presenting the state of art concerning the chemistry of iodine in the atmosphere. This chapter devotes a brief review on the natural sources of iodine, the chemical reactivity of iodine species in the gas phase, the heterogeneous reactivity of gaseous iodine species with atmospheric aerosols. Finally, a short review of the experimental methods that can be applied to have insights on bulk processes and mechanism of heterogeneous reactivity is also given at the end of this chapter.

Chapter 3 goes through the study of molecular interactions that can occur between CH_3I and water and CH_3I deposited on ice surface by using a cryogenic experimental technique. Further, this chapter devotes the theoretical calculation, which are used to support the experimental results.

Chapter 4 is dedicated to the study of interaction between CH_3I and NaCl as a model of the main sea salts aerosols using bulk gas-surface experimental tools. This chapter reports mainly the adsorption process as well as kinetics results using DRIFTS (Diffuse Reflectance Infrared Fourier Transform Spectroscopy) experiments. The methodology as well as the experimental uptake coefficients are reported in this chapter.

Chapter 5 deals with the interaction process of CH_3I with inorganic and organic solids as main constituent models of primary and secondary atmospheric aerosols. This chapter reports the evolution of the gas phase.

Conclusion and perspectives will summarize the main insights of this work and the complementary works to perform.

References

[1] Le nucléaire en chiffres, Source RTE- Billan Électrique 2017- Électricité Fr., (2017). https://www.edf.fr/groupe-edf/espaces-dedies/l-energie-de-a-a-z/tout-sur-l-energie/ produire -de-l-electricite/le-nucleaire-en-chiffres   [Citation in April 2020].

[2] Operational & Long-Term Shutdown Reactors, (2020). https://pris.iaea.org/PRIS/WorldStatistics/ [Citation in April 2020].

[3] EDF "CO_2 emissions". https://www.edf.fr/en/edf/co-sub-2-sub-emissions [Citation in April 2020].

[4] IRSN mission Report, Safety and Radiation Protection at Nuclear Power Plants in France in 2015, Fontenay-aux-Roses, France, IRSN Nuclear Safety Division, IRSN/DG/2016-0004, 2017.

[5] L.S. Lebel, R.S. Dickson, G.A. Glowa, Radioiodine in the atmosphere after the Fukushima Dai-ichi nuclear accident, J. Environ. Radioact. 151 (2016) 82–93. https://doi.org/10.1016/j.jenvrad.2015.06.001.

[6] K. Chevalier-Jabet, F. Cousin, L. Cantrel, C. Séropian, Source term assessment with ASTEC and associated uncertainty analysis using SUNSET tool, Nucl. Eng. Des. 272 (2014) 207–218. https://doi.org/10.1016/j.nucengdes.2013.06.042.

[7] M. Tombette, E. Quentric, D. Quélo, J. Benoit, A. Mathieu, I. Korsakissok, D. Didier, C^3X : A software platform for assessing the consequences of an accidental release of radioactivity into the atmosphere, 4th European IRPA Congress, Geneva, Switzerland, June 2014.

[8] J. Trincal, Thèse de Doctorat Modélisation du comportement de l'iode dans l'atmosphère, Lille university, France 2015.

[9] C. Fortin, V. Fèvre-Nollet, F. Cousin, P. Lebègue, F. Louis, Box modelling of gas-phase atmospheric iodine chemical reactivity in case of a nuclear accident, Atmos. Environ. 214 (2019) 116838. https://doi.org/10.1016/j.atmosenv.2019.116838.

[10] J.C. Mossinger, R.A. Cox, Heterogeneous Reaction of HOI with Sodium Halide Salts, Phys. Chem. Chem. Phys. 105 (2001) 5165–5177. https://doi.org/10.1021/jp0044678.

[11] A. Allanic, R. Oppliger, H. van den Bergh, M.J. Rossi, The Heterogeneous Kinetics of the Reactions $ClONO_2$ + HX/ice (X = Br, I), $BrONO_2$ + HI/ice and the Reactivity of the Interhalogens BrCl, ICl and IBr with HX/ice (X = Cl, Br, I) in the Temperature Range 180 to 205 K, Zeitschrift Fur Phys. Chemie. 214 (2000) 1479–1500. https://doi.org/10.1524/zpch.2000.214.11.1479.

[12] N.S. Holmes, J.W. Adams, J.N. Crowley, Uptake and reaction of HOI and $IONO_2$ on frozen and dry NaCl/NaBr surfaces and H_2SO_4, Phys. Chem. Chem. Phys. 3 (2001) 1679–1687. https://doi.org/10.1039/b100247n.

[13] W. Wang, M. Ge, Y. Tian, L. Yao, A flow tube study of methyl iodine uptake on soot surface, Chem. Phys. Lett. 440 (2007) 348–351. https://doi.org/10.1016/j.cplett.2007.04.053.

[14] Y. Shi, W. Weigang, G. MaoFa, The uptake of ethyl iodide on black carbon surface, Chinese Sci. Bull., 53 (2008) 733–738. https://doi.org/10.1007/s11434-007-0488-2.

[15] F. Ito, Infrared studies of the CH_3I-H_2O complex and large CH_3I clusters in Ar matrices, J. Mol. Struct., 1035 (2013) 54–60. https://doi.org/10.1016/j.molstruc.2012.09.027.

[16] S. Taamalli, D. Khiri, S. Suliman, S. Khanniche, C. Ivan, L. Cantrel, M. Ribaucour, F. Louis, Unraveling the Tropospheric Microhydration Processes of Iodous Acid HOIO, ACS Earth Sp. Chem., 4 (2020) 92–100. https://doi.org/10.1021/acsearthspacechem.9b00257.

[17] S. Khanniche, F. Louis, L. Cantrel, I. Černušák, A theoretical study of the microhydration of iodic acid (HOIO2), Comput. Theor. Chem., 1094 (2016) 98–107. https://doi.org/10.1016/j.comptc.2016.09.010

[18] B. Fluckiger, A. Thielmann, L. Gutzwiller, M.J. Rossi, Real Time Kinetics and Thermochemistry of the Uptake of HCl , HBr and HI on Water Ice in the Temperature Range 190 to 210 K, Berichte der bunsen-gesellschaft-physical Chem. Chem. Phys., 928 (1998) 915–928. https://doi.org/10.1002/bbpc.19981020704.

[19] S.B. Barone, M.A. Zondlo, M.A. Tolbert, Investigation of the Heterogeneous Reactivity of HCl, HBr, and HI on Ice Surfaces, Phys. Chem. A, 103 (1999) 9717–9730. https://doi.org/10.1021/jp990400c.

[20] L.T. Chu, L. Chu, Uptake and Interaction of HI on Ice Films, Phys. Chem. B, 101 (1997) 6271–6275. https://doi.org/10.1021/jp963185y.

[21] C.J. Percival, J.C. Mo, R.A. Cox, The uptake of HI and HBr on ice, Phys. Chem. Chem. Phys., 1 (1999) 4565–4570. https://doi.org/10.1039/A904651H.

Chapter 1: Context

In this first chapter, the general context of this thesis is exposed. A brief description of a Pressurized Water Reactor (PWR) and severe accident scenario are presented. The consequences of radioactive nuclide release following severe accident are then discussed. Finally, the problematic of iodine dispersion in the atmosphere is explained.

1.1 Pressurized water reactor (PWR)

1.1.1 Description and operation of a Pressurized Water Reactor (PWR)

In an archetypal design of a PWR, as represented in Figure 1.1, the reactor comprises a nuclear island housed in the containment building, a turbine island, a water intake and discharge structures and, in some cases, a cooling tower. The heat is created inside the reactor core from fission chain reaction in the U-Ox or MOx fuel pellets assembled in rods. High-pressurized water is pumped to the core where it is heated by the energy produced by the fission of ^{235}U or ^{239}Pu atoms. In PWR, pressurized water circulates in the primary coolant loop and, via the steam generator vaporized water circulates in a secondary coolant loop, producing steam. The secondary-side steam is delivered to the main turbine, powering it and further creating electricity. Any unused steam is subsequently condensed via cooled water through a tertiary loop, which is a heat sink consisting of a sea, river (open-loop system) or the atmosphere via cooling towers (closed-loop system). Then after, the condensed water is pumped back to the steam generator to be reheated where the cycle begins again.
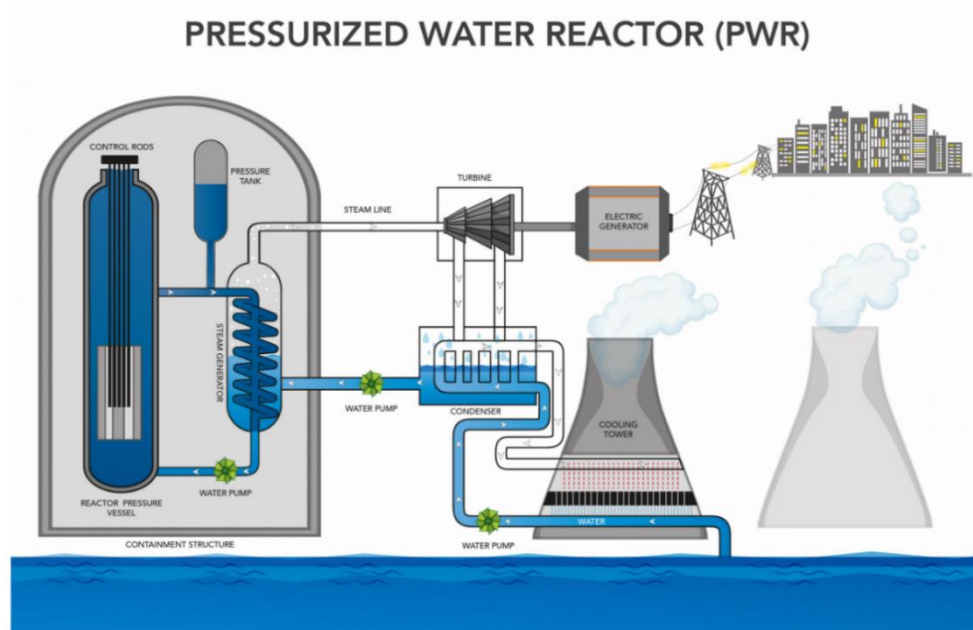
Figure 1. 1 Pressurized Water Reactor [1].

Meanwhile, for pressurized water reactors (PWRs), there are three successive barriers that prevent any release (accidental or incidental) of radionuclide to the environment, and protect the reactor from external hazards:

- The fuel rod cladding, made of zirconium alloy, which retains the radioactive products created in the fuel pellets.
- The reactor coolant system, which constitutes a second isolation that prevents the spread of radioactive products if the cladding fails.
- The containment vessel, which consist of a concrete building, housing the reactor coolant system. It forms a strong barrier that prevents radioactive substances from escaping into the outside environment.

Furthermore, the safety of nuclear power plants is based on the principle of defence-in-depth, which ensure basic safety functions that are necessary to ensure all barriers remain effective, for instance reactivity control, removal of heat from the core and isolation of fuel. The concept of defence-in-depth has been implemented to prevent accidents, and if prevention fails, limit accident consequences and prevent any evolution to more severe situation. For reactors currently in operation, defence-in-depth is based on five levels (see Table 1.1) intended to prevent the occurrence and limit the consequences of technical, human and organizational failures. The various levels of defence-in-depth apply at the various states of the facility, from normal operation to core melt accidents. Table 1.1 summarizes both the objectives of each level of protection and the means of achieving them.

Table 1. 1 The various levels of defence-in-depth [2].

Level	Objectives	Main Measures	Corresponding facility condition
1	Preventing the operation of malfunctions and system failures	Conservative design and high quality in construction and operation	Normal operation
2	Detecting failures and comprehensive management of operating malfunctions	Control, limiting and protection systems and other surveillance features	Operating malfunctions or failure
3	Comprehensive accident management (including design-basis accidents)	Safeguard systems and accident procedure	Accidents including "design-basis accidents" (single initiating event)
4	Comprehensive management of severe accidents, prevention of accident progression and mitigation of consequences	Additional measures and accident management (emergency procedures and associated equipment resources, severe accident operating guidelines, on-site emergency plan)	Multiple failures Core melt accidents
5	Limiting radiological consequences in the event of a release of radioactive substances	Off-site emergency plan (Evacuation, taking of potassium iodide tablets…)	Accidents with radioactive release

1.1.2 Production of fission products

Most reactors in the world are fueled with uranium that is typically enriched with 3-5% of the isotope uranium-235 of half-life 7.038×10^8 years and that can undergo the following fission reaction [2-4]:

$$_{0}^{1}n + _{92}^{235}U \rightarrow PF1 + PF2 + 2.5_{0}^{1}n + 200 MeV \qquad \text{[R1-1]}$$
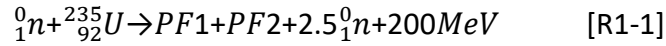
Fission occurs when the nucleus of a uranium-235 atom splits into fragments referred to as fission products (FPs). These fission products are mostly radioactive and accumulate inside the fuel pellets. Based on elemental analysis of irradiated fuels and with regard to the behavior of fission products, the chemical state of the fission products under nominal burnup conditions of a PWR can be classified into the following main groups [2, 5, 6]:

- In the form of dissolved oxides, in particular for strontium (Sr), yttrium (Y), zirconium (Zr), lanthanum (La), cerium (Ce) and neodymium (Nd);
- In the form of oxide precipitates primarily for barium (Ba) and niobium (Nb);
- In the form of metal precipitates for molybdenum (Mo), technetium (Tc), ruthenium (Ru), rhodium (Rh) and palladium (Pd);
- Mainly in the form of dissolved atoms for the volatile FPs: bromine (Br), rubidium (Rb), tellurium (Te), iodine (I) and cesium (Cs). However, the chemical state of these FPs is not fully known. Above a certain temperature, they can migrate radially within the fuel pellets and condense in the colder sections, where they form more complex compounds with fuel elements or other FPs. For example, cesium can form compounds such as cesium molybdates and cesium uranates;
- In the form of dissolved atoms or intergranular or intragranular gas bubbles: xenon (Xe) and krypton (Kr) in the case of fission gases. It should be noted that gases that accumulate at the grain boundaries are more easily released during accident situations.

Although many hundreds of FPs isotopes are formed in the reactor, most have very short half-lives and decay days to weeks after their creation. It should be highlighted that ^{131}I isotope has a short half-life of 8 days which means that it is of concern only with respect to the fuel in an operating nuclear power plant or with fuel from a reactor core that has been recently shut down. However, [129]I who has a long half-life of 15.7 million year is potentially significant in the spent nuclear fuel stored at NPPs [7, 8] and in the nuclear spent fuel reprocessing plant [9, 10]. In fact, it was found that the total mass of iodine in the core of a 900 MWe PWR with UO_2 fuel, after reactor emergency shutdown is 12.7 kg [2, 11]. Additionally, the isotopic iodine mass distribution and activity[1] in the fuel bundle of a 900 MWe PWR was estimated based on

Phébus-FPT2 test inventory data [2] (2000). Results are displayed in Table 1.2. Although the ^{128}I, ^{130m}I and ^{138}I isotopes have the lowest mass (~ 10^{-4} g), their activity (~ 10^{15}-10^{17} Bq) can be higher than that of the ^{129}I isotope (~ 10^{10} Bq) which displays the highest mass (~10^4 g), see Table 1.2. This indicates that the activity of the iodine isotopes does not rely on the isotopic mass distribution only, it relies also to the isotope's specific activity[3]. In spite of that ^{132}I isotope has the highest activity (~ 10^{18} Bq) but due to it very short half-life (2.3 hours) it cannot be of major concern in case of accidental release. Thus, based on half-life, activity and mass, the following isotopes can be predicted to be of major concern following a severe accident: ^{129}I, ^{131}I, and ^{133}I.

Table 1.2 Estimated Iodine isotopic composition and activity in the spent fuel of a 900 MWe PWR estimated from Phébus FPT2 test initial inventory [12] and total iodine mass reported in [2]. ^{m}I: Excited nuclear isomer (m:metastable).

Isotope	Half life	Estimated isotopic distribution (g)	Specific activity (Bq/g)	Activity (Bq)
^{127}I	stable	2.03×10^3	no	-
^{128}I	24.99 minutes	4.67×10^{-4}	2.18×10^{18}	1.02×10^{15}
^{129}I	1.57×10^7 years	1.04×10^4	6.74×10^6	7.03×10^{10}
$^{130\,m}$I	9.0 minutes	6.28×10^{-4}	5.95×10^{18}	3.73×10^{15}
^{130}I	12.36 hours	3.64×10^{-2}	7.22×10^{16}	2.63×10^{15}
^{131}I	8.02 days	1.46×10^2	4.59×10^{15}	6.68×10^{17}
$^{132\,m}$I	1.39 hours	3.30×10^{-3}	6.31×10^{17}	2.08×10^{15}
^{132}I	2.30 hours	3.50×10^0	3.82×10^{17}	1.34×10^{18}
^{133}I	20.8 hours	2.32×10^1	4.19×10^{16}	9.73×10^{17}
$^{134\,m}$I	3.60 minutes	9.06×10^{-3}	1.40×10^{19}	1.27×10^{17}
^{134}I	52.5 minutes	4.60×10^{-1}	9.88×10^{17}	4.55×10^{17}
^{135}I	6.57 hours	1.37×10^0	1.30×10^{17}	1.78×10^{17}
^{136}I	1.4 minutes	9.87×10^{-3}	3.66×10^{19}	3.61×10^{17}
$^{136\,m}$I	45 seconds	3.63×10^{-3}	6.83×10^{19}	2.48×10^{17}
^{138}I	6.4 seconds	4.10×10^{-4}	4.72×10^{20}	1.94×10^{17}

---

[1]Activity, in radioactive-decay processes, the number of disintegrations per second, or the number of unstable atomic nuclei that decay per second in a given sample.

[2] Test of PHEBUS FP program by IRSN: Aimed to reproduce the physical phenomena that govern reactor core meltdown, the transfer of fission products from the fuel to the containment vessel, and their fate.

[2] Specific activity is defined as the activity per quantity of atoms of a particular radionuclide.

1.2 Nuclear severe accident

Incidents and accidents at nuclear facilities are divided into seven categories according to their severity as established by the International Nuclear and Radiological Event Scale (INES) presented in Figure 1.2.

During the lifetime of one generation, there were 3 major industrial nuclear accidents with area contamination in different countries. The first, in 1979, in the second reactor at the Three Mile Island nuclear power plant at United States. Fortunately, the accident did not have significant environmental consequences and was rated as level 5 accident (Figure 1.2). The second, in 1986, on the fourth reactor of the Chernobyl plant in Ukraine. The third, in 2011, at three of the six reactors at the TEPCO's Fukushima Daiichi NPS in Japan. Chernobyl and Fukushima accidents, were provisionally rated as Level 7 accident (See Figure 1.2). Unfortunately, major accident resulted in significant amounts of radioactivity being released into the environment, for instance 5.2×10^{18} Bq (Chernobyl) and 6.3×10^{17} Bq (Fukushima) [13-15].
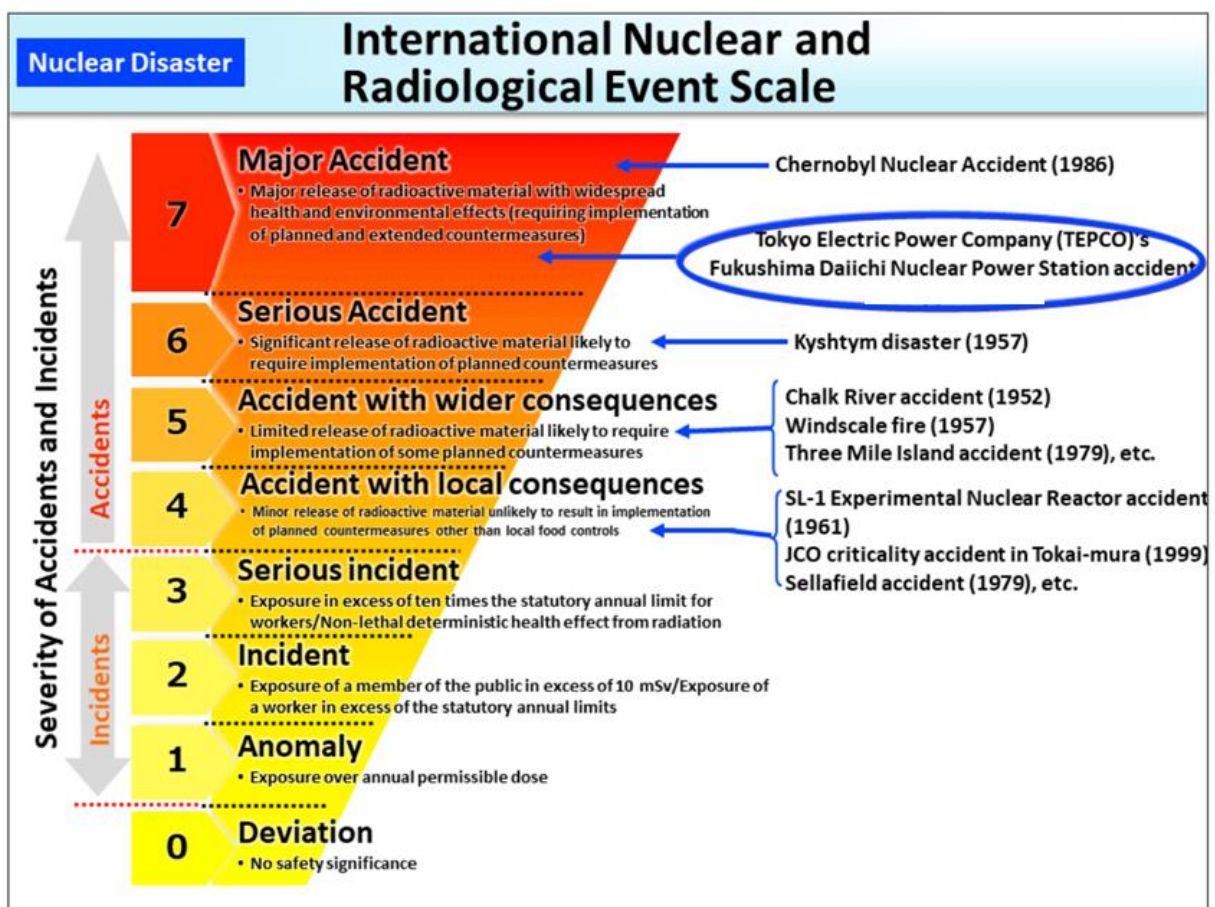
Figure 1. 2 The International Nuclear and Radiological Event Scale (INES) [16].

Indeed, these severe nuclear accidents have released significant quantities of radioactive iodine into the atmosphere as shown in Table 1.3. Of the radioactive iodines, iodine-131 is one of the most significant in terms of environmental and dosimetry impacts, considering its activity and half-life impact.

Table 1. 3 Released radioactive iodine quantity into the atmosphere, during the main accidents (NPPs and reprocessing plants).
PBq: PetaBq and TBq: TerraBq. 1TBq = 1012 Bq and 1PBq = 1015 Bq.

Accident - date (Score - INES)	^{131}I (equivalent mass)	Total iodine	Reference
Kyshtym 29/09/1957 (6)	1-10 PBq (0-2 g)	undetermined	Rapport IRSN [17]
Windscale pile 1 10/10/1957 (5)	0.74 -1.8 PBq (0.15 -0.38 g)	undetermined	Garland et al. 2007 [18]
Three Miles Island-2 28/03/1979 (5)	0.48 - 0.63 TBq (0.10 - 0.13 g)	0.56 TBq	Levin et al., 2013 [19]
Chernobyl 26/04/1986 (7)	1760 PBq (100 - 375 g)	5200 PBq	UNSCEAR, 2000 [20] IAEA, 2006 [21]
Fukushima 11/03/2011 (7)	100-200 PBq (21-42 g)	Maximum 300 PBq	NISA, 2011 [22] UNSCEAR, 2014 [23] MEXT, 2011 [24] Lebel et al., 2016 [25] Masson et al., 2019 [26]

1.2.1 Nuclear severe accident scenarios
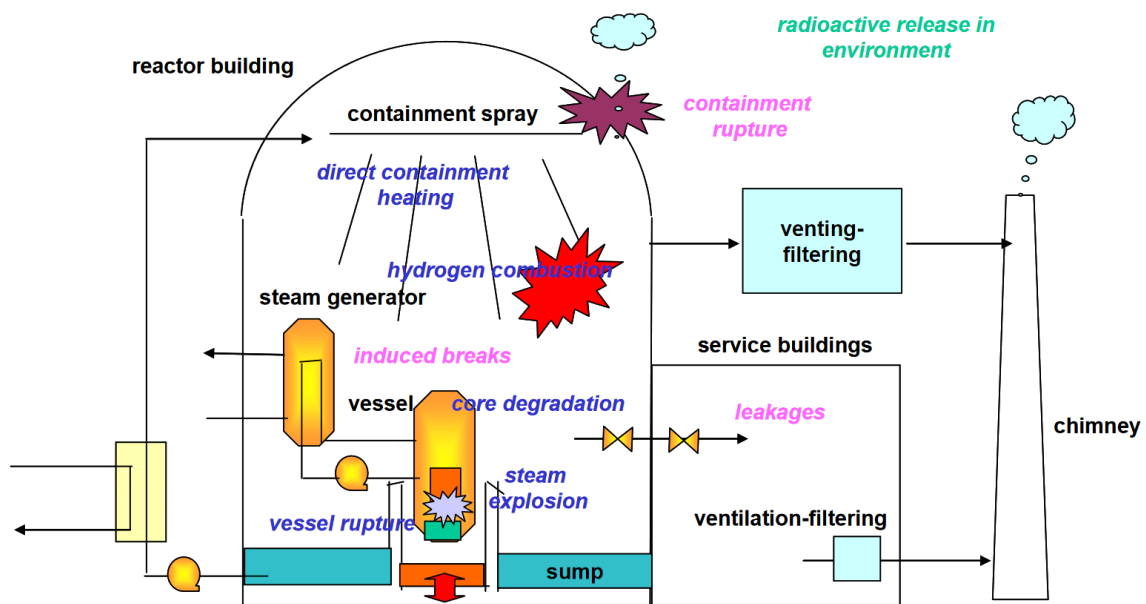
Figure 1. 3 Physical phenomena during a severe accident [27].

45

In a typical nuclear accident scenario, the initiating event(s) can be a series of failures in the primary or secondary cooling circuit, pump, etc. which can lead to partial or total loss of cooling systems [28]. Severe accidents are characterized by extended core degradation i.e., by losing its geometrical integrity induced by melting and debris formation when the non-submerged parts of the core undergo significant temperature rise (more than 1200°C). At this stage of core degradation, significant material release occurs in vapor form (volatile fission products and control rod material) which is then transported through the primary circuit and released into the containment vessel. During a severe accident, chemical reactivity in the containment vessel must take into account the released fission products, the presence of steam, water, organic material, metal and concrete surfaces, high temperatures and dose rates. Figure 1.4 summarizes the sequence of the processes involved in the release and transfer of FPs to the environment during a core melt accident.
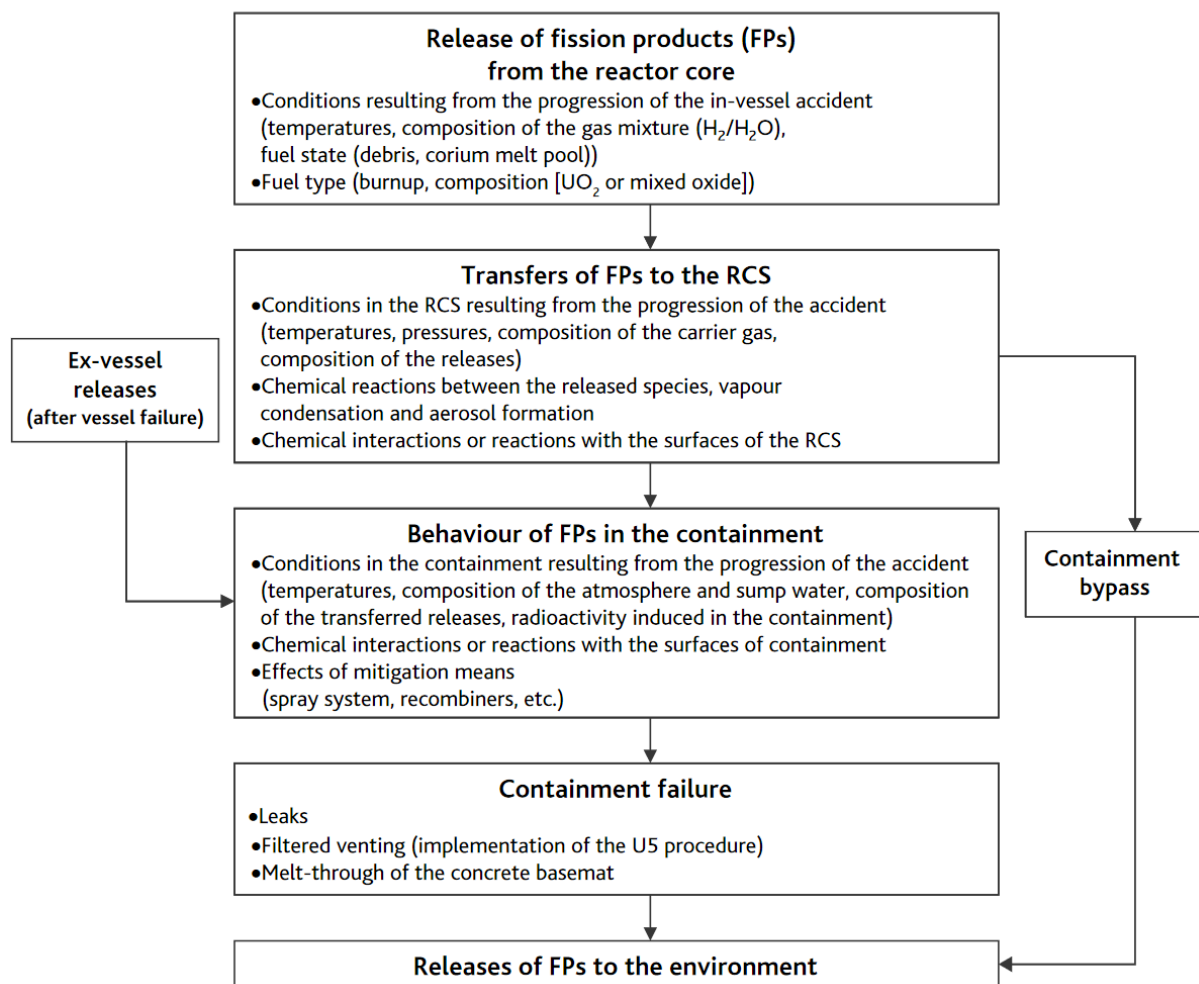
Figure 1. 4 Summary description of the processes involved in the release and transfer of fission products (FPs) to the environment during a core melt accident [2].

46

Moreover, different physical phenomena are liable to occur progressively with core degradation such as vessel rupture inducing the escape of the degraded core in the lower part of the containment and then molten core/concrete interaction in the reactor pit, or steam explosion when the molten core encounters water accumulated in the sump. In the containment atmosphere, hydrogen combustion can cause direct containment heating and finally, containment rupture, and leakages as presented in Figure 1.3. This mode of containment failure is very important as it can allow radioactive species to be released directly to the environment from virtually the very start of an accident.

It is highlighted that the main radiological significant fission products that are believed to be released into the environment in case of severe nuclear accident are iodine, cesium and tellurium. Strontium, ruthenium, barium, molybdenum and the lanthanides are less released. Among them, special attention is focused on the behavior of iodine given its complexity and the potential short-term radiological consequences of releases of radioactive iodine to the environment. The main physical and chemical forms of iodine that can be found in the containment after a core melt accident are gaseous molecular iodine (I_2), particulate iodine (i.e., in aerosol form, such as cesium iodide [CsI]) and gaseous organic iodine (i.e., methyl iodide [CH_3I]). Among these three physical and chemical forms, organic iodine is the hardest for existing filtration systems to trap. Additionally, unlike gaseous molecular iodine, the paints on the wall of the containment do not adsorb gaseous organic iodine but instead they may be released outside the containment by direct or indirect leak paths [2, 29, 30].

1.2.2 Source term

The amount and isotopic composition of the released radioactive material released from the core is called "Source Term", and its quantification has been the main objective of several international research programs for more than thirty years as it can predict the environmental consequences from radioactive product release. IRSN defines the source term as a specific type of release characteristic to a family of reactors and representative of the accident type, i.e., in general a containment failure mode following complete core melt [1]. The source term is taken into consideration when defining corrective actions that have to be taken to protect people under these conditions. Three source terms, listed in decreasing order of severity, were defined in 1979 as [2]:

– Source term S1 corresponds to short-term containment failure occurring no more than a few hours after the onset of the accident;

– Source term S2 corresponds to direct releases to the atmosphere following loss of containment integrity occurring one or more days after the onset of the accident;

– Source term S3 corresponds to indirect, delayed releases to the atmosphere through pathways allowing a significant amount of fission products to be retained.

For instance, the retained iodine source terms for a 900 MWe reactor are listed in Table 1.4. Data in Table 1.4 shows the importance of avoiding an early containment failure and the role of filtration i.e., strong reduction of the source term by limiting iodine release to the atmosphere.

Table 1. 4 Evaluated iodine source terms S1, S2 and S3 in 2000 for a 900 MWe PWR [2,31]. Source terms are given in percentages of the initial activity present in the reactor core.

Source Term		S1	S2	S3
% Inorganic iodine	% aerosols	60	2.7	4.2×10^{-3}
	% molecular iodine			2.5×10^{-8}
% Organic iodine		0.7	0.55	0.55

The source terms for a given accident can be evaluated by the ASTEC software (Accident Source Term Evaluation Code) developed by IRSN since 1995 [32]. The ASTEC code is dedicated to the detailed modelling of the phenomenology of a severe accident and its consequences. In general, the ASTEC code models release of FPs according to three categories: (1) volatile FP releases (Xe, Kr, I, Br, Cs, Rb, Sb, Te) (2) semi-volatile FP releases (3) non-volatile FP releases. In the case of iodine, IRSN published a summary in 2010 [33] and 2014 [34] detailing the model of the iodine chemistry in the containment during a core melt accident implemented in the ASTEC code and its use to conduct safety studies for power reactors during a core meltdown accident.

1.3 Lessons learned from radioiodine release into the atmosphere

The understanding of the environmental behavior of radioiodine starts with the understanding of the different chemical and physical forms that radioiodine can take, and how each of these, individually, behave in the atmosphere. As mentioned in the previous section, radioiodine can be emitted into the atmosphere either in gaseous or in aerosol form. Once in the atmosphere, each of the different chemical forms of radioiodine would have been subject to different chemical and photochemical processes with naturally occurring atmospheric species as gases and aerosols. Deposition processes are also identified as one of the iodine depletion pathways from the atmosphere [35].

1.3.1 Dispersion of radioiodine

Both Chernobyl and Fukushima accidents caused radionuclide contamination of the atmosphere. Unlike Chernobyl, the impact of the Fukushima accident was concentrated on a local scale, but the duration of radioactive release was longer than a month. According to various studies [13, 15, 23, 36] 131-Iodine isotope has the highest activity in both accidents in comparison to other Iodine isotope (^{129}I, ^{133}I) as shown in Table 1.5.

Table 1. 5 Comparison of the estimated atmospheric release of radioiodine from the nuclear accidents at Chernobyl and Fukushima [13].

Radionuclide	Half life	Activity (PBq)	
		Chernobyl	Fukushima
^{129}I	1.57×10^7 years	4×10^{-5}- 4.8×10^{-5}	6.6×10^{-6}
^{131}I	8.02 days	~1760	200
^{133}I	20.8 hours	910	146

Notably and by recalling section 1.1.2, this high activity of ^{131}I is linked to its mass in the spent fuel and its high specific activity. In addition, its several days long half-life allow significant persistence of this isotope in the atmospheric compartment in case of releases. The other iodine isotopes which present higher activities in the spent fuel (as shown in Table 1.2), have nevertheless shorter half lifes (20.8 hours for ^{133}I) so that their persistence in the atmosphere remains limited in time (and distance). 131-Iodine (^{131}I) is thus considered as one of the important radionuclides released during a major severe nuclear accident.

Activity concentrations of ^{131}I in air after the accident of Chernobyl and Fukushima, arranged by distance to the respective NPPs are listed in Table 1.6. This table shows that although, the half-life of ^{131}I is short enough (8.02 days) to cause high specific activities, but long enough to allow long-distance (>3000 km) atmospheric dispersion when released into the atmosphere. Moreover, it should be noted that local meteorological conditions cause great variability in activity concentrations in environmental media and can result in locations further away being higher in concentration than closer locations [13, 15, 36].

Table 1. 6 Selected maximum radionuclide concentrations in air after the accidents of Chernobyl and Fukushima, arranged by distance from the NPPs [13]. Conversion to ppt volumic based on ^{131}I specific activity of 4.6 $10^{15}bq.g^{-1}$.

Location	Distance from NPPs in Km	Activity of ^{131}I in Bq.m^{-3}	[^{131}I] in ppt
Chernobyl			
Chernobyl NPP	0	750,000	3×10^{-2}
Chernobyl UA	1	58,000	2×10^{-3}
Berezinsky Natural Res. BY	400	200	8×10^{-6}
Sweden	1150	12	5×10^{-7}
Chilton. UK	2200	0.96	4×10^{-8}
Chiba. JP	8200	1	4×10^{-8}
Livermore.CA. US	9800	0.074	3×10^{-9}
Fukushima			
Fukushima Daiichi	0	5600	2×10^{-4}
Fukushima Daiichi	10	2100	9×10^{-5}
Futoba. JP	25	530	2×10^{-5}
Wako. JP	220	47	2×10^{-6}
Busan. ROK	1100	0.00132	5×10^{-11}
Midway island	4000	0.0093	4×10^{-10}
Reykjavik. IS	8600	0.003	1×10^{-10}
Tessaloniki. GR	9300	0.000497	2×10^{-11}

Environmentally, ^{131}I releases in gaseous form can travel at relatively low altitudes (400 – 1200 m) [36]. In addition, following the Fukushima accident, measurements of radioiodine release from both near and far sites (Lebel et al., 2016 [25]), (Masson et al., 2011 [38]) during the largest releases are listed in Table 1.7. These measurements showed that particulate fraction in the near sites could be dominant depending on the release events. For instance, it was measured that in the 2nd release event the composition of the released ^{131}I airborne was 61% in a volatile form, with the remainder being emitted as particulates. Whereas, during the 3rd release event the composition was 70% in particulate form. However, at the far sites from NPPs the gaseous forms were in the majority. Thus, this indicates that the nature of released iodine varies strongly with the distance. This variation reflects possible unidentified exchange cycles of the particulate and gaseous forms of iodine in the atmosphere, which can be due to photo dissociation or/and reactivity with the atmospheric species. For example, even if the release occurs only in gaseous form, iodine in air can transform to less volatile aerosol species or attach to existing particles.

Table 1. 7 Estimated volatile ^{131}I composition of major releases during the Fukushima Daiichi accident. The particulate fraction is the supplement to 100% [25].

		Volatile iodine fraction		
	Location (Distance from NPPs)	14-16 March 2011 (1st release)	19-26 March 2011 (2nd release)	29-31 March 2011 (3rd Release)
Near sites	Daiichi (1 km)	undetermined	61%	31%
	Daini (11 km)	undetermined	15%	34%
Far sites	NSRI (112 km)	49%	47%	78%
	NCL (116 km)	52%	51%	69%

With this intention, the French Institute of Radioprotection and Nuclear Safety (IRSN) has developed specific simulation software's (C3X plateform) capable of reproducing the release and dispersion of the radionuclides in the atmosphere [39]. However, one potential problem with such simulation tools is that the transport of 131-Iodine products following an accident is currently modelled without considering the reactivity of iodine in the atmosphere.

1.3.2 Radioprotection

After a nuclear accident and the release of radionuclides, into the environment, human health can be affected in several ways, including external and internal exposure as presented in Figure 1.5. Indeed, gaseous radioactive iodine, especially the ^{131}I isotope, with a half-life of 8 days, poses a health hazard if present in high concentrations due to its easy and almost irreversible transport to the human thyroid gland, where it can locally induce cancer. In the case of Chernobyl accident, ^{131}I was largely responsible for absorbed doses to the thyroid, which were delivered over a relatively short period after the accident (via inhalation and ingestion) [23, 40].
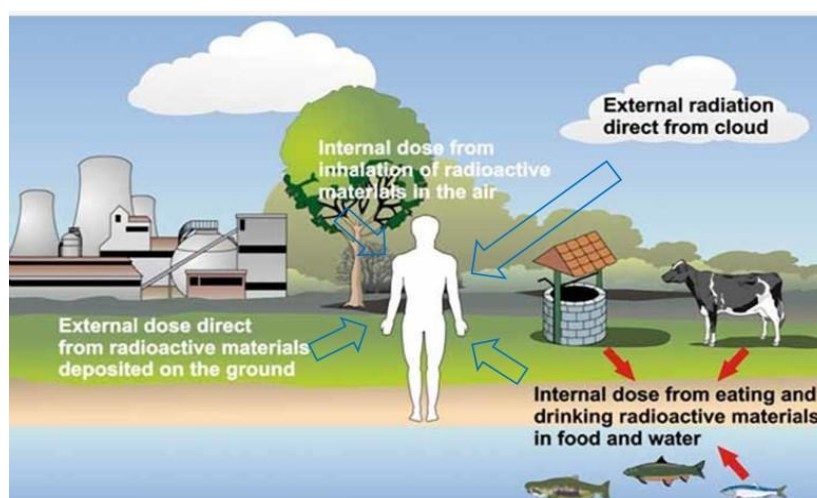
Figure 1. 5 Exposure pathways from releases of radioactive material to the environment [41].

The knowledge of thyroid equivalent dose (TED) is essential for evaluating a causal association of thyroid cancer. As reported previously [42], the estimated TED (mSv) via inhalation is proportional to the ^{131}I incorporated activity (Bq) by a conversion factor called the dose coefficient (Sv.Bq^{-1}). Dose coefficients are dependent of the chemical form and three chemical forms are referenced in the literature for ^{131}I-particulate, ^{131}I-elemental vapor, and ^{131}I-methylated. As an example, the dose coefficient of the three ^{131}I chemical forms for 1-year-old, 5-years-old, 10-years-old, 15-years-old, and adults that further will be used to calculate the estimated thyroid equivalent dose via inhalation in Fukushima prefecture are listed in Table 1.8. As can be seen, the children of 1 year old have the highest dose coefficient for the three ^{131}I chemical forms. Notably, then the dose coefficients decrease with increasing age. Therefore, younger population can be exposed to greater health risks.

Table 1. 8 Dose coefficient in Sv.Bq^{-1} for ^{131}I to calculate estimated thyroid equivalent dose for 1-years-old, 5-years-old, 10-years-old, 15-years-old, and adults via Inhalation [42, in supplementary information].

A	Conversion factor		
	Methyl form (^{131}I)	Elemental vapor form (^{131}I)	Particle aerosol (^{131}I), AMAD=1.0 μm, Type F
Unit	Sv/Bq		
1-year-old	2.5×10^{-6}	3.2×10^{-6}	1.4×10^{-6}
5-year-old	1.5×10^{-6}	1.9×10^{-6}	7.3×10^{-7}
10-year-old	7.4×10^{-7}	9.5×10^{-7}	3.7×10^{-7}
15-year-old	4.8×10^{-7}	6.2×10^{-7}	2.2×10^{-7}
Adult	3.1×10^{-7}	3.9×10^{-7}	1.5×10^{-7}

Further, at different ages, the aerosol form of iodine has the lowest dose coefficient and elemental vapor iodine form has the highest dose coefficient (see Figure 1.6). Indeed, as the TED is proportional to incorporated activity, the release of elementary gaseous iodine can be more dangerous to population health than with aerosols and methyl iodine forms release. Thus, this indicate that the estimation of TED is dependent on the chemical form of the released iodine and needs a good knowledge of the fate of each form of iodine that will be emitted and then transported to avoid any underestimation or overtestimation of the TED. Furthermore, it should be recalled that the concentration and chemical form of released iodine varies strongly with the distance (see section 1.3.1- Table 1.6 and 1.7), therefore, TED is also dependent on the dispersion of radioiodine in the atmosphere after a nuclear severe accident. This has been already proven by the measurements and estimation of TED from different sites with respect to the Fukushima NPPs [42, 43]. However, current estimations did

not consider the fate of the iodine species in the atmosphere, which it may influence the ^{131}I-TEDs. This suggest the following:

- Dose estimation, which takes into account the iodine reactivity in the atmosphere, will be more valuable.

- The necessity to improve current dispersion tools by considering the reactivity of iodine species in the atmosphere in order to better predict the thyroid equivalent dose.
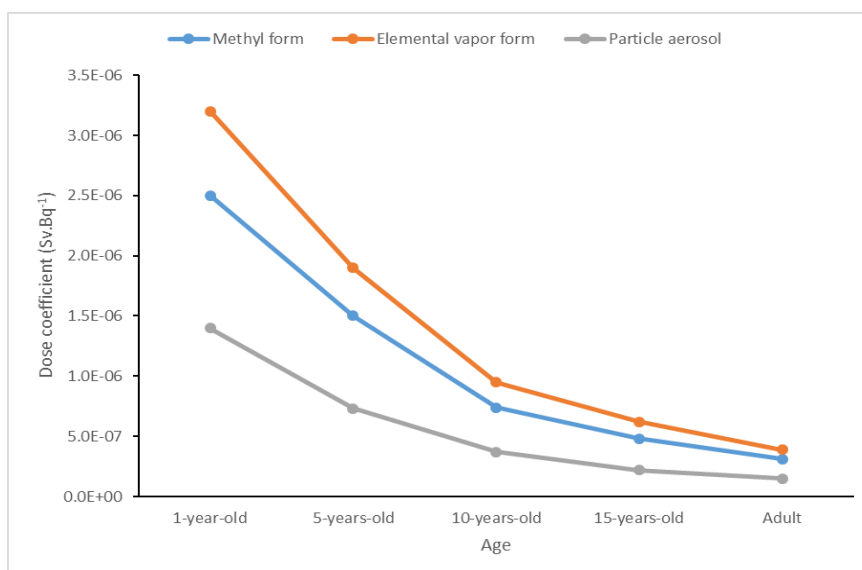
Figure 1. 6 Evolution of dose coefficient as function age via inhalation [42].

1.4 Conclusion

Unfortunately, in the event of a PWR severe accident, an important amount of volatile radioactive in gaseous form (mainly, I_2 and RI-type CH_3I) can be released into the atmosphere compartment where it can induce dramatical consequences on human in case of inhalation / ingestion. These iodine species are highly reactive and will interact, at least in the near field (i.e. at least within 11 km with respect to the point of emission) with the other species present in the atmosphere (gas or particles), where they can evolve either in gaseous or particulate form. Thus, the knowledge of the reactivity of iodine and its behavior in the atmosphere is also of prime importance to better predict the dispersion of iodine in the atmosphere in case of severe accident. Additionally, it will help to better evaluate the radiological health impact of the accidental releases of iodine. To date, IRSN has launched preliminary research studies to develop a comprehensive modelling approach to better predict the iodine source term (ASTEC), and its transfer to the biosphere (SYMBIOSE platform) and more specifically its dispersion in the atmospheric compartment (C3X software) following a severe nuclear power plant reactor accident. Currently, these tools integrate the iodine transfer in the environment

without considering the possible iodine behavior in the atmosphere. In this context, reactivity of both gaseous molecular iodine (I_2) and iodomethane (CH_3I) appears to be of central importance in understanding the radioiodine dispersion in the atmosphere if a severe nuclear power plant accident type Chernobyl (Ukraine) and the more recent Fukushima (Japan) disaster were to occur. Such knowledge is of a major importance to complete the understanding of iodine dispersion in the atmosphere in order to better protect the population in case of nuclear severe accident.

References

[1] How Does a Nuclear Reactor Work?, (2019). https://www.energy.gov/ne/articles/nuclear-101-how-does-nuclear-reactor-work. [Citation in April 2020].

[2] D. Jacquemain et al., Nuclear Power Reactor Core Melt Accidents. IRSN book, ISBN: 978-2-7598-1835-8, France, 2015.

[3] C. Alejano, D. Boulanger, M. Brady-raap, l. Jutier, C. Riffard, Y. Rugama, Spent nuclear fuel assay data for isotopic validation, 2011. OECD,NEA/NSC/NPNCS/DOC(2011)5.

[4] Uranium Enrichment, World Nucl. Assoc. [Citation in April 2020].

https://www.world-nuclear.org/information-library/nuclear-fuel-cycle/conversionenrichment-and-fabrication/uranium-enrichment.aspx#.UWrver-IRAs.

[5] H. Kleykamp, The chemical state of the fission'products in oxide fuels, J. Nucl. Mater. 131 (1985) 221–246. https://doi.org/10.1016/0022-3115(85)90460-X

[6] B.J. Lewis, W.T. Thompson, F.C. Iglesias, Fission Product Chemistry in Oxide Fuels, J. Nucl. Mater. 2 (2012) 515-546. https://doi.org/10.1016/B978-0-08-056033-5.00042-2.

[7] Y. Ando, K. Nishihara, H. Takano, Estimation of spent fuel compositions from light water reactors, J. Nucl. Sci. Technol. 37 (2000) 924–933. https:// doi.org/10.1080/18811248.2000. 9714974.

[8] Spent fuel composition, Radioactivity. [Citation in April 2020]. https://www.radioactivity.eu.com/site/pages/Spent_Fuel_Composition.htm.

[9] J.E. Moran, S. Oktay, P.H. Santschi, D.R. Schink, Atmospheric Dispersal of 129 Iodine from Nuclear Fuel Reprocessing Facilities, 33 (1999) 2536–2542. https://doi.org/10.1021/ es9900050.

[10] C.Frechou, D.Calmet, 129I in the environment of the La Hague nuclear fuel reprocessing plant - from sea to land, J. Environ. Radioact. 70 (2003) 43–59. https://doi.org/10.1016/ S0265-931X(03)00127-9.

[11] D. Jacquemain et al., Les accident de fusion du coeur des réacteur nucléaires de puissance, IRSN book, ISBN : 978-2-7598-0972-1, France, 2013.

[12] A.C. Gregoire, P. March, F. Payot, G. Ritter, E. Al., Phébus FPPT2 final report – Appendix A – Material inventory IRSN Report DPAM/DIR 2008-272 Phebus IP/08/579, 2008.

[13] G. Steinhauser, A. Brandl, T.E. Johnson, Comparison of the Chernobyl and Fukushima nuclear accidents: A review of the environmental impacts, Sci. Total Environ. 470–471 (2014) 800–817. https://doi.org/10.1016/j.scitotenv.2013.10.029.

[14] V. Kortov, Y. Ustyantsev, Chernobyl accident: Causes, consequences and problems of radiation measurements, Radiat. Meas. 55 (2013) 12–16.https://doi.org/10.1016/j.radmeas.2012.05.015.

[15] T. Imanaka, G. Hayashi, S. Endo, Comparison of the accident process , radioactivity release and ground contamination between Chernobyl and Fukushima-1, J. Radiat. Res. 56 (2015) 56–61. https://doi.org/10.1093/jrr/rrv074.

[16] International Nuclear and Radiological Event Scale, Int. Nucl. Event Scale. (2016). https://www.env.go.jp/en/chemi/rhm/basic-info/1st/02-02-01.html. [Citation in April 2020].

[17] A.C. Grégoire, L'iode dans l'atmosphère : du terme source à la dose, Rapport interne IRSN, n° IRSN/2019-00035, 2019.

[18] J.A. Garland, R. Wakeford, Atmospheric emissions from the Windscale accident of October 1957, Atmos. Environ. 41 (2007) 3904–3920. https://doi.org/10.1016/j.atmosenv .2006.12.049.

[19] R.J. Levin, N.F. De Simone, J.F. Slotkin, B.L. Henson, Incidence of thyroid cancer surrounding three mile island nuclear facility: The 30-year follow-up, Laryngoscope. 123 (2013) 2064–2071. https://doi.org/10.1002/lary.23953.

[20] Unscear, sources and effects of ionizing radiation, Annex J: Exposures and effects of the Chernobyl accident, 2000. https://www.unscear.org/unscear/publications.html.

[21] IAEA, Radiological Assessment Reports Series. Environmental Consequences of the Chernobyl Accident and their Remediation: Twenty Years of Experience, International Atomic Energy Agency report, ISBN 92–0–114705–8, 2006.

[22] NISA, Evaluation of the status of reactor cores in units 1-3 of the Fukushima Daiichi nuclear power plant, 2011. [Citation in April 2020]. http://www.meti.go.jp/press/2011/06/20110606008/20110606008-2.pdf (in Japanese).

[23] Unscear, report to the general assembly scientific annex A: Volume I, 2014.https://www.unscear.org/unscear/publications.html.

[24] MEXT, Radioactive Substance Emission Data, press release, October 20, 2011 in Japanese, 2011. www.meti.go.jp/press/2011/10/20111020001/20111020001.pdf. [Citation in April 2020].

[25] L.S. Lebel, R.S. Dickson, G.A. Glowa, Radioiodine in the atmosphere after the Fukushima Dai-ichi nuclear accident, J. Environ. Radioact. 151 (2016) 82–93. https://doi.org/10.1016/j.jenvrad.2015.06.001.

[26] O. Masson, J. Tschiersch, L.S. Lebel, H. Wershofen, J.W. Mietelski, G. Steinhauser, É.Blanchardon, L.Cantrel, A.C. Grégoire, D. Quélo, Radioiodine Releases in Nuclear Emergency

Scenarios, In: Nuclear Emergencies. Springer, ISBN: 978-981-13-8327-4, Singapore, 2019. https://doi.org/10.1007/978-981-13-8327-4_15.

[27] Research and development with regard to severe accidents in pressurised water reactors: Summary and outlook. Report IRSN-2007/83, 2007.

[28] A. Karhu, Gas Phase Chemistry and Removal of CH_3I during a Severe Accident; Report: NKS-25, ISBN 87-7893-076-6. Corpus ID: 59022982. Danka Services International, DSI., Denmark, 2001.

[29] H. Bruchertseifer, R. Cripps, S. Güntay, B. Jäckel, Experiments on the Retention of the fission product iodine in nuclear reactor accidents (CH--0401). Report NIS/IAEA, reference number 36002863 Gschwend, B. (Ed.). Switzerland, 2004.

[30] S. Dickinson, A. Auvinen, Y. Ammar, L. Bosland, B. Clément, F. Funke, G. Glowa, T. Kärkelä, D.A. Powers, S. Tietze, G. Weber, S. Zhang, Experimental and modelling studies of iodine oxide formation and aerosol behaviour relevant to nuclear reactor accidents, Ann. Nucl. Energy. 74 (2014) 200–207. https://doi.org/10.1016/j.anucene.2014.05.012.

[31] M. Manesse, D., Fallot, A., Billarand, Y., Durin, Réévaluation des termes sources de référence; Note de synthèse, Note technique DPEA/SEAC/2000-036., 2000.

[32] J.P. Van Dorsselaere, C. Seropian, P. Chatelard, F. Jacq, J. Fleurot, P. Giordano, N. Reinke, B. Schwinges, H.J. Allelein, W. Luther, The ASTEC integral code for severe accident simulation, Nucl. Technol. 165 (2009) 293–307. https://doi.org/10.13182/NT09-A4102.

[33] L. Bosland, L. Cantrel, N. Girault, B. Clement, L. Bosland, N. Girault, B. Clement, Modeling of Iodine Radiochemistry in the ASTEC Severe Accident Code : Description and Application to FPT-2 PHEBUS Test, Nucl. Technol. 171 (2010) 99–107. https://doi.org/10. 13182/NT10-A10774.

[34] K. Chevalier-Jabet, F. Cousin, L. Cantrel, C. Séropian, Source term assessment with ASTEC and associated uncertainty analysis using SUNSET tool, Nucl. Eng. Des. 272 (2014) 207–218. https://doi.org/10.1016/j.nucengdes.2013.06.042.

[35] O.T. Bah, Communication prive, determination expérimentale du dépôt par temps sec de l'iode moléculaire.

[36] T. Christoudias, J. Lelieveld, Modelling the global atmospheric transport and deposition of radionuclides from the Fukushima Dai-ichi nuclear accident, Atmos. Chem. Phys. 13 (2013) 1425–1438. https://doi.org/10.5194/acp-13-1425-2013.

[37] R. Pollanen, I. Valkama, H. Toivonen, Transport of radioactive particles from the Chernobyl accident, Atmos. Environ. 31 (1997) 3575–3590. https://doi.org/10.1016/S1352-2310(97)00156-8.

[38] O. Masson, A. Baeza, J. Bieringer, K. Brudecki, S. Bucci, et al., Tracking of Airborne Radionuclides from the Damaged Fukushima Dai-Ichi Nuclear Reactors by European Networks, Environ. Sci. Technol. 45 (2011) 7670–7677. https://doi.org/10.1021/es2017158.

[39] M. Tombette, E.Quentric, D. Quélo, J. Benoit, A. Mathieu, I. Korsakissok, D. Didier, C3X : A software platform for assessing the consequences of an accidental release of radioactivity into the atmosphere, Poster, France, 2014.http://venus.iis.u-tokyo.ac.jp/English/workshop/Poster/3rd March/Damien Didier.pdf.

[40] A. V Brenner, M.D. Tronko, M. Hatch, T.I. Bogdanova, V.A. Oliynik, J.H. Lubin, L.B. Zablotska, V.P. Tereschenko, R.J. Mcconnell, G.A. Zamotaeva, P.O. Kane, A.C. Bouville, L. V Chaykovskaya, E. Greenebaum, I.P. Paster, V.M. Shpak, E. Ron, I - 131 Dose Response for Incident Thyroid Cancers in Ukraine Related to the Chornobyl Accident, Environ. Health Perspect. 119 (2011) 933–939. https://doi.org/10.1289/ehp.1002674.

[41] M. del R. Perez, E. Van Deventer, B. Amzal, L. Anspaugh, Health Risk Assessment from the Nuclear Accident after the 2011 Great East Japan Earthquake and Tsunami. World health organization report, ISBN 978 92 4 150513 0, Switzerland, 2013.

[42] T. Ohba, T. Ishikawa, H. Nagai, S. Tokonami, A. Hasegawa, Reconstruction of residents thyroid equivalent doses from internal radionuclides after the Fukushima Daiichi nuclear power station accident, Nat. Sci. Reports. 10 (2020) 3639. https://doi.org/10.1038/s41598-020-60453-0.

[43] E. Kim, K. Yajima, S. Hashimoto, K. Tani, Y. Igarashi, T. Iimoto, N. Ishigure, H. Tatsuzaki, M. Akashi, O. Kurihara, Reassessment of internal thyroid doses to 1,080 children examined in a screening survey after the 2011 fukushima nuclear disaster, Health Phys. (2020) 36–52. https://doi.org/10.1097/HP.0000000000001125.

Chapter 2: State of art
Iodine chemistry in the atmosphere

In the event of a major nuclear accident, the gaseous iodine species, which are likely to be emitted into the atmosphere, are essentially identified as I_2 and CH_3I. Once released into the atmosphere, they can undergo reactions leading to their conversion into various iodine species. The quantities emitted can be significant at the point of release compared to naturally occurring emissions, and are of crucial importance due to the radiotoxicity of radioactive iodine (131-Iodine in particular). However, the life cycle of these radioactive species emitted to the atmosphere will be the same as that of the same natural stable species under similar atmospheric conditions.

In addition to its nuclear safety interests, iodine has a strong interest in the atmospheric chemistry field due to its oxidizing properties and photochemical reactivity, which play an important role in tropospheric chemistry. For more than 40 years, numerous experimental and theoretical works have been carried out on the quantification of iodine forms (gaseous or particulate) in the troposphere, on the identification of natural sources of iodine release and finally on its reactivity, with the aim of better understanding the iodine cycle and its interaction with other compounds present in the troposphere, whether of natural or anthropogenic origin (ozone, radicals, VOCs, nitrogen oxides, etc.). Thus, many mechanisms of iodine have been developed and a large database of the iodine cycle data is now available.

This chapter briefly presents the sources of gaseous iodine and its reactivity in the atmosphere related to the iodine cycle. The sources of atmospheric aerosols and gas-aerosols heterogeneous interactions are briefly exposed. The experimental approaches described in the literature to study this reactivity are then briefly presented. Finally, a critical review of the interaction of gaseous iodine species with atmospheric aerosols is given.

2.1 Main sources of iodine compounds

Iodine is a natural trace element of biological significance, where 127-Iodine is a naturally occurring iodine isotope, and it is the only non-radioactive and stable iodine isotope. Biogenic processes in the oceans represent a substantial source of iodine in the lower atmosphere. Molecular iodine (I_2) and organic iodide species such as methyl iodide (CH_3I), ethyl iodide (C_2H_5I), propyl iodide (isomers :1 and 2-C_3H_7I), butyl iodide (isomers: 2 and i-C_4H_9I), methylene

iodide (CH_2I_2), chloroiodomethane (CH_2ICl), bromoiodomethane (CH_2IBr) are mainly emitted from algae and phytoplankton in the oceans [1, 2], whereas inorganic iodine species, such as I_2, HOI and IO, come mainly from heterogeneous reactions at the ocean/atmosphere interface [3, 4].

Measurements of iodine species in the atmosphere are performed since several decades. They indicate that natural iodine is present in the atmosphere with levels in the ppt range for both organic and inorganic species in the marine environment (coastal or open sea) [5-7] as shown in Table 2.1. Significant variations are observed depending on the location (marine environment, open sea, latitude) and seasonality.

Table 2. 1 Field measurements of the concentration range of iodine species [6-8] and their estimated atmospheric lifetime [9, 10].

Iodine species	Concentration (ppt V/V)		Abundance descending order of iodine species	Atmospheric lifetime in the lower troposphere
	Minimum	**Maximum**		
I_2	0.02	302	**CH_3I**	5-11 days
I	2	22	**$1-C_4H_9I$**	Undetermined
OIO	0.5	27	**I_2**	~10 seconds
IO	0.2	54	**C_2H_5I**	4 days
HOI		0.014	**IO**	Few seconds
HOIO		8.28	**$1-C_3H_7I$**	12 hours
$HOIO_2$		9.93	**OIO**	1 hour
CH_3I	0.004	1830	**I**	Undetermined
CH_2I_2	0.01	19.8	**CH_2I_2**	2-10 minutes
C_2H_5I	0.02	96.9	**$i-C_4H_9I$**	undetermined
$1-C_3H_7I$	0.01	34.8	**CH_2ICl**	2.4 hours
$2-C_3H_7I$	0.02	9.1	**$2-C_4H_9I$**	undetermined
$1-C_4H_9I$	0.2	321	**CH_2IBr**	1 hour
$2-C_4H_9I$	0.02	12.3	**$HOIO_2$**	undetermined
$i-C_4H_9I$	0.04	14.4	**$2-C_3H_7I$**	28.8 hours
CH_2ICl	0.04	12.4	**HOIO**	undetermined
CH_2IBr	0.01	9.9	**HOI**	undetermined

Oceanic emissions of methyl iodide are believed to be the dominant source of iodine [5]. Indeed, CH_3I was first observed in the atmosphere in the ppt (v/v) range [11] and recently was highly observed (1830 ppt) at Brittany, France [8]. Estimation of CH_3I global annual emission rate in the marine boundary layer is 114- 1163 Gg.year^{-1} with atmospheric lifetime of 5-11 days [5, 12-15]. Methyl iodide, has also several terrestrial sources such as natural wetlands, rice paddies and biomass burning that together are believed to contribute up to 80–110 Gg.year^{-1} [14, 16-18]. Additionally, other volatile halogenated iodocarbons mainly including ethyl iodide (C_2H_5I), 1- and 2- propyl iodide (C_3H_7I), butyl iodide (1, 2 and $i-C_4H_9I$), methylene

iodide (CH_2I_2), chloroiodomethane (CH_2ICl) and bromoiodomethane (CH_2IBr), have been detected in the atmosphere mostly in coastal regions [8, 19, 20]. Furthermore, methyl iodide has the highest lifetime among the organic iodide species. Thus, methyl iodide is the major contribute to the amount of organic iodine in the atmosphere.

Alternatively, inorganic iodine compounds (I_2, HOI, IO) produced in the ocean surface layer from the reaction of O_3 with iodide are thought to be a dominant global source of iodine mainly at the coastal margin [3, 21]. For instance, it has been shown that reactive I_2 can escape directly from the ocean surface to the atmosphere when brown algea (*kelp, Laminaria digitate)* are subjected to oxidative stress such as by exposure to high irradiance, desiccation, and atmospheric O_3 [3, 22,23]. The emission rate of I_2 from the action of O_3 at the sea surface is 0.4-1 Tg.year^{-1}. I_2 is highly photo reactive, as its photolysis lifetime is very short ~15 seconds [4, 24, 25]. Additionally, laboratory data have suggested that inorganic iodide such as molecular Iodide (I_2) [3, 21], hypoiodous acid (HOI) [3], iodine oxide (IO) [21] can be produced from heterogeneous reactions at the ocean-atmosphere interface.

Field measurements evidenced the presence of iodine rich aerosols in the atmosphere [26, 27]. Recently, iodine aerosol concentrations have been reported to be the highest in the tropical marine boundary layer (MBL), averaging 5 ng.m^{-3} with monthly maximum concentrations of 90 ng.m^{-3} [28].

Numerous experimental and theoretical works have been carried out on the quantification of iodine forms (gaseous or particulate) in the troposphere, on the identification of sources of iodine release and finally on its reactivity, with the aim of better understanding the iodine cycle and its interaction with other compounds present in the troposphere, whether of natural or anthropogenic origin (ozone, radicals, VOCs, nitrogen oxide.). Figure 2.1 summarizes the main sources and fate of iodine species in the atmosphere.

It should be highlighted that anthropogenic releases of atmospheric iodine species are believed to be negligible on a global scale compared to natural sources. Finally, iodine species are commonly observed in the atmosphere following severe nuclear accident as shown in Chapter 1 – though at levels much more lower than the natural occurrence, even at the close proximity of the accident (see chapter 1, Table 1.6).
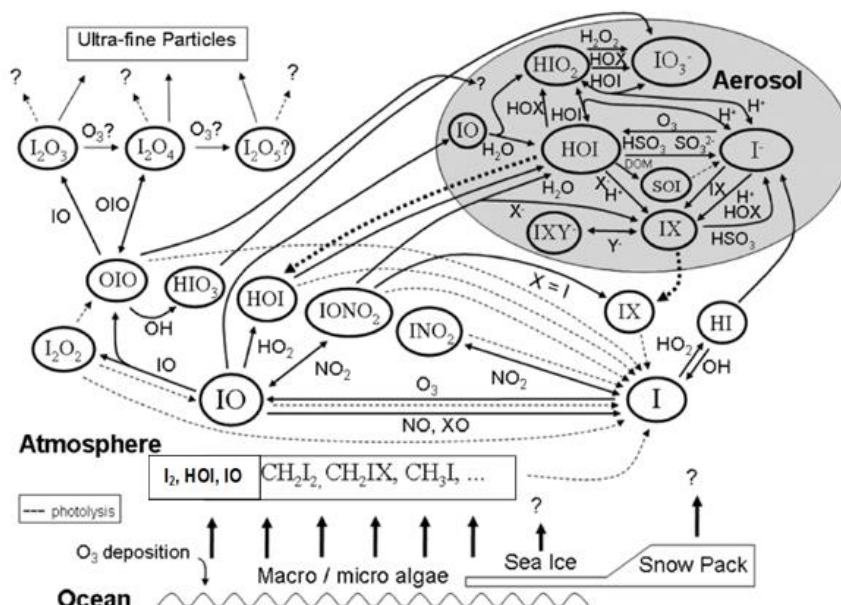
Figure 2. 1 Simplified Diagram representing the reactivity of iodine in the atmosphere taken from [5].

2.2 Gaseous Iodine reactivity

Although iodine is present only in trace amounts (pptv level), it may participate in the destruction of ozone layer like other halogen species (Cl, Br), in the removal of large variety of organic and inorganic species, in the formation of ultrafine aerosols and cloud condensation nuclei, and may play a role in climate change [5, 29, 30].

To date, it is well known that iodine species significantly influence a variety of atmospheric processes. Field campaign measurements, do not only provide the knowledge regarding the sources, and atmospheric concentrations of organic and inorganic iodine compounds in the atmosphere, but also can give insights on the chemical reactivity of iodine species in atmosphere. Measurements of the iodine gas reactivity have been mostly based on the observation of the key reactive iodine radicals which are mainly I, IO and OIO [25, 31, 32]. Indeed, the main source of such radicals are molecular iodine and alkyl iodide that are emitted from ocean and undergo photolysis on timescales of seconds to days, releasing their constituent iodine atoms, which then react with ozone, forming the iodine oxide radicals. On the other hand, direct observation of reactive iodine species in the atmosphere can demonstrate the presence of the iodine activity, which contributes to the ozone destruction as well as to the oxidation capacity of the troposphere via catalytic destruction and by affecting the NO/NO_2 and OH/HO_2 partitioning ratios [33-35]. In addition, the observation of new ultra-fine particles (I_xO_y molecules) indicates the key role of iodine in the aerosol formation [36, 37].

The observations from field measurements have been accompanied by laboratory and modelling studies to improve knowledge regarding the reactivity of iodine species in the atmosphere which can involve an important number of chemical species and reactions (homogeneous and heterogeneous). During the day, the major fate of iodine-emitted species by natural oceanic sources is photolysis leading rapidly to the formation of iodine atoms [34, 38, 39], for instance:

$CH_3I + h\nu \rightarrow CH_3 + I$, $k= (0.5\text{-}6.6) \times 10^{-6}$ s^{-1} [R2-1]

$C_2H_5I + h\nu \rightarrow C_2H_5 + I$, $k=6.6 \times 10^{-6}$ s^{-1} [R2-2]

$1\text{-}C_3H_7I + h\nu \rightarrow C_3H_7 + I$, $k=2.6 \times 10^{-5}$ s^{-1} [R2-3]

$CH_2I_2 + h\nu \rightarrow CH_3I + I$, $k=7.3 \times 10^{-3}$ s^{-1} [R2-4]

$I_2 + h\nu \rightarrow I + I$, $k= (1.2 \pm 0.3) \times 10^{-1}$ s^{-1} [R2-5]

$HOI + h\nu \rightarrow OH + I$, $k=3.3 \times 10^{-4}$ s^{-1} [R2-6]
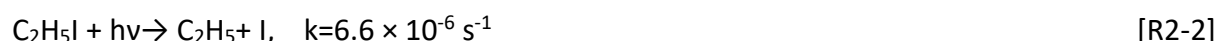
A summary have been provided on all the photochemical cross sections available in the literature for different inorganic and organic iodine species [40]. Table 2.2 summarize the maximum absorption cross section[1] in cm^{-2} for the major observed iodine species.

Table 2. 2 Maximum absorption cross section (σ) at 298K [40].

Iodine species	Maximum $\sigma \times 10^{20}$ (cm^2)	λ (nm)
CH$_3$I	120	265
CH$_2$I$_2$	407	205
C$_2$H$_5$I	121	260
1-C$_3$H$_7$I	141	255
I$_2$	229	500
IO	2050	420
OIO	1030	564
HOI	39.2	340

---

[1] Absorption cross section is the probability that a photon passing through a molecule will be absorbed by that molecule multiplied by the average cross-sectional area of the molecule.

It should be highlighted that in the case of I_2, which photodissociates rapidly (~10 s) with a photodisociation rate coefficient 0.12 ± 0.03 s^{-1} [41], I atoms are produced just above the ocean surface. The longer-lived compounds, such as CH_3I which has a lifetime of about 5-11 days with a photo dissociation rate coefficient ranges between $(0.5-6.6) \times 10^{-6}$ s^{-1} [42], provides a source of iodine throughout the whole troposphere.

Following the photolysis reaction and the production of atomic iodine, ozone destruction can occur via the three following catalytic cycles [5, 43]:

Cycle 1:

$I + O_3 \rightarrow IO + O_2$, k=1.2×10^{-12} cm^3.molecule^{-1}.s^{-1}	[R2-7]
$IO + IO \rightarrow I + OIO$, k=8.0×10^{-12} cm^3.molecule^{-1}.s^{-1}	[R2-8]
OIO + hv → I + O_2, k=2.6 × 10^{-1} s^{-1}	[R2-9]
$2O_3 \rightarrow 3O_2$	[R2-10]

Cycle 2:

$I + O_3 \rightarrow IO + O_2$, k=1.2×10^{-12} cm^3.molecule^{-1}.s^{-1}	[R2-11]
$IO + HO_2 \rightarrow HOI + O_2$, k= 8.6×10^{-11} cm^3.molecule^{-1}.s^{-1}	[R2-12]
HOI +hv → I + OH, k=3.3 × 10^{-4} s^{-1}	[R2-13]
$HO_2 + O_3 \rightarrow OH + 2O_2$	[R2-14]

Cycle 3:

$I + O_3 \rightarrow IO + O_2$, k=1.2×10^{-12} cm^3.molecule^{-1}.s^{-1}	[R2-15]
$IO + NO_2 \rightarrow IONO_2$, k=1.5×10^{-11} cm^3.molecule^{-1}.s^{-1}	[R2-16]
$IONO_2$ + hv → I + NO_3, k=1.2 × 10^{-2} s^{-1}	[R2-17]
NO_3 + hv → NO + O_2, k=2.8 ×10^{-11} cm^3.molecule^{-1}.s^{-1}	[R2-18]
$NO + O_3 \rightarrow NO_2 + O_2$, k=1.9×10^{-14} cm^3.molecule^{-1}.s^{-1}	[R2-19]
$2O_3 \rightarrow 3O_2$	[R2-20]

The reaction of atomic iodine with O_3 (R2-7, R2-11 or R2-15) with a reaction rate coefficient $1.2×10^{-12}$ cm^3.molecule^{-1}.s^{-1} [40, 44], form the iodine monoxide (IO) radical. This reaction is believed to be the major fate of iodine radicals (I) and the key step in the iodine catalyzed O_3 destruction cycles [45]. Additionally, a number of temporary inorganic reservoir products ($IONO_2$, HOI, and OIO) can be formed via the IO reactions with NO_x, HO_2, and IO. This indicates that IO can disrupt the oxidizing capacity of the atmosphere by modifying the abundance and distribution of HOx (OH/HO_2) and NOx (NO/NO_2) mainly through the reactions R2-12 and R2-16.

Further, the regeneration of I through photolysis of IO is rapid (few seconds) with a photo dissociation rate coefficient 4.5×10^{-1} s^{-1} [46, 47].

Iodine radical (I) is also involved in the partitioning of the NO/NO$_2$ ratio leading to the formation of INOx species such as iodine nitrite (INO), nitryl iodide (INO$_2$), iodine nitrite (cis and trans IONO) and iodine nitrate (IONO$_2$) [39, 48]. The formation reaction of INOx species are given below:

$I + NO \rightarrow INO$,   k=1.7 ×10^{-11} cm^3.molecule^{-1}.s^{-1} [R2-21]
$I + NO_2 \rightarrow INO_2$,   k=1.1 ×10^{-10} cm^3.molecule^{-1}.s^{-1} [R2-22]
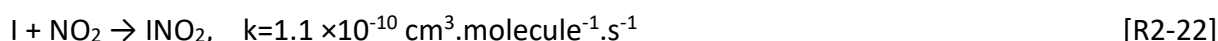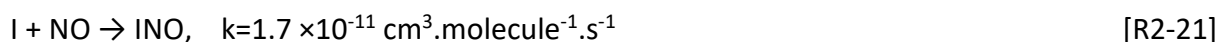
Additionally, IONO isomers have been shown to be formed as nascent intermediates in the IO + NO and I + NO$_2$ atmospheric reactions.
On the other hand, during the night it is believed that I$_2$ and HOI emitted from the ocean mainly interact with the NO$_3$ radical to produce IONO$_2$ (R2-23 and R2-24) [38, 49, 50].

$I_2 + NO_3 \rightarrow I + IONO_2$,   k=1.5 ×10^{-12} cm^3.molecule^{-1}.s^{-1} [R2-23]
$HOI + NO_3 \rightarrow IO + HNO_3$,   k=2.8 ×10^{-12} cm^3.molecule^{-1}.s^{-1} [R2-24]

Reaction rate coefficient for IONO$_2$ via I$_2$ is $(1.5 \pm 0.5) \times 10^{-12}$ cm^3.molecule^{-1}.s^{-1} [50]. Globally, at night I$_2$, HOI and IONO$_2$ species accumulate, whereas they are destroyed during the day by photolysis [7, 38]. The formation mechanism of INO$_x$ species is summarized in Figure 2.2.
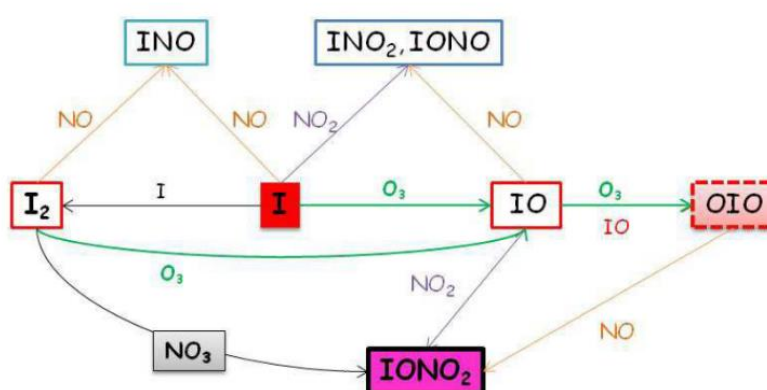
Figure 2. 2 Gas-phase iodine chemistry leading to the formation of INOx species [48].

In addition, experimental [51, 52] and theoretical studies [7, 53] have shown that CH$_3$I can interact with NO$_3$ (R2-25) with a reaction rate coefficient $(4.1\pm0.2)\times10^{-13}$ cm^3.molecule^{-1}.s^{-1}.

$CH_3I + NO_3 \rightarrow CH_2I + HNO_3$,   k= $(4.1\pm0.2)\times10^{-13}$ cm^3.molecule^{-1}.s^{-1} [R2-25]
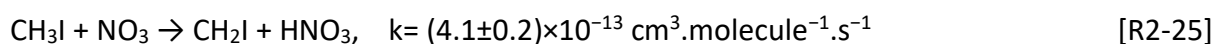
The review on the understanding of the atmospheric gaseous iodine reactivity and the proposed mechanism by Saiz Lopez et al. [5] only considered the destruction of organic iodine species by photolysis. However, CH_3I can decompose via OH (R2-26) and O (R2-27,31) radicals [7, 54]:

$CH_3I + OH \rightarrow CH_2I + H_2O$, k=$6.2 \times 10^{-14}$ cm^3.molecule^{-1}.s^{-1} [R2-26]

$CH_3I + O \rightarrow IO + CH_3$, k=$1.0 \times 10^{-11}$ cm^3.molecule^{-1}.s^{-1} [R2-27]

$CH_3I + O \rightarrow CH_2I + HO$, k=$1.1 \times 10^{-12}$ cm^3.molecule^{-1}.s^{-1} [R2-28]

$CH_3I + O \rightarrow H + I + HC(O)H$, k=$1.5 \times 10^{-12}$ cm^3.molecule^{-1}.s^{-1} [R2-29]

$CH_3I + O \rightarrow I + CH_3O$, k=$6.8 \times 10^{-13}$ cm^3.molecule^{-1}.s^{-1} [R2-30]

$CH_3I + O \rightarrow HI + HC(O)H$, k=$1.2 \times 10^{-12}$ cm^3.molecule^{-1}.s^{-1} [R2-31]
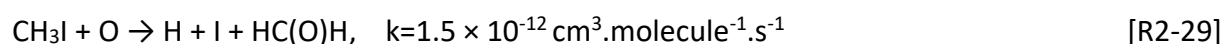
Further, it should be highlighted that the self-reaction of iodine oxides (IO and OIO) and hydroiodic acid (HI) are known to be predominantly responsible for the production of the iodine ultra-fine particles (I_xO_y) [5, 36, 55- 58]. Iodine oxide particles that have been detected in the atmosphere include I_2O_2, I_2O_3, I_2O_4, and I_2O_5. A recent study [7] has shown that the I_2O_5 formation is promoted with a high release of I_2 during summer. The gas phase scheme based on several oxidation steps for the generation of I_2O_5 was proposed [R2-32] with a reaction coefficient rate 5×10^{-16} cm^3.molecule^{-1}.s^{-1} for each oxidation step [56]:

$I_2O_2 + O_3 \rightarrow I_2O_3 + O_3 \rightarrow I_2O_4 + O_3 \rightarrow I_2O_5$, k=$5 \times 10^{-16}$ cm^3.molecule^{-1}.s^{-1} [R2-32]
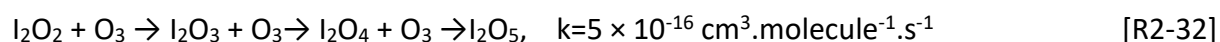
I_2O_3 and I_2O_4 could also form from the reaction of IO_x radicals with a reaction rate coefficient ranging from 1.1 to 1.7×10^{-16} cm^3.molecule^{-1}.s^{-1} [56]. Moreover, it has been suggested that I_2O_5 would appear as a result from the polymerization, [R2-33] [59]:

$5I_2O_4 \rightarrow 4I_2O_5 + I_2$, k= not reported [R2-33]

Briefly, many reaction pathways are known for iodine oxides, however there are still gaps in the knowledge on the fate of the iodine oxides of I_xO_y particle form.

All the available data in the field of atmospheric chemistry had highlighted the complexity of the reactivity of iodine in the atmosphere. In nuclear context, two studies [6, 7] have developed a gaseous iodine reaction mechanism which consisted into two parts: (1) an inorganic part with 99 reactions including 11 photolysis reactions involving 23 iodine species and (2) an organic part composed of 133 reactions including 2 photolysis reaction, for a total of 55 additional iodine species divided into 23 RACM (Regional Atmospheric Chemistry Mechanism, [60]) categories [6, 7]. The organic part is new compared to the proposed mechanism by Sais Lopez et al. [5], who only considered the destruction of organic iodine

species by photolysis. Further, the two studies [6, 7] have summarized the overall behavior of iodine reactivity as shown in Figure 2.3 using ASTEC/SOPHAEROS code (IRSN severe accident simulation tool [61]) with 0D model calculations. The 0D model is a 0-dimensional model used to calculate the concentration of chemical species. They describe a system of differential equations with respect to the time variable without any notion of variation in space and are therefore very fast to execute. Traditionally, these models are represented in the form of a box. They allow the determination of speciation and the predominant reactions.
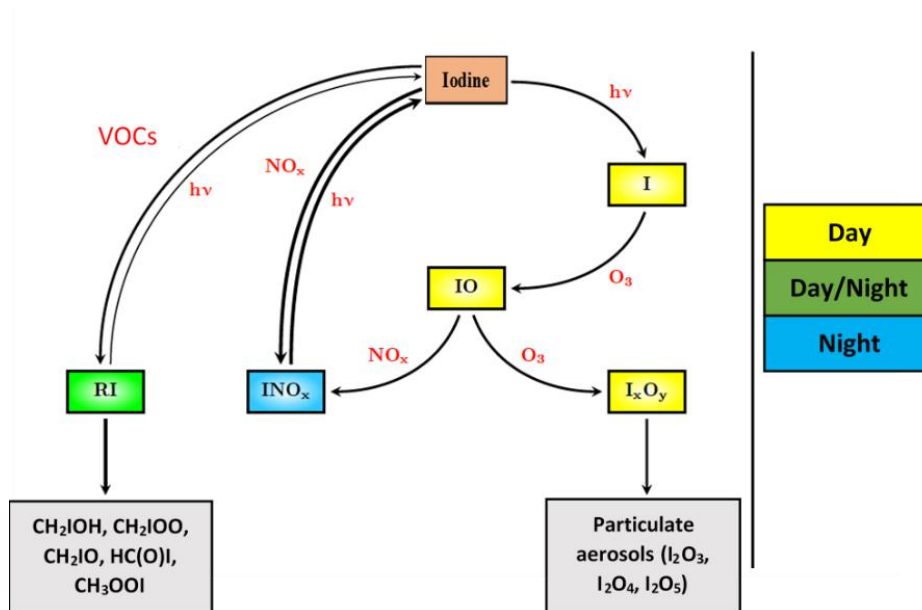
Figure 2. 3 Summary diagram of the iodine reactivity in the atmosphere [6, 7].

In order to better understand the speciation of iodine, the iodine gas-phase mechanism containing 248 reactions combined to the RACM air quality mechanism was implemented into the ASTEC simulation tool of IRSN and calculations were performed at 0D. These calculations were performed by taking into account input parameters that were chosen to represent an accidental release of iodine from a Pressurized water reactor (Gravelines site) taking into account realistic air pollutant concentration (O_3, NO_x, VOCs), meteorological situation, day-night conditions, and finally nature and concentration of iodine release (I_2 or CH_3I). As an example, Figure 2.4 shows the evolution of iodine compounds grouped under 5 main families (organic and inorganic iodine, iodine-nitrogen species, iodine oxide and radicals) for a release of I_2 (98 ppt) and CH_3I (196 ppt) in winter daylight. The rapid evolution of I_2 and CH_3I gaseous forms according to the day/night phases, in connection with photolysis processes, and the presence of certain pollutants in the atmosphere, indicates the strong reactivity of molecular iodine (I_2) under atmospheric conditions. Whereas, less reactivity has been seen for methyl iodide (CH_3I) as shown in Figure 2.4.
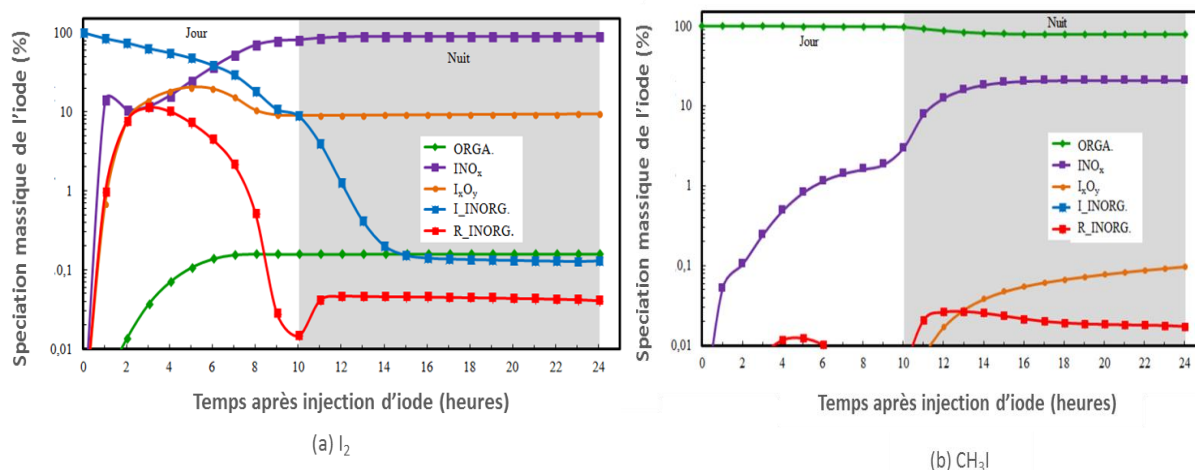
Figure 2. 4 Family mass evolution of iodine, injection 2013 January 1st, at 7 am as a function of time with iodine release (a) 98 ppt of I2 and (b) 196 ppt of CH3I. (Organic in green, iodine in violet, iodine oxide in orange, inorganic in blue and radicals in red) [62].

Despite, the exhaustive literature studies carried out over years on iodine chemistry that made it possible to understand the iodine atmospheric cycle and its speciation in the atmosphere, the role of water vapor on the iodine cycle has not been investigated yet which is nevertheless one of the most important atmospheric compounds. The amount of water in the atmosphere varies greatly depending on the region and altitude. It was shown that water has an influence on formation of iodine particles [63]. However, some modelling studies have investigated the microhydration process of several inorganic iodine species such as HOIO [64], $HOIO_2$ [65], INOx [48] as well as CH_3I hydrolysis processes [66] and micro solvation process of CH_3I [67-69].

2.3 Iodine heterogeneous reactivity

Atmospheric aerosols particles have a strong impact on climate, atmospheric chemistry, hydrological cycle and public health [70-72]. To better understand these impacts, it is necessary not only to identify their sources and sinks and to be able to measure their concentration, size and chemical composition (elemental and molecular), but also to understand the mechanisms of formation and/or physio-chemical transformation (ageing) of particles during their transport in the atmosphere. For instance, gaseous reactive species in the atmosphere may interact with the aerosols when they collide with their surface. This interaction can proceed in a heterogeneous chemical reaction at the surface or/and in the bulk of aerosol particles. The nature of the surface of these particles and the properties of the condensed phase play a large role in the kinetics of reactive uptake and the subsequent chemical transformations that may occur.

2.3.1 Atmospheric aerosols

Atmospheric aerosol particles originate from a wide variety of natural (i.e., wind-borne dust, sea spray, volcanic debris, biogenic aerosol) and anthropogenic sources (i.e., industrial emissions, agricultural activities, fossil fuel combustion, recycling wastes and biomass burning) as primary particles [73-75]. Primary particles are defined as particles directly emitted to the atmosphere and have a typical micrometric size.

Secondary particles, on the other hand, are defined as particles formed by gas-to-particle conversion or by chemical transformation of primary particles in the atmosphere as shown in Figure 2.5 [73, 76-80]. The sizes of particles formed from gas-to-particle conversion are typically in the nanometric and submicrometric ranges.
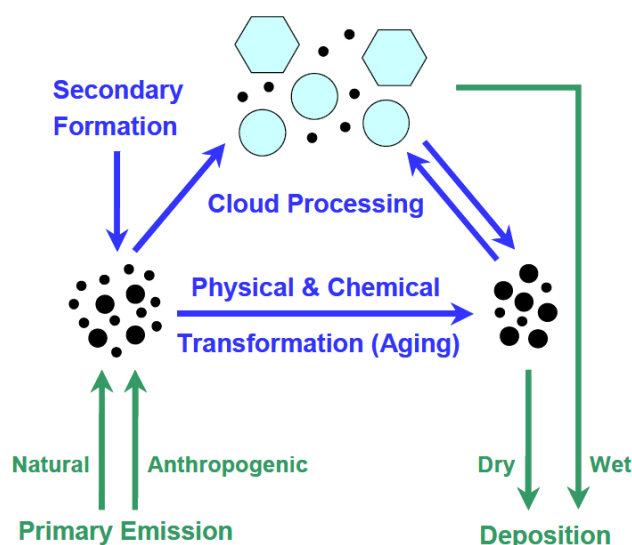
Figure 2. 5 Atmospheric cycling of aerosols, issued from Pöschl, 2005 [73].

The typical secondary aerosols may be inorganic (i.e., sulfates, nitrates), organic (Secondary Organic Aerosols – SOA) or a mixture of inorganic-organic particles. The gaseous precursor may originate from both natural (i.e., SO_2 from volcanic activity, biogenic volatile organic compounds, dimethyl sulfide from ocean, etc) or anthropogenic sources (i.e., SO_2 from industry, NOx from automotive, volatile organic compounds). The formation and ageing of secondary organic containing aerosols are two of the main present research in the field of atmospheric chemistry because the processes are complex and numerous of them still remain unknown [73, 74].

Table 2.3 summarizes the main sources of aerosols emitted into the atmosphere (primary and secondary sources) – for instance the flux of particulate emissions from the ocean is estimated to be between 1000 and 10000 Tg.yr^{-1}, and constitutes nearly 50% in mass of the atmospheric aerosols produced naturally each year [71, 81]. At a global scale, natural emissions account for about 90% in mass of total particulate emissions [77]. Nevertheless, this proportion varies considerably when estimates are made on a regional or urban scale [73, 82-85]. The

geographical distribution of particle sources is non uniform, thus tropospheric aerosols vary widely in concentration and composition over the Earth [86, 87]. Further, in the lower atmosphere the total particle number and mass concentration can vary in the range of about 10^2–10^5 particles.cm^{-3} and 1–100 µg.m^{-3}, respectively [73, 77, 88-90].

Table 2. 3 Estimates of the annual global natural emissions of primary and secondary aerosols measured in Teragram per year (1Tgyr^{-1}=106 ton. yr-1). Note that the actual range of uncertainty may encompass values larger and smaller than those reported here. These values are based on review of Laj et Sellegri (2003) [91].

Origin of source	Source	Annual global emission (Tg.year^{-1})		
		Average	Minimum	Maximum
Natural				
	Primary			
	Sea salt aerosols	1300	1000	10000
	Mineral dust	1500	1000	3000
90 %	Biological debris	50	26	80
	Volcanic ash	33	50	1000
	Secondary			
	Biological sulfate	90	80	150
	Volcanic sulfate	12	5	60
	Organic aerosols	55	40	200
	Nitrates	22	15	50
	TOTAL	3060	2170	23540
Anthropogenic				
	Primary			
	Soot	20	5	20
	Industrial dust	100	40	130
	Secondary			
	Vegetation fires	80	60	160
10 %	Organic aerosols	10	5	52
	Sulfate	140	120	250
	Nitrate	36	25	65
	TOTAL	390	300	710

The main constituents of the atmospheric aerosols are inorganic species (such as sulfate, nitrate, ammonium, sea salt), organic species (also termed organic aerosol - OA), carbonaceous, mineral species (mostly desert dust) and primary biological aerosol particles (PBAPs). In fact, atmospheric aerosol particles at the particle scale may present complex heterogeneous structures featuring both organic and inorganic part due to the complexity of atmospheric reaction [92- 94]. The chemical composition of aerosols differs considerably, depending on its source (primary or secondary) and its atmospheric lifetime (ageing) [90, 95, 96].

For instance, measurements in the marine boundary layer (MBL) reveal that the primary inorganic sea salt component dominates the marine aerosols [97- 99]. It is well known that sea salt aerosols are constituted of inorganic species mainly sodium chloride (NaCl) as well as various organic species. In many investigations, fatty acids (FA) are reported to be major constituents of the organic fraction on marine aerosols [100- 103]. Fatty acids are carboxylic acids with an unbranched aliphatic tail (hydrocarbon chain) which is either saturated (palmitic acid C16 , myristic acid C14, lauric acid C12 and stearic acid C18) or unsaturated (oleic acid C18:1 and palmitoleic acid C16:1) [104 -106]. At molecular scale, the organization of FA on the particle surface is complex and not stable due to influence of water [107]. In contrast, urban aerosols have a more complex composition and are dominated by sulfate, nitrate and carbonceaous aerosols [108] with a significant contribution of carboxylic acids such as malonic, succinic and glutaric acids [109-110].

Lifetime and aerosol size are strongly linked. As can be seen from Figure 2.6 aerosol particles of 0.001-10 µm diameter can have average lifetimes up to 10 days in the troposphere and up to 1 year in the stratosphere. However, large particles (> 10 µm) have relatively short average atmospheric lifetimes (maximum 1 day). This is due to that large particles (large cloud droplets, ice crystal, etc) tend to precipitate (wet deposition) or settle more rapidly by deposition under the influence of gravity [111, 112]. On the other hand, the aerosol composition can also affect its average lifetime as shown in Table 2.4.
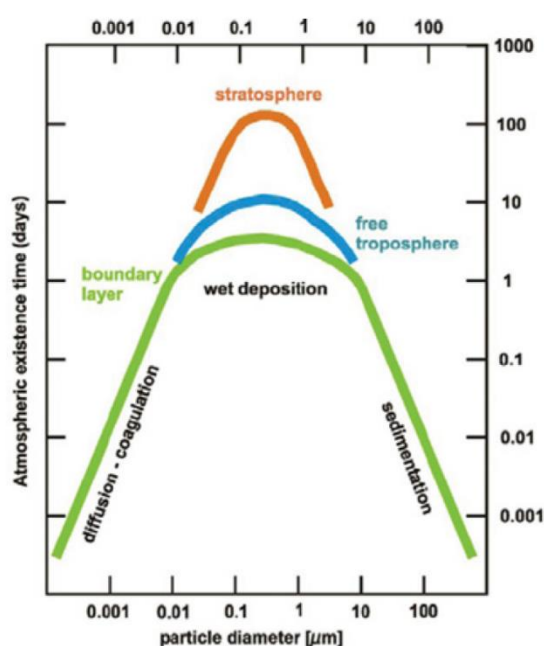
Figure 2. 6 Average lifetime dependence on the size of atmospheric aerosol particle [111].

Table 2. 4 Average lifetimes of various aerosol type [113].

Aerosol type	Size (diameter range)	Average lifetime (days)
Sea salt	< 1 µm	7.1
	2.5 - 10µm	0.7
Mineral dust	< 1 µm	10.4
	2.5 - 10 µm	2.2
Sulfate	< 10 µm	3.8-10
Nitrate	< 10 µm	9-9.9
Organic	< 10 µm	2-10.4
Carbonaceous (Biomass burning)	< 1 µm	3

2.3.2 Role of water

The amount of water vapor in the atmosphere varies greatly depending on region and altitude. It is controlled by the variation of its vapor pressure with temperature. For a given temperature T, the water vapor pressure is characterized by the relative humidity RH according to the following equations [114]:

$$RH = \frac{p_{H2O}}{p_{H2O}^0} \qquad [E2\text{-}1]$$

$$RH = 5(T_d - T) + 100 \qquad [E2\text{-}2]$$

Where p_{H2O} is the partial pressure of water vapor contained in air, p_{H2O}^0 is the saturating vapour pressure of water, T_d is the dew point temperature and T is the observed temperature.

The variations of temperature and pressure may result in the formation of water droplets or iced particles [115] as described by the Clausius–Clapeyron equation (E2-3).

$$Ln\left(\frac{P1}{P2}\right) = \frac{\Delta H_{vap}}{R}\left(\frac{1}{T2} - \frac{1}{T1}\right) \qquad [E2\text{-}3]$$

Where P1 and P2 are the vapor pressures at two temperatures T1 and T2, R is the specific gas constant and ΔH_{vap} is the the molar enthalpy of vaporization.

Water has also a crucial role in the gas-to-particle conversion, particle reactivity or Cloud Condensation Nuclei (CCN) formation as observed during field measurements or determined experimentally [116-118] or demonstrated by molecular simulation [119- 121].

The hygroscopic properties of atmospheric aerosol particles describe how the particles may uptake water vapor in the atmosphere [122, 123]. As explained by the Köhler theory [124] the

phase transition of dry particle material into a saturated aqueous solution is called deliquescence and occurs when a substance-specific relative humidity (RH) threshold value (deliquescence relative humidity, DRH) is exceeded. The reverse transition and its RH threshold value are called efflorescence relative humidity (ERH). For instance, upon hydration (increase of RH) NaCl particles undergo a deliquescence transition at %DRH=75% at 296 K. The reverse efflorescence transition occurs %ERH=45% at 296 K [125].

Furthermore, when relative humidity exceeds 100% (super-saturation) ice crystals in the atmosphere can be formed homogeneously from water droplets in a medium without aerosols or other impurities at about -38 °C [126]. The diagram of the kinetic states of humidity (Figure 2.7) highlights the variation of water super-saturation as a function of the temperature [127]. However, the presence of atmospheric aerosols (nuclei) can greatly increase the ice nucleating temperature and thus catalyzing the ice formation. In this case, the formation of ice on atmospheric aerosols occur from the interaction of water molecules with the surface of the aerosol [128].
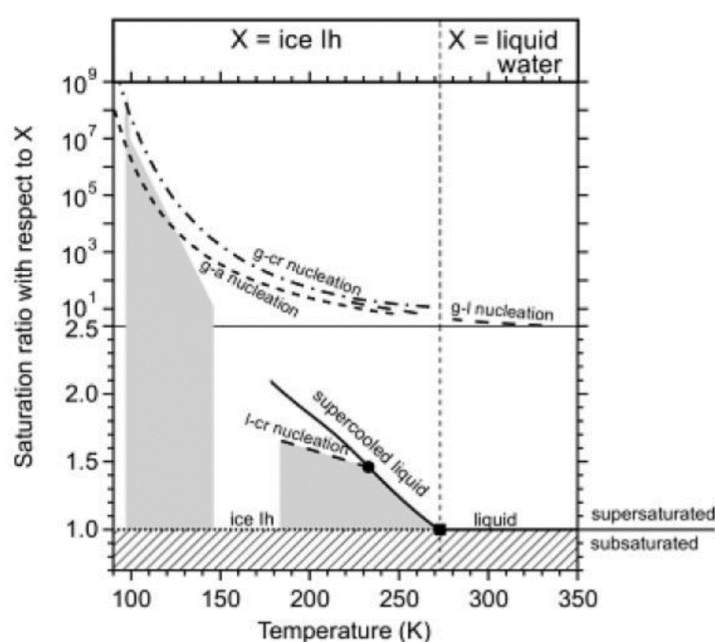
Figure 2. 7 Diagram of kinetic states of atmospheric humidity [127].
Between 90 and 273K, the water saturation rate is taken relative to that of hexagonal ice (solid line, part top of the figure).Along the horizontal dotted line (lower part of the figure), the partial pressure of water is in equilibrium with the saturating vapor pressure above a surface of ice. The inclined dotted line indicates the oversaturation required to form ice from a droplet of aqueous solution of a few microns in a homogeneous manner, i.e. without any particle being present in the droplet. Along the diagonal solid line, the partial water pressure is in equilibrium with the saturating vapor pressure above a droplet. Between 273 and 350K, the rate of water saturation is taken relative to liquid water (solid line, upper part of the figure). The dashed curves and dashes represent areas of homogeneous nucleation from one state to another: g: water vapor, Cr: crystalline ice, l: liquid water, and a: amorphous ice.

2.3.3 Gas-aerosol interaction – overview of the general concepts

Heterogeneous interactions of trace gases with liquid and solid particles strongly influence the atmospheric properties. Heterogeneous uptake by particles changes the gas phase concentration of reactive compounds (such as photochemical oxidants, acid gases, free radical, etc.) which significantly influences the atmospheric processes (such as formation of photochemical smog, ozone layer depletion, etc.). Moreover, the heterogenous reactivity affects important physical properties of atmospheric aerosols, such as size, optical properties, and ability to nucleate cloud droplets [129]. Thus, determination of kinetics and mechanism of heterogeneous reactions has become increasingly important in understanding the chemistry of the troposphere.

One of the comprehensive kinetic model framework for heterogeneous interactions was proposed [130- 135] and provided a basis for consistent description of chemical reactions and mass transport at the surface and in the bulk of liquid and solid atmospheric particles of both simple and complex systems. This model is based on NASA–JPL and IUPAC evaluations, which are a set and a combination of kinetic theories of gases, condensed phases, and interfaces.

Considering the kinetic model cited above, when a gas is in contact with a condensed phase, gaseous molecules driven by thermal agitation can diffuse towards it and hit the surface. A fraction of the molecules that hit the liquid or solid surface can be taken up due to heterogeneous elementary processes including gas phase diffusion, accommodation, desorption and possible reaction at the gas/surface interface, and for liquids and some amorphous solid surfaces, absorption, dissolution and bulk reaction. In fact, the observable interaction of a species on a particle or a droplet surface is the results of a complex process, which can be decomposed on several elementary processes as shown in Figure 2.8.

[1] _Collision:_ Based on gas kinetic theory and assuming the gas phase concentration is constant, the rate of collisions of gas species X with a surface can be expressed as R_{coll}.

$$\mathbf{R_{coll}} = \frac{\omega\,[X]_g}{4} \qquad\qquad \text{[E2-4]}$$

$[X]_g$ is the gas phase concentration (molecule.m^{-3}) of X and ω is its mean thermal velocity (m.s^{-1}) given by $\omega = [8RT/(\pi M)]^{1/2}$, M is the molar mass (kg.mol^{-1}) of X, R is the gas constant (J.mol^{-1}), and T is the temperature in kelvin.

 [2] _Gas diffusion_: When efficient heterogeneous loss leads to local depletion of gaseous molecules $[X]_g$ close to the droplet or solid surface and gives rise to a diffusional flux from the bulk gas directed towards the surface.

The diffusion factor (C_{diff}) is commonly defined in terms of the trace gas concentrations near the surface ($[X]_{gs}$) and far from the particle ($[X]_g$) (see Equation 2-5).

$$C_{diff} = \frac{[X]_{gs}}{[X]_g} \qquad \text{[E2-5]}$$

$$\text{Then,} \quad R_{diff} = R_{coll} \times C_{diff} \qquad \text{[E2-6]}$$

However, it should be noted that under appropriate steady state assumptions, a diffusional resistance term that depends on the particle size and the gas-phase diffusion factor should be considered.

[3] Adsorption or surface accommodation: When the gas molecule colliding with the liquid or surface neither reacts nor bounces off immediately but stays within a distance on the order of a chemical bond ($\sim 10^{-10}$ m) for a duration longer than the average duration of a (quasi-)elastic gas-surface collision or molecular scattering process. From gas kinetic theory, this duration can be approximated in the order of $\sim 10^{-12}$ s under ambient conditions in the lower atmosphere. Surface accommodation can be also generally defined as physisorption or trapping, which means that the accommodated or adsorbed molecule is bound to the surface by relatively weak forces, such as van der Waals forces or hydrogen bonds.

Thus, the rate of adsorption (R_{ads}) of gas molecules X can be described by:

$$R_{ads} = R_{coll} \times \alpha_s \qquad \text{[E2-7]}$$

Where, α_s is the surface accommodation coefficient.

[4] Desorption: It is the reverse process of adsorption, where the gas desorbs back to the gas phase from the surface. The desorption is usually parameterized by a first order rate expression:

$$R_{des} = K_{des} \times [X]_s \qquad \text{[E2-8]}$$

K_{des} denotes the desorption rate constant and $[X]_s$ is the concentration of surface species.

[5] Surface reaction: It is the chemical transformation at the liquid or solid interface. Reaction in which the molecule arriving at the surface reacts with a second species, which is present on the surface in the adsorbed state to form either un-volatile or volatile products which partition back to the gas phase. It can be also defined as a chemisorption, which means that the adsorbed molecule is bound to the surface by strong and irreversible bonds (chemical bonds). In this case, surface species concentration (Y) should be considered to calculate the reaction rate (R_s).

[6] Bulk accommodation: After surface accommodation, gas molecules may be incorporated into the bulk of the condensed phase by interfacial mass transport processes. The term α_b,

bulk accommodation coefficient, can be expressed in term of surface accommodation coefficient (α_s), surface to bulk transfer rate coefficient (K_{sb}) and desorption rate coefficient (K_{des}) as shown in (E2-6).

$$\alpha_b = \alpha_s \times \left(\frac{K_{sb}}{(K_{sb} + K_{des})} \right) \qquad \text{[E2-9]}$$

[7] Bulk reaction: Reaction throughout the bulk, mostly in relation with liquid. The main parameters of this process are the rate coefficient for reaction of species taken up into the bulk (k_b), Henry's Law constant, H (M.atm^{-1}) and the liquid phase diffusion coefficient (D_l, in cm^2.s^{-1}).

[8] Dissolution or solubility: In the absence of surface or bulk reactions, uptake into the bulk of liquid particles proceeds until the solubility is reached. The equilibrium between the gas and liquid phase concentrations is characterized by the Henry's law constant, H. The main parameters of this process are Henrys Law coefficient, H (M.atm^{-1}) and the liquid phase diffusion coefficient, D_l (cm^2.s^{-1}).
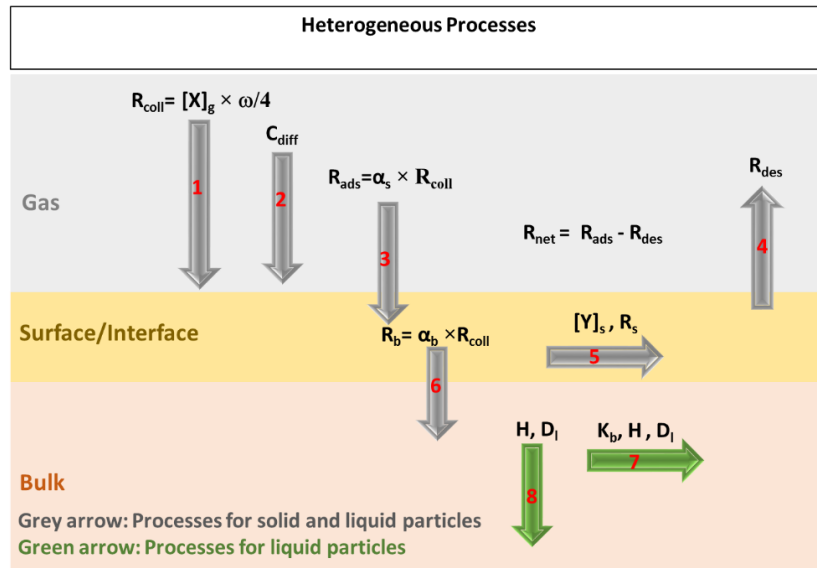
Figure 2. 8 Schematic illustration of the key processes describing gas uptake by atmospheric particles. The symbols represent the following processes : gas rate of surface collisions (Rcoll), the adsorption rate onto the particle surface (Rads), diffusion factor (Cdiff), rate of adsorption into the particle bulk (Rb), desorption from the surface (Rdes), rate of surface reaction (Rs), Henry's law coefficient (H), diffusion coefficient (Dl), the rate constant of the bulk reaction (Kb), gas species [X]g and [Y]s is the surface species. The grey arrows indicate the processes occurring with the solid or liquid particles and green arrow indicate the processes occurring with liquid particles. A is the effective surface area, ω is the mean free path of X and X is the gas phase species. Based on [129].

It should be highlighted that in the scientific literature, different rate parameters and formalisms have been defined and used for the quantitative description and modelling of these processes.

It is often difficult to experimentally determine which ones, if any, of the processes defined above, is actually controlling the heterogeneous uptake of trace gas species on a given surface (solid aerosols, liquid droplets) in either laboratory experiments or in the atmosphere. Thus, the overall process can be described with a global parameter: the uptake coefficient which is the ratio of the number of collisions of a given trace gas species leading to uptake on the surface to the total number of possible collisions per unity of surface and time (γ) [133-136]:

$$\gamma = \frac{\textit{Number of taken up molecules per unity of surface and time}}{\textit{Number of colliding molecules per unity of surface and time}}$$

γ is then a dimensionless parameter and represents the probability ($0 < \gamma < 1$) that a gas phase species is removed irreversibly from the gas phase to an active surface at a given temperature. The actual quantity measured with most of heterogeneous experimental studies is the observed overall trace gas uptake, γ_{obs}. Observed uptake is usually determined from the decrease of the concentration of the trace gaseous (x) species of interest [E2-10] [136-140]. To a lesser extent, and for a purely reactive uptake, γ_{obs} in some measurements can also be obtained by quantification of the surface product (Y) concentration [E2-11] [141, 142].

$$\gamma_{obs\,(g)} = \frac{d[X]_g}{dt} \times \frac{1}{A \times [X]_g \times \omega/4} \qquad [E2\text{-}10]$$

$$\gamma_{obs\,(s)} = \frac{d\{Y\}_s}{dt} \times \frac{1}{A \times [X]_g \times \omega/4} \qquad [E2\text{-}11]$$

$[X]_g$ is the gas phase concentration of X and $\{Y\}_s$ is the surface species concentration. ω is the mean thermal velocity (m.s^{-1}) given by $\omega = [8RT/(\pi M)]^{1/2}$, M is the molar mass (kg.mol^{-1}) of X, R is the gas constant (J.mol^{-1}), and T is the temperature in Kelvin.

Corrections of the uptake are frequently necessary to be taken into account. For instance, in case of strong uptake leading to local depletion of X close to the surface, a correction factor (C_{diff}) is commonly applied ($\gamma_{corrected} = C_{diff} \times \gamma_{obs}$). If the surface is changing with time (in case of strong uptake), the uptake is time dependent and correction to zero time must be considered.

The uptake coefficients are presented in literature in a variety of experimental symbols form depending on experimental measurements. An example of the main used experimental symbols is shown in Table 2.5.

Table 2. 5 Main used experimental symbols for the uptake coefficient.

Symbol	Meaning
γ_{obs}	Experimentally observed, results in loss of the molecule from the gas phase or gain of species in solid phase under defined experimental conditions
	Experimentally observed, used if the uptake is not precised γ_0 and γ_{ss}
$\gamma_{ss\ or}$ $\gamma_{average}$	Experimentally observed, steady state (time independent) uptake coefficient
γ_0	Experimentally determined initial uptake coefficient that was changing rapidly with time
$\gamma_{corrected}$	The correction of the observed uptake, such as by gas diffusion factor

The advantage of expressing the kinetics in terms of uptake coefficients lies in the fact that the results are transferable from one experiment to another, even if those experiments involve significant differences in the surface-to-volume ratio. This would not be the case if kinetic results were expressed in terms of rate coefficients which are however the primary experimental observables.

To sum up, the uptake coefficient is a time and concentration dependent quantity. For extracting information about a specific aspect of the uptake process, i.e. the accommodation on the surface, specific corrections or experimental conditions have to be used. Thus, the uptake coefficient can be further parametrized by including the possible occurring heterogeneous processes. A complete description of the interaction parametrization has been previously discussed in [129, 131, 133, 134].

2.3.4 Experimental tools and techniques for studying aerosol-gas interactions

Several experimental methods dedicated to laboratory experiments can be used to study heterogeneous interactions and to determine uptake coefficients. The general principle of these methods is to put a gaseous phase in contact with a solid or liquid phase of known surface. The number of gaseous molecules taken up by the solid or the liquid is measured during a known time interval through either surface or gas monitoring. In this section, the experimental methods that are most frequently used in the measurement of uptake are presented. Most methods rely on the determination of loss rates or time dependent

concentration changes of gas-phase species in contact with a surface. These include internally coated flow tube reactors and Knudsen cells for bulk surfaces and films, and aerosol flow tubes and aerosol chambers for dispersed surfaces. Surface adsorbed reactants and products have frequently been observed using surface-sensitive techniques, such as reflectance infrared spectroscopy (Diffuse Reflectance for Infrared Fourier Transform Spectroscopy (DRIFTS)) and these have in a few cases been applied to kinetics studies [99, 129, 143, 144].

Table 2.6 summarizes the commonly used methods for the measurement of reactive uptake in gas-solid / liquid reactions. The surface characteristics, the range of accessible ɣ, the gas-solid contact time and the working pressure range for each method are listed [126, 119]. In this section, a brief description of the laboratory techniques that can be used to determine kinetic parameters that characterize heterogeneous reactions in the atmosphere, is given.

Table 2. 6 Summary of the principle commonly used methods for the measurement of reactive uptake in gas-solid / liquid reactions. The surface characteristics, the accessible range of ɣ, the gas-solid contact time and the working pressure range are reported [126, 119].

Method	Surface	Monitoring phase	Accessible ɣ range	Contact time	Working pressure (Bar)
Coated/wetted flow tube	Solid or liquid film	Gaseous	$<10^{-1}$	$0-10^3$ s	0.0007-1.013
Aerosol flow tube	Solid or liquid aerosol particles	Gaseous and solid or liquid	$10^{-4}-1$	0- 30 s	0.001-1.013
Knudsen Cell	Powder sample or aerosol particles	Gaseous	$10^{-5}-1$	$10-10^4$ s	$< 1.33 \times 10^{-5}$
DRIFTS Cell	Solid surface or aerosol particles	Solid	$10^{-10}-10^{-2}$	40 -800 min	0.003-1.013
Droplet train flow reactor	Liquid droplets	Gaseous and droplet	$10^{-3}-1$	2-20 ms	0.080-0.03
Atmospheric simulation Chamber	Aerosol particles	Gaseous and solid	$10^{-8}-10^{-4}$	100 -900 min	1.013

2.3.4.1 Flow tube and flow tube-like techniques

➢ **Internally coated or wetted flow tube**

Coated and wetted wall flow tubes have been used extensively to measure uptake and reactions of gases with both liquid and solid surfaces. A detailed review on flow tube technique is available in [145] which provides also a critical analysis of the interpretation of flow tube data for gas uptake measurements [145].

The flow tube walls can be coated with the condensed phase (liquid or solid) film of interest. In a first configuration, the liquid flows down the inner surface of a vertical flow tube as shown in Figure 2.9. The flow tube has an annular lip at the top over which the liquid spills to create a thin, uniform film over the entire surface. In the horizontal configuration, the liquid can be contained in a holder in the flow tube, or it can coat the walls. Alternatively, the flow tube can be rotated to keep the coating uniform. The second configuration, can be also used for solid films where the solid phase is deposited on the internal wall of the tube, which is placed inside the reactor. The vertically mounted wetted wall flow tube is the favored configuration. Unlike horizontal configuration, the inside wall of the tube is completely covered with a slowly flowing film of the liquid of interest (see Figure 2.9), thus the liquid surface is constantly renewed so that a surface of constant composition, free of saturation and reaction products, is obtained. The gaseous reactant can then be added through a movable injector. The gas phase composition is continuously monitored by using a suitable analytic technique depending on the gaseous species or the experimental conditions. A variety of online sensitive detection for gas phase analysis have been used either spectroscopic (mostly UV and IR absorption, laser-induced fluorescence) or mass spectrometry with differential pumping (MS). Values for ɣ above 10^{-1} are difficult to measure accurately in a wetted wall flow reactor because of gas-phase diffusion limitations.
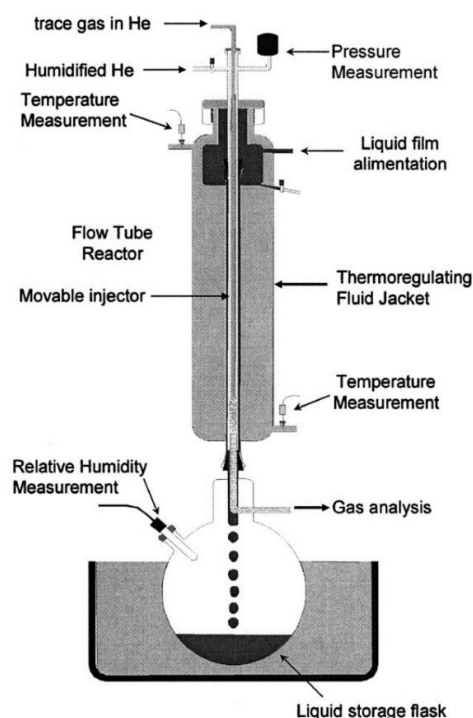
Figure 2. 9 Example of wetted flow tube used for measurements of uptake of trace gases on liquid film adapted from Dievart et., [146].

> ### Aerosol flow tube

An evolution of the internally coated flow tube is the aerosol flow tube, aerosol particles (as solid or liquid) are sprayed into the flow tube reactor, as shown in Figure 2.10. This allows the study of reactions on a condensed phase under conditions more representative of the real atmosphere. Aerosols are injected mostly as polydispersed population in the submicrometric range. The use of sub-micron particles and the fact of mixing gas and aerosols overcome the uptake rate limitation caused by gas phase diffusion. Additionally, constant renewal of the aerosols (liquid or solids) avoids surface ageing. This type of system allows the uptake coefficient measurements in the range of 10^{-4} -1 [147, 148].

Aerosol suspension can be generated by wet process (nebulization of an aqueous solution or a liquid suspension) or by dry process (vibrating membrane aerosol generator). The suspended particles are diluted in the carrier gas (usually N_2 or air) and passed through a conditioner where the aerosols equilibrate to the temperature and humidity conditions before injection. Together with, the reagent trace gas is diluted in the carrier gas and enters the reactor through a sliding injector, allowing different exposure times to the aerosols.
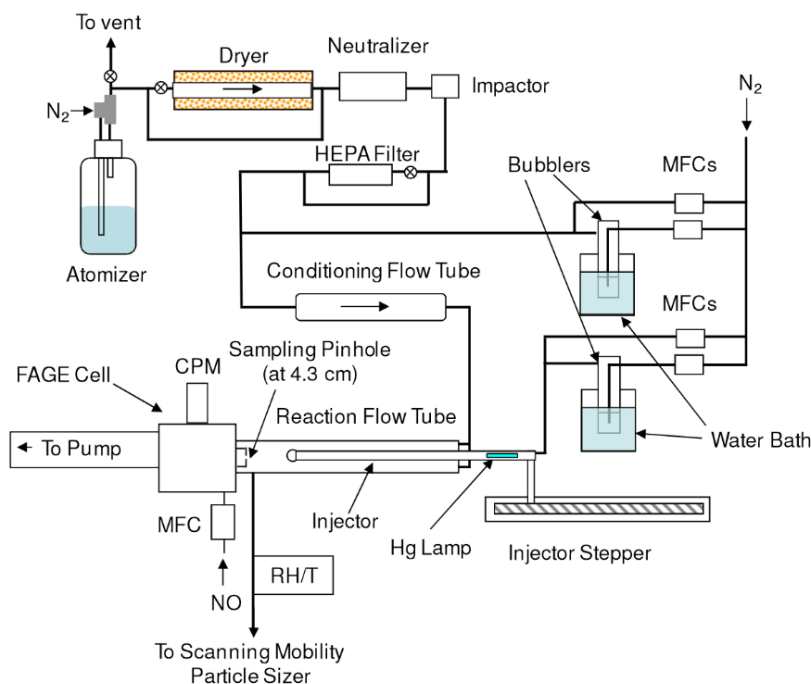
Figure 2. 10 Example of aerosol flow tube experimental set-up used to measure HO_2 uptake coefficients adapted from I. George et al., [150]. MFC-mass flow controller; RH/T-temperature and humidity probe; CPM-channel photomultiplier, FAGE-Fluorescence Assay by Gas Expansion; HEPA–High Efficiency Particulate Air.

Physiochemical characterization of the aerosol population can be determined before and after exposure to the reactive gas to gain information about condensed-phase reaction products. In addition, the trace gas concentration can be online monitored with mass or optical spectrometric techniques [129, 149].

2.3.4.2 Droplet train reactor

The droplet train flow reactor (Figure 2.11) is a technique used to measure the rate of uptake of gases into liquid droplets. It is composed of a droplet generation chamber, which ejects droplets of uniform size and spacing via a vibrating orifice aerosol generator (VOAG) shown in Figure 2.12, into a flow tube at linear flow velocities typically in the range 1500–4500 cm.s^{-1}, and total pressure in the range 0.080-0.003 bar (to maintain laminar flow of droplets). The reactant gas can be injected in the flow tube at various positions and changes in the concentration of the reactant gas are measured at the downstream end following exposure to the droplets. Typical detection techniques used for trace gases are mass spectroscopy and tunable diode laser infrared spectroscopy. The droplets leaving the interaction zone can also be collected and analyzed, typically using liquid chromatography methods, to determine changes in composition resulting from reactive gas uptake [129, 151]. All experimental parameters are computer monitored and controlled.

The gas-droplet interaction time can be varied between 2 and 20 ms, allowing solubility effects to be investigated. The pressure and droplet diameter in the droplet train flow reactor causes gas-phase diffusion limitations.
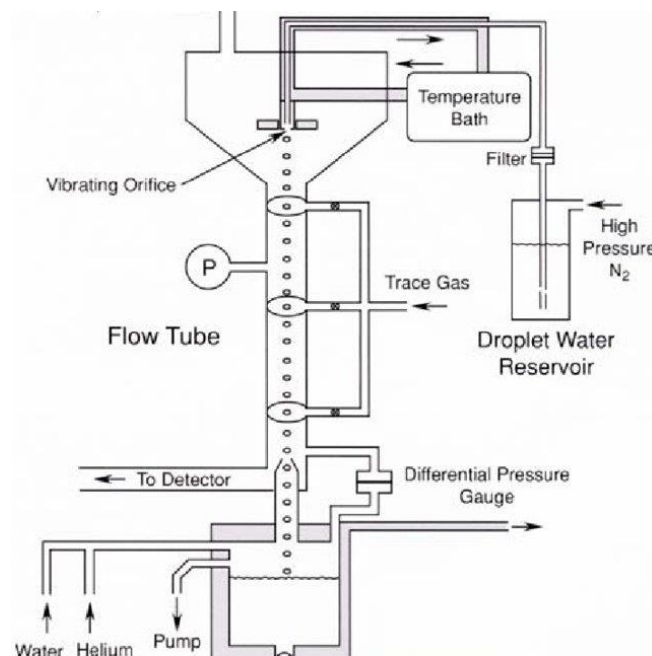
Figure 2. 11 Schematic diagram of typical droplet train flow reactor for measurement of uptake coefficients of trace gases into liquids [151].
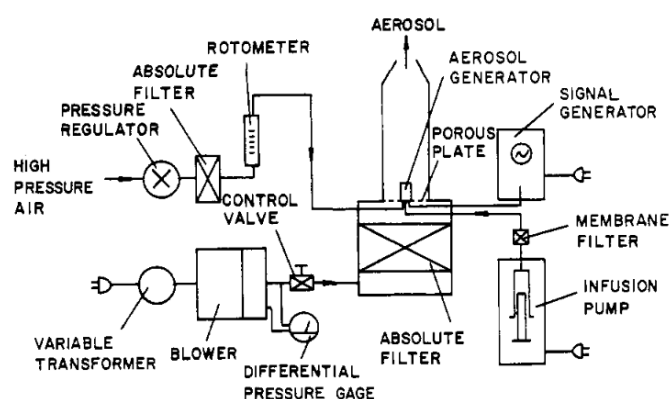
Figure 2. 12 Example of vibrating orifice monodisperse aerosol generator [152].

2.3.4.3 Knudsen cell

Much of the data on heterogeneous reactions in the atmosphere, particularly the earliest work, were generated using Knudsen cells [153- 157]. Knudsen cell are used for the analysis of loss from the gas phase due to surface reactions or adsorption. Figure 2.13 presents a simple schematic diagram of a Knudsen cell. The Knudsen cell reactor consists of a chamber with an isolated sample compartment and a small orifice through which gas phase reactant and product species can escape to be detected by mass spectrometry. The orifice (small hole)

and the low pressure (<1.33 × 10^{-5} bar) ensures a molecular regime which overcomes gas phase diffusion effects. The design of the gas system makes it possible to introduce the reactive gas in two configurations. The pulsed valve configuration experiment is when a known number of gas molecules is admitted across a pulsed solenoid valve (0.8-millimeter orifice) into the reactor and interacts with the reactive surface. The mass spectrometer signal is recorded as function of time and proportional to the flow of gaseous species out of the reactor. In the steady state experiment a dual needle valve (Nupro) is used to regulate the gas allowing a continuous constant flow of the injected gas. The pulsed valve technique has the advantage that it avoids surface saturation.

When the gas is exposed to a surface that takes up the gas, the concentration of the gas in the cell and hence the amount exiting the orifice decreases. From the gas phase concentration change, the net uptake of the gas by the surface can be determined. Uptake coefficient is accessible between 10^{-5} and 1 and can be measured accurately. The main advantage of this experimental set-up is the wide range of condensed phases that can be used; the condensed phase can be a liquid, a powder, a thin layer, a frozen surface or a monocrystal. The main disadvantages are the limited use for low vapor pressure samples, and the very low pressure which is not representative of low tropospheric conditions.
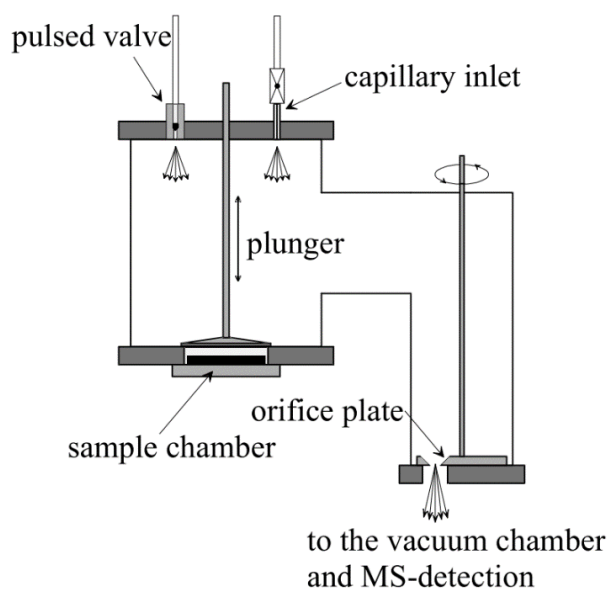
Figure 2. 13 Example of a Knudsen cell for the investigation of heterogeneous reactions using either continuous flow or pulsed gas admission. The rotatable orifice plate can put up to four molecular-beam forming orifices into line of sight with the ionizer of the mass spectrometric (MS) detector from M. Rossi et al., [153].

2.3.4.4 Diffuse Reflectance Infrared Fourier Transform Spectroscopy (DRIFTS)

Diffuse Reflectance Infrared Fourier Transform Infrared spectroscopy (DRIFTS), is a reactor that allows the *in situ* monitoring of a solid phase put in contact with a reactive gas phase. This technique requires the solid to be a diffusing medium.

The fine powdered sample is put in the reaction chamber (DRIFTS), which is located inside an FTIR instrument as shown on the Figure 2.14. A parabolic mirror focuses the probe beam on the solid sample and the diffused reflected radiation is focused by another parabolic mirror on to the detector surface. Moreover, it is possible to monitor the gas phase by coupling the gas outlet of DRIFTS reactor with a suitable technique implemented at the gas outlet (i.e., Gas chromatography coupled to mass spectrometer or long path cell connected to UV-Vis or FTIR spectroscopy). Complementary information on FTIR spectroscopy and DRIFTS techniques are displayed in annex 2.

DRIFTS is a technique of choice for studying gas-solid interactions, this technique is widely used in catalysis science [158- 160]. However, it has been proven that DRIFTS is very useful for providing structural information for all types of solid surfaces and it is extremely useful for examining samples that are difficult to analyze in transmission [161]. DRIFTS is also very useful for studying the kinetics and mechanisms of the reactions of infrared-transparent solids (such NaCl) and gaseous species [142, 162-165].

Measurements difficulties may arise with highly IR absorbing solids. Moreover, DRIFTS can provide signal of gas phase near the surface [166]. Sometimes it is difficult to estimate the extent and kinetics of the gas-phase diffusion inside the powdered macroscopic sample. Solid sample cannot be renewed during the experiment thus surface ageing of the solid sample can be a limitation. Its main advantages are that it is a fast and non-destructive technique.

This method allows the measurements of solid-phase products when a flow of gases is passed through the solid. The uptake coefficients (in the range of 10^{-10} to 10^{-2}) and formation rates of absorbed/adsorbed product on the solid is determined by quantitative interpretation of the DRIFTS spectra coupled to post-test complementary techniques allowing the determination of the total amount of adsorbed/absorbed products during an experiment (IR pellets, ionic chromatography, inductively coupled plasma mass spectrometer [142]).
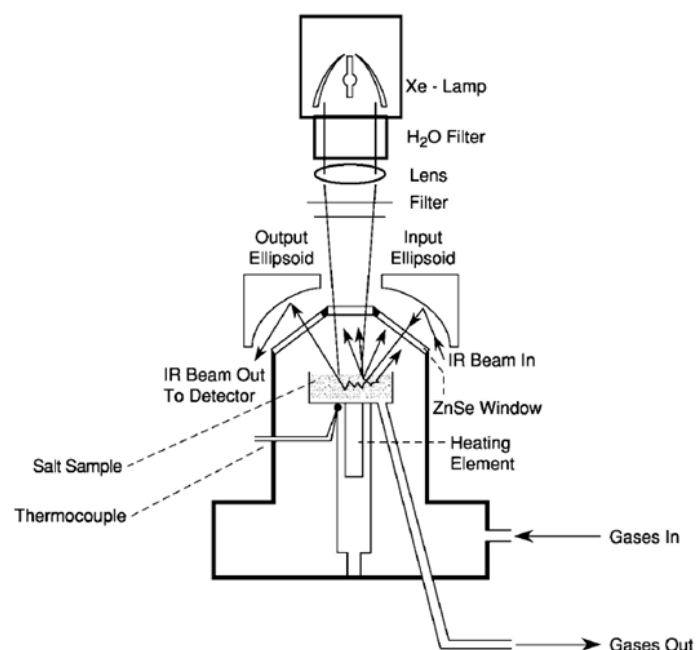
Figure 2. 14 Example of DRIFTS apparatus [162].

2.3.4.5 Atmospheric simulation chamber

The reaction volume of Atmospheric Simulation Chamber [167] is much larger than in the previously described reactors: it can range from few m^3 (HIRAC chamber) to more than 270 m^3 (SAPHIR chamber). Atmospheric simulation chambers are among the most advanced tools for investigating the atmospheric processes to derive physico-chemical parameters which are required for air quality and climate models. Atmospheric chambers are used to investigate both gaseous and/or aerosol-gas interaction processes as SAPHIR chamber shown in Figure 2.15.

Indeed, depending on the irradiation used, atmospheric simulation chambers can be divided into two categories: outdoor and indoor chambers. Outdoor chambers are often large transparent reactors (e.g. SAPHIR, HELIOS) that are directly irradiated by solar radiation. Indoor chambers equipped with artificial irradiation sources (e.g. Xenon lamp, Fluorescent lamp, halogen lamp) are smaller than the outdoors ones and are mostly dedicated to specific studies (e.g. CESAM, HIRAC).

Atmospheric chambers can be equipped with a wide range of analytical instruments for online and offline measurements [168-170] allowing studies of homogeneous or heterogeneous chemical reactions. As an example, the subsequent temporal decay, composition, and/or growth of gas phase species is monitored, usually with long optical length FTIR, Mass Spectrometer or UV-Vis techniques. Additionally, the aerosol composition can be determined on-line by steam jet aerosol collection/ion chromatography. In some cases, a particle analyzer

is coupled to the simulation chamber, such that information on the evolution of particle size distribution and particle number can also be followed.
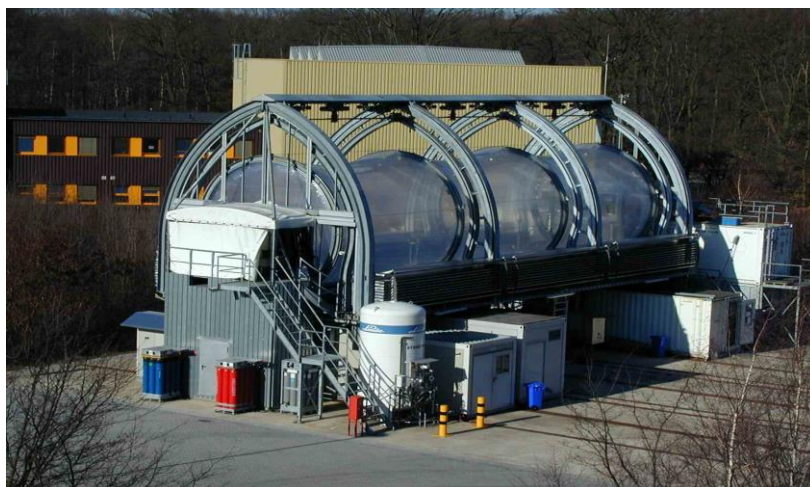
Figure 2. 15 Outdoor SAPHIR atmosphere reaction chamber in Jülich, Germany dedicated for both homogenous and heterogenous interaction processes [167].

2.3.5 Single particle and molecular mechanism approach

2.3.5.1 Single particle approach

Single particle approaches have been generally used to investigate the hygroscopicity of particles [171], photo reactivity of particles [172], phase partitioning [173] and particle viscosity [174] as well as chemical characterization of individual particles [175, 176]. To some extent, each single particle may be considered as a micro-reactor undergoing multiphasic interactions. Chemical, morphological (size and shape) and phase data of an individual aerosol particle are of crucial importance for purposes of tracing and understanding the formation and reaction mechanisms of aerosols. The chemical composition and microphysical state influence the response of the particle to environmental changes. For instance, a variation in chemical composition or size of an individual aerosol particle prior and post to exposure to gas species can be directly linked to its heterogeneous process with gas phase species. As an example, Figure 2.16 shows the morphological change of $CaCO_3$ particles before and after exposure to HNO_3. Indeed, relating the changes of particles can help in elucidate the underlying type of heterogeneous process (accommodation, reaction). Additionally, comparing the morphology from particle scale to the bulk scale can be a challenging step to confirm the observed heterogeneous process [177-180]. Therefore, studying the physiochemical properties of particles at particle scale will help in better understanding the heterogeneous interactions. Nevertheless, it should be highlighted that up to date there are no experimental system to study the gas-single particle interaction because the volume of one particle is too small regarding the gas volume.
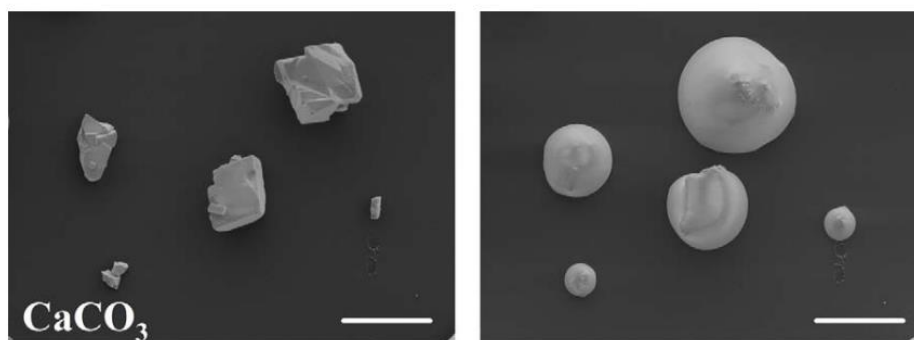
Figure 2. 16 Secondary electron (SE) images of CaCO3 particles before (images on left) and after (images on right) reaction with gaseous HNO3 in the presence of water vapor (PHNO3 =14±1 µTorr and 36±1% RH for 2h) [180].

2.3.5.2 Molecular approach

Studying the reactivity at molecular scale can help in better understanding the chemical processes. One technique to study chemical processes in the gas phase such understanding aggregate and/or nuclei formation is cryogenic or supersonic jet technique.

The technique of cryogenic matrices is the isolation of stable or unstable species in an inert crystal of noble gas or of neutral molecules at low temperature (3-40K). The idea was firstly proposed by Pimentel et al [181] to observe unstable species (intermediate, free radical, ions and reaction intermediate or high-energy isomers). The matrix isolation technique consists in trapping gaseous chemical species known as guest molecules or atoms in an unreactive solid matrix, called the host. The technique is very useful to study both intra and intermolecular interactions [63, 182, 183]. Finally, depending on the concentration of the gaseous species, the formation of polymers and aggregates can be studied. By coupling the matrix isolation technique with various beams (Tunable Laser, X-ray irradiation, electron and proton bombardment, ultrasound, microwave discharge and electrical discharges), photolysis, pyrolysis, chemical reactions of isolated molecules can be scrutinized with in situ conditions. Cryogenic matrix isolation technique is composed of a cooling system, a vacuum system, a chamber containing the cold window, on which the matrix will be formed and detected by a spectroscopic technique. The type of window used depends on the analysis technique. When infrared spectroscopy is used, the CsBr and CsI windows are the best choices because of their transparency to IR. The host material can generally be an inert gas such as a noble gas (Ne, Ar, Kr, Xe) or N_2. Neon requires a working temperature below 11 K, it is possible to work at higher temperatures with krypton and xenon but their costs are quite high. Due to their good working temperature/cost balance/relative availability, Ar and N_2 are the best choices for the gas

matrix and are therefore the two most commonly used gases [184]. Cryogenic matrix isolation principle is schematically presented in Figure 2.17.
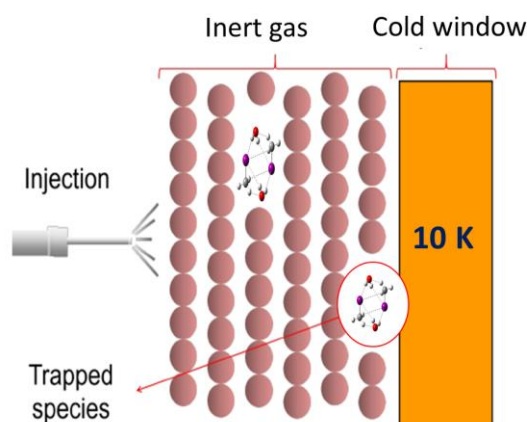
Figure 2. 17 Schematic presentation of the cryogenic matrix isolation principle [185].

The working temperature is an essential point of the matrix isolation technique. With temperatures below 10 K, the movement of trapped species is very limited and very good spectral resolution can be obtained.

Over the years, several crucial developments improved this technique significantly; among them, the application of lasers for selective photolysis. However, major limitation of cryogenic matrix techniques is the very low temperature which is not representative for tropospheric temperature. However, in some case, gas phase interaction can occur before being trapped in the argon matrix in conditions much closer to that of the atmosphere.

2.3.5.3 Theoretical calculation

Quantum-chemical calculations are commonly used to support experimental vibrational spectral assignments [186, 187]. Atmospheric aerosol particles provide surfaces where a multitude of processes may take place, and the molecular-level properties of these surfaces determine how they interact with gas phase species. Complementary to experiments, theoretical calculations [110, 119, 188] at the molecular level can provide valuable insights on the elementary chemical and physical mechanisms responsible for particle growth, formation, ageing or reactivity.

Further, theoretical analyses and molecular simulations can improve the understanding of the heterogeneous interaction processes. For instance, surface reaction can be predicted [76, 130]. Density functional theory (DFT) calculations and ab-initio molecular dynamics

simulations can be used to understand the adsorption and chemical reaction of gaseous species on surface by investigating their thermodynamic properties [189-196]. Such simulation can compute the adsorption energy, adsorption structure, dissociation energy and possible reactions. Additionally, it is possible to study the evolution of surface coverage as a function of partial pressure. This evolution can give insights on the adsorption isotherm type as well as the uptake coefficient [195, 196].

2.4 Literature review on interaction between atmospheric aerosols and iodine compounds

Some aspects of the atmospheric chemistry of iodine are not yet well covered by studies, such as the interaction of gaseous iodine compounds with atmospheric aerosols and its resulting speciation. Indeed, only few studies have been currently published on this topic between 1998-2013. Only few publications addressed the reactivity of HOI, ICl and IBr with halide salts [138, 197, 198]. Other publications [197, 199-206] have investigated the interaction between ice and iodine species such as HOI, $IONO_2$, HI, IBr, ICl, I_2 and CH_3I. Most of these experiments were investigated under temperatures representative of the troposphere (180-298 K) [138, 197-202]. Two studies investigated the uptake of organic iodine species, CH_3I and C_2H_5I by soot particles [207, 208]. Modelling work [9] mentioned loss rate of IO, OIO, I_2O_5, INO_2 and $IONO_2$ with undefined surfaces.

2.4.1 Heterogeneous reaction of inorganic iodine species with halide salt aerosols

The heterogeneous reaction of HOI [197] or HOI/$IONO_2$ [138] with halide salt particles was investigated experimentally. It has been shown that HOI could be involved in the activation of halogens from halide salt aerosols (NaCl, KBr, NaBr) due to the formation of interhalogen species (ICl, IBr) via reaction [R2-31]

$$HOI + NaX\ (Cl,Br)\ or\ KBr \rightarrow IX\ (Cl,Br) + (K,Na)YOH \quad [R2\text{-}31]$$
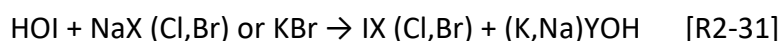
The reaction was investigated for HOI ranging from 3.0×10^{10} to 2.0×10^{13} molecule.cm^{-3} on NaCl and KBr powder salts (source of salts is not precised by the authors) at ambient temperature (temperature range is not precised by the author) using a Knudsen cell coupled to a mass spectrometer [197]. They reported maximum value for the initial uptake coefficient γ_0 of $(4 \pm 2) \times 10^{-2}$ and of $(5 \pm 2) \times 10^{-2}$ for the reaction of HOI on NaCl and KBr respectively, measured at zero time or very close to it. Authors [197] have found that the uptake coefficient decreases with increasing residence time in the Knudsen cell reactor and explained it as "Surface ageing effects" due to HOI adsorption on the Knudsen cell surface (stainless steel)

and subsequent decomposition. The only gaseous product observed in the study of the reaction of HOI on NaCl was I_2, whereas both I_2 and IBr were observed with the reaction of HOI on KBr. Additional experiments were conducted [197] with $NaNO_3$ salts to probe the decomposition reaction of HOI. The observed initial uptake coefficient on $NaNO_3$ was of the same order as on NaCl and KBr with a value of $\gamma_0 = (5\pm2) \times 10^{-2}$. Only I_2 was observed as a gaseous product with reaction of HOI on $NaNO_3$. Here it should be highlighted that the major formation of the observed I_2 can be due to the decomposition of HOI with Knudsen cell surface (side product).

To investigate further the possible release of interhalogens via the reaction of HOI with halide salts, a comprehensive study of the heterogeneous interaction of gaseous HOI $((0.2-8) \times 10^{12}$ molecule.cm^{-3}) with NaBr thin films (prepared from saturated solution of NaBr (Lancaster 99%+)), commercial NaCl grains (Breckland Scientific, 99%+) and sea-salt granular crystallites (Community Food Ltd, 99%+, obtained from solar evaporation of seawater free from any additives or processing aids) was conducted [198]. The authors [198] reported that, during the course of the optimization of the HOI gaseous source the formation of I_2 was noticed, suggesting a decomposition reaction of HOI on the inner wall of the outer sliding injector. They have also determined the overall error on the uptake coefficient, which is in the 18%-35% under their experimental conditions. The interaction was investigated by using a wall halocarbon coated flow reactor coupled to a mass spectrometer at 278 and 298 K. Additionally, the authors [198] conducted measurements in the presence of water vapor up to 23% relative humidity with NaCl and NaBr, and up to 11% relative humidity with sea-salt at 278 K. Experiments with higher relative humidity in the flow tube were not possible. The initial time dependent uptake (γ_0) was not very reproducible. As a result, authors have reported that the heterogeneous interaction of HOI with sodium halide salts to form interhalogens (ICl, IBr) features a steady state uptake coefficient (after the uptake state had settled to a constant value) of $\gamma_{ss} = (3.4 \pm 0.9) \times 10^{-2}$ on NaBr, $\gamma_{ss} = (1.6 \pm 0.4) \times 10^{-2}$ on NaCl and $\gamma_{ss} = (6.1 \pm 2.1) \times 10^{-2}$ on sea-salt independently of the temperature between 278 and 298 K. Moreover, they determined that the uptake of HOI in the clean reactor (e.g. without salt) is insignificant ($\gamma_{ss} = (5.0 \pm 1.0) \times 10^{-4}$) compared to the uptake on salts. This indicates that the uptake is quite significant for the reaction of HOI on halide salts but lower for pure NaCl than for HOI on sea-salts. This can be due to the increase in defect sites in sea-salt particles, caused by Br$^-$ dislocations and the presence of additional species such as $MgCl_2$. Moreover, the authors [198] observed a decrease in surface reactivity (surface ageing) as described previously [197]. The γ for the reaction decreased with the time exposure of HOI, i.e., after $\sim$30 mins, γ_{ss} was determined to be $(8.0 \pm 3.0) \times 10^{-3}$, $(7.0 \pm 0.3) \times 10^{-3}$, and $(1.4 \pm 0.4) \times 10^{-2}$ for NaBr, NaCl, and

sea-salts, respectively. In all cases, no dependence of γ_{ss} on relative humidity was observed. On the exposure of HOI to sea-salts both ICl and IBr were observed as products, with a bromine release favored over chlorine considering that the composition of sea-salts is 99.5 wt %Cl⁻ compared to 0.2 wt % Br⁻. The maximum amount of ICl and/or IBr released to the gas phase after reaction of HOI with NaCl, NaBr, and sea salt surfaces was 3×10^{14} molecule.cm⁻², 1×10^{16} molecule.cm⁻² and 3×10^{15} molecule.cm⁻² (Cl⁻)/2×10^{15} molecule.cm⁻²(Br⁻), respectively. It should be noted that the amount of ICl and IBr released was time dependent. Authors [198] reported only ICl and IBr as the products detected in the gas phase for the reaction of HOI on NaCl and NaBr, respectively, whereas a previous study [197] has observed I_2 as the main product.

Furthermore, the authors [198] investigated the interaction of products i.e. ICl, IBr, and I_2 with NaCl, NaBr and Sea-Salts. No interaction of I_2, ICl, or IBr was observed with the NaCl surface. I_2 and IBr did not interact with the NaBr surface either. In contrast, ICl was lost rapidly to the NaBr surface with production of IBr. The steady state uptake coefficient of ICl (3.1×10^{11} molecule.cm⁻³) on NaBr was determined to be $\gamma_{ss} = (6.8 \pm 1.8) \times 10^{-3}$. On the other hand, I_2 did not interact with the sea-salts. The physisorption interaction of IBr (3.0×10^{11} molecule.cm⁻³) with sea salts revealed a $\gamma_{ss}= (6.0 \pm 2.0) \times 10^{-4}$, whereas, the reaction of ICl (3.6×10^{11} molecule.cm⁻³) with sea salts leads to the formation of IBr with a $\gamma_{ss}= (1.2 \pm 0.4) \times 10^{-3}$. It should be highlighted that after 40 mins, IBr production was no longer observed.

An additional study [138] dedicated to the uptake and reaction of HOI/IONO$_2$ with dry NaCl, NaBr and mixed salt (NaCl/NaBr) surfaces was achieved using a coated-wall flow tube reactor coupled to a mass spectrometer at 298 K. Dry and mixed salts of NaCl and NaBr were made from aqueous solutions of composition (Aldrich, 99+%) 2 M NaCl, 3×10^{-3} M NaBr. The bulk flow rate was between 400-600 cm³.min⁻¹. It was shown that the reaction of HOI/IONO$_2$ with mixed salts revealed an immediate release of IBr and a delayed release of ICl as the surface bromide was depleted. Similarly, on NaCl and NaBr surfaces, the IBr was observed to be released immediately on the timescale of the experiment, whereas release of ICl was delayed, respectively. Nevertheless, the authors reported that dry salts might have trace of adsorbed water, which may facilitate the reaction with HOI/IONO$_2$. The authors only reported a lower limit for the uptake coefficient on dry salt surfaces $\gamma_{obs} > 10^{-2}$ without stating if it is an initial or steady state uptake.

Similar to dry salts, the authors [138] have also reported the uptake and reaction of mixed frozen salt film (inserting NaCl/NaBr solution into a precooled flow reactor 258 K, solution

concentration was not precised by the author) surfaces using a coated-wall flow tube reactor coupled to a mass spectrometer at 243 K. With mixed frozen salts, the uptake of HOI/IONO$_2$ produced stoichiometric conversion to a molecular di-halogen (ICl, IBr). However, they observed that HOI reacts initially with Br$^-$ to form IBr, which is immediately released to the gas phase. The delayed detection of ICl could then be explained by a competition for HOI (or IONO$_2$) between Br$^-$ and Cl$^-$ ions. In fact, as the exposure time of HOI/IONO$_2$ to frozen mixed salts increases, the rate of production of IBr decreases and a concomitant increase in the signal of ICl is observed. In the case of IONO$_2$ alone, the surface reaction was proceeded directly with Cl$^-$ (or Br$^-$) ions to form ICl (or IBr) and a nitrate ion NO$_3^-$. Thus, in this study [138] they could not distinguish between product formations resulting from HOI or IONO$_2$ uptake into mixed surfaces. There was no evidence for the formation of I$_2$ in the gas phase. Additionally, the variation of the initial IONO$_2$/HOI ratio by a factor of three did not alter the observed results. Finally, they [138] proposed that for the frozen salt, the initial step in the uptake of HOI and IONO$_2$ may be adsorption at the ice surface, before surface migration to reactive sites (i.e. with Br$^-$ or Cl$^-$) takes place. The observed uptake of both HOI/IONO$_2$ onto a frozen mixed salt surface were found to be > 5 × 10^{-2} (uptake value was not precised by the authors if it is initial or steady state uptake). Additionally, they have found that ICl initial uptake by frozen mixed salts is > 10^{-2} and that one molecule of IBr is released per molecule of ICl lost from the gas phase. On the other hand, the uptake of IBr by frozen mixed salts was observed to be reversible with no formation of ICl, or Br$_2$ (unreactive).

Therefore, we can conclude that for pure halide salts such as NaCl and NaBr, IBr and ICl were produced respectively, from the interaction with HOI or HO/IONO$_2$. IBr and ICl were the major gas products from the interaction of HOI or HOI/IONO$_2$ with mixed dry or frozen halide salts (NaCl, NaBr). Similarly, IBr was also formed from the uptake of ICl on sea salts, frozen mixed halide salts (NaCl/Br) and pure NaBr. Additionally, it was proposed that the interaction of HOI/IONO$_2$ on frozen salts initially takes place at the frozen surface before surface migration into the reactive sites. Both initial and steady state uptake of HOI and ICl were observed in the range of 10^{-3}-10^{-2}. Similarly, the uptake of HOI/IONO$_2$ was observed in the range of 10^{-2}, but limited by gas diffusion. Thus, the uptake coefficients of HOI or HOI/IONO$_2$ are in the same range for all halide salts.

Table 2. 7 Table summarizing the used methods for the measurement of uptake in HOI-Halide interactions. The interaction, the temperature, the observed γ and the products observed are reported [138, 197, 198]. $γ_o$: uptake coefficient at zero time, $γ_{ss}$: uptake at steady state condition, $γ_{obs}$ = uptake coefficient observed and not precised if it is at zero time or steady state conditions.

Interaction	Technique	Temperature	Uptake coefficient	Products	Reference
HOI + NaCl	Knudsen cell	Ambient	$γ_o = (4 \pm 2) \times 10^{-2}$	I_2	[197]
HOI + KBr			$γ_o = (5 \pm 2) \times 10^{-2}$	I_2 , IBr	
HOI + NaNO₃			$γ_o = (5 \pm 2) \times 10^{-2}$	I_2	
HOI + NaCl	Coated flow reactor	278 - 298 K	$γ_{ss} = (1.6 \pm 0.4) \times 10^{-2}$	ICl	[198]
HOI + NaBr			$γ_{ss} = (3.4 \pm 0.9) \times 10^{-2}$	IBr	
HOI + Sea salt			$γ_{ss} = (6.1 \pm 2.1) \times 10^{-2}$	IBr, ICl	
ICl + NaBr		298 K	$γ_{ss} = (6.8 \pm 1.8) \times 10^{-3}$	IBr	
IBr + Sea salt			$γ_{ss} = (6 \pm 2) \times 10^{-4}$	No products	
ICl + Sea salt			$γ_{ss} = (1.2 \pm 0.4) \times 10^{-3}$	IBr	
HOI/IONO₂ + dry NaCl/NaBr	Coated flow reactor	298 K	$γ_{obs} > 10^{-2}$	IBr, ICl	[138]
HOI/IONO₂ + NaBr			$γ_{obs} > 10^{-2}$	ICl	
HOI/IONO₂ + NaCl			$γ_{obs} > 10^{-2}$	IBr	
HOI/IONO₂ + frozen NaCl/NaBr		243 K	$γ_{obs} > 5 \times 10^{-2}$	IBr, ICl	
ICl + frozen NaCl/NaBr			$γ_0 > 10^{-2}$	IBr	

2.4.2 Interaction between iodine species and ice

2.4.2.1 Uptake of iodine species on ice

As mentioned previously, most of studies dealing with interaction between aerosols and iodine species concern the role of ice and snowpack in the reactivity of iodine species found in the atmosphere such as HOI, IONO₂, HI, IBr, ICl and I_2.

The interaction of HOI have been investigated [197] in the temperature range 180 to 200 K with both pure amorphous ice and doped ice films (not precised if amorphous or crystalline) using a Knudsen cell coupled to a mass spectrometer of volume 1800 cm³. Pure ice was prepared as thick ice film of up to 2x10⁵ monolayers corresponding to approximately 20 µm of thickness. HX doped ice was prepared by exposing ice to a flow of HX (X = Cl, Br) of the order of a few times 10¹⁵ molecule.s⁻¹ for a time duration long enough to ensure the adsorption of about 10 formal monolayers of HX at the interface depending on the uptake coefficient.

In the case of pure amorphous ice, the uptake of HOI between 180 to 200 K varied between 2×10^{-2} -8×10^{-2} and the initial uptake was determined to be $(6.4\pm2)\times10^{-2}$.

In the case of doped ice, the following reaction may take place:

$$HOI + HX\ (Cl,\ Br) \rightarrow IX\ (Cl,\ Br) + H_2O \quad [R2-32]$$
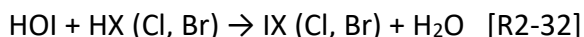
Comparatively to pure amorphous ice, the values of the reactive uptake coefficients were not significantly influenced by the presence of HX at the interface [197]. The initial uptake coefficients were $(5\pm2)\times10^{-2}$ and $(4\pm2)\times10^{-2}$ at 200 K for doped ice with HCl and HBr, respectively. The only reaction product observed with doped ice and pure amorphous ice upon thermal desorption was I_2, via the decomposition reaction of HOI. None of the products (ICl, IBr) were observed as a result of the heterogeneous reaction on both amorphous ice and ice doped samples even after thermal desorption and complete evaporation of the ice sample. Thus, the uptake seems to lead to an irreversible loss of HOI on both amorphous ice and ice doped samples.

The adsorption and desorption of HI with amorphous ice have been studied using Knudsen cell coupled to a mass spectrometer of volume 1830 cm^3 [199]. The experiments were carried out in the temperature range of 190 to 210 K. The high solubility of HI in amorphous ice may be the reason that the desorption of HI from the ice sample was never observed. The kinetics of adsorption was found to have a negative temperature dependence. The observed uptake of HI was temperature dependent and in the range, $(1.7-3.3)\times10^{-1}$.

Complementary, the interactions of pure HI gas with thin crystalline ice films have been studied using a Knudsen cell reactor. In addition to the mass spectrometer, the Knudsen cell reactor was coupled to a Fourier transform infrared-reflection absorption (FTIR-RAS) spectroscopic probe, a highly sensitive surface/bulk probe [200]. The experiments were investigated in a wide range of temperatures (185-210 K), flow rates of HI (1.5- 500) $\times10^{13}$ molecules.s^{-1}, and ice film thicknesses of 10-100 nm. As observed for studies with HOI in Knudsen cell, the walls of the Knudsen chamber can act as a small and continuous sink for HI gas-phase. However, HI was efficiently and continuously taken up by ice surfaces with $\gamma_{obs} \geq$ 2x 10^{-2} over a range of atmospherically relevant temperatures (180-210 K) and in all cases of exposure. The uptake, further, showed no temporal dependence for exposure times up to 60 minutes. At the same time, the incorporation of HI into ice resulted in the formation of amorphous mixed HI:H$_2$O product layers. The concentrated amorphous HI:H$_2$O mixtures were shown to be proportional to the flow rate of HI. Authors concluded that HI exist primarily in

an ionized or solvated state upon reaction with ice, with no possibility to investigate the nature of the amorphous multilayer product.

Comparatively, the uptake kinetics of HI was also investigated on stable ice films (thickness 12.5 ± 3.5 μm; not precised if amorphous or crystalline) in the temperature range 200-233 K using flow tube reactor [201]. The mean value obtained for the steady state uptake for all conditions was (2.2 ± 0.4) x 10^{-2} independently of pressure and HI surface concentration in the temperature range 213-233 K. The uptake below 212 K was limited by diffusion. Thus, an approximate lower limit of γ ≥0.1 below 212 K was obtained. On the other hand, authors [201] supposed that stable HI multilayers were likely to be formed between 190 and 230 K by the large continuous uptake of HI on ice.

The reactivity of the Interhalogens (ICl and IBr) and I_2 with doped ice "HX/ice" (i.e thin ice film sample was exposed to a high flow of HX, X = Cl, Br, I, (not stated if amorphous or crystalline ice film) was investigated in the temperature range 180 to 205 K using Knudsen cell of volume 1830 cm^3 [202]. The gaseous flow rate ranges from 3.0 x 10^{10} to 2.0 x 10^{13} molecule.cm^{-3}. The reaction mechanism of interhalogens with doped ice may lead to halogen exchange. Table 2.9, summarizes the reactions, initial uptake coefficients with ice and HX-doped ice and the observations including the confirmed reaction products observed after thermal desorption. It should be highlighted that I_2 was actually taken up by HX-doped ice already at 200 K in a non-reactive way:

$$I_2 + HX \ (Cl, Br) \rightarrow H^+I_2X^- \ (Cl, Br) \qquad [R2-33]$$
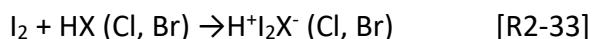
The authors [202] suggested that the interaction of I_2, IBr and ICl with pure amorphous ice is ionic type. Significantly, the $γ_0$ found on pure ice was highest for ICl (2.3 - 9.0) x 10^{-2} which has the highest difference in electronegativity ΔEN of the atoms and has therefore the highest dipole moment in comparison to IBr and I_2. Thus, the expected decrease sequence according to the known value of ΔEN in γ was as follows ICl>IBr >I_2.

In all the cases of interhalogen interaction with HX-doped ice, the authors [202] reported that the reaction is driven by the possibility to form the most stable hydrohalic acid as for reactions R2-38, R2-39, R2-43 as shown in Table 2.8. Thus, for instance the apparent non-reactive character of reaction (R2-41) was due to that HCl already represents the most stable hydrohalic acid relative to HBr. Further, on HX-doped ice they observed a generally increasing trend of $γ_0$ with increasing molecular weight of HX. The only exception to this was the interaction of ICl with HI. Additionally, in the case for reactions (R2-37) and (R2-42) where IX

was exposed to HX-doped ice, thermal desorption displaced the equilibrium to the left side of the reaction and regenerated the initial reactants.

Table 2. 8 Uptake and interfacial reactions of halogen compounds on ice and HX-doped ice at 200K. (H, halogen, HI: Interhalogen). The initial uptake measurement refers to the net effect of combined adsorption and desorption rate [202].

	Reaction	γ_0 (10^{-2})	Observations
R2-33	I_2 on amorphous ice	No uptake	Below detection limits
R2-34	I_2 +HCl-doped ice	5 ± 1	Reversible uptake
R2-35	I_2 +HBr -doped ice	15 ± 2	Reversible uptake
R2-36	ICl on amorphous ice	9 ± 2	Saturation. Reversible uptake
R2-37	ICl +HCl-doped ice	30 ± 5	No reaction observed
R2-38	ICl +HBr-doped ice →HCl + IBr	30 ± 2	Reactive uptake: HCl observed upon desorption. Strong negative temperature dependence
R2-39	ICl +HI-doped ice →HCl + I_2	32 ± 2	Reactive uptake: HCl and I_2 observed upon desorption.
R2-40	IBr on amorphous ice	2.5 ± 0.2	Instant saturation. Reversible uptake
R2-41	IBr +HCl-doped ice	20 ± 5	No reaction observed
R2-42	IBr +HBr-doped ice	30 ± 5	No reaction observed
R2-43	IBr +HI-doped ice →HBr + I_2	50 ± 2	Reactive uptake: HBr and I_2 observed upon desorption.

Therefore, we can conclude that interaction of HOI with amorphous or doped ice was in the uptake coefficient range of (4-5) x 10^{-2}. ICl and IBr were the gas products observed from the reaction of HOI with doped ice. The ice structure affects the interaction with HI, where the observed uptake with amorphous ice ((1.7-3.3) x 10^{-1})) was higher than steady state uptake observed with crystalline ice film ((2.2 ± 0.4) x 10^{-2})). IBr and ICl were observed from the interaction of HI with ice films only. I_2 was reversibly taken by doped ice with an initial uptake range between ((5-15) x 10^{-2})). Interhalogens, IBr and ICl were taken by doped ice to produce HCl, HBr, HI, I_2 based on the halogen type of both the doped ice and the interhalogen. The initial uptake ranged between ((2-5) x 10^{-1})) for IBr and ICl on doped ice. On the other hand, the interaction of IX (X=Cl, Br) with amorphous ice showed a lower initial uptake ((2.5-9.0) x 10^{-2})). Thus, the uptake coefficient can vary with the type and structure of ice and inorganic gaseous species.

Table 2. 9 summarizing the used methods for the measurement of uptake in HOI-Halide interactions. The interaction, the temperature, the γ and the products observed are reported [197, 199, 200, 201, 202]. γ_o : uptake coefficient at zero time, γ_{ss} : uptake at steady state condition, γ_{obs} = uptake coefficient observed and not precised if it is at zero time or steady state conditions.

Interaction	Technique	Temperature	Uptake coefficient	Products	Reference
HOI + amorphous ice	Knudsen cell	180-200 K	$\gamma_0=$ $(6 \pm 2) \times 10^{-2}$	-	[197]
HOI + HX/amorphous ice (X=Cl,Br)		200 K	$\gamma_0=$ $((4\text{-}5) \pm 2) \times 10^{-2}$	ICl, IBr	
HI + amorphous ice	Knudsen cell	190-210 K	$\gamma_{obs}=$ $(1.7\text{-}3.3) \times 10^{-1}$	-	[199]
HI + crystalline ice thin film	Knudsen cell	185-210 K	$\gamma_{obs} \geq 2 \times 10^{-2}$	Amorphous HI:H_2O layers	[200]
HI + Ice film	Flow tube reactor	213-233 K	$\gamma_{ss} =$ $(2.2 \pm 0.4) \times 10^{-2}$	IBr, ICl	[201]
I_2 + HX/ice (X= Cl, Br)	Knudsen cell	200 K	$\gamma_0 =$ $(5\text{ -}15) \times 10^{-2}$	-	[202]
ICl + HX/ice (X= I, Cl, Br)			$\gamma_0 =$ $(3.0\text{ - }3.2) \times 10^{-1}$	- HCl and IBr with HBr/ ice - HI and I_2 with HI/ice	
IBr + HX/ice (X= I, Cl, Br)			$\gamma_0 =$ $(2\text{-}5) \times 10^{-1}$	HBr and I_2 with HBr/ice	
IX + amorphous ice (X= Cl, Br)			$\gamma_0 =$ $(2.5\text{ -}9) \times 10^{-2}$	ICl	

2.4.2.2 Photodissociation of CH_3I on ice

Studies dealing with interactions between aerosols and methyl iodide (CH_3I) species concern the role of ice and snowpack in photo reactivity of CH_3I species found in the atmosphere. The measurements performed during field campaigns showed that photochemical processes occurring within the snowpack may alter the atmospheric composition including the organo-halogen content [203, 209]. There have been extensive experimental and theoretical studies on the photodissociation of CH_3I in the gas phase [210- 212] or adsorbed on different solid metallic substrates [213- 216]. Along with this wealth of information, the observation of organic iodide from field measurements on or in ice (snow) [203] and the discovery of organic iodide compounds as potential sources of reactive halogen species during ozone depletion

processes [217] have motivated investigations of photo dissociation of CH_3I adsorbed on ice [204- 206].

Here, it should be noted that the ice grown in vacuum could exist in several different structural forms depending on the temperature of the cold substrate. The deposition of water vapor at substrate temperatures below 130 K results in the formation of low-density porous amorphous solid water (PASW), while dosing water vapor at higher temperatures (≥130 K) results in formation of amorphous solid water (ASW). Unlike ASW, PASW contains many surface defects that facilitate trapping of adsorbates. Crystalline ice is formed by dosing water vapor at temperatures ≥ 140 K [204].

The photo dissociation of CH_3I on PASW (porous amorphous solid water) and ASW (amorphous solid water) ice was investigated using ultra high vacuum (UHV) chamber with a base pressure of 6.6×10^{-13} bar [204]. 50 monolayers (1.7×10^{-11} bar) of PASW and ASW ice were grown on zirconia substrate at 90 K and 130 K, respectively. The 50 monolayers were grown to assure that interactions associated with the zirconia substrate were removed or minimized. CH_3I was deposited on ice substrate by dosing the CH_3I vapor at 1.3×10^{-11} bar for 10 s. Authors [204] performed measurements using time-of-flight mass spectrometer (ToF-MS) and Temperature programmed desorption (TPD) coupled to a quadrupole mass spectrometer (QMS) analysis. A pulsed laser light at either 290 or 260 nm was used to irradiate the sample. The substrate was heated linearly using a rate of 3 K/s.

I_2 formation was observed on ASW at both excitation wavelengths (260 nm and 290 nm), but it was not detectable within sensitivity of author technique on PASW at both wavelengths. The I_2 formation occurred with a much greater yield when using 260 nm compared to 290 nm. However, the mechanism of I_2 formation was not clearly stated, but the authors suggested that small adsorbed clusters of CH_3I on ASW can be ideal for the formation of I_2. Additionally, the authors [204] suggested that the presence of pores in PASW can either make the trapped CH_3I molecules unavailable for photodissociation or trap iodine photo fragments within the ice substrate. CH_3 and I photofragments that were trapped within pores of PASW may recombine or react to form products that were not detected in this experiment, such as CH_3CH_3I or CH_3OH.

TPD spectra between 100-220 K of CH_3I on ASW, indicated that almost all of the CH_3I monomer and clusters had desorbed at 120 K before water began desorbing [204]. No bonding interaction between CH_3I and ASW was observed. However, the authors suggested that the

overall average symmetry of CH$_3$I likely changes from C$_{3v}$ to C$_s$ as it adsorbs. Whereas, for CH$_3$I deposited on PASW, the pores were filled before CH$_3$I began to accumulate on the surface, thus the TPD spectrum showed a three-desorption state at 120 K, 150 and 160 K. The structure of CH$_3$I adsorbed on PASW was not identified. This experiment demonstrated that ice porosity enhances the trapping of adsorbed CH$_3$I, while pore-free ice likely allows monomer adsorption and the formation of CH$_3$I clusters.

The photo dissociation of methyl iodide on D$_2$O ASW ice was investigated using ultra high vacuum (UHV) chamber with a base pressure of 5.3 × 10^{-13} bar [205]. 1 layer (1.3 × 10^{-19} bar. s) of D$_2$O ASW ice was grown on Cu substrate at 100 K. Then CH$_3$I was deposited on ice substrates by dosing the CH$_3$I vapor at 1.3 × 10^{-19} bar for 1 s. For photoirradiation, UV photons were generated from a 100 W high-pressure mercury arc lamp (Oriel). Temperature programmed desorption (TPD) spectra were collected using time-of-flight mass spectrometry (TOF-MS) while heating the substrate at a rate of 2 K/s. TPD and X-ray photoelectron spectroscopy (XPS) analysis were performed before and after irradiation. Ultra- violet photoelectron spectroscopy (UPS) analysis was performed for Cu, D$_2$O and CH$_3$I/D$_2$O/Cu substrates.

Before irradiation, the TPD spectra between 100-500 K of CH$_3$I on ASW, showed that all the mono and multilayers of CH$_3$I desorb from the ice layer at 120 and 130 K, respectively [205] which is consistent with [204]. The authors suggested that during photo-irradiation between 130-145 K, the dissociated products (CH$_3$ and I) seems to diffuse into the ice film and be trapped. Moreover, at 430 K the authors suggested a chemisorption of CH$_3$I on Cu substrate since all ice layers should be removed up to 300 K. No new photodissociated product (such as I$_2$) was observed.

XPS spectra were measured as function of photo irradiation time (up to 30 minutes) for CH$_3$I on ice at 100 K [205]. The spectra showed a dramatical change (area of the band and shift by 3 e.v) in the I 3d$_{5/2}$ XPS band (621 e.v) observed as function of photoirradiation time. This was explained by that at the beginning of photo irradiation the band observed was for both un-dissociated and dissociated CH$_3$I. Upon further photo-irradiation, the dissociated CH$_3$I becomes dominant which results in decrease in area of the band. Additionally, with increasing photo-irradiation time, the authors suggested an increase in solvated I$^-$, I radical, and/or chemisorbed I on Cu which explains the shift in the I 3d$_{5/2}$ XPS band. No other chemical species formed and/or desorbed from the surface were observed. No bands were observed from the XPS spectra for CH$_3$I photo irradiated for 5 minutes at 100K and followed by TPD up to 800 K.

This confirmed that the diffusion of CH$_3$I towards Cu substrate and that I radicals (or solvated I$^-$) do not desorb, instead they chemisorb on the Cu surface.

Finally, based on UPS spectra a small shift (-1.0 eV) was observed from electronic work function[2] of all analyzed systems Cu, D$_2$O/Cu and CH$_3$I/D$_2$O/Cu. The authors [205] concluded that the electrons photo excited from Cu transferred to ice to generate solvated electrons in the ice film. The solvated electrons then quickly transfer to CH$_3$I to proceed the cleavage of C-I bond. Thus, the ice is being an important intermediate by efficiently capturing photoelectrons emitted from the underlying metal substrate.

Similarly, the system of CH$_3$I adsorbed on thin films of D$_2$O ASW ice grown on Cu at 90 K was studied using an ultra-high vacuum system with a base pressure of 1.3×10^{-12} bar [206]. Up to 2- 120 monolayers of D$_2$O were deposited on the Cu surface. 0.2-1 monolayer of CH$_3$I was then deposited on D$_2$O/Cu. The exact dosing quantity of D$_2$O and CH$_3$I have not been precised by the authors [206]. The authors used time of flight quadrupole mass spectrometer (TOF-QMS) to analyse the distributions of the desorbing CH$_3$ fragments after photodissociation using linearly polarized λ=248 nm light [206]. Observation of photo dissociation of CH$_3$I on ASW D$_2$O ice in this study are quite similar to the one observed by CH$_3$I on ASW H$_2$O ice [204]. The authors indicated that CH$_3$I adsorbed on D$_2$O forms clusters at low coverages, with a C–I bond axis orientation. However, no I$_2$ formation upon photodissociation was observed. Additionally, authors noted that the overall TOF spectrum distribution does not change significantly with increasing CH$_3$I dose [206]. More photo dissociation yield was observed for thicker D$_2$O films. In contrast to [205], the authors [206], did not find an evidence of the dissociation of CH$_3$I mechanism via the temporary solvation of photoelectrons in localized states of the D$_2$O ASW ice.

---

[2] The work function: acquired spectroscopically by measuring the difference between the Fermi Level and the cutoff of the 'tail' at the low kinetic energy end of the spectrum and then subtracting this value from the incident photon energy.

To sum up and as shown in Table 2.10, that adsorption, diffusion, and desorption of organic molecules depend largely on the morphology of the ice substrate. Porous ice enhances the trapping of adsorbed CH_3I, whereas pore-free ice likely allows monomer adsorption and the formation of CH_3I clusters. Dissociation can be observed when adsorbed CH_3I molecules in (or on) ASW ice are irradiated by UV photons. A significant dissociation to form either I, I^- or I_2 is likely to occur. No clear mechanism for I_2 has been reported, in contrast, to gas phase where only atomic Iodine is observed (see section 2.2). On the other hand, PASW can hinder the CH_3I molecule photodissociation. Nor photodissociation rate or uptake coefficient of CH_3I on ice was reported.

Table 2. 10 Table summarizing the used methods for the photodissociation of CH_3I on ice.
The ice type, the temperature, the pressure, wavelength and the products observed are reported [204, 205, 206]. ASW: Amorphous solid water and PASW: porous amorphous solid water. REMPI: resonance enhanced multiphoton ionization (REMPI). UHV: Ultra high Vacuum chamber, XPS: X-ray photoelectron spectroscopy, TOF-MS: time-of-flight mass spectrometer, TPD-QMS: Temperature programmed desorption coupled to quadrupole mass spectrometer (QMS) and UPS: Ultra- violet photoelectron spectroscopy.

Ice type	Technique	Temperature	Pressure	Wavelength	Products	Reference
H_2O ASW	UHV TOF-MS REMPI TPD-QMS	90K	6.6×10^{-13} bar	260nm 290 nm	CH_3, I, I_2	[204]
H_2O PASW	UHV TOF-MS REMPI TPD-QMS	130 K	6.6×10^{-13} bar	260nm 290 nm	CH_3, I	[204]
D_2O ASW	UHV TOF-MS XPS UPS	100K	5.3×10^{-13} bar	Hg lamp	CH_3, I^-	[205]
D_2O ASW	UHV TOF-QMS	90 K	1.3×10^{-12} bar	248 nm	CH_3, I	[206]

2.4.3 Heterogeneous interaction of organic iodine with carbonaceous aerosols

The heterogeneous interaction of organic iodine species with carbonaceous particles was investigated in only two papers [207, 208].

The uptake of CH_3I on commercial soot film (composition and source of soot is not precised by the authors) was studied using a coated wall flow tube combined with Time of Flight Mass Spectrometer at 298 K and with a bulk flow rate of 200 and 500 $cm^3.min^{-1}$ [207]. A fast-initial consumption of CH_3I followed by rapid soot surface deactivation, leading to a decrease of the CH_3I loss rate was observed. CH_3I loss on soot film was assumed to be due to two processes:

irreversible CH_3I uptake and, to less extent, reversible non-reactive adsorption–desorption processes. The estimated residence time of the reversibly adsorbed CH_3I molecules on the soot surface was of the order of a few seconds. The initial uptake was determined to be $(1.03\pm0.15) \times 10^{-2}$. Finally, the authors stated that the fate of the organoiodines on the soot surfaces needs more research, as the heterogeneous loss of CH_3I on soot may influence the concentration of CH_3I throughout the atmosphere.

Further, the uptake of ethyl iodine (C_2H_5I) on black carbon (Degussa FW2) thin film surface at 298 K was investigated [208] by using a coated wall flow tube combined with a differentially pumped time-of-flight mass spectrometer. As observed for soot surface when exposed to CH_3I [208], a fast-initial consumption of C_2H_5I followed by rapid deactivation of the black carbon leading to a decrease of the C_2H_5I loss rate was observed. In addition, a partial desorption of C_2H_5I was observed when C_2H_5I was no longer in contact with the black carbon surface. The initial uptake was determined to be $(2.3\pm0.9) \times 10^{-2}$. Finally, the authors stated that to get more conclusive answers on the interaction of C_2H_5I with black carbon surface, future research should be directed for characterizing atmospheric carbon aerosol samples and understanding their heterogeneous interactions.

Therefore, we can conclude that the initial uptake of methyl iodide on black carbon or ethyl iodide on soot was of the same magnitude. No data on the reaction or the products formed was given.

2.4.4 Modelling of inorganic species with undefined surfaces

A tropospheric Halogen Chemistry model (THAMO) was developed to investigate the halogen chemistry chemical mechanism. THAMO is a one-dimensional chemical and transport model that uses time-implicit integration [9, 39]. This model can simulate the iodine observations, and thus explore the impact of iodine chemistry in the polar boundary layer. In this model, the authors [9] computed a first-order rate loss of uptake for halogen heterogeneous uptake on aerosols, for a number of gas phase species. Table 2.11 shows the calculated first order rate loss due to uptake of iodine gaseous species (IO, OIO, HI, HOI, INO_2, $IONO_2$, I_2O_5) into undefined aerosol species of inorganic species. These rate losses seem to confirm the experimental observations stated before (section 2.4) that iodine species can be reactive with atmospheric aerosols.

Table 2. 11 Estimated rate loss of iodine on aerosols based on free-regime approximation [9].

Loss to undefined aerosols	
Species	**Rate loss**
IO	0.02
OIO	1
HI	0.02
HOI	0.02
INO_2	0.02
$IONO_2$	0.02
I_2O_5	0.02

2.5 Conclusion

To sum up, CH_3I and I_2 that can be emitted naturally or released in case of severe nuclear accident into the atmosphere may react in gaseous phase and may interact with ice or with atmospheric aerosols. Although the gaseous phase reaction of halogen compounds is well documented, there is still a lack of knowledge about the interaction between atmospheric aerosols and CH_3I and I_2 gaseous species which are of nuclear interest.

References

[1] S. Solomon, On the role of iodine in ozone depletion, J. Geophys. Res. 99 (1994) 491–499. https://doi.org/10.1029/94JD02028.

[2] A.R. Baker, D. Thompson, M.L.A.M. Campos, S.J. Parry, T.D. Jickells, Iodine concentration and availability in atmospheric aerosol, Atmos. Environ. 34 (2000) 4331–4336.https://doi.org /10.1016/S1352-2310(00)00208-9.

[3] L.J. Carpenter, S.M. Macdonald, M.D. Shaw, R. Kumar, R.W. Saunders, R. Parthipan, J. Wilson, J.M.C. Plane, Atmospheric iodine levels influenced by sea surface emissions of inorganic iodine, Nat. Geosci. 6 (2013) 108–111. https://doi.org/10.1038/ngeo1687.

[4] A. Saiz-Lopez, J.M.C. Plane, Novel iodine chemistry in the marine boundary layer, Geophys. Res. Lett. 31 (2004) L04112. https://doi.org/10.1029/2003GL019215.

[5] A. Saiz-Lopez, J.M.C. Plane, A.R. Baker, L.J. Carpenter, R. Von Glasow, C.G. Juan, G. Mcfiggans, R.W. Saunders, Atmospheric Chemistry of Iodine, Chem. Rev. 112 (2012) 1773–1804. https://doi.org//10.1021/cr200029u.

[6] J. Trincal, Thèse de Doctorat Modélisation du comportement de l'iode dans l'atmosphère, Lille university, 2015.

[7] C. Fortin, These de Doctorat Etudes par simulations numériques et moléculaires de la réactivité atmosphérique de l'iode, Lille university, 2019.

[8] C. Peters, S. Pechtl, J. Stutz, K. Hebestreit, G. Hönninger, K.G. Heumann, A. Schwarz, J. Winterlik, U. Platt, Reactive and organic halogen species in three different European coastal environments, Atmos. Chem. Phys. 5 (2005) 3357–3375. https://doi.org/10.5194/acp-5-3357-2005.

[9] A.Saiz-Lopez, J.M.C. Plane, A.S. Mahajan, P.S. Anderson, A.E. Jones, H.K. Roscoe, R.A. Salmon, W.J. Bloss, J.D. Lee, On the vertical distribution of boundary layer halogens over coastal Antarctica : implications for O_3, HO_x, NO_x and the Hg lifetime, Atmos. Chem. Phys. 8 (2008) 887–900. https://doi.org/10.5194/acp-8-887-2008.

[10] K. Law, W. Struges, Chapter 2 Halogenated short-lived substances, in: scientific assessment of ozone depletion: 2006 Report No. 50, (2007).

[11] J.E. Lovelock, R.J. Maggs, R.J. Wade, Halogenated hydrocarbons in and over the Atlantic, Nature. 241 (1973) 194–196. https://doi.org/10.1038/241194a0.

[12] R. Huang, Ph.D. thesis on Reactive Halogen Compounds in the Marine Boundary Layer: Method Developments and Field Measurements, Johannes Gutenberg-Universität, 2009.

[13] C. Ordonez, J.-F. Lamarque, S. Tilmes, D.E. Kinnison, D.R.B. E. L. Atlas, G.S. Santos, G. Brasseur, A. Saiz-Lopez, Bromine and iodine chemistry in a global chemistry-climate model: description and evaluation of very short-lived oceanic sources, Atmos. Chem. Phys. 12 (2012) 1423–1447. https://doi.org/10.5194/acp-12-1423-2012.

[14] N. Bell, L. Hsu, D.J. Jacob, M.G. Schultz, D.R. Blake, J.H. Butler, D.B. King, J.M. Lobert, E. Maier-Reimer, Methyl iodide: Atmospheric budget and use as a tracer of marine convection in global models, J. Geophys. Res. Atmos. 107 (2002) 8/1-8/12. https://doi.org/10.1029/200IJD001151.

[15] R.A. Rasmussen, M.A.K. Khalil, R. Gunawardena, S.D. Hoyt, Atmospheric methyl iodide (CH_3I), J. Geophys. Res. 87 (1982) 3086–3090. https://doi.org/10.1029/JC087iC04p03086.

[16] C.H. Dimmer, P.G. Simmonds, G. Nickless, M.R. Bassford, Biogenic fluxes of halomethanes from Irish peatland ecosystems, Atmos. Environ. 35 (2001) 321–330. https://doi.org/10.1016/S1352-2310(00)00151-5.

[17] K.R. Redeker, N.Y. Wang, J.C. Low, A. McMillan, S.C. Tyler, R.J. Cicerone, Emissions of methyl halides and methane from rice paddies, 290 (2000) 966-969. https://doi.org/10.1126/science.290.5493.966.

[18] M.O. Andreae, P.Merlet, Emission of trace gases and aerosols from biomass burning, Glob. Biogeochem. 15 (2001) 955–966. https://doi.org/10.1029/2000GB001382.

[19] A. Ekdahl, M. Pedersén, K. Abrahamsson, A study of the diurnal variation of biogenic volatile halocarbons, Mar. Chem. 63 (1998) 1–8. https://doi.org/10.1016/S0304-4203(98)00047-4.

[20] C.E. Jones, K.E. Hornsby, R. Sommariva, R.M. Dunk, R. Von Glasow, G. McFiggans, L.J. Carpenter, Quantifying the contribution of marine organic gases to atmospheric iodine, Geophys. Res. Lett. 37 (2010) L18804. https://doi.org/10.1029/2010GL043990.

[21] Y. Sakamoto, A. Yabushita, M. Kawasaki, S. Enami, Direct emission of I_2 molecule and IO radical from the heterogeneous reactions of gaseous ozone with aqueous potassium iodide solution, J. Phys. Chem. A. 113 (2009) 7707–7713. https://doi.org/10.1021/jp903486u.

[22] F.C. Kupper, C.J. Carrano, Key aspects of the iodine metabolism in brown algae : a brief critical review, R. Soc. Chem., Met. 11 (2019) 756–764. https://doi.org/10.1039/c8mt00327k.

[23]F.C. Kupper, L.J. Carpenter, Gordon B. McFiggans, C.J. Palmere, T.J. Waite, E.-M. Boneberg, S. Woitsch, M. Weiller, R. Abelaj, D. Grolimund, P. Potin, A. Butler, G.W.L. III, P.M.H. Kroneck, W. Meyer-Klaucke, M.C. Feiters, Iodide accumulation provides kelp with an inorganic antioxidant impacting atmospheric chemistry, Proc. Natl. Acad. Sci. U. S. A. 105 (2008) 6954–6958. https://doi.org/10.1073/pnas.0709959105.

[24] J.A. Garland, H. Curtis, Emission of Iodine from the Sea Surface in the Presence of Ozone, Geophys. Res., 86 (1981) 3183–3186. https://doi.org/10.1029/JC086iC04p03183.

[25] A. Saiz-Lopez, J.A. Shillito, H. Coe, J.M.C. Plane, Measurements and modelling of I_2, IO, OIO, BrO and NO_3 in the mid-latitude marine boundary layer, Atmos. Chem. Phys. 6 (2006) 1513–1528. Open source.

[26] J. Rancher, M.A. Kritz, Diurnal Fluctuations of Br and I in the Tropical Marine, J. Geophys. Res. 85 (1980) 5581–5587. https://doi.org/10.1029/JC085iC10p05581.

[27] B.S. Gilfedder, R. Chance, U. Dettmann, S.C. Lai, Determination of total and non-water soluble iodine in atmospheric aerosols by thermal extraction and spectrometric detection (TESI), Anal. Bioanal. Chem. 398 (2010) 519–526. https://doi.org/10.1007/s00216-010-3923-1.

[28] T.M. Sherwen, M.J. Evans, D. V Spracklen, L.J. Carpenter, R. Chance, A.R. Baker, J.A. Schmidt, T.J. Breider, Global modeling of tropospheric iodine aerosol, Geophys. Res. Lett. 43 (2016) 10012–10019. https://doi.org/10.1002/2016GL070062.

[29] A. Saiz-Lopez, R.P. Fernandez, C. Ordóñez, D.E. Kinnison, J.C.G. Martín, J.F. Lamarque, S. Tilmes, Iodine chemistry in the troposphere and its effect on ozone, Atmos. Chem. Phys. 14 (2014) 13119–13143. https://doi.org/10.5194/acp-14-13119-2014.

[30] T.K. Koenig, S. Baidar, P. Campuzano-Jost, C.A. Cuevas, B. Dix, R.P. Fernandez, H. Guo, S.R. Hall, D. Kinnison, B.A. Nault, K. Ullmann, J.L. Jimenez, A. Saiz-Lopez, R. Volkamer, Quantitative detection of iodine in the stratosphere, Proc. Natl. Acad. Sci. U. S. A. 117 (2020) 1860–1866. https://doi.org/10.1073/pnas.1916828117.

[31] K. Seitz, J. Buxmann, D. Pöhler, T. Sommer, J. Tschritter, T. Neary, C. O'Dowd, U. Platt, The spatial distribution of the reactive iodine species IO from simultaneous active and passive DOAS observations, Atmos. Chem. Phys. 10 (2010) 2117–2128. https://doi.org/10.5194/acp-10-2117-2010.

[32] C.S.E. Bale, T. Ingham, R. Commane, D.E. Heard, W.J. Bloss, Novel measurements of atmospheric iodine species by resonance fluorescence, J. Atmos. Chem. 60 (2008) 51–70. https://doi.org/10.1007/s10874-008-9108-z.

[33] R. Vogt, R. Sander, R. Von Glasow, P.J. Crutzen, Iodine chemistry and its role in halogen activation and ozone loss in the marine boundary layer: A model study, J. Atmos. Chem. 32 (1999) 375–395. https://doi.org/10.1023/A:1006179901037.

[34] W.L. Chameides, D.D. Davis, Iodine : Its Possible Role in Tropospheric Photochemistry, J. Geophys. Res. 85 (1980) 7383–7398. https://doi.org/10.1029/JC085iC12p07383.

[35] U. Platt, G. Hönninger, The role of halogen species in the troposphere, Chemosphere. 52 (2003) 325–338. https://doi.org/10.1016/S0045-6535 (03)00216-9.

[36] C.D. O'Dowd, Jose L. Jimenez, Roya Bahreini, R.C. Flagan, J.H. Seinfeld, K. Ha¨meri, L. Pirjola, M. Kulmala, S.G.J.T. Hoffmann, Marine aerosol formation from biogenic iodine emissions, Lett. to Nat. 417 (2002) 632–636. https://doi.org/10.1038/nature00773.1.2.3. 4.5.6.7.8.9.10.

[37] A.S. Mahajan, M. Sorribas, J.C.G. Martín, S.M. MacDonald, M. Gil, J.M.C. Plane, A. Saiz-Lopez, Concurrent observations of atomic iodine, molecular iodine and ultrafine particles in a coastal environment, Atmos. Chem. Phys. 11 (2011) 2545–2555. https://doi.org/10.5194/acp-11-2545-2011.

[38] A. Saiz-Lopez, J.M.C. Plane, C.A. Cuevas, A.S. Mahajan, J.F. Lamarque, D.E. Kinnison, Nighttime atmospheric chemistry of iodine, Atmos. Chem. Phys. 16 (2016) 15593–15604. https://doi.org/10.5194/acp-16-15593-2016.

[39] A.S. Mahajan, H. Oetjen, A. Saiz-Lopez, J.D. Lee, G.B. McFiggans, J.M.C. Plane, Reactive iodine species in a semi-polluted environment, Geophys. Res. Lett. 36 (2009) 1–6. https://doi.org/10.1029/2009GL038018.

[40] J.B. Burkholder, S.P. Sander, J.P.D. Abbat, J.R. Barker, R.E. Huie, C.E. Kolb, M.J.K. Goddard, V.L. Orkin, P.H. Wine, D.M. Wilmouth, Chemical Kinetics and Photochemical Data for Use in Atmospheric Studies Evaluation Number 18, JPL Publication 15-10, Jet Propulsion Laboratory, Pasadena, 2015. http://jpldataeval.jpl.nasa.gov.

[41] A. Saiz-Lopez, R.W. Saunders, D.M. Joseph, S.H. Ashworth, J.M.C. Plane, Absolute absorption cross-section and photolysis rate of I2, Atmos. Chem. Phys. Discuss. 4 (2004) 2379–2403. https://doi.org/10.5194/acpd-4-2379-2004.

[42] O. V. Rattigan, D.E. Shallcross, R.A. Cox, UV absorption cross-sections and atmospheric photolysis rates of CF_3I, CH_3I, C_2H_5I and CH_2ICl, J. Chem. Soc. - Faraday Trans. 93 (1997) 2839–2846. https://doi.org/10.1039/a701529a.

[43] R. Sommariva, W.J. Bloss, R. Von Glasow, Uncertainties in gas-phase atmospheric iodine chemistry, Atmos. Environ. 57 (2012) 219–232. https://doi.org/10.1016/j.atmosen v.2012.04.032.

[44] E. Jenkin, R.A. Cox, Kinetics Study of the Reactions $IO + NO_2 + M \rightarrow IONO_2+M$, $IO+IO \rightarrow$ products and $I + O_3 \rightarrow IO + O_2$, J. Phys. Chem. 89 (1985) 192–199. https://doi.org/10.1021 /j100247a040.

[45] L.J. Carpenter, Iodine in the Marine Boundary Layer, Chem. Rev. 103 (2003) 4953–4962. https://doi.org/10.1021/cr0206465.

[46] J.C.G. Martin, P. Spietz, J.P. Burrows, Spectroscopic studies of the I_2 / O_3 photochemistry Part 1: Determination of the absolute absorption cross sections of iodine oxides of atmospheric relevance, 176 (2005) 15–38. https://doi.org/10.1016/j.jphotochem.200 5.09.024.

[47] W.J. Bloss, D.M. Rowley, R.A. Cox, R.L. Jones, Kinetics and products of the IO self-reaction, J. Phys. Chem. A. 105 (2001) 7840–7854. https://doi.org/10.1021/jp0044936.

[48] A. Villard, S. Khanniche, C. Fortin, L. Cantrel, I. Černušák, F. Louis, A theoretical study of the microhydration processes of iodine nitrogen oxides, Int. J. Quantum Chem. 119 (2019) 1–11. https://doi.org/10.1002/qua.25792.

[49] N. Kaltsoyannis, J.M.C. Plane, Quantum chemical calculations on a selection of iodine-containing species (IO, OIO, INO$_3$, (IO)$_2$, I$_2$O$_3$, I$_2$O$_4$ and I$_2$O$_5$) of importance in the atmosphere, Phys. Chem. Chem. Phys. 10 (2008) 1723–1733. https://doi.org/1 0.1039/b715687c.

[50] R.M. Chambers, A.C. Heard, R.P. Wayne, Inorganic Gas-Phase Reactions of the Nitrate Radical : I$_2$ + NO$_3$ and I + NO$_3$, J. Phys. Chem. 96 (1992) 3321–3331. https://doi.org/10.1021/j100187a028.

[51] Y. Nakano, Y. Hosho, K. Sadamori, T. Ishiwata, Determination of the rate constant of the reaction of NO3 with C2H5I using time-resolved cavity ring-down spectroscopy, Chem. Phys. Lett. 535 (2012) 26–29. https://doi.org/10.1016/j.cplett.2012.03.040.

[52] N. Yukio, I.T. Ukeguchi Hiromi, K. Yugo, T. Hiroto, I. Atsushi, K.M. Sakaki Shigeyoshi, Study of the Temperature Dependence of the Reaction of NO$_3$ with CH$_3$I and the Estimation of Its Impact on Atmospheric Iodine Chemistry, Chem. Phys. Lett. 208 (2008) 938–946. https://doi.org /10.1246/bcsj.81.938

[53] F.Y. Bai, X. Wang, Y.Q. Sun, X.M. Pan, Atmospheric chemistry of alkyl iodides : theoretical studies on the mechanisms and kinetics of CH$_3$I/C$_2$H$_5$I+NO$_3$ reactions, RSC Adv. 5 (2015) 88087–88095. https://doi.org/ 10.1039/c5ra16215g.

[54] F. Louis, I. Černušák, S. Canneaux, K. Mečiarová, Atmospheric reactivity of CH$_3$I and CH$_2$I$_2$ with OH radicals: A comparative study of the H- versus I-abstraction, Comput. Theor. Chem. 965 (2011) 275–284. https://doi.org/10.1016/j.theochem.2010.09.022.

[55] O. Galvez, J.C.G. Martin, P.C. Gomez, A. Saiz-Lopez, L.F. Pacios, A theoretical study on the formation of iodine oxide aggregates and monohydrates, Phys. Chem. Chem. Phys. 15 (2013) 15572–15583. https://doi.org/10.1039/c3cp51219c.

[56] J.C.G. Martin, O. Galvez, b M.T. Baeza-Romero, T. Ingham, J.M.C. Plane, M.A. Blitz, On the mechanism of iodine oxide particle formation, Phys. Chem. Chem. Phys. 15 (2013) 15612–15622. https://doi.org/10.1039/c3cp51217g.

[57] T. Hoffmann, C.D.O. Dowd, J.H. Seinfeld, Iodine oxide homogeneous nucleation' for coastal new particle production, Geophys. Res. Lett. 28 (2001) 1949–1952. https://doi.org /10.1029/2000GL012399.

[58] J. Curtius, Nucleation of atmospheric aerosol particles, Comptes Rendus Phys. 7 (2006) 1027–1045. https://doi.org/10.1016/j.crhy.2006.10.018.

[59] B.R.W. Saunders, R. Kumar, J.C.G. Martín, A.S. Mahajan, B.J. Murray, J.M.C. Plane, Studies of the Formation and Growth of Aerosol from Molecular Iodine Precursor, Zeitschrift Für Phys. Chemie. 224 (2010) 1095–1117. https://doi.org/10.1524/zpch.2010.6143.

[60] W.R. Stockwell, F. Kirchner, M. Kuhn, S. Seefeld, A new mechanism for regional atmospheric chemistry modeling, 102 (1997) 25847–25879. https://doi.org/10.1029/9 7JD00849.

[61] K. Chevalier-Jabet, F. Cousin, L. Cantrel, C. Séropian, Source term assessment with ASTEC and associated uncertainty analysis using SUNSET tool, Nucl. Eng. Des. 272 (2014) 207–218. https://doi.org/10.1016/j.nucengdes.2013.06.042.

[62] C. Fortin, V. Fèvre-Nollet, F. Cousin, P. Lebègue, F. Louis, Box modelling of gas-phase atmospheric iodine chemical reactivity in case of a nuclear accident, Atmos. Environ. 214 (2019) 116838. https://doi.org/10.1016/j.atmosenv.2019.116838.

[63] S. Zhang, Thèse de Doctorat: Etudes cinétiques de l'oxydation radicalaire en phase gazeuse d'iodures organiques et de la formation de particules d'oxydes d'iode sous conditions simulées de l'enceinte d'un réacteur nucléaire en situation d'accident grave, Aix-Marseille Université, 2012

[64] S. Taamalli, D. Khiri, S. Suliman, S. Khanniche, C. Ivan, L. Cantrel, M. Ribaucour, F. Louis, Unraveling the Tropospheric Microhydration Processes of Iodous Acid HOIO, ACS Earth Sp. Chem. 4 (2020) 92–100. https://doi.org/10.1021/acsearthspacechem.9b00257.

[65] S. Khanniche, F. Louis, L. Cantrel, I. Černušák, A theoretical study of the microhydration of iodic acid ($HOIO_2$), Comput. Theor. Chem. 1094 (2016) 98–107. https://doi.org/10.1016/j.comptc.2016.09.010.

[66] M. Ruan, H. Hou, B. Wang, W. Li, Y. Chen, X. Deng, X. Zuo, Computational study on the hydrolysis of halomethanes, Theor. Chem. Acc. 137:181 (2018) 1–10. https://doi.org/10.1007/s00214-018-2389-7.

[67] J. Xie, X. Ma, J. Zhang, P.M. Hierl, A.A. Viggiano, W.L. Hase, Effect of microsolvation on the $OH^-(H_2O)_n$ + CH_3I rate constant. Comparison of experiment and calculations for $OH^-(H_2O)_2$ + CH_3I, Int. J. Mass Spectrom. 418 (2017) 122–129. https://doi.org/10.1016/j.ijms.2016.10.017.

[68] J. Xie, R. Otto, R. Wester, W.L. Hase, Chemical dynamics simulations of the monohydrated $OH^-(H_2O)$ + CH_3I reaction. Atomic-level mechanisms and comparison with experiment, J. Chem. Phys. 142 (2015) 2443081-2443088. https://doi.org/10.1063/1.4922451.

[69] B. Bastian, T. Michaelsen, L. Li, M. Ončák, J. Meyer, D.H. Zhang, R. Wester, Imaging Reaction Dynamics of $F-(H_2O)$ and $Cl-(H_2O)$ with CH_3I, J. Phys. Chem. A. 124 (2020) 1929–1939. https://doi.org/10.1021/acs.jpca.0c00098.

[70] J. Lelieveld, K. Klingmüller, A. Pozzer, U. Pöschl, M. Fnais, A. Daiber, T. Münzel, Cardiovascular disease burden from ambient air pollution in Europe reassessed using novel hazard ratio functions, Eur. Heart J. 40 (2019) 1590–1596. https://doi.org/10.1093/eurheartj/ehz135.

[71] O. Boucher, D. Randall, P. Artaxo, C. Bretherton, G. Feingold, P. Forster, V.-M. Kerminen, Y. Kondo, H. Liao, U. Lohmann, P. Rasch, S.K. Satheesh, S. Sherwood, B. Stevens, X.Y. Zhang, Chapter 7: Clouds and Aerosols. In Climate Change, IPCC report 2013: The Physical Science Basis. Contribution of Working Group I to the Fifth Assessment Report of the Intergovernmental Panel on Climate Change. Cambridge University Press, Cambridge, United Kingdom and New York, USA, 2013. https://doi.org/10.1017/CBO978110741 5324.016.

[72] M. Andreae, H. Annegarn, L. Barrie, J. Feichter, D. Hegg, A. Jayaraman, R. Leaitch, D. Murphy, J. Nganga, G. Pitari, J.E. Penner, Chapter 5:Aerosols, their Direct and Indirect Effects. In Climate Change, IPCC report 2001: The Scientific Basis. Contribution of Working Group I to the Third Assessment Report of the Intergovernmental Panel on Climate Change, Cambridge University Press, Cambridge, United Kingdom and New York, USA 2001. https://doi.org/10.1029/JD091iD01p01089.

[73] U. Pöschl, Atmospheric aerosols: Composition, transformation, climate and health effects, Angew. Chemie-Int. Ed. 44 (2005) 7520–7540. https://doi.org/10.1002/anie.200 501122.

[74] V.R. Després, J. Alex Huffman, S.M. Burrows, C. Hoose, A.S. Safatov, G. Buryak, J. Fröhlich-Nowoisky, W. Elbert, M.O. Andreae, U. Pöschl, R. Jaenicke, Primary biological aerosol particles in the atmosphere: A review, Tellus, Ser. B Chem. Phys. Meteorol. 64 (2012) 155981-1559859. https://doi.org/10.3402/tellusb.v64i0.15598.

[75] Y. Lei, Q. Zhang, K.B. He, D.G. Streets, Primary anthropogenic aerosol emission trends for China, 1990-2005, Atmos. Chem. Phys. 11 (2011) 931–954. https://doi.org/10.5194/acp-11-931-2011.

[76] B.J. Finlayson-Pitts, Reactions at surfaces in the atmosphere: integration of experiments and theory as necessary (but not necessarily sufficient) for predicting the physical chemistry of aerosols, Phys. Chem. Chem. Phys. 11 (2009) 7760–7779. https://doi.org/10. 1039/b916865f.

[77] F. Raes, R. Van Dingenen, V. Elisabetta, J. Wilson, J.P. Putaud, J.H. Seinfeld, P. Adams, Formation and cycling of aerosols in the global troposphere, Atmos. Environ. 34 (2000) 4215–4240. https://doi.org/10.1016/S1474-8177(02)80021-3.

[78] S. Fuzzi, M.O. Andreae, B.J. Huebert, M. Kulmala, T.C. Bond, M. Boy, S.J. Doherty, A. Guenther, M. Kanakidou, K. Kawamura, V.M. Kerminen, U. Lohmann, L.M. Russell, U. Pöschl, Critical assessment of the current state of scientific knowledge, terminology, and research needs concerning the role of organic aerosols in the atmosphere, climate, and global change, Atmos. Chem. Phys. 6 (2006) 2017–2038. https://doi.org/10.5194/acp-6-2017-2006.

[79] J.M. Andino, A. Vivier-Bunge, Chapter 14 Tropospheric Chemistry of Aromatic Compounds Emitted from Anthropogenic Sources. In : Advances in Quantum Chemistry, 1st edition, volume 55, Academic Press, ISBN 9780123743350, 2008. https://doi.org/10.1016/S0065-3276(07) 00214-6.

[80] A.G. Carlton, C. Wiedinmyer, J.H. Kroll, A review of Secondary organic aerosol (SOA) formation from isoprene, Atmos. Chem. Phys. 9 (2009) 4987–5005. https://doi.org/ 10.5194/acp-9-4987-2009.

[81] A. Laskin, D.J. Gaspar, W. Wang, S.W. Hunt, J.P. Cowin, S.D. Colson, B.J. Finlayson-pitts, Reactions at Interface As a Source of Sulfate Formartion in Sea-Salt Particles, Science 301 (2003) 340–345. https://doi.org/10.1126/science.1085374.

[82] P. Laj, J. Klausen, M. Bilde, C. Plaß-Duelmer, et al., Measuring atmospheric composition change, Atmos. Environ. 43 (2009) 5351–5414. https://doi.org/10.1016/j.atmosen v.2009.08.020.

[83] P.S. Monks, C. Granier, S. Fuzzi, et al., Atmospheric composition change - global and regional air quality, Atmos. Environ. 43 (2009) 5268–5350. https://doi.org/10.1016 /j.atmosenv.2009.08.021.

[84] K. Mohiuddin, V. Strezov, P.F. Nelson, E. Stelcer, T. Evans, Mass and elemental distributions of atmospheric particles nearby blast furnace and electric arc furnace operated industrial areas in Australia, Sci. Total Environ. 487 (2014) 323–334. https:// doi.org/10.1016/j.scitotenv.2014.04.025.

[85] M. Viana, T.A.J. Kuhlbusch, X. Querol, A. Alastuey, R.M. Harrison, P.K. Hopke, W. Winiwarter, M. Vallius, S. Szidat, A.S.H. Prévôt, C. Hueglin, H. Bloemen, P. Wåhlin, R. Vecchi, A.I. Miranda, A. Kasper-Giebl, W. Maenhaut, R. Hitzenberger, Source apportionment of particulate matter in Europe: A review of methods and results, J. Aerosol Sci. 39 (2008) 827–849. https://doi.org/10.1016/j.jaerosci.2008.05.007.

[86] J.H. Seinfeld, S.N. Pandis, Atmospheric Chemistry and Physics: From Air Pollution to Climate Change, 3rd Edition, Stockholm, Sweden, ISBN: 978-1-118-94740-1, 1998.

[87] G.M. Hidy, V. Mohnen, C.L. Blanchard, Tropospheric aerosols: Size-differentiated chemistry and large-scale spatial distributions, J. Air Waste Manag. Assoc. 63 (2013) 377–404. https://doi.org/10.1080/10962247.2012.760499.

[88] R. Krejci, J. Ström, M. de Reus, J. Williams, H. Fischer, M.O. Andreae, H.-C. Hansson, Spatial and temporal distribution of atmospheric aerosols in the lowermost troposphere over the Amazonian tropical rainforest, Atmos. Chem. Phys. Discuss. 5 (2005) 1527–1543. https://doi.org/10.5194/acpd-4-3565-2004.

[89] J.H. Murillo, S.R. Roman, J.F.R. Marín, B. Cardenas, Source Apportionment of PM2.5 in the Metropolitan Area of Costa Rica Using Receptor Models, Atmos. Clim. Sci. 03 (2013) 562–575. https://doi.org/10.4236/acs.2013.34059.

[90] J.P. Putaud, R. Van Dingenen, A. Alastuey, et al., A European aerosol phenomenology - 3: Physical and chemical characteristics of particulate matter from 60 rural, urban, and kerbside sites across Europe, Atmos. Environ. 44 (2010) 1308–1320. https://doi.org/10.1016/j.atmosenv.2009.12.011.

[91] P. Laj, K. Sellegri, Les aérosols atmosphéeriques: Impacts locaux, effete globaux, Revue Française des Laboratoires, numero 349, 2003, 23–34. https://doi.org/S0338-9898(03)804663.

[92] M.J. Ezell, S.N. Johnson, Y. Yu, V. Perraud, E.A. Bruns, M.L. Alexander, A. Zelenyuk, D. Dabdub, B.J. Finlayson-Pitts, A new aerosol flow system for photochemical and thermal studies of tropospheric aerosols, Aerosol Sci. Technol. 44 (2010) 329–338. https://doi.org/10.1080/02786821003639700.

[93] H. Tervahattu, J. Juhanoja, V. Vaida, A.F. Tuck, J. V. Niemi, K. Kupiainen, M. Kulmala, H. Vehkamäki, Fatty acids on continental sulfate aerosol particles, J. Geophys. Res. D Atmos. 110 (2005) D062071-D062079. https://doi.org/10.1029/2004JD005400.

[94] W.R. Barger, W.D. Garrett, Surface-active organic material in air over the Mediterranean and over the eastern equatorial Pacific, J. Geophys. Res. 81 (1976) 3151–3157. https://doi.org/10.1029/jc081i018p03151.

[95] J.L. Jimenez, M.R. Canagaratna, N.M. Donahue, A.S.H. Prevot, Q. Zhang, at al., Evolution of Organic Aerosols in the Atmosphere, Science. 326 (2009) 1525–1530. https://doi.org/10.1126/science.1180353.

[96] F. Karagulian, C.A. Belis, C. Francisco, C. Dora, A.M. Prüss-ustün, S. Bonjour, H. Adair-rohani, M. Amann, Contributions to cities ' ambient particulate matter (PM): A systematic review of local source contributions at global level, Atmos. Environ. 120 (2015) 475–483. https://doi.org/10.1016/j.atmosenv.2015.08.087.

[97] J.M. Schiffer, L.E. Mael, K.A. Prather, R.E. Amaro, and V.H. Grassian, Sea Spray Aerosol: Where Marine Biology Meets Atmospheric Chemistry, ACS Cent. Sci. 4 (2018) 1617–1623. https://doi.org/10.1021/acscentsci.8b00674.

[98] B.J. Finlayson-Pitts, J. James N. Pitts, Chemistry of the Upper and Lower Atmosphere: Theory, Experiments, and Applications, Academic Press, California, ISBN: 978-0-12-257060-5, 2000. https://doi.org/10.1016/B978-0-12-257060-5.X5000-X.

[99] J.W. Chi, W.J. Li, D.Z. Zhang, J.C. Zhang, Y.T. Lin, X.J. Shen, J.Y. Sun, Sea salt aerosols as a reactive surface for inorganic and organic acidic gases in the arctic troposphere, Atmos. Chem. Phys. 15 (2015) 16715–16745. https://doi.org/10.5194/acpd-15-16715-2015.

[100] A.P. Ault, R.C. Moffet, J. Baltrusaitis, D.B. Collins, M.J. Ruppel, L.A. Cuadra-Rodriguez, D. Zhao, T.L. Guasco, C.J. Ebben, F.M. Geiger, T.H. Bertram, K.A. Prather, V.H. Grassian, Size-dependent changes in sea spray aerosol composition and properties with different seawater conditions, Environ. Sci. Technol. 47 (2013) 5603–5612. https://doi.org/10.1021/es400416g.

[101] T.H. Bertram, R.E. Cochran, E.A. Stone, V.H. Grassian, Sea spray aerosol chemical composition: elemental and molecular mimics for laboratory studies of heterogeneous and multiphase reactions, Chem. Soc. Rev. 47 (2018) 2374–2400. https://doi.org /10.1039/c7cs00008a.

[102] L.M. Russell, L.N. Hawkins, A.A. Frossard, P.K. Quinn, T.S. Bates, Carbohydrate-like composition of submicron atmospheric particles and their production from ocean bubble bursting, Proc. Natl. Acad. Sci. U. S. A. 107 (2010) 6652–6657. https://doi.org/10.1073 /pnas.0908905107.

[103] C.D. O'Dowd, M.C. Facchini, F. Cavalli, D. Ceburnis, M. Mircea, S. Decesari, S. Fuzzi, J.Y. Young, J.P. Putaud, Biogenically driven organic contribution to marine aerosol, Nature. 431 (2004) 676–680. https://doi.org/10.1038/nature02959.

[104] A.P. Ault, D. Zhao, C.J. Ebben, M.J. Tauber, F.M. Geiger, K.A. Prather, V.H. Grassian, Raman microspectroscopy and vibrational sum frequency generation spectroscopy as probes of the bulk and surface compositions of size-resolved sea spray aerosol particles, Phys. Chem. Chem. Phys. 15 (2013) 6206–6214. https://doi.org/10.1039/c3cp43899f.

[105] H.M. Hung, P. Ariya, Oxidation of oleic acid and oleic acid/sodium chloride (aq) mixture droplets with ozone: Changes of hygroscopicity and role of secondary reactions, J. Phys. Chem. A. 111 (2007) 620–632. https://doi.org/10.1021/jp0654563.

[106] K. Stemmler, A. Vlasenko, C. Guimbaud, M. Ammann, The effect of fatty acid surfactants on the uptake of nitric acid to deliquesced NaCl aerosol, Atmos. Chem. Phys. 8 (2008) 5127–5141. https://doi.org/10.5194/acp-8-5127-2008.

[107] J. Lovrić, D. Duflot, M. Monnerville, C. Toubin, S. Briquez, Water-Induced Organization of Palmitic Acid at the Surface of a Model Sea Salt Particle: A Molecular Dynamics Study, J. Phys. Chem. A. 120 (2016) 10141–10149. https://doi.org/10.1021/acs.jpca.6b07792.

[108] C. Liang, F. Duan, K. He, Y. Ma, Review on recent progress in observations, source identifications and and countermeasures of PM2.5, Environ. Int. 86 (2016) 150–170. https://doi.org/10.1016/j.envint. 2015.10.016.

[109] Z. Kitanovski, I. Grgić, M. Veber, Characterization of carboxylic acids in atmospheric aerosols using hydrophilic interaction liquid chromatography tandem mass spectrometry, J. Chromatogr. A. 1218 (2011) 4417–4425. https://doi.org/10.1016/j.chroma.2011.05.020.

[110] M.N. Chan, M.Y. Choi, N.L. Ng, C.K. Chan, Hygroscopicity of water-soluble organic compounds in atmospheric aerosols: Amino acids and biomass burning derived organic species, Environ. Sci. Technol. 39 (2005) 1555–1562. https://doi.org/10.1021/es049584l.

[111] J. Feichter, T. Leisner, Climate engineering : A critical review of approaches to modify the global energy balance, Eur. Phys. J. Spec. Top. 176 (2009) 81–92. https://doi.org/ 10.1140 /epjst/e2009-01149-8.

[112] G. Pellerin, D. Maro, P. Damay, E. Gehin, O. Connan, P. Laguionie, D. Hébert, Aerosol particle dry deposition velocity above natural surfaces : Quanti fi cation according to the particles diameter, J. Aerosol Sci. 114 (2017) 107–117. https://doi.org/10.1016/j.jaer osci.2017.09.004.

[113] C. Tomasi, A. Lupi, Atmospheric Aerosols: Life Cycles and Effects on Air Quality and Climate, Weinheim, Germany, ISBN: 9783527336449, 2016. https://doi.org/10.1002 /9783 527336449.

[114] P. M. Doran, Bioprocess Engineering Principles, Second Edition, Elsevier Academic Press, Oxford, UK, ISBN: 978-0-12-220851-5, 926, 2013. https://doi.org/10.1016/C2009-0-22348-8.

[115] A.S. Dennis, Chapter III: The formation of clouds and precipitation, in: Weather Modif. by Cloud Seeding, Internatio, Academic press, ISBN 0-12-210650-4, 1980: pp. 28–63.

[116] Y. Deng, S. Kagami, S. Ogawa, K. Kawana, T. Nakayama, R. Kubodera, K. Adachi, T. Hussein, Y. Miyazaki, And, M. Mochida, Hygroscopicity of Organic Aerosols and Their Contributions to CCN Concentrations Over a Midlatitude Forest in Japan, Geophys. Res. Atmos. 123 (2018) 9703–9723. https://doi.org/10.1029/2017JD027292.

[117] J. Hong, S.A.K. Häkkinen, M. Paramonov, M. Äijälä, J. Hakala, T. Nieminen, J. Mikkilä, N.L. Prisle, M. Kulmala, I. Riipinen, M. Bilde, V.M. Kerminen, T. Petäjä, Hygroscopicity , CCN and volatility properties of submicron atmospheric aerosol in a boreal forest environment during the summer of 2010, Atmos. Chem. Phys. 14 (2014) 4733–4748. https://doi.org/10.5194/acp-14-4733-2014.

[118] Z.J. Wu, L. Poulain, W. Birmili, J. Größ, N. Niedermeier, Z.B. Wang, H. Herrmann, A. Wiedensohler, Some insights into the condensing vapors driving new particle growth to CCN sizes on the basis of hygroscopicity measurements, Atmos. Chem. Phys. 15 (2015) 13071–13083. https://doi.org/10.5194/acp-15-13071-2015.

[119] Z. Zhao, K. Kong, S. Wang, Y. Zhou, D. Cheng, W. Wang, X.C. Zeng, H. Li, Understanding Hygroscopic Nucleation of Sulfate Aerosols: Combination of Molecular Dynamics Simulation with Classical Nucleation Theory, Phys. Chem. Lett. 10 (2019) 1126–1132. https://doi.org/10.1021/acs.jpclett.9b00152.

[120] A. Roose, C. Toubin, V.R. Sébastien Dusanter, D. Duflot, Classical Molecular Dynamics Study of Small-Chain Carboxylic Acid Aerosol Particles̕, ACS Earth Space Chem. 3 (2019) 380–389. https://doi.org/10.1021/acsearthspacechem.8b00172.

[121] M. Tang, D. Cziczo, V. Grassian, and Interactions of Water with Mineral Dust Aerosol : Water Adsorption, Cloud condensation, and Ice Nucleation, Chem. Rev. 116 (2016) 4205-4259. https://doi.org/10.1021/acs.chemrev.5b00529.

[122] E. Swietlicki, H. Hansson, K. Hämeri, B. Svenningsson, et al., Hygroscopic properties of submicrometer atmospheric aerosol particles measured with H- TDMA instruments in various environments - a review, Tellus B Chem. Phys. Meteorol. 60B (2008) 432–469. https://doi.org/10.1111/j.1600-0889.2008.00350.x.

[123] M. Stock, Y.F. Cheng, W. Birmili, A. Massling, B. Wehner, T. M¨uller, S. Leinert, N. Kalivitis, N. Mihalopoulos, A. Wiedensohler, Hygroscopic properties of atmospheric aerosol particles over the Eastern Mediterranean : implications for regional direct radiative forcing under clean and polluted conditions, Atmos. Chem. Phys. 11 (2011) 4251–4271. https://doi.org/10.5194/acp-11-4251-2011.

[124] H. Köhker, The nucleus in and the growth of hygroscopic droplets, Trans. Faraday Soc. 32 (1936) 1152–1161. https://doi.org/10.1039/TF9363201152.

[125] A. Alshawa, O. Dopfer, S.A.N. Christopher W. Harmon, J.S. Underwood, Hygroscopic growth and deliquescence of NaCl nanoparticles mixed with surfactant SDS, J. Phys. Chem. B. 114 (2010) 2435–2449. https://doi.org/10.1021/jp909661q.

[126] H.R. Pruppacher, New look at homogeneous ice nucleation in supercooled water drops, Atmos. Sci. 11 (1994) 1924–1933. https://doi.org/10.1175/1520-0469(1995)052.

[127] T. Koop, Ebook: Water: Fundamentals as the Basis for Understanding the Environment and Promoting Technology, Volume 187, IOS Press, Amsterdam, ISBN: 978-1-61499-507-4, 2015. https://doi.org/10.3254/978-1-61499-507-4-45.

[128] C. Hoose, O. Möhler, Heterogeneous ice nucleation on atmospheric aerosols : a review of results from laboratory experiments, Atmos. Chem. Phys. 9817 (2012) 9817–9854. https://doi.org/10.5194/acp-12-9817-2012.

[129] C.E. Kolb, R.A. Cox, J.P.D. Abbatt, M. Ammann, E.J. Davis, D.J. Donaldson, B.C. Garrett, C. George, P.T. Griffiths, D.R. Hanson, M. Kulmala, G. McFiggans, U. Pöschl, I. Riipinen, M.J. Rossi, Y. Rudich, P.E. Wagner, P.M. Winkler, D.R. Worsnop, C.D. O'Dowd, An overview of current issues in the uptake of atmospheric trace gases by aerosols and clouds, Atmos. Chem. Phys. 10 (2010) 10561–10605. https://doi.org/10.5194/acp-10-10561-2010.

[130] R.A. Cox, Evaluation of laboratory kinetics and photochemical data for atmospheric chemistry applications, Chem. Soc. Rev. 41 (2012) 6231–6246. https://doi.org/10.1039/c2cs35092k.

[131] T. Berkemeier, A.J. Huisman, M. Ammann, M. Shiraiwa, T. Koop, U. Pöschl, Kinetic regimes and limiting cases of gas uptake and heterogeneous reactions in atmospheric aerosols and clouds: A general classification scheme, Atmos. Chem. Phys. 13 (2013) 6663–6686. https://doi.org/10.5194/acp-13-6663-2013.

[132] U. Pöschl, Y. Rudich, M. Ammann, Kinetic model framework for aerosol and cloud surface chemistry and gas-particle interactions: Part 1: general equations, parameters, and terminology, Atmos. Chem. Phys. Discuss. 7 (2007) 5989–6023. https://doi.org/10.5194/acpd-5-2111-2005.

[133] J.N. Crowley, M. Ammann, R.A. Cox, R.G. Hynes, M.E. Jenkin, A. Mellouki, M.J. Rossi, J. Troe, T.J. Wallington, Evaluated kinetic and photochemical data for atmospheric chemistry: Volume v -heterogeneous reactions on solid substrates, Atmos. Chem. Phys. 10 (2010) 9059–9223. https://doi.org/10.5194/acp-10-9059-2010.

[134] M. Ammann, U. Pöschl, Y. Rudich, Effects of reversible adsorption and Langmuir-Hinshelwood surface reactions on gas uptake by atmospheric particles, Phys. Chem. Chem. Phys. 5 (2003) 351–356. https://doi.org/10.1039/b208708a.

[135] M. Ammann, R.A. Cox, J.N. Crowley, M.E. Jenkin, A. Mellouki, M.J. Rossi, J. Troe, T.J. Wallington, Evaluated kinetic and photochemical data for atmospheric chemistry: Volume VI - Heterogeneous reactions with liquid substrates, Atmos. Chem. Phys. 13 (2013) 8045–8228. https://doi.org/10.5194/acp-13-8045-2013.

[136] S. Scolaro, Ph.D. thesis on effects of humidity and fatty acid surfactants on the uptake of NO_2 to NaCl : Combined study of kinetics and surface analysis, Lille university, 2009.

[137] J.W. Adams, D. Rodriguez, R.A. Cox, The uptake of SO_2 on Saharan dust: A flow tube study, Atmos. Chem. Phys. 5 (2005) 2679–2689. https://doi.org/10.5194/acp-5-2679-2005.

[138] N.S. Holmes, J.W. Adams, J.N. Crowley, Uptake and reaction of HOI and $IONO_2$ on frozen and dry NaCl/NaBr surfaces and H_2SO_4, Phys. Chem. Chem. Phys. 3 (2001) 1679–1687. https://doi.org/10.1039/b100247n.

[139] P. Li, H.A. Al-Abadleh, V.H. Grassian, Measuring heterogeneous uptake coefficients of gases on solid particle surfaces with a Knudsen cell reactor: Complications due to surface saturation and gas diffusion into underlying layers, J. Phys. Chem. A. 106 (2002) 1210–1219. https://doi.org/10.1021/jp011828q.

[140] D.J. Stewart, R.A. Cox, Reactive uptake coefficients for heterogeneous reaction of N_2O_5 with submicron aerosols of NaCl and natural sea salt, Atmos. Chem. Phys. Discuss. 4 (2004) 569–590. https://doi.org/10.5194/acpd-4-569-2004.

[141] H. Li, T. Zhu, J. Ding, Q. Chen, B. Xu, Heterogeneous reaction of NO_2 on the surface of NaCl particles, Sci. China, Ser. B Chem. 49 (2006) 371–378. https://doi.org/10.1007/s11426-006-0371-z.

[142] L.D. Kong, X. Zhao, Z.Y. Sun, Y.W. Yang, H.B. Fu, S.C. Zhang, T.T. Cheng, X. Yang, L. Wang, J.M. Chen, The effects of nitrate on the heterogeneous uptake of sulfur dioxide on hematite, Atmos. Chem. Phys. 14 (2014) 9451–9467. https://doi.org/10.5194/acp-14-9451-2014.

[143] P. Davidovits, C.E. Kolb, L.R. Williams, J.T. Jayne, D.R. Worsnop, Mass Accommodation and Chemical Reactions at Gas − Liquid Interfaces, Chem. Rev. 106 (2006) 1323–1354. https://doi.org/10.1021/cr040366k.

[144] C.E. Kolb, D.R. Worsnop, M.S. Zahniser, P. Davidovits, L.F. Keyser, M.T. Leu, M.J. Molina, D.R. Hanson, A.R. Ravishankara, L.R. Williams, M.A. Tolbert, Laboratory studies of atmospheric heterogeneous chemistry, in: J.R. Barker (Ed.), Prog. Probl. Atmos. Chem., 1995: pp. 771–875. https://doi.org/10.1142/9789812831712_0018.

[145] E.J. Davis, Interpretation of Uptake Coefficient Data Obtained with Flow Tubes, Phys. Chem. A. 112 (2008) 1922–1932. https://doi.org/10.1021/jp074939j.

[146] P. Diévart, B. Lyassine Allou, F. Louis, S. Le Calve, Tropospheric multiphase chemistry of 2, 5- and 2, 6-dimethylphenols : Determination of the mass accommodation, Phys. Chem. Chem. Phys. 8 (2006) 1714–1723. https://doi.org/10.1039/b516193b.

[147] C.L. Badger, P.T. Griffiths, I. George, J.P.D. Abbatt, R.A. Cox, Reactive Uptake of N 2 O 5 by Aerosol Particles Containing Mixtures of Humic Acid and Ammonium Sulfate, Phys. Chem. A. 110 (2006) 6986–6994. https://doi.org/10.1021/jp0562678.

[148] C. Wagner, G. Schuster, J.N. Crowley, An aerosol flow tube study of the interaction of N_2O_5 with calcite , Arizona dust and quartz, Atmos. Environ. 43 (2009) 5001–5008. https://doi.org/10.1016/j.atmosenv.2009.06.050.

[149] J.D. Hearn, A.J. Lovett, G.D. Smith, Ozonolysis of oleic acid particles: evidence for a surface reaction and secondary reactions involving Criegee intermediates, Physic. 7 (2005) 501–511. https://doi.org/10.1039/B414472D.

[150] I.J. George, P.S.J. Matthews, L.K. Whalley, B. Brooks, A. Goddard, M.T. Baeza-Romero, D. E. Heard, Measurements of uptake coefficients for heterogeneous loss of HO_2 onto submicron inorganic salt aerosols, Phys. Chem. Chem. Phys. 15 (2013) 12829–12845. https://doi.org/10.1039/c3cp51831k.

[151] J.T. Jayne, S.X. Duan, P. Davidovits, B. College, D.R. Worsnop, M.S. Zahniser, C.E. Kolb, Uptake of Gas-Phase Aldehydes by Water Surfaces, Phys. Chem. 96 (1992) 5452–5460. https://doi.org/10.1021/j100192a049.

[152] R.N. Berglund, B.Y.H. Liu, Generation of Monodisperse Aerosol Standards, Environ. Sci. Technol. 7 (1973) 147-153. https://doi.org/10.1021/es60074a001.

[153] F. Caloz, F.F. Fenter, K.D. Tabor, M.J. Rossi, M. Carlo, Paper I : Design and construction of a Knudsen-cell reactor for the study of heterogeneous reactions over the temperature range 130-750 K : Performances and limitations, Rev. Sci. Instrum. 68 (1997) 3172–3179. https://doi.org/10.1063/1.1148263

[154] P. Beichert, B.J. Finlayson-pitts, Knudsen Cell Studies of the Uptake of Gaseous HNO_3 and Other Oxides of Nitrogen on Solid NaCl: The Role of Surface-Adsorbed Water, J. Phys. Chem. 100 (1996) 15218–15228. https://doi.org/10.1021/jp960925u.

[155] G.M. Underwood, P. Li, V.H. Grassian, A Knudsen Cell Study of the Heterogeneous Reactivity of Nitric Acid on Oxide and Mineral Dust Particles, Phys. Chem. 1005 (2001) 6609–6620. https://doi.org/10.1021/jp002223h.

[156] G.M. Underwood, T.M. Miller, V.H. Grassian, Transmission FT-IR and Knudsen Cell Study of the Heterogeneous Reactivity of Gaseous Nitrogen Dioxide on Mineral Oxide Particles, Phys. Chem. 103 (1999) 6184–6190. https://doi.org/10.1021/jp991586i.

[157] M. Ullerstam, M.S. Johnson, R. Vogt, E. Ljungstr, DRIFTS and Knudsen cell study of the heterogeneous reactivity of SO_2 and NO_2 on mineral dust, Atmos. Chem. Phys. 3 (2003) 2043–2051. https://doi.org/10.5194/acp-3-2043-2003.

[158] T. Armaroli, T. Bécue, S. Gautier, Diffuse Reflection Infrared Spectroscopy (Drifts): Application to the in Situ Analysis of Catalysts, Oil Gas Sci. Technol. 59 (2004) 215–237. https://doi.org/10.2516/ogst:2004016.

[159] Y. Peng, W. Si, X. Li, J. Luo, J. Li, J. Crittenden, J. Hao, Applied Catalysis B : Environmental Comparison of MoO_3 and WO_3 on arsenic poisoning V_2O_5/TiO_2 catalyst : DRIFTS and DFT study, Appl. Catal. B Environ. 181 (2016) 692–698. https://doi.org/10.1016/j.apcatb. 2015.08.030.

[160] Z. Ma, X. Wu, H. Härelind, D. Weng, B. Wang, Z. Si, NH_3-SCR reaction mechanisms of $NbO_x/Ce_{0.75}Zr_{0.25}O_2$ catalyst: DRIFTS and kinetics studies, Mol. Catal. A, Chem. 423 (2016) 172–180. https://doi.org/10.1016/j.molcata.2016.06.023.

[161] G. Accardo, R. Cioffi, F. Colangelo, R. D'Angelo, L. De Stefano, F. Paglietti, Diffuse Reflectance Infrared Fourier Transform Spectroscopy for the Determination of Asbestos Species in Bulk Building Materials, Materials (Basel). 7 (2014) 457–470. https://doi.org/10.3390/ma7010457.

[162] R. Vogt, B.J. Finlayson-Pitts, A Diffuse Reflectance Infrared Fourier Transform Spectroscopic (DRIFTS) study of the surface reaction of NaCl with gaseous NO_2 and HNO_3, J. Phys. Chem. 98 (1994) 3747–3755. https://doi.org/10.1021/j100065a033.

[163] L. Li, Z.M. Chen, Y.H. Zhang, T. Zhu, S. Li, H.J. Li, L.H. Zhu, B.Y. Xu, Heterogeneous oxidation of sulfur dioxide by ozone on the surface of sodium chloride and its mixtures with other components, J. Geophys. Res. Atmos. 112 (2007) 1–13. https://doi.org/10.1029/2006JD008207.

[164] S. Seisel, C. Börensen, R. Vogt, R. Zellner, Kinetics and mechanism of the uptake of N_2O_5 on mineral dust at 298 K, Atmos. Chem. Phys. 5 (2005) 3423–3432. https://doi.org/10.5194/acp-5-3423-2005.

[165] H.J. Li, T. Zhu, D.F. Zhao, Z.F. Zhang, Z.M. Chen, Kinetics and mechanisms of heterogeneous reaction of NO_2 on $CaCO_3$ surfaces under dry and wet conditions, Atmos. Chem. Phys. 10 (2010) 463–474. https://doi.org/10.5194/acp-10-463-2010.

[166] A. Paredes-Nunez, I. Jbir, D. Bianchi, F.C. Meunier, Spectrum baseline artefacts and correction of gas-phase species signal during diffuse reflectance FT-IR analyses of catalysts at variable temperatures, Appl. Catal. A Gen. 495 (2015) 17–22. https://doi.org/10.1016/j.apcata.2015.01.042.

[167] Outdoor Atmospheric Simulation Chamber SAPHIR. https://helios-cnrs.org/. [citation in April may 2020].

[168] A.P. Prince, J.L. Wade, V.H. Grassian, P.D. Kleiber, M.A. Young, Heterogeneous reactions of soot aerosols with nitrogen dioxide and nitric acid: Atmospheric chamber and Knudsen cell studies, Atmos. Environ. 36 (2002) 5729–5740. https://doi.org/10.1016/S1352-2310(02)00626-X.

[169] M. Folkers, T.F. Mentel, A. Wahner, Influence of an organic coating on the reactivity of aqueous aerosols probed by the heterogeneous hydrolysis of N_2O_5, Geophys. Res. Lett. 30 (2003) 1644. https://doi.org/10.1029/2003GL017168.

[170] P.K. Mogili, P.D. Kleiber, M.A. Young, V.H. Grassian, Heterogeneous Uptake of Ozone on Reactive Components of Mineral Dust Aerosol : An Environmental Aerosol Reaction Chamber Study, Phys. Chem. A. 3 (2006) 13799–13807. https://doi.org/10.1021/jp063620g.

[171] J.R. Butler, L. Mitchem, K.L. Hanford, L. Treuel, J.P. Reid, In situ comparative measurements of the properties of aerosol droplets of different chemical composition, Faraday Discuss. 137 (2008) 351–366. https://doi.org/10.1039/b706770b.

[172] Y.A. Tobon, S. Seng, L.A. Picone, Y.B. Bava, L.C. Juncal, M. Moreau, R.M. Romano, J. Barbillat, S. Sobanska, Photochemistry of single particles using acoustic levitation coupled with Raman microspectrometry, J. Raman Spectrosc. 48 (2017) 1135–1137. https://doi.org /10.1002/jrs.5181.

[173] A.A. Zardini, U.K. Krieger, C. Marcolli, White light Mie resonance spectroscopy used to measure very low vapor pressures of substances in aqueous solution aerosol particles, Opt. Express. 14 (2006) 6951-6962. https://doi.org/10.1364/oe.14.006951.

[174] S. Bastelberger, U.K. Krieger, B. Luo, T. Peter, Diffusivity measurements of volatile organics in levitated viscous aerosol particles, Atmos. Chem. Phys. 17 (2017) 8453–8471. https://doi.org/10.5194/acp-17-8453-2017.

[175] S. Sobanska, H. Hwang, M. Choël, H.J. Jung, H.J. Eom, H. Kim, J. Barbillat, C.U. Ro, Investigation of the chemical mixing state of individual asian dust particles by the combined use of electron probe X-ray microanalysis and raman microspectrometry, Anal. Chem. 84 (2012) 3145–3154. https://doi.org/10.1021/ac2029584.

[176] B.J. Krueger, V.H. Grassian, M.J. Iedema, J. P. Cowin, A. Laskin, Probing Heterogeneous Chemistry of Individual Atmospheric Particles Using Scanning Electron Microscopy and Energy-Dispersive X-ray Analysis, Anal. Chem. 75 (2003) 5170–5179. https://doi.org/10.1021/ac034455t.

[177] U.K. Krieger, C. Marcolli, J.P. Reid, Chem Soc Rev Exploring the complexity of aerosol particle properties and processes using single particle techniques, Chem. Soc. Rev. 41 (2012) 6631–6662. https://doi.org/10.1039/c2cs35082c.

[178] A.P. Ault, J.L. Axson, Atmospheric Aerosol Chemistry: Spectroscopic and Microscopic Advances, Anal. Chem. 89 (2017) 430–452. https://doi.org/10.1021/acs.analchem.6b04670.

[179] M.J. Tang, J.C.J. Camp, L. Rkiouak, J. Mcgregor, I.M. Watson, R.A. Cox, M. Kalberer, A.D. Ward, F.D. Pope, Heterogeneous Interaction of SiO_2 with N_2O_5 : Aerosol Flow Tube and Single Particle Optical Levitation – Raman Spectroscopy Studies, Phys. Chem. 118 (2014) 8817–8827. https://doi.org/10.1021/jp506753c.

[180] A. Laskin, J.P. Cowin, M.J. Iedema, Analysis of individual environmental particles using modern methods of electron microscopy and X-ray microanalysis, Electron Spectros. Relat. Phenomena, 150 (2006) 260–274. https://doi.org/10.1016/j.elspec.2005.06.008.

[181] E. Whittle, D.A. Dows, G.C. Pimentel, Matrix Isolation Method for the Experimental Study of Unstable Species, Chem. Phys. 22 (1954) 1943–1944. https://doi.org/10.1063 /1.1739957.

[182] Z. Guennoun, C. Aupetit, J. Mascetti, Photochemistry of pyrene with water at low temperature: Study of atmospherical and astrochemical interest, J. Phys. Chem. A. 115 (2011) 1844–1852. https://doi.org/10.1021/jp108713n.

[183] S. Lopes, T. Nikitin, R. Fausto, Matrix isolation study of methyl propiolate in argon and nitrogen matrices, Chem. Phys. Lett. 749 (2020) 137427. https://doi.org/10.1016/j.cp lett.2020.137427.

[184] I. Dunkin, Matrix-isolation Techniques: A Practical Approach, Oxford University Press, New yourk, U.S, ISBN:0198558635, 1998. https://doi.org/10.1021/ja9857099.

[185] N.E.Lopez, Thesis: Etude du transfert de protons dans les systemes moleculaires, Aix-Marseille university, (2017).

[186] Z. Guennoun, C. Aupetit, J. Mascetti, Photochemistry of coronene with water at 10 K: First tentative identification by infrared spectroscopy of oxygen containing coronene products, Phys.Chem.Chem.Phys. 13 (2011) 7340-7347. https://doi.org/1 0.1039/c0cp01756f.

[187] F. Duvernay, A. Trivella, F. Borget, S. Coussan, J. Aycard, T. Chiavassa, Matrix Isolation Fourier Transform Infrared Study of Photodecomposition of Formimidic Acid, Phys. Chem. A. 109 (2005) 11155–11162. https://doi.org/10.1021/jp054903w.

[188] M. Johansson, J. Lovric, X. Kong, E.S. Thomson, M. Hallquist, J.B.C. Pettersson, Experimental and Computational Study of Molecular Water Interactions with Condensed Nopinone Surfaces Under Atmospherically Relevant Conditions, Phys. Chem. A. 124 (2020) 3652–3661. https://doi.org/10.1021/acs.jpca.9b10970.

[189] Y. Sun, Q. Zhang, W. Wang, Adsorption and heterogeneous reactions of $ClONO_2$ and N_2O_5 on/with NaCl aerosol, RSC Adv. 6 (2016) 46336–46344. https://doi.org/10.1039 /c6ra03961h.

[190] S.A. Tacey, L. Xu, T. Szilvási, J.J. Schauer, M. Mavrikakis, Quantum chemical calculations to determine partitioning coefficients for $HgCl_2$ on iron-oxide aerosols, Sci. Total Environ. 636 (2018) 580–587. https://doi.org/10.1016/j.scitotenv.2018.04.289.

[191] C. Zhang, X. Zhang, L. Kang, N. Wang, M. Wang, X. Sun, W. Wang, Adsorption and transformation mechanism of NO2 on NaCl(100) surface: A density functional theory study, Sci. Total Environ. 524–525 (2015) 195–200. https://doi.org/10.1016/j.scitotenv.2015.04.010.

[192] H. Chun, J. Kang, B. Han, First principles computational study on the adsorption mechanism of organic methyl iodide gas on triethylenediamine impregnated activated carbon, Phys. Chem. Chem. Phys. 18 (2016) 32050–32056. https://doi.org/10.1039 /c6cp06483c.

[193] A. Kuwabara, Y. Saito, Y. Koyama, F. Oba, K. Matsunaga, I. Tanaka, First Principles Calculation of CO and H_2 Adsorption on Strained Pt Surface, Mater. Trans. 49 (2008) 2484–2490. https://doi.org/10.2320/matertrans.mb200817.

[194] B.T. Teng, W.X. Huang, F.M. Wu, X.D. Wen, S.Y. Jiang, CH2I2 adsorption and dissociation on Ag(1 1 1) surface using density functional theory study, Chem. Phys. Lett. 461 (2008) 47–52. https://doi.org/10.1016/j.cplett.2008.06.082.

[195] A. Jadon, Ph.D. thesis on the interactions between Sodium Carbonate Aerosols and Iodine Fission-Products, Lille university, 2018.

[196] A. Kundu, G. Piccini, K. Sillar, J. Sauer, Ab Initio Prediction of Adsorption Isotherms for Small Molecules in Metal-Organic Frameworks, J. Am. Chem. Soc. 138 (2016) 14047–14056. https://doi.org/10.1021/jacs.6b08646.

[197] A. Allanic, M.J. Rossi, Heterogeneous reactions of HOI on substrates of atmospheric importance, Geophys. Res. Lett. 104 (1999) 18689–18696. https://doi.org/10.1029 /1999JD900285.

[198] J.C. Mossinger, R.A. Cox, Heterogeneous Reaction of HOI with Sodium Halide Salts, Phys. Chem. Chem. Phys. 105 (2001) 5165–5177. https://doi.org/10.1021/jp0044678.

[199] B. Fluckiger, A. Thielmann, L. Gutzwiller, M.J. Rossi, Real Time Kinetics and Thennochemistry of the Uptake of HCl , HBr and HI on Water Ice in the Temperature Range

190 to 210 K, Berichte der bunsen-gesellschaft-physical Chem. Chem. Phys. 928 (1998) 915–928. https://doi.org/10.1002/BBPC.19981020704.

[200] S.B. Barone, M.A. Zondlo, M.A. Tolbert, Investigation of the Heterogeneous Reactivity of HCl , HBr , and HI on Ice Surfaces, Phys. Chem. A. 103 (1999) 9717–9730. https://doi.org/10.1021/jp990400c.

[201] C.J. Percival, J.C. Mo, R.A. Cox, The uptake of HI and HBr on ice, Phys. Chem. Chem. Phys. 1 (1999) 4565–4570. https://doi.org/10.1039/A904651H.

[202] A. Allanic, R. Oppliger, H. van den Bergh, M.J. Rossi, The Heterogeneous Kinetics of the Reactions ClONO$_2$ + HX/ice (X = Br, I), BrONO$_2$ + HI/ice and the Reactivity of the Interhalogens BrCl, ICl and IBr with HX/ice (X = Cl, Br, I) in the Temperature Range 180 to 205 K, Zeitschrift Fur Phys. Chemie. 214 (2000) 1479–1500. https://doi.org/10.1524/zpch.2000.214.11.1479.

[203] A.L. Swanson, N.J. Blake, J.E. Dibb, M.R. Albert, D.R. Blake, F.S. Rowland, Photochemically induced production of CH3Br , CH3I , C2H5I , ethene , and propene within surface snow at Summit , Greenland, Atmos. Environ. 36 (2002) 2671–2682. https://doi.org/10.1016/S1352-2310(02)00127-9.

[204] A.J. Desimone, B.O. Olanrewaju, G.A. Grieves, T.M. Orlando, Photodissociation of methyl iodide adsorbed on low-temperature amorphous ice surfaces, Chem. Phys. 138 (2013) 084703. https://doi.org/10.1063/1.4790585.

[205] Y. Sohn, J.M. White, Thermal and photochemistry of methyl iodide on ice film grown on Cu(111), Bull. Korean Chem. Soc. 30 (2009) 1470–1474. https://doi.org/10.5012/bkcs.2009.30.7.1470.

[206] E.R. Miller, G.D. Muirhead, E.T. Jensen, Mechanisms for the near-UV photodissociation of CH$_3$I on D$_2$O/Cu(110), J. Chem. Phys. 138 (2013) 084702. https://doi.org/10.1063/1.4770225.

[207] W. Wang, M. Ge, Y. Tian, L. Yao, A flow tube study of methyl iodine uptake on soot surface, Chem. Phys. Lett. 440 (2007) 348–351. https://doi.org/10.1016/j.cplett.2007.04.053.

[208] Y. Shi, W. Weigang, G. MaoFa, The uptake of ethyl iodide on black carbon surface, Chinese Sci. Bull. 53 (2008) 733–738. https://doi.org/10.1007/s11434-007-0488-2.

[209] F. Domine, Should We Not Further Study the Impact of Microbial Activity on Snow and Polar Atmospheric Chemistry ?, Microorganisms. 7 (2019) 2601-2068. https://doi.org/10.3390/microorganisms7080260.

[210] G. Li, Y.K. Shin, H.J. Hwang, State-to-state reaction dynamics of CH3I photodissociation at 304 nm, J. Phys. Chem. A. 109 (2005) 9226–9231. https://doi.org/10.1021/jp054421k.

[211] A.B. Alekseyev, H.P. Liebermann, R.J. Buenker, An ab initio study of the CH$_3$I photodissociation. II. Transition moments and vibrational state control of the I* quantum yields, J. Chem. Phys. 126 (2007) 2341031- 23410311. https://doi.org/10.1063/1.2736696.

[212] I. Powis, J.F. Black, Rotational population and alignment of CD$_3$(v=0) photofragments from the A-band excitation of methyl-D$_3$ iodide, J. Phys. Chem. 93 (1989) 2461–2470. https://doi.org/10.1021/j100343a047.

[213] A. Srivastava, R.M. Osgood, State-resolved dynamics of 248 nm methyl-iodide fragmentation on GaAs(110), J. Chem. Phys. 119 (2003) 10298–10306. https://doi.org/10.1063/1.1619944.

[214] E.T. Jensen, Near-UV photodissociation of oriented CH_3I adsorbed on Cu(110)-I, J. Chem. Phys. 123 (2005) 204709. https://doi.org/10.1063/1.2126593.

[215] D.H. Fairbrother, K.A. Briggman, P.C. Stair, E. Weitz, The role of adsorbate structure in the photodissociation dynamics of adsorbed species: Methyl iodide/MgO(100), J. Chem. Phys. 102 (1995) 7267–7276. https://doi.org/10.1063/1.469038.

[216] S.R. Coon, K.B. Myli, V.H. Grassian, Photoproduct characterization and dynamics in the 248 nm photolysis of CH_3I thin films on Ag(III), J. Phys. Chem. 99 (1995) 16416–16424. https://doi.org/10.1021/j100044a032.

[217] J.G. Calvert, Glossary of atmospheric chemistry terms, Pure Appl. Chem. 62 (1990) 2167–2219. https://doi.org/10.1351/pac199062112167.

This page is left empty

Chapter 3: Cryogenic experiments

Chapter 3 presents the study of the interactions between gaseous CH_3I and gaseous H_2O to give insights on the micro hydration of CH_3I in the gas phase as a first step of interaction with hydrated aerosols. The matrix- isolation Fourier Transform Infrared (FTIR) technique was used for studying at the molecular level the formation of CH_3I clusters and/or CH_3I-H_2O complexes. To help in the spectral interpretation, the molecular structure, infrared spectra and energetics of the CH_3I species in various conformations, we have used Density Functional Theory (DFT) calculation. Additionally, a preliminary cryogenic experiment was conducted to study the interaction of CH_3I with amorphous ice. This study will give, in the future, insights on the interaction of CH_3I with atmospheric ice.

A detailed description of the experimental setup and experimental conditions for interaction of gaseous CH_3I with gaseous H_2O is given. A preliminary experiment for the interaction of gaseous CH_3I with amorphous ice is described. Then, the approach of density functional theory (DFT) used is described. A special attention is paid on the results of DFT calculations and spectral interpretation for describing the interactions between gaseous CH_3I molecules and gaseous H_2O. The spectral interpretation on the preliminary results concerning the interaction of gaseous CH_3I with amorphous ice is reported. Finally, the conclusion and perspectives are given.

3.1. Material and Methods

3.1.1 Description of the cryogenic experimental set ups

Experiments were conducted in two laboratories with two different experimental devices: (1) experimental device at ISM (Institut des Sciences Moléculaires) laboratory / Bordeaux University and (2) experimental device at PIIM (Physics of Ionic and Molecular Interactions) laboratory / Aix-Marseille University.

3.1.1.1 Experimental setup at ISM laboratory

Experiments were conducted in a high vacuum experimental set up consisting in a stainless steel chamber (10^{-5} mbar at room temperature) containing an IR transparent NaCl internal window cooled to 10K by means of a closed cycle He cryostat (Cryophysics Cryodine M22) (Figure 3.1). The use of high vacuum conditions is necessary in order to maintain clean surfaces free of contamination for the duration of the experiments. The sample holder can be rotated, thus getting to the desired position (i.e. deposition and FTIR measurements). The sample temperature was monitored with a Si diode thermometer affixed to the cold window. By

means of a temperature controller and a heating resistor the temperature was carried in the range of 10 K-35 K. The chamber was cubic in shape and has two external transparent windows on two opposite sides, allowing recording FTIR spectra when placed in the sample compartment of the spectrometer as shown in Figure 3.1. The injection and deposition of gaseous samples on the window were carried out by a gas inlet nozzle.
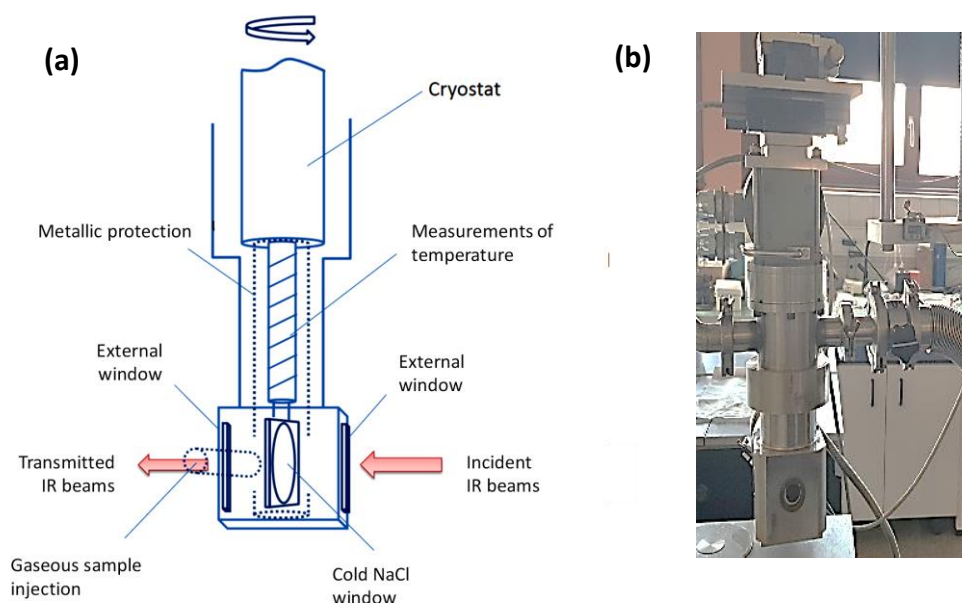
Figure 3. 1 (a) Matrix chamber seen from the front [1] adapted for FTIR spectrometer coupling (b) photo of the matrix chamber at ISM.

To reach as low temperatures as 10 K and at the same time to avoid contaminants in the sample from the outside impurities, it is necessary to attain low pressures not only in the sample chamber but in the mixing ramps too. Thus, high-vacuum pumps were used for the evacuation of the sample preparation line. A gaseous mixture of desired ratio was prepared in a glass bulb (reservoir) under vacuum before being injected into the matrix chamber as shown in Figure 3.2. Rate of sample flow was controlled by means of a micrometer needle valve (flow meter) on the sample outlet line which leads to the matrix chamber.
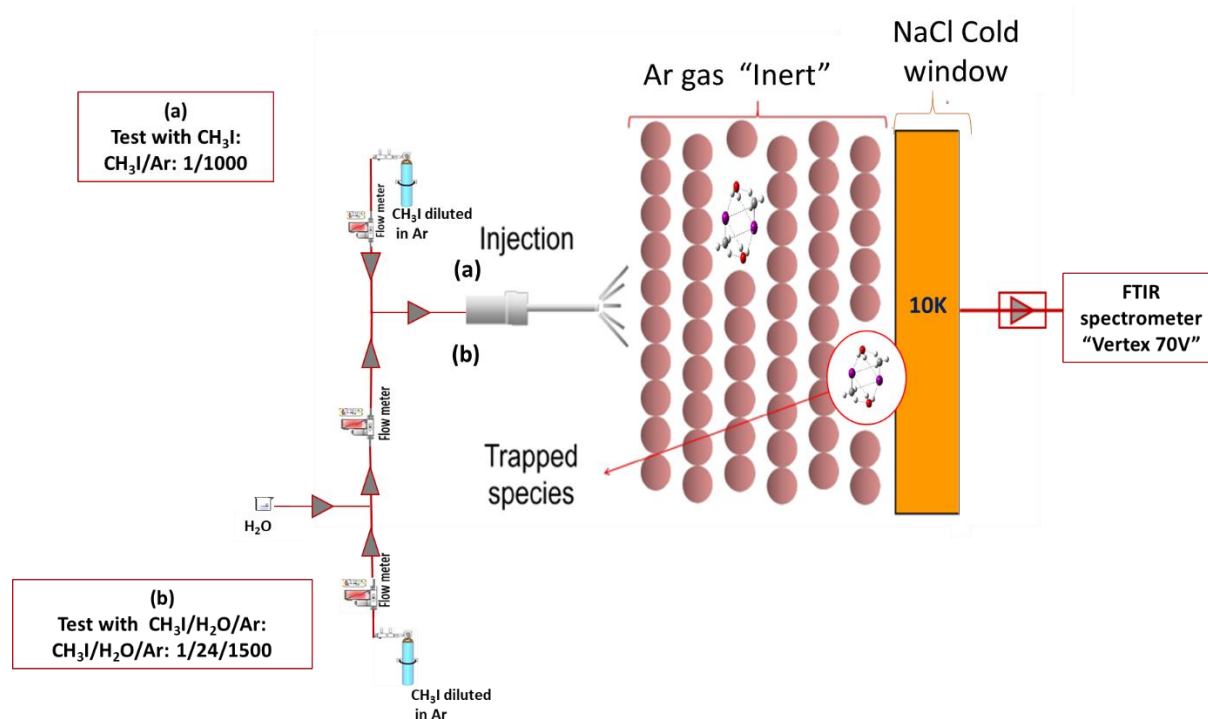
Figure 3. 2 Schematic diagram of the experimental setup of (a) CH$_3$I in Ar matrix from 10 to 35 K, (b) CH$_3$I and H$_2$O in Ar matrix from 10 to 35 K. The scheme was adapted from [2].

The infrared spectra of the gas-isolated samples were recorded in transmission mode using a Bruker Vertex 70V FTIR spectrometer with a DTGS detector in the spectral range of 4000-400 cm^{-1}, with a spectral resolution of 0.5 cm^{-1} and each spectrum averaged over approximately 200 scans. Spectra were recorded at 10K. All spectra are ratioed to a background spectrum which includes the cold window.

3.1.1.2 Experimental setup at PIIM laboratory

Similarly to experiments at ISM laboratory, experiments at PIIM laboratory were conducted in a high vacuum experimental set up consisting in a stainless-steel chamber (10^{-5} mbar at room temperature) containing a gold-plated copper cube cooled to 4K by a closed cycle cryostat (PT-405 Cryomech). Cryostat head can be rotated to get the desired position (deposition and reflection spectroscopy measurements). The copper cube is gold plated to protect it from damage due to deposits of samples that could potentially react with the copper and assure optimal reflectivity. The sample temperature was monitored with two Si diodes, one was fixed in the close vicinity of the sample (at less than 1 cm), while the second was located on the second cooler stage (2.8 K) of the cryogenic head. Temperature was controlled between 4 to 50 K by means of temperature controller and a heating resistance. The chamber was cylinder in shape with one external transparent window, allowing recording reflection infrared spectra when the cryostat is placed in a special bench beside the spectrometer (see Figure 3.3). The

injection of the gas mixture was regulated through an Iota microvalve (electromagnetic) or a manual valve and then deposited on the cold gold-plated copper cube.

The sample mixtures in defined proportions were prepared according to the manometric technique in a stainless-steel ramp pumped under vacuum (10^{-4} to 10^{-5} mbar) before being injected into the cryogenic chamber.
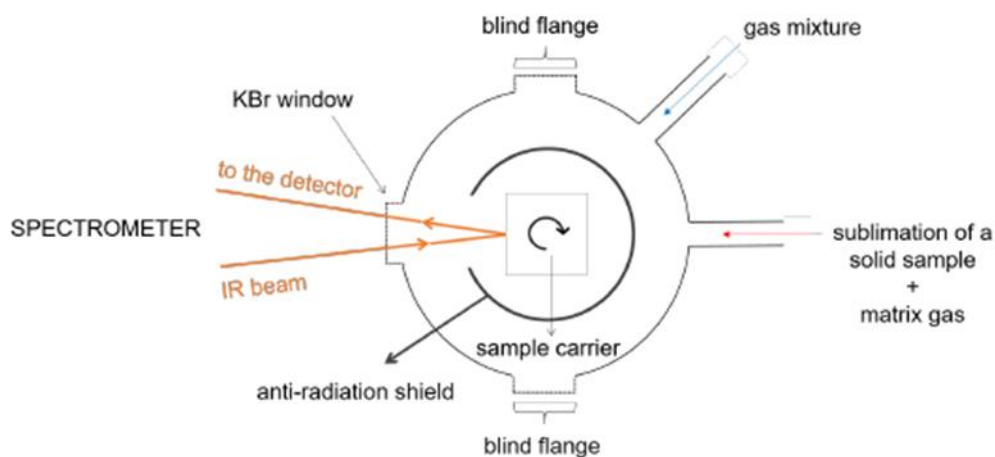
Figure 3. 3 Schematic diagram of the experimental setup adapted from [2] with two possible injection positions: for gas mixtures and for solids. The chromium-platted anti-radiation shield reduces the useful surface of deposition to a disc of 10 mm diameter

The infrared spectra of the deposited samples were recorded in the reflection mode using a Bruker IFS 66/S spectrometer with a MCT detector in the spectral range of 4000-600 cm^{-1} and at a spectral resolution of 0.12 cm^{-1}. Each spectrum was averaged over approximately 128 scans. Spectra were recorded at 4K.

3.1.2 Sample deposition and spectral acquisition methods

Gases were mixed in the desired proportion in a mixture ramp. The mixture was then injected at a desired proportion onto the cold deposition window (i.e. NaCl) or metallic cube (i.e. gold-plated copper cube). During this operation the deposition of the gas samples was essentially perpendicular to the cold surface. After the matrix has been formed, the cryostat was rotated to move the deposition window or cube at the observation position.

Depending on the experimental device and the quality of the sample which is required, the gas mixture can be deposited by two injection methods:

(1) Effusion method so called "slow spray-on method": When the gas mixture is deposited at a desired flow rate via needle valve onto the cold deposition window (i.e. NaCl) or metallic cube (i.e. gold-plated copper).

(2) Pulsed method: When the gas phase mixture is deposited in short and repeated pulses onto the sample holder, i.e. either a NaCl window or a gold-plated copper cube.

3.1.3 Experimental grid

3.1.3.1 Preparation of samples for studying CH₃I-H₂O interactions at ISM laboratory

Two sets of experiments were conducted to scrutinize the CH_3I-H_2O interactions at low temperature using the experimental setup in ISM laboratory (see Figure 3.2):

(a) CH_3I in Ar matrix from 10 to 35 K in order to obtain reference spectra when CH_3I was trapped in Ar matrix

(b) CH_3I and H_2O in Ar matrix from 10 to 35 K.

The two samples were prepared using effusive methodology as described previously. Gaseous samples of CH_3I/Ar (0.1% CH_3I - 99.9% Ar, Airproduct) were used without any further purification at a flow of $1mL.min^{-1}$. The matrix ratio was CH_3I/Ar = 1/1000. For the observation of the formation of $(CH_3I)_m$-$(H_2O)_n$ complexes, the vapor of ultrapure H_2O (conductivity of 18.2 MΩ Millipore system) was introduced from a glass flask and mixed with CH_3I/Ar in a glass reservoir in the proportion CH_3I/ H_2O/Ar = 1/24/1500 and injected into the chamber at a rate of $1 mL.min^{-1}$. Deionized water was previously subjected to multiple freeze-pump-thaw cycles under vacuum to remove dissolved gases. The concentration of H_2O/Ar equal to 1/60 was used to introduce water in a large excess for mimmicking the CH_3I environment in the atmosphere. This CH_3I/H_2O ratio is chosen to ensure both high water concentration in matrix and CH_3I signal detection since beyond this ratio, signals of water aggregates would overlap those of $(CH_3I)_m$-$(H_2O)_n$. Although the injected CH_3I concentration (1000 ppm) is higher than atmospheric CH_3I concentration (0.004-2000 ppt) (see section 2.1), it is weak enough to prevent the formation of CH_3I aggregates after deposition. A reference experiment with H_2O trapped in Ar matrix (7/1000) was also recorded at 4 K for comparison. The gaseous samples were introduced by gas nozzle inlet in effusive mode as described previously and deposited directly in the vacuum chamber on an NaCl window for 2 hours. The deposited samples at 10 K were annealed to 35 K, close to the sublimation temperature of the argon crystal.

3.1.3.2 Preparation of samples for studying CH₃I- amorphous ice (ASW) interactions in PIIM laboratory

Preliminary experiment at PIIM laboratory was conducted in this work to study the CH_3I-amorphous ice interactions at low temperature (4 K-50 K) using cryogenic technique with pulsed deposition method and FTIR analysis in reflection mode.

Gaseous samples of CH_3I/Ar (0.1% CH_3I - 99.9% Ar, Airproduct) were used without any further purification. As reported in section 3.1.3.1 for the experiment with amorphous ice, deionized

water was subjected to multiple freeze–pump–thaw cycles under vacuum to remove dissolved gases.

A mixture of purified H_2O and helium (Air Liquide, ≥99.9999%) gas were prepared in the mixture ramp previously pumped down to 10^{-3} mbar at a ratio of H_2O/He: 1/25. Amorphous ice was formed by injecting 22 mbar in 1s of H_2O/He gas at 50 K to avoid mainly nitrogen trapping. The sample was then cooled to 4K. If adsorbed N_2 is nevertheless observable, one could re-increase the temperature up to 50 K to clean the surface and then re cool it back to 4 K. 3 mbar in 500 ms of CH_3I/Ar: 1/1000 mixture was then successively injected at the ASW surface at various temperatures in order to trap uniquely methyl iodide. The temperatures used were close to or above the argon sublimation temperature (≈ 45 K) to avoid trapping argon on the surface of the ice.

3.1.4 Density Functional Theory (DFT) calculation

The structure and harmonic vibrational spectra of CH_3I monomer, dimers and trimers, and CH_3I-water complexes such as $(CH_3I)_n$-$(H_2O)_m$ (with n = 1,2,3 and m = 1,2,3) were calculated with Gaussian 09 suit of programs [3] using long range corrected functional ωB97XD [4] with the aug-cc-pVTZ basis set for hydrogen, carbon and oxygen atom, while aug-cc-pVTZ-PP basis set [5] was used for iodine atom that incorporates a small-core relativistic pseudo potential [6]. Harmonic vibrational frequencies were calculated at the same level of theory, and remained unscaled. The standard molar entropy (S°10 K) and the heat capacity at constant pressure (1 bar) were calculated with the script thermo.pl published by the National Institute of Standards and Technology [7]. The Gibbs energy (ΔG°) in kJ.mol^{-1} for both CH_3I clusters and complexes was calculated at the ωB97XD/ aug-cc-pVTZ-PP level of theory. The total basis set superposition error (BSSE) correction is known to be negligible in micro hydration energetics [6, 8], therefore this correction was not included in the energetics calculation of this study. It should be highlighted that DFT calculations were only preformed to support the experimental results of CH_3I-H_2O interaction (section 3.1.3.1).

Sections 3.2.1 and 3.2.2 are under review for publication (Title: Infrared matrix- isolation and theoretical studies of interactions between CH$_3$I and water, Authors: S. Sobanska, H. Houjeij, S. Coussan, C. Aupetit, S. Taamalli, F. Louis, L. Cantrel, A.C. Gregoire, J. Mascetti).

3.2. Results and discussion

3.2.1 Formation of $(CH_3I)_x$ clusters

3.2.1.1 DFT calculation results

Structures of CH_3I monomer, dimers and trimers were investigated using experimental spectra supported by calculations presented above. Two isomers of $(CH_3I)_2$, shown in Figure 3.4, are found to be stable and will be hereafter referred as Head-to-Tail (HT) and Head-to-Head (HH) structures. These structures were previously reported using the MP2/ LanL2DZ+fdp level of theory [9]. It should be highlighted that both levels of theory using MP2/ LanL2DZ+fdp [9] and ωB97XD/aug-cc-pVTZ-PP (this work) predict the same $(CH_3I)_2$ stable isomers, i.e. HH and HT, with a difference in the intermolecular distance not exceeding 0.2 Å. A Gibbs free energy difference of 3.0 and 3.8 kJ/mol is found for HH and HT isomers respectively, between the method used in this study and the one used previously [9].
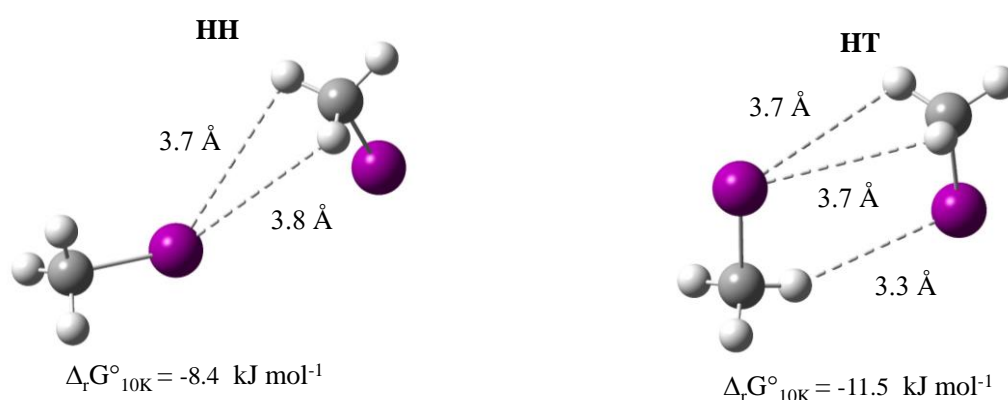
HH

3.7 Å

3.8 Å

$\Delta_r G°_{10K} = -8.4$ kJ mol^{-1}

HT

3.7 Å

3.7 Å

3.3 Å

$\Delta_r G°_{10K} = -11.5$ kJ mol^{-1}

Figure 3. 4 ωB97X-D/ aug-cc-pVTZ-PP-predicted geometries (distances in Å) and Gibbs free energies (ΔG in kJ/mol) of CH_3I dimers.

Two $(CH_3I)_3$ isomers are found to be stable (Figure 3.5) and will be hereafter referred as Tail-to-Head-to-Tail (THT) and Tail-to-Tail-to-Head (TTH). The TTH structure was previously discussed by Ito et al., [10, 11] to be the most stable structure of $(CH_3I)_3$ using the MP2 method. In the present work the Gibbs free energy difference between the 2 isomers is less than 1 kJ/mol at the ωB97X-D/ aug-cc-pVTZ-PP level of theory. As a result, THT and TTH could be considered as isoenergetic. The difference in the intermolecular distance between the level of theory used in this study and the one used previously [10] does not exceed 0.2 Å. Moreover, a difference of about 5 kJ/mol in the Gibbs free energy was found between the two levels of theory.

THT

3.6 Å

3.3 Å

3.3 Å

3.3 Å

3.4 Å

$\Delta_r G°_{10K}$ = -27.7 kJ mol^{-1}

TTH

3.7 Å

3.2 Å

3.3 Å

3.2 Å

$\Delta_r G°_{10K}$ = -28.3 kJ mol^{-1}

Figure 3. 5 ωB97X-D/ aug-cc-pVTZ-PP-predicted geometries (distances in Å) and Gibbs free energies (ΔG in kJ/mol) of CH$_3$I trimers.

As a result, the difference in binding energies shows that $\Delta E(\omega$B97X, this work) is lower than ΔE calculated using MP2 method [9, 10] for both CH$_3$I dimers and trimers. This interaction between CH$_3$I molecules is more accurately evaluated using the ωB97X-D functional that includes dispersion for a better characterization of the intermolecular complexes under study. Moreover, the size of the basis set is larger in our work (aug-cc-pVTZ-PP) than the one used in Ito's studies (LANDZ+fdp) [9, 10].

The calculated vibrational spectra together with bands relative intensities of the monomer and the most stable HH, HT, TTH, THT isomers are gathered in Table 3.1. For a more reliable analysis of CH$_3$I clusters infrared spectra, we used unscaled IR frequencies. It should be noted that the calculated wavenumber position is likely dependent of the level of theory. For example, the wavenumber position of the monomer CH$_3$ symmetric deformation mode is calculated at 1334 cm^{-1} using the MP2/ LanL2DZ+fdp level of theory [9], whereas it is calculated at 1297 cm^{-1} in this work using the ωB97X-D/aug-cc-pVTZ-PP level of theory. It is known that the shift from the monomer band due to clustering can be evaluated by theoretical calculations. For instance, in the CH$_3$ symmetric deformation region the shift of the dimer mode, with respect to that of the monomer, ranges between -4 and 2 cm^{-1} using the MP2/ LanL2DZ+fdp level of theory [9], against of -1 to 3 cm^{-1} in this work using the ωB97X-D/aug-cc-pVTZ-PP level of theory. Similar observation is found for the trimer, where the shift ranges between -7 to -1 cm^{-1} using the MP2/ LanL2DZ+fdp level of theory [10] and -3 to 8 cm^{-1} using the ωB97X-D/aug-cc-pVTZ-PP one (Table 3.1). It shows that the bands of dimers and trimers are in close vicinity with those of monomer, what underlies that perturbation induced by CH$_3$I homo-complexation is weak. Considering that shifts calculated at both levels of theory, that of the present work and the one used by Ito et al., [9, 10] are of the same magnitude, it is

more accurate to uniquely consider those shifts rather than scaled harmonic frequencies to identify present species. The calculation performed in this study will be used as a support to discriminate between monomers, dimers and trimers observed by FTIR-isolation matrix experiments. Those theoretical vibrational spectra will be studied in fingerprint regions in which they will help to identify species trapped in the matrix.

Table 3. 1 Calculated wavenumbers (cm^{-1}) and intensities (I) of CH$_3$I monomer, HH and HT dimers and THT and TTH trimers. The IR bands are predicted at the ωB97X-D/aug-cc-pVTZ-PP level of theory. The frequency shifts are calculated with respect to the monomer position ($\Delta\nu = \nu_{monomer} - \nu$).

Vibrational Modes		CH$_3$I	(CH$_3$I)$_2$ dimers				(CH$_3$I)$_3$ trimers			
		monomer	HT	Δν	HH	Δν	THT	Δν	TTH	Δν
ν$_4$	C-H stretching degenerated	3214 (0)	3221 (0)	7	3214 (0)	0	3221 (0)	7	3215 (1)	1
			3217 (1)	3	3214 (1)	0	3216 (1)	2	3214 (0)	0
			3215 (0)	1	3211 (1)	-3	3214 (1)	0	3213 (2)	-1
			3214 (1)	0	3211 (1)	-3	3213 (1)	-1	3211 (0)	-3
							3210 (1)	-4	3210 (2)	-4
							3206 (1)	-8	3206 (1)	-8
ν$_1$	Symmetric CH$_3$ stretching	3101 (11)	3103 (8)	2	3100 (9)	-1	3101 (8)	0	3097 (10)	-4
			3099 (13)	-2	3100 (14)	-1	3097 (10)	-4	3096 (10)	-5
							3094 (14)	-7	3093 (11)	-8
ν$_5$	CH$_3$ deformation degenerated	1477 (6)	1485 (14)	8	1477 (8)	0	1482 (3)	6	1486 (7)	9
			1480 (7)	3	1477 (6)	0	1479 (12)	2	1485 (3)	8
			1477 (5)	0	1474 (10)	-3	1477 (8)	0	1478 (7)	1
			1474 (2)	-3	1473 (12)	-4	1474 (2)	-3	1477 (7)	0
							1473 (12)	-4	1474 (3)	-3
							1470 (2)	-7	1470 (9)	-7
ν$_2$	Symmetric CH$_3$ deformation	1297 (23)	1300 (41)	3	1297 (12)	0	1300 (39)	3	1305 (2)	8
			1297 (1)	0	1296 (40)	-1	1297 (10)	0	1296 (46)	-1
							1295 (16)	-2	1294 (27)	-3
ν$_6$	CH$_3$ rocking degenerated	903 (5)	913 (15)	10	906 (7)	3	921 (8)	18	914 (7)	11
			910 (4)	7	905 (7)	2	917 (15)	14	911 (10)	7
			909 (4)	6	902 (3)	-1	911 (7)	8	909 (15)	6
			908 (5)	5	901 (4)	-2	910 (7)	7	907 (3)	4
							906 (10)	3	906 (7)	3
							904 (2)	1	905 (4)	2

3.2.1.2 Experimental vibrational spectra

A typical matrix-isolation infrared (IR) spectrum of CH_3I in Ar matrix at 10 K at a mixing ratio of 1/1000 is shown in Figure 3.6. The spectrum clearly shows CH_3-stretching, deformation and rocking regions centered at 3000, 1250 and 890 cm^{-1}, respectively while the C-I stretching mode is outside of the observed spectral region (< 600 cm^{-1}). Additional bands related to traces of water are observed at ~3750 cm^{-1} and 1600 cm^{-1}.
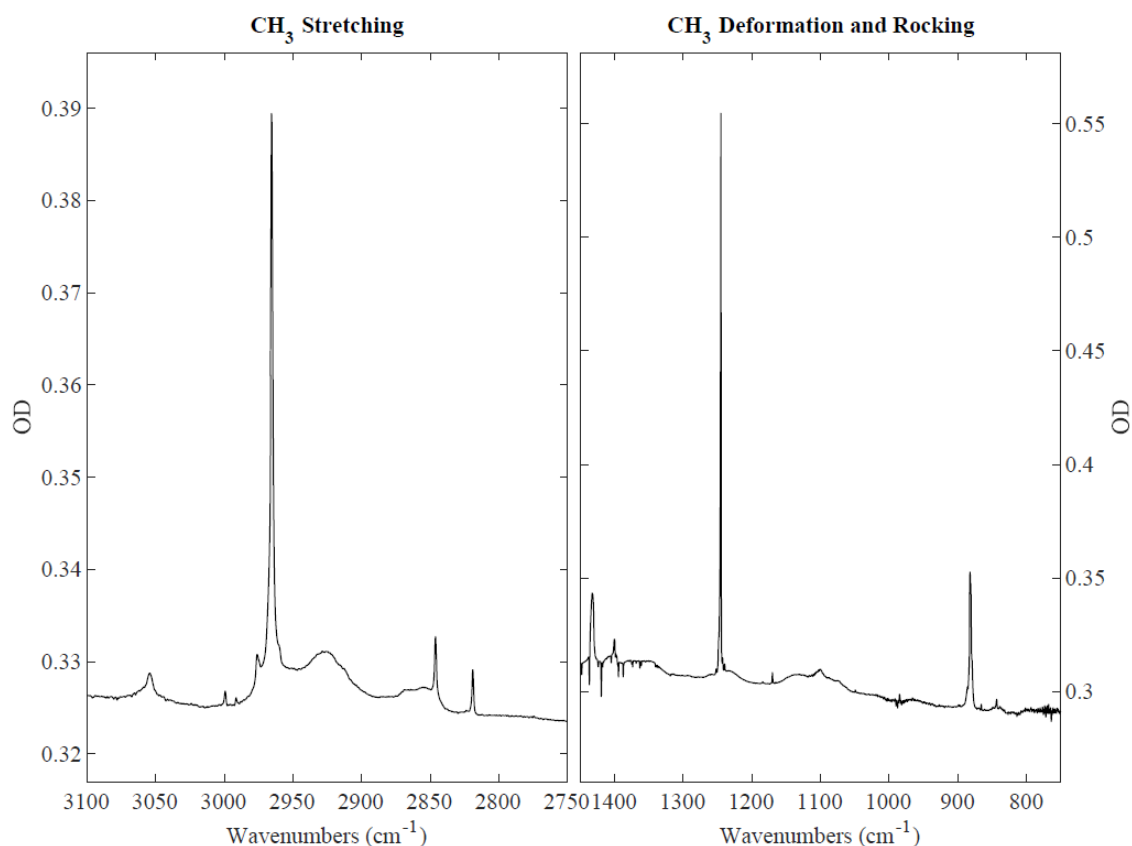
Figure 3. 6 IR spectra of CH_3I/Ar sample at 10 K in the 3100-2750 cm^{-1} and 1350-750 cm^{-1} spectral range corresponding to the CH_3 stretching, deformation and rocking regions, respectively.

In Figure 3.6 the fundamental bands of the CH_3I monomer are observed at 3054, 2965, 1432, 1245, 882 and 881 (doublet) cm^{-1} for ν_4, ν_1, ν_5, ν_2 and ν_6 respectively. These band positions are consistent with those previously reported within 1 cm^{-1} for CH_3I monomer [9, 12]. Some additional bands appear on both sides of the monomer bands, especially for ν_1, ν_2 and ν_6, which are the most intense bands on the FTIR spectrum.

The observed wavenumbers and the shifts from the monomer are listed in Table 3.2 and compared with those obtained by the calculations. As previously reported [9, 12], the set of

additional bands are due to the formation of CH_3I clusters. Considering the concentration 1/1000 of CH_3I in Ar matrix, the presence of the monomer is the most favored resulting in intense bands for this species. However, regarding the calculated and experimental bands the additional bands are tentatively assigned to the HT and HH dimers with typical bands observed at 2967, 2960, 1248, 1246, 1245, 886 cm^{-1} and 2960, 1244, 886, 881, 878 cm^{-1}, respectively. Additionally, the formation of trimers cannot be excluded with characteristic IR bands at 2965, 2960, 1248, 1246, 1243, 886 cm^{-1} tentatively assigned to the THT CH_3I isomer (see Fig. 3.6). This is supported by the calculations demonstrating the $(CH_3I)_3$ THT isomer to be as one of the most stable. The wavenumbers for both monomer and polymers of CH_3I are almost degenerated, which can be understood in terms of weakness of interaction energy of such clusters. As a result, dimer and trimer frequencies are very close to those of monomers.

Table 3. 2 Experimental IR band positions for ν_1, ν_2 and ν_6 (in cm^{-1}) for CH_3I (1000 ppm) in Ar matrix, observed and calculated shift from the monomer and tentative assignment (in bold the most intense IR bands).

Vibrational modes		ν experimental cm^{-1}	$\Delta\nu$ from monomer		Tentative assignement
			observed	calculated	
ν_1	CH$_3$ stretching	2976	11	?	?
		2967	2	2	dimer HT
		2965	0	0	monomer / trimer THT
		2960	-5	2 / -2 /-4	dimer HT / dimer HH / trimer THT
ν_2	Symmetric CH$_3$ deformation	1248	3	3	dimer HT / trimer THT
		1246	1	0	dimer HT / trimer THT
		1245	0	0	monomer / dimer HT
		1244	-1	-1	dimer HH
		1243	-2	-2	trimer THT
		1240	-5	?	?
ν_6	CH$_3$ rocking	886	4	5 / 3	dimer HT / dimer HH / trimer THT
		882	0	0	monomer / dimer HH
		881	-1	-1	monomer/ dimer HH
		878	-4	-2	dimer HH

The formation of CH_3I clusters is confirmed by annealing the matrix from 10 to 35K. The FTIR spectra (see Figure 3.7) clearly shows the decrease of the bands of monomer when the IR bands assigned to dimers or trimers increase. This typical behavior in matrix experiments is explained by the diffusion of CH_3I molecules in the Ar matrix during the annealing and the formation of polymers. Because the iodine atom is heavy, the diffusion of CH_3I within the Ar matrix is expected to be limited and cannot occur at long distance. Thus, we can hypothesis that the dimers and trimers of CH_3I are formed in the gaseous phase and the molecules are likely separated as monomers, for a part, during the matrix deposition. During the annealing the proximity of the CH_3I molecules are small enough to re-form polymers of CH_3I.

Figure 3. 7 IR spectra of the annealing of CH₃I/Ar sample until 35 K in the spectral range (a) 3080-2944 cm⁻¹ (b) 1270-1237 cm⁻¹ (c) 905-870 cm⁻¹. Bands denoted in green, pink and orange are assigned to CH₃I monomer, CH₃I dimer and CH₃I trimer, respectively.
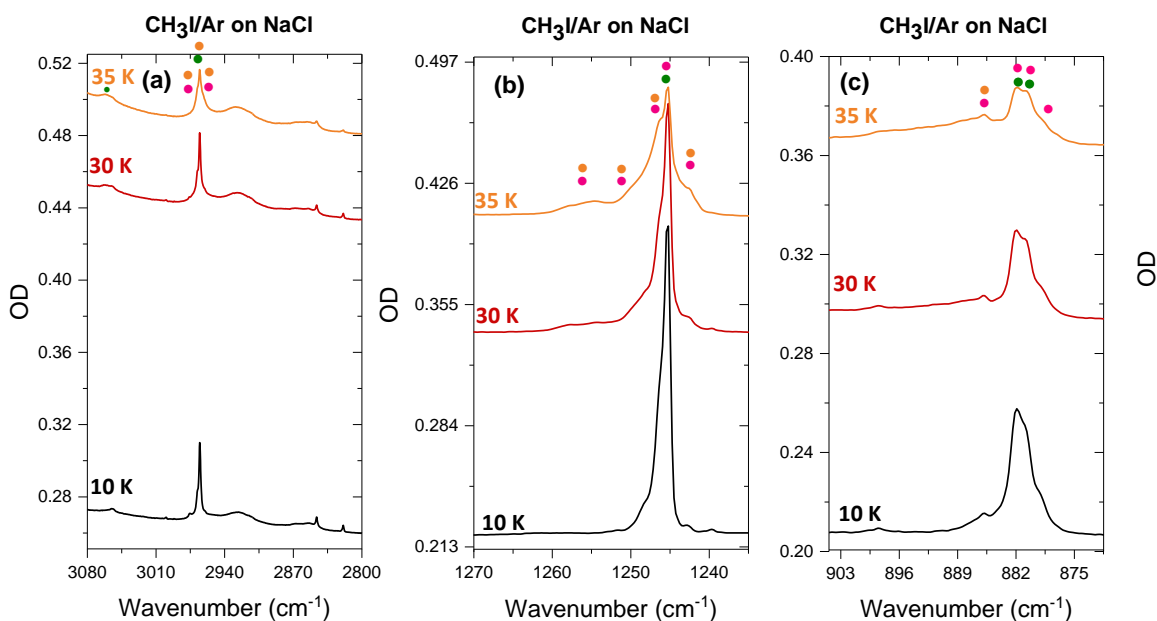
3.2.2 Formation of CH₃I-H₂O complexes

3.2.2.1 DFT calculation results

The structure and the vibrational spectra of various $(CH_3I)_m–(H_2O)_n$ complexes calculated by ωB97XD/aug-cc-pVTZ-PP method for m=1, 2 and n=1, 2, 3 was investigated. From this theoretical work, valuable information can be retrieved on relative stabilities of each species together with the structure of their vibrational spectra. Indeed, from those results we should try to define the most accurate spectral regions to discriminate between $(CH_3I)_m$, $(H_2O)_n$, $(CH_3I)_m-(H_2O)_n$ aggregates and complexes. Ito et al., [11] have demonstrated that B971/LanL2DZ+fdp reproduce well MP2/aug-cc-pVTZ method, while MP2/LanL2DZ +fdp method underestimate the intermolecular interaction between 1CH₃I and 1H₂O. In the present work, the calculations are performed with ωB97XD functional with a relativistic effective core potential and an extended valence basis-set, i.e., aug-cc-pVTZ-PP.

The 1:1 structure was optimized revealing the predicted most stable isomers. The geometry and the standard Gibbs energy of the 1:1 isomers are presented in Figure 3.8.

1:1a
$\Delta_rG°_{10K} = -13.5$ kJ mol^{-1}

1:1b
$\Delta_rG°_{10K} = -7.5$ kJ mol^{-1}

Figure 3. 8 ωB97X-D/ aug-cc-pVTZ-PP-predicted geometry (distances in Å) and Gibbs free energy (ΔG in kJ.mol^{-1}) of CH$_3$I.H$_2$O isomers.

The 1:1 hetero-dimer it presents two stable forms, one pseudo-cyclic, referred as 1:1a, more stable than an unexpected one, 1:1b, which displays an I....O interaction ($\Delta_rG°_{10K} = -13.5$ kJ mol^{-1}, for 1:1a, against -7.5 kJ mol^{-1}, for 1:1b). Indeed, one could have expected to observe, in 1:1b case, an I…H H-bond interaction, rather than this long-distance interaction between iodine and oxygen atoms. Is it so surprising? If one compares, iodine's Pauling electronegativity of 2.7 with that of hydrogen, which is 2.2, it is perfectly plausible to observe a hydrogen-bond type interaction between iodine and oxygen, this latter presenting a Pauling electronegativity of 3.4. Moreover, the methyl iodide dipole moment is oriented toward carbon atom, which leads a partial positive Mulliken's charge for iodine atom in this configuration. It is thus perfectly understandable we observe this I…O interaction.

On the vibrational spectra side, one observes a stronger perturbation for 1:1a, with respect to each monomer, H$_2$O and CH$_3$I, vibration frequencies, than for 1:1b (see Table 3.3). Water ν_3 and ν_1 modes are both red-shifted by -28 and -41 cm^{-1}, while the most promising shift concerning CH$_3$I moiety seems to be that of the CH$_3$ rocking with a blue-shift of 22 cm^{-1}. For 1:1b, water partner presents two almost equivalent free OH bonds, however red-shifted by -11 and -10 cm^{-1} that illustrates the methyl iodide polarity.

Vibrational Mode		H$_2$O monomer	H$_2$O dimer	CH$_3$I monomer	CH$_3$I-H$_2$O (1 :1a)	Δv	CH$_3$I-H$_2$O (1 :1b)	Δv
v_3 H$_2$O	Anti-symmetric stretching	3986 (63)	3974 (85)		3958 (106)	-28	3975 (63)	-11
			3954 (86)					
v_1 H$_2$O	Symmetric stretching	3879(5)	3871 (11)		3838 (48)	-41	3869 (11)	-10
			3751 (339)					
v_2 H$_2$O	Bending	1637 (63)	1658 (39)		1642 (49)	5	1636 (67)	-1
			1637 (94)					
v_4	C-H stretching			3214 (0)	3215 (0)	1	3207 (1)	-7
					3213 (5)	-1	3207 (1)	-7
v_1	Symmetric CH$_3$ stretching			3101 (11)	3096 (12)	-5	3097 (15)	-4
v_5	CH$_3$ deformation			1477 (6)	1484 (5)	7	1478 (6)	1
					1474 (4)	-3	1478 (6)	1
v_2	Symmetric CH$_3$ deformation			1297 (23)	1301 (22)	4	1296 (23)	-1
v_6	CH$_3$ rocking			903 (5)	925 (7)	22	900 (5)	-3
					909 (5)	6	899 (5)	-4

The 1:2 structure was optimized revealing the predicted most stable isomers. The geometry and the standard Gibbs energy of the 1:2 isomers are presented in Figure 3.9.
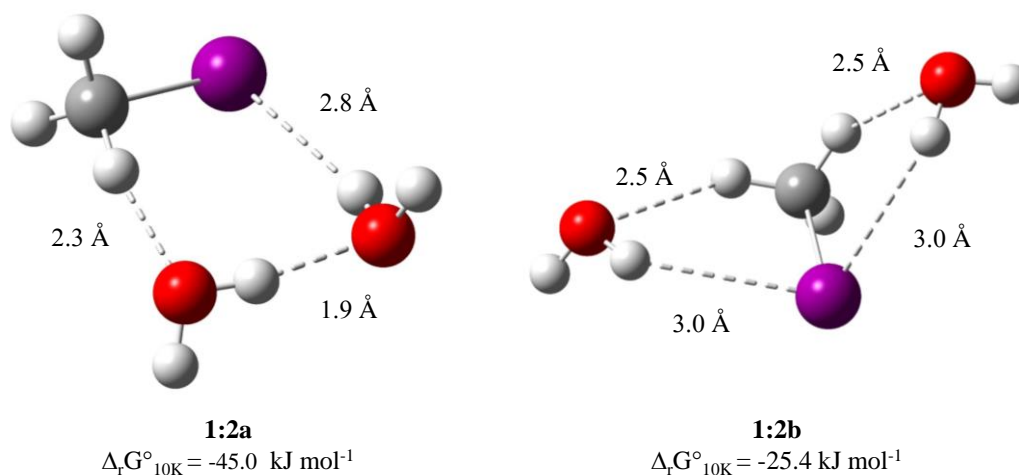
1:2a
$\Delta_rG°_{10K}$ = -45.0 kJ mol^{-1}

1:2b
$\Delta_rG°_{10K}$ = -25.4 kJ mol^{-1}

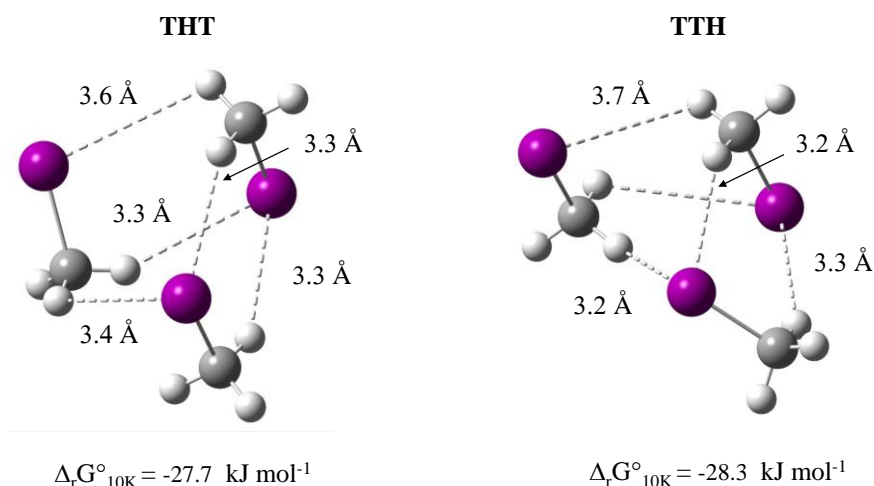*Figure 3. 9 ωB97X-D/ aug-cc-pVTZ-PP-predicted geometry (distances in Å) and Gibbs free energy (ΔG in kJ.mol^{-1}) of CH$_3$I.(H$_2$O)$_2$ isomers.*

For the CH$_3$I.(H$_2$O)$_2$ complexes, there are two stable structures denoted, 1:2a and 1:2b, with $\Delta_rG°_{10K}$ of -45.0 and -25.4 kJ mol^{-1}, respectively. If the former one presents a cyclic structure which can be summarized as a water dimer interacting by two H-bond type interactions with

CH$_3$I, the latter displays an almost symmetrical structure with the two water monomers on each side of the CH$_3$I partner, *i.e.* a kind of double 1:1a (1:1 complex) structure with respect to the ICH methyl iodide plane. As a result, on the vibrational spectra of those two forms, one should observe in 1:2a case, a typical water dimer spectrum, with one proton acceptor, PA, and one proton donor, PD, partner, perturbed by CH$_3$I, but at the difference that PA partner also gives its proton to iodine atom, while for 1:2b, one should find a vibrational spectrum close to that of 1:1a.

From Table 3.4, for 1:2b species, one observes, indeed, comparable shifts with those of 1:1a, for water monomers while CH$_3$ rocking mode presents more pronounced blue-shifts, by 33 instead of 22 and 14 against 5 cm^{-1}, with respect to 1:1a ones. Another noticeable red-shift is that of CH$_3$ symmetrical stretching which is -14 cm^{-1}. If we come back to 1:2a species, it is clearly a water dimer spectrum perturbed by CH$_3$I as illustrated by ν_3 and ν_1 water modes red-shifts. These red-shifts, namely that of -205 cm^{-1} (typical of a ν_1 water dimer PD), coupled to OH…O distance of 1.87 Å (typical of a water dimer), put in evidence that H$_2$O-H$_2$O interaction is stronger than interactions of each water monomer with CH$_3$I partner. As a result, it would be difficult to discriminate between 1:2a (water region) spectrum and that of the pure water dimer.

Table 3. 4 Calculated wavenumbers (cm⁻¹) and intensities (I) of CH₃I.(H₂O)₂ complexes compared to the calculated wavenumber (cm⁻¹) and intensities (I) of CH₃I monomer and H₂O monomer and dimer. The IR bands are predicted at the ωB97X-D/aug-cc-pVTZ-PP level of theory. The frequency shifts are calculated with respect to the monomer position (Δv = vmonomer-v).

Vibrational Mode		H₂O monomer	H₂O dimer	CH₃I monomer	CH₃I-2H₂O 1 :2a	Δv	vCH₃I-2H₂O 1 :2b	Δv
ν₃ H₂O	Anti-symmetric stretching	3986 (63)	3974 (85)		3950 (74)	-36	3960 (18)	-26
			3954 (86)		3940 (131)	-46	3960 (188)	-26
ν₁ H₂O	Symmetric stretching	3879(5)	3871 (11)		3782 (256)	-97	3845 (35)	-34
			3751 (339)		3674 (358)	-205	3845 (35)	-34
ν₂ H₂O	Bending	1637 (63)	1658 (39)		1662 (40)	25	1639 (92)	2
			1637 (94)		1638 (61)	1	1638 (9)	1
ν₄	C-H stretching			3214 (0)	3215 (1)	1	3216 (1)	2
					3205 (34)	-9	3215 (14)	1
ν₁	Symmetric CH₃ stretching			3101 (11)	3087 (28)	-14	3093 (9)	-8
ν₅	CH₃ deformation			1477 (6)	1491 (4)	14	1484 (3)	7
					1475 (4)	-2	1478 (2)	4
ν₂	CH₃ Symmetric deformation			1297 (23)	1312 (27)	5	1303 (20)	6
ν₆	CH₃ rocking			903 (5)	935 (4)	31	937 (9)	33
					917 (5)	14	925 (5)	22

The 2:1 structure was optimized revealing the predicted most stable isomers. The geometry and the standard Gibbs energy of the 2:1 isomers are presented in Figure 3.10.
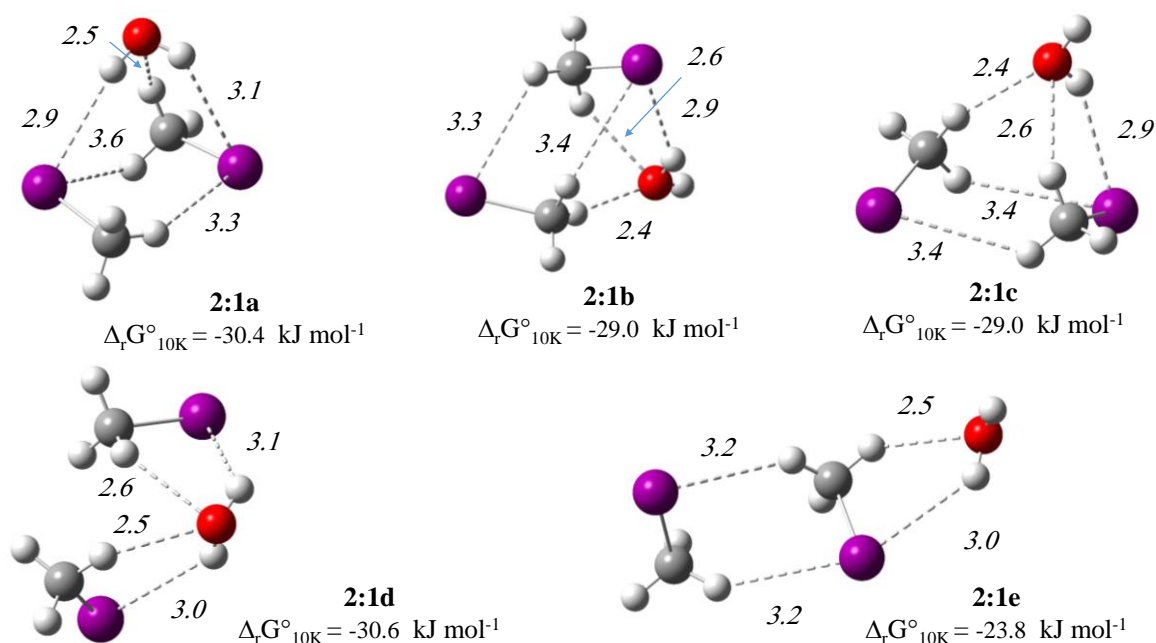
Figure 3. 10 ωB97X-D/ aug-cc-pVTZ-PP-predicted geometry (distances in Å) and Gibbs free energy (ΔG in kJ mol⁻¹) of (CH₃I)₂.(H₂O) isomers.

For the $(CH_3I)_2$-H_2O complexes, shown in Figure 3.10 we count non less than five stable structures denoted, 2:1a to 2:1e, with $\Delta_r G°_{10K}$ lying in a close range of energies (-30.6 to -29.0 kJ mol^{-1}, 2:1b and 2:1c being degenerated), with the exception of 2:1e one which is a little bit disfavored at -23.8 kJ mol^{-1}). If the three first ones, 2:1a, 2:1b and 2:1c, present quite similar structures, *i.e.* CH_3I dimer interacting with a water monomer (2:1a presenting a subtle double PD, on time PA, character, which gives a low stabilization compared to 2:1b and 2:1c, whose one OH bond remains free), the 2:1d displays water molecule bridging between the two CH_3I molecules while 2:1e presents again the 1:1a moiety in interaction with the other CH_3I partner. Not surprisingly, the most "3D" interacting structures, are the most stable.

On the vibrational point of view, from Table 3.5, one can guess that indeed, in the water stretching region 2:1e presents red-shifts comparable with those of 1:1a but also overlapping with those of 1:2b. Having regard to 2:1a and 2:1d, also in water stretching region, they present comparable red-shifts of -61 cm^{-1} (v_3), while 2:1a shares its n_1 red-shift of -54 cm^{-1} with 2:1b and 2:1c. In the CH_3 rocking region, all the species should present the same spectrum, with blue-shifts overlapping with those of the above studied forms.

Vibrational modes	H$_2$O monomer	H$_2$O dimer	CH$_3$I monomer	2CH$_3$I-H$_2$O 2 :1a	Δv	2CH$_3$I-H$_2$O 2 :1b	Δv	2CH$_3$I-H$_2$O 2 :1c	Δv	2CH$_3$I-H$_2$O 2 :1d	Δv	2CH$_3$I-H$_2$O 2 :1e	Δv
v_3 H$_2$O Anti-symmetric stretching	3986 (63)	3974 (85) 3954 (86)		3925 (106)	-61	3957 (114)	-29	3957 (114)	-29	3925 (106)	-61	3959 (103)	-27
v_1 H$_2$O Symmetric stretching	3879 (5)	3871 (11) 3751 (339)		3825 (84)	-54	3825 (65)	-54	3825 (66)	-54	3833 (28)	-46	3842 (40)	-32
v_2 H$_2$O Bending	1637 (63)	1658 (39) 1637 (94)		1643 (70)	6	1634 (63)	-3	1633 (61)	-4	1646 (71)	9	1640 (49)	3
v_4 CH$_3$I C-H stretching			3214 (0)	3217 (1)	3	3218 (0)	4	3218 (0)	3	3214 (2)	0	3213 (3)	-1
				3216 (0)	2	3217 (8)	3	3216 (9)	2	3214 (0)	0	3213 (1)	-1
				3212 (4)	-2	3215 (2)	1	3214 (1)	0	3212 (2)	-2	3210 (1)	-4
				3211 (2)	-3	3209 (1)	-5	3209 (2)	-5	3211 (2)	-1	3208 (7)	-6
v_1 CH$_3$I Symmetric CH$_3$ stretching			3101 (11)	3097 (11)	-4	3099 (4)	-2	3098 (4)	-3	3097 (16)	-4	3098 (9)	-3
				3095 (11)	-6	3096 (7)	-5	3096 (7)	-5	3096 (3)	-5	3091 (7)	-10
v_5 CH$_3$I CH$_3$ deformation			1477 (6)	1483 (11)	6	1496 (7)	19	1495 (6)	18	1488 (3)	11	1484 (5)	7
				1477 (3)	0	1483 (25)	6	1482 (28)	4	1481 (19)	4	1481 (3)	4
				1473 (2)	-4	1477 (8)	0	1478 (8)	1	1475 (10)	-2	1478 (9)	1
				1469 (8)	-8	1472 (12)	-5	1474 (9)	-2	1470 (7)	-7	1472 (9)	-5
v_2 CH$_3$I Symmetric CH$_3$ deformation			1297 (23)	1302 (35)	5	1308 (10)	11	1307 (8)	10	1302 (16)	5	1302 (27)	5
				1297 (5)	0	1301 (45)	0	1301 (48)	4	1298 (28)	1	1297 (21)	0
v_6 CH$_3$I CH$_3$ rocking			903 (5)	926 (6)	23	924 (8)	21	925 (8)	22	925 (8)	22	930 (12)	27
				916 (11)	13	914 (2)	11	913 (5)	10	921 (6)	18	915 (4)	12
				913 (7)	10	913 (5)	10	913 (3)	10	910 (8)	7	911 (8)	7
				908 (4)	5	910 (7)	7	908 (7)	5	907 (5)	4	904 (6)	1

The 1:3 structure was optimized revealing the predicted most stable isomers. The geometry and the standard Gibbs energy of the 1:3 isomers are presented in Figure 3.11.
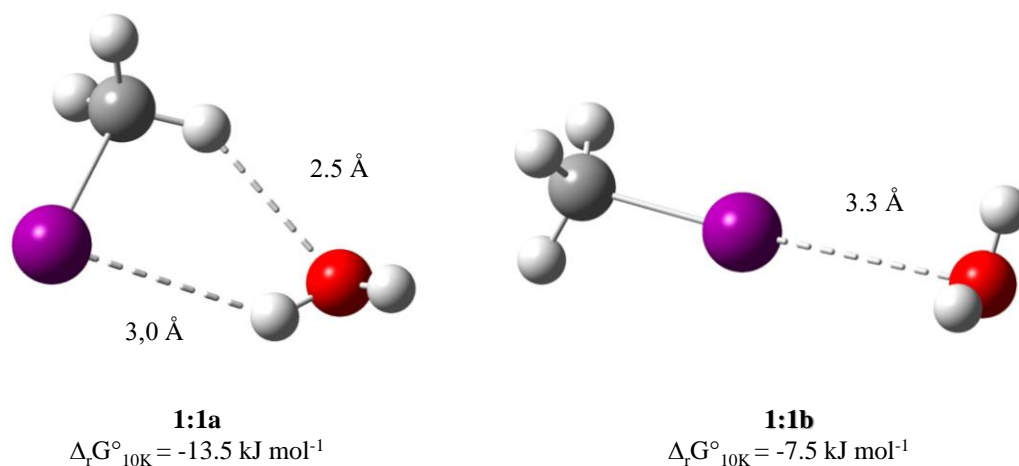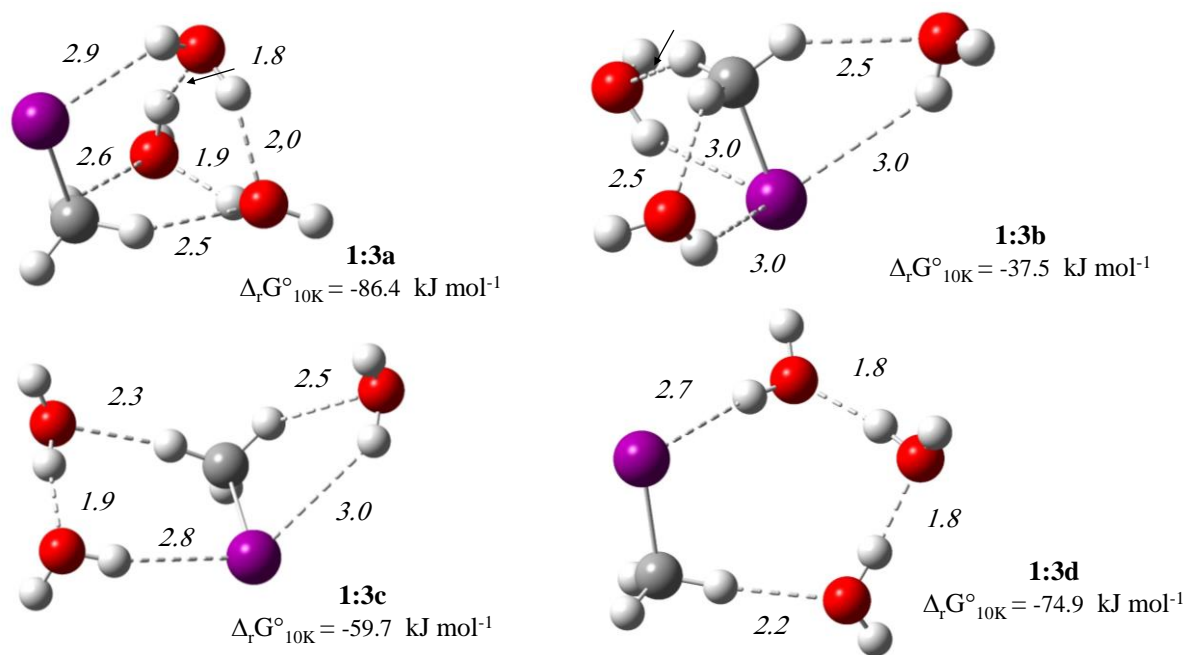

Figure 3. 11 ωB97X-D/ aug-cc-pVTZ-PP-predicted geometry (distances in Å) and Gibbs free energy (ΔG in kJ mol⁻¹) of CH₃I.(H₂O)₃ isomers.

The CH₃I.(H₂O)₃ one, displayed in Figure 3.11, could be considered as the first step of CH₃I water embedding, leadimg to models of CH₃I trapped in water environment as aggregates or Amorphous Solid Water (ASW). We found four different stable structures: 1:3a, the most stable one ($\Delta rG°_{10K}$ = -86.4 kJ mol⁻¹) which is a cyclic water trimer perturbed by CH₃I molecule which should present a vibrational spectrum close to that of cyclic water trimer; 1:3b, the least stable one ($\Delta_rG°_{10K}$ = -37.5 kJ mol⁻¹), which is some kind of spinning top structure with the three water molecules interacting independently from each other (i.e. three times 1:1a structure) with the central CH₃I molecule, which should exhibit a spectrum close to that of 1:1a; 1:3c ($\Delta_rG°_{10K}$ = -59.7 kJ mol⁻¹) which displays a kind of "1:1a+1:2a" structure and should therefore share much in common with these two structures; 1:3d ($\Delta_rG°_{10K}$ = -74.9 kJ mol⁻¹) which is a cyclic structure comprising a non-cyclic water trimer bridging between iodine and H methyl atoms of methyl iodide. It should be noted that 1:3b and 1:3c should present the strongest CH₃ blue-shifts.

One more time, it is obvious the most there are water molecules involved in self H-bond association, the most the hetero-complex is stable. It come partly from H-bond interaction efficiency which induces cooperative effects. From the observation of theoretical harmonic frequencies values (Table 3.6), it is clear that those signals overlap with those of the other forms.

Table 3. 6 Calculated wavenumbers (cm^{-1}) and intensities (I) of CH$_3$I.(H$_2$O)$_3$ complexes compared to the calculated wavenumber (cm^{-1}) and intensities (I) of CH$_3$I monomer and H$_2$O monomer and dimer. The IR bands are predicted at the ωB97X-D/aug-cc-pVTZ-PP level of theory. The frequency shifts are calculated with respect to the monomer position ($\Delta\nu$ = νmonomer-ν).

Vibrational modes	H$_2$O monomer	H$_2$O Dimer	CH$_3$I monomer	CH$_3$I-3H$_2$O 1:3a	Δν	CH$_3$I-3H$_2$O 1:3b	Δν	CH$_3$I-3H$_2$O 1:3c	Δν	CH$_3$I-3H$_2$O 1:3d	Δν
ν$_3$ H$_2$O Anti-symmetric stretching	3986 (63)	3974 (85)		3950 (60)	-36	3962 (54)	-24	3961 (94)	-25	3949 (74)	-37
		3954 (86)		3948 (99)	-38	3961 (124)	-25	3951 (71)	-35	3948 (132)	-38
				3861 (205)	-125	3960 (119)	-26	3941 (140)	-45	3943 (78)	-43
ν$_1$ H$_2$O Symmetric stretching	3879(5)	3871 (11)		3716 (294)	-63	3849 (19)	-30	3848 (29)	-31	3761 (354)	-118
		3751 (339)		3663 (358)	-216	3848 (32)	-31	3788 (246)	-91	3660 (499)	-219
				3557 (276)	-322	3848 (32)	-31	3680 (342)	-199	3606 (545)	-273
ν$_2$ H$_2$O Bending	1637 (63)	1658 (39)		1669 (27)	32	1640 (27)	3	1661 (40)	24	1677 (36)	40
		1637 (94)		1653 (138)	16	1640 (27)	3	1640 (74)	3	1662 (32)	25
				1647 (58)	10	1638 (94)	1	1639 (37)	2	1636 (76)	-1
ν$_4$ CH$_3$I C-H stretching			3214 (0)	3219 (2)	5	3216 (12)	2	3216 (2)	2	3215 (0)	1
				3218 (2)	4	3213 (13)	-1	3206 44)	-8	3199 (50)	-15
ν$_1$ CH$_3$I Symmetric CH$_3$ stretching			3101 (11)	3101 (6)	0	3088 (2)	-13	3085 (18)	-16	3079 (47)	-25
ν$_5$ CH$_3$I CH$_3$ deformation			1477 (6)	1485 (21)	8	1484 (1)	7	1493 (3)	16	1491 (5)	14
				1475 (7)	-2	1484 (2)	7	1476 (3)	-1	1474 (4)	-3
ν$_2$ CH$_3$I Symmetric CH$_3$ deformation			1297 (23)	1310 (27)	13	1305 (20)	8	1314 (26)	17	1316 (28)	19
ν$_6$ CH$_3$I CH$_3$ rocking			903 (5)	918 (5)	15	946 (7)	44	951 (5)	48	940 (3)	37
				916 (11)	13	945 (7)	43	929 (5)	26	919 (5)	16

The last category of complexes we calculated is $(CH_3I)_2$-$(H_2O)_2$ complexes, shown in Figure 3.12.
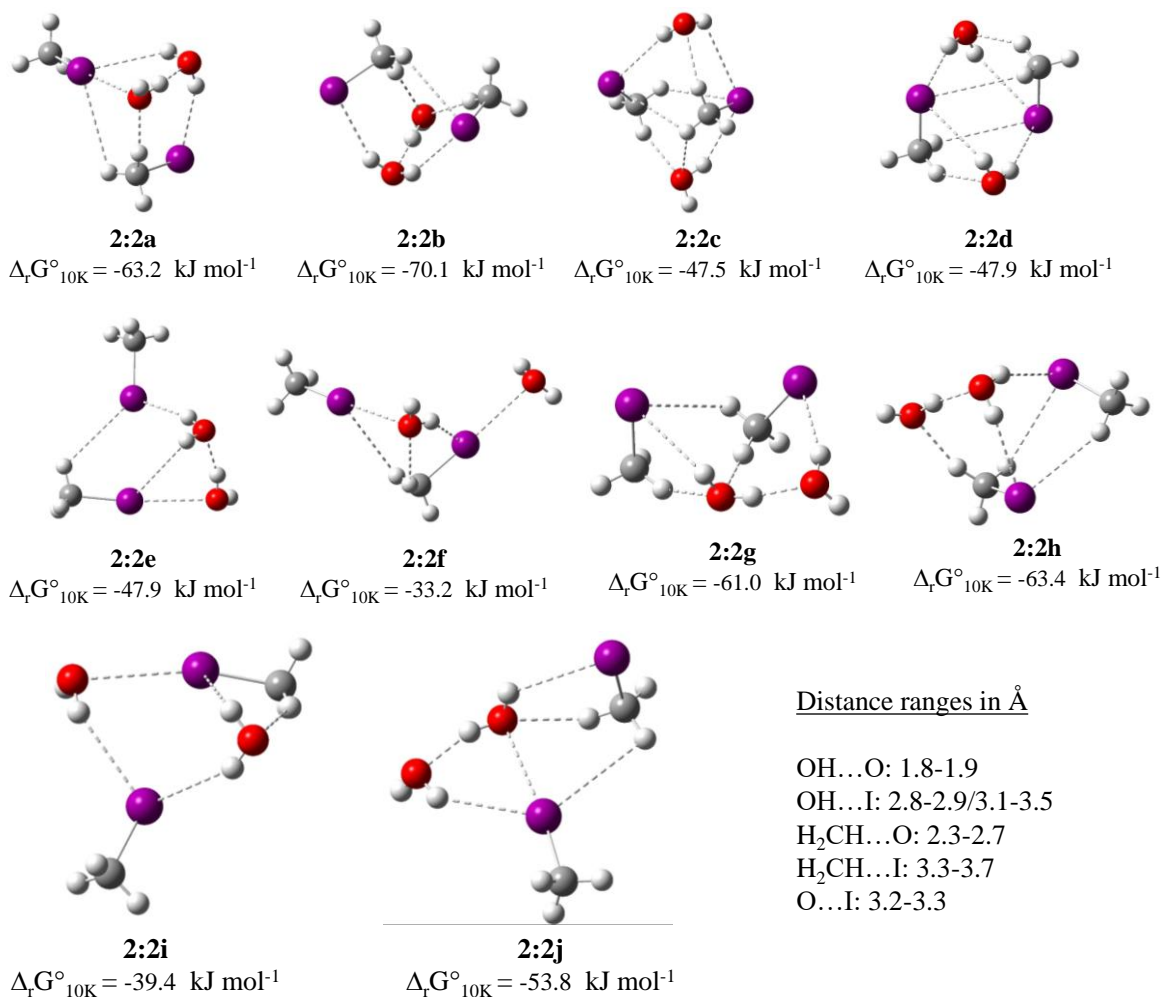
2:2a
$\Delta_rG°_{10K}$ = -63.2 kJ mol^{-1}

2:2b
$\Delta_rG°_{10K}$ = -70.1 kJ mol^{-1}

2:2c
$\Delta_rG°_{10K}$ = -47.5 kJ mol^{-1}

2:2d
$\Delta_rG°_{10K}$ = -47.9 kJ mol^{-1}

2:2e
$\Delta_rG°_{10K}$ = -47.9 kJ mol^{-1}

2:2f
$\Delta_rG°_{10K}$ = -33.2 kJ mol^{-1}

2:2g
$\Delta_rG°_{10K}$ = -61.0 kJ mol^{-1}

2:2h
$\Delta_rG°_{10K}$ = -63.4 kJ mol^{-1}

2:2i
$\Delta_rG°_{10K}$ = -39.4 kJ mol^{-1}

2:2j
$\Delta_rG°_{10K}$ = -53.8 kJ mol^{-1}

Distance ranges in Å

OH…O: 1.8-1.9
OH…I: 2.8-2.9/3.1-3.5
H_2CH…O: 2.3-2.7
H_2CH…I: 3.3-3.7
O…I: 3.2-3.3

Figure 3. 12 ωB97X-D/ aug-cc-pVTZ-PP-predicted geometry (distances in Å) and Gibbs free energy (ΔG in kJ mol^{-1}) of $(CH_3I)_2$.$(H_2O)_2$ isomers.

We can easily discriminate between two kinds of complexes: those which display a water dimer part, and those which display two separated water molecules. Excepted for 2:2e ($\Delta_rG°_{10K}$ = -47.9 kJ mol^{-1}), all the former class present the most stable potentials with $\Delta_rG°_{10K}$ ranging from -70.1 (2:2b) to -53.8 (2:2j) kJ mol^{-1}. The latter class displays less stable structures with $\Delta_rG°_{10K}$ ranging from -47.9 (2:2d) to -33.2 (2:2f) kJ mol^{-1}. It could be understood in terms of H-bond type interaction strength. Indeed, in the case of a water dimer, there is a strong interaction (as illustrated by short OH…H bonds of 1.8-1.9 Å), due to the quasi-linear interaction between the PD O-H bond and the sp^3 doublet of the PA partner, while in the second category complexes, the one without a water dimer part, interactions between PD and PA are less effective.

On the vibrational side, from Table 3.7 it is obvious that one more time considering OH stretching regions and CH_3 one, if all these isomers coexist, it will induce a spectral congestion. However, some blue shifts in the ν_2 water bending mode (2:2b, 28 cm^{-1}; 2:2e, 32 cm^{-1}; 2:2g, 35 cm^{-1}; 2:2h, 26 cm^{-1}) could be of some help, even if the 1:2a isomer presents also a blue-shift in this region of 25 cm^{-1}.

Table 3. 7 Calculated wavenumbers (cm^{-1}) and intensities (I) of $(CH_3I)_2.(H_2O)_2$ complexes compared to the calculated wavenumbers (cm^{-1}) and intensities (I) of CH_3I monomer and H_2O monomer and dimer. The IR bands are predicted at the ωB97X-D/aug-cc-pVTZ-PP level of theory. The frequency shifts are calculated with respect to the monomer position ($\Delta\nu = \nu$monomer-ν).

Vibrational modes	H₂O monomer	H₂O dimer	CH₃I monomer	2CH₃I-2H₂O 2 :2a	Δν	2CH₃I-2H₂O 2 :2b	Δν	2CH₃I-2H₂O 2 :2c	Δν	2CH₃I-2H₂O 2 :2d	Δν	2CH₃I-2H₂O 2 :2e	Δν
ν_3 H₂O Anti-symmetric stretching	3986 (63)	3974 (85)		3949 (77)	-37	3950 (74)	-36	3954 (126)	-28	3937 (146)	-49	3948 (74)	-38
		3954 (86)		3888 (164)	-98	3864 (235)	-122	3937 (94)	-39	3934 (29)	-52	3922 (111)	-64
ν_1 H₂O Symmetric stretching	3879(5)	3871 (11)		3793 (152)	-86	3787 (142)	-92	3818 (151)	-61	3823 (159)	-56	3803 (156)	-76
		3751 (339)		3631 (310)	-248	3607 (370)	-266	3814 (58)	-65	3822 (18	-57	3685 (318)	-194
ν_2 H₂O Bending	1637 (63)	1658 (39)		1655 (49)	18	1665 (42)	28	1643 (42)	6	1642 (3)	5	1665 (39)	32
		1637 (94)		1645 (81)	8	1646 (82)	9	1631 (57)	-6	1642 (136)	5	1649 (82)	12
ν_4 CH₃I C-H stretching			3214 (0)	3217 (3)	3	3213 (3)	-1	3216 (1)	2	3219 (1)	5	3213 (0)	1
				3213 (17)	-1	3211 (4)	-3	3215 (10)	1	3218 (1)	4	3213 (0)	-1
				3208 (1)	-6	3209 (24)	-5	3214 (11)	0	3216 (8)	2	3206 (1)	-8
				3208 (1)	-6	3206 (13)	-8	3213 (1)	-1	3213 (7)	-1	3203 (1)	-11
ν_1 CH₃I Symmetric CH₃ stretching			3101 (11)	3098 (13)	-3	3091 (26)	-10	3096 (10)	-5	3097 (11)	-4	3100 (12)	-1
				3095 (15)	-6	3088 (10)	-13	3092 (9)	-9	3095 (12)	-6	3095 (16)	-6
ν_5 CH₃I CH₃ deformation			1477 (6)	1492 (13)	15	1496 (4)	19	1486 (20)	9	1488 (16)	11	1478 (4)	1
				1478 (5)	1	1486 (13)	9	1482 (7)	5	1486 (4)	9	1478 (3)	1
				1477 (6)	0	1476 (7)	-1	1473 (14)	-4	1471 (9)	-6	1476 (7)	-1
				1475 (8)	-2	1473 (9)	-4	1472 (2)	-5	1470 (2)	-7	1476 (7)	-1
ν_2 CH₃I Symmetric CH₃ deformation			1297 (23)	1312 (28)	15	1312 (17)	15	1304 (36)	7	1303 (37)	6	1296 (29)	-1
				1296 (21)	-1	1307 (34)	10	1304 (12)	7	1300 (0)	3	1296 (22)	-1
ν_6 CH₃I CH₃ rocking			903 (5)	931 (5)	28	932 (5)	29	937 (7)	34	932 (2)	29	902 (4)	-1
				917 (6)	14	932 (5)	29	922 (4)	19	931 (10)	28	901 (5)	-2
				901 (3)	-2	916 (9)	13	921 (7)	18	913 (9)	10	900 (6)	-3
				900 (6)	-3	914 (4)	11	914 (9)	11	913 (6)	10	898 (3)	-5

Table 3. 7 continued

Vibrational modes	H₂O monomer	H₂O dimer	CH₃I monomer	2CH₃I-2H₂O 2 :2f	Δν	2CH₃I-2H₂O 2 :2g	Δν	2CH₃I-2H₂O 2 :2h	Δν	2CH₃I-2H₂O 2 :2i	Δν	2CH₃I-2H₂O 2 :2j	Δν
ν_3 H₂O Anti-symmetric stretching	3986 (63)	3974 (85)		3977 (64)	-19	3945 (132)	-41	3951 (77)	-35	3955 (102)	-31	3946 (129)	-40
		3954 (86)		3950 (122)	-36	3911 (106)	-75	3870 (200)	-116	3935 (83)	-51	3901 (173)	-85
ν_1 H₂O Symmetric stretching	3879(5)	3871 (11)		3871 (12)	-8	3782 (236)	-97	3794 (134)	-85	3844 (44)	5	3817 (112)	-62
		3751 (339)		3803 (132)	-76	3683 (360)	-196	3659 (411)	-200	3843 (46)	4	3710 (288)	-169
ν_2 H₂O Bending	1637 (63)	1658 (39)		1638 (67)	1	1672 (59)	35	1663 (37)	26	1646 (100)	9	1653 (60)	16
		1637 (94)		1636 (65)	-1	1635 (36)	-2	1646 (120)	9	1639 (63)	2	1638 (45)	1
ν_4 CH₃I **C-H stretching**			3214 (0)	3217 (2)	3	3214 (5)	0	3218 (0)	4	3215 (0)	1	3221 (4)	7
				3210 (1)	-4	3212 (1)	-2	3216 (0)	2	3214 (0)	0	3216 (2)	2
				3206 (1)	-8	3210 (5)	-4	3209 (30)	-5	3210 (0)	-4	3209 (1)	-5
				3205 (1)	-9	3201 (16)	-13	3206 (3)	-8	3207 (3)	-7	3208 (1)	-7
ν_1 CH₃I Symmetric CH₃ stretching			3101 (11)	3099 (10)	-2	3094 (17)	-7	3094 (11)	-7	3101 (10)	0	3100 (11)	-1
				3096 (16)	-5	3084 (15)	-9	3091 (24)	-10	3093 (15)	-8	3098 (13)	-3
ν_5 CH₃I CH₃ deformation			1477 (6)	1482 (16)	5	1490 (6)	13	1491 (7)	14	1487 (4)	10	1506 (8)	29
				1478 (6)	1	1483 (16)	6	1477 (4)	0	1476 (6)	-1	1478 (7)	1
				1478 (5)	1	1475 (6)	-2	1474 (3)	-3	1476 (7)	-1	1478 (11)	1
				1474 (7)	-3	1469 (10)	-8	1471 (4)	-6	1474 (4)	-3	1477 (0)	0
ν_2 CH₃I Symmetric CH₃ deformation			1297 (23)	1302 (23)	5	1306 (26)	9	1310 (27)	13	1298 (14)	1	1304 (26)	7
				1295 (26)	-2	1301 (25)	4	1298 (13)	2	1296 (41)	-1	1296 (26)	-1
ν_6 CH₃I CH₃ rocking			903 (5)	921 (5)	18	937 (5)	34	934 (4)	31	920 (7)	17	935 (8)	32
				907 (7)	4	926 (9)	23	920 (10)	17	907 (5)	5	914 (5)	11
				899 (7)	-4	915 (7)	12	912 (9)	9	904 (3)	1	901 (5)	-2
				897 (4)	-6	908 (5)	5	909 (4)	6	902 (4)	-1	898 (4)	-5

Considering, if all those species are co-existing, the spectral congestion that will ensue, a careful examination of spectral conditions (namely of sample ratio) will be necessary to identify unambiguously forms present in argon matrices.

3.2.2.2 Experimental vibrational spectra

In Figures 3.13 and 3.14, are displayed on one hand, two methyl iodide spectral regions, *i.e.* ν_2 (bending CH) and ν_6 (rocking mode), and, on the other hand the three water spectral regions, *i.e.* ν_3 (antisymmetric stretching), ν_1 (symmetric stretching) and ν_2 (bending). We selected those spectral domains because, as discussed above, with the help of theoretical results, we should be able to identify which aggregates and complexes are present in those experimental conditions (with a large excess of water) supposed to mimic atmospheric ones. In both figures we present a comparison of pure CH_3I spectra (labelled as (a) in Figure 3. 13) with mixed $(CH_3I)_m(H_2O)_n$ ones and of pure water polymers (labelled as (a) in Figure 3. 14). New or increasing bands, observed in mixed species spectrum, with respect to those of pure water or methyl iodide ones, are marked with a dashed line (Traces (b) in Figures 3.13 and 3.14
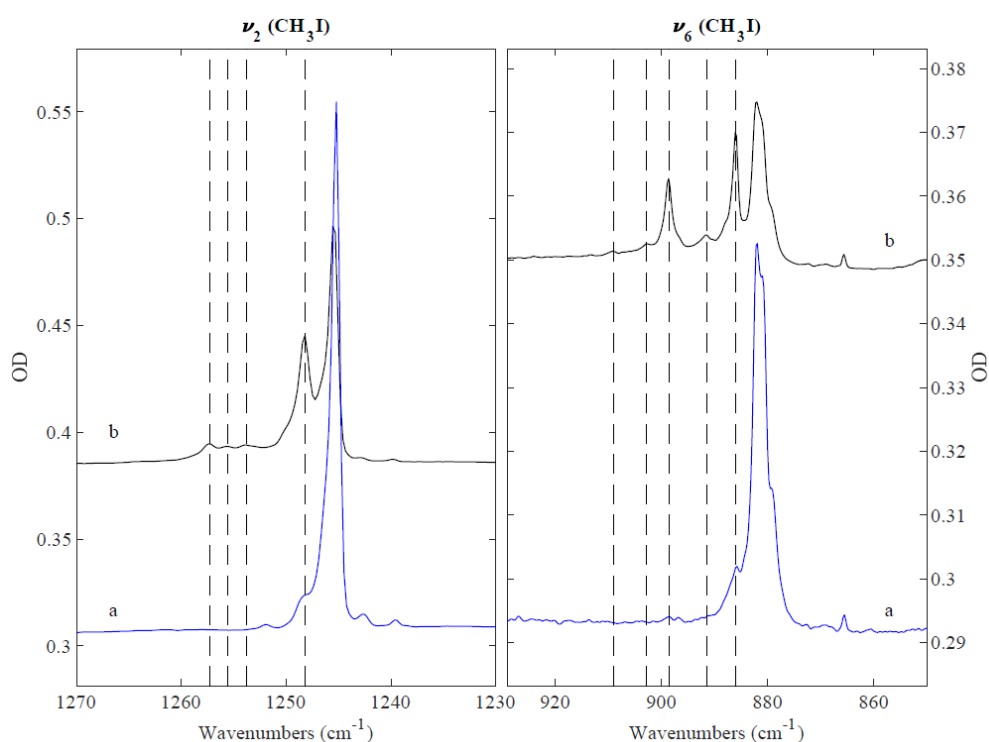
Figure 3. 13 IR spectra in ν_2 (bending CH), ν_6 (rocking CH_3) regions of pure methyl iodide matrix (trace (a)) ($CH_3I/Ar = 1/1000$), recorded at 10 K, and of mixed $CH_3I/H_2O/Ar = 1/24/1500$, recorded at 10 K (trace (b)).
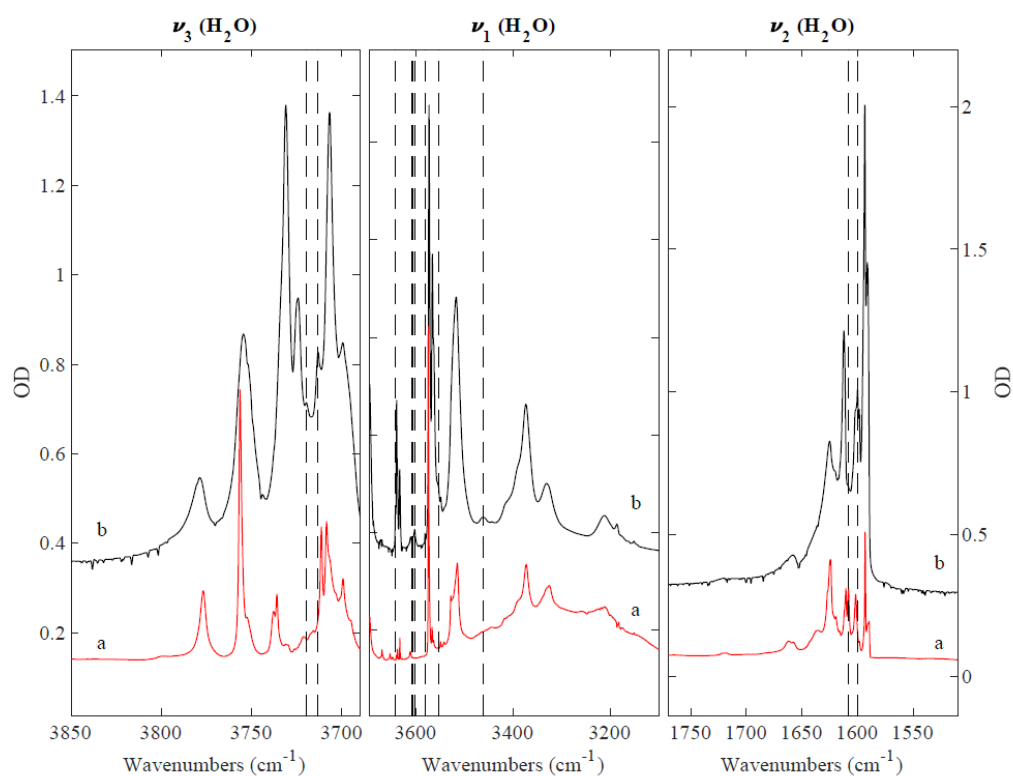
Figure 3. 14 IR spectra in the ν_1 (symmetric stretching), ν_3 (antisymmetric stretching) and ν_2 (bending mode) regions of pure water polymer matrix (trace (a)) ($H_2O/Ar = 7/1000$), recorded at 4 K, and of mixed $CH_3I/H_2O/Ar = 1/24/1500$, recorded at 10 K (trace (b)).

The frequencies and tentative assignment are reported in Tables 3.8 and 3.9.

Table 3. 8 Experimental IR band positions for ν_1, ν_2, and ν_6 (in cm^{-1}) in CH$_3$I spectral range for mixed CH$_3$I/H$_2$O/Ar = 1/24/1500, recorded at 10 K, calculated spectral shifts ($\Delta\nu$) to experimental spectrum of CH$_3$I monomer and tentative assignments. ($\Delta\nu$ = $\nu_{calculated} - \nu_{experimental}$).

Vibrational Mode	CH$_3$I monomer	CH$_3$I-H$_2$O	$\Delta\nu$	Tentative assignments
ν_1 CH$_3$I	**2965**	2976	11	CH$_3$I
		2968	3	dimer HT
		2965	0	monomer / trimer THT
		2961	-4	dimer HT / dimer HH / trimer THT
		2925		
		2868		
		2855		
		2846		
		2825		
		2819		
ν_2 CH$_3$I	1246	1257	12	CH$_3$I-3H$_2$O (1 :3a)
	1245	1256	11	CH$_3$I-3H$_2$O (1 :3a)
		1254	9	see text
		1250	5	CH$_3$I-2H$_2$O (1 :2a)
		1248	3	dimer HT / trimer THT / CH$_3$I-H$_2$O (1:1a)
		1246	1	dimer HT / trimer THT
		1245	0	monomer / dimer HT /
		1243	-2	dimer HH/ trimer THT
		1240	-5	CH$_3$I
ν_6 CH$_3$I		909	27	CH$_3$I-2H$_2$O (1:2a) / CH$_3$I-3H$_2$O (1:3c)
	882	903	21	CH$_3$I-H$_2$O(1 :1a)
	881	899	17	CH$_3$I-2H$_2$O (1:2a) / CH$_3$I-3H$_2$O (1:3a)
		896	14	CH$_3$I-3H$_2$O (1:3a)
		891	11	CH$_3$I-H$_2$O(1 :1a)
		888	6	see text
		886	4	dimer HT / dimer HH / trimer THT / CH$_3$I-3H$_2$O (1:3a)
		882	0	monomer / dimer HH
		881	-1	monomer/ dimer HH
		879	-2	dimer HH

Table 3. 9 Experimental IR band positions for ν_1, and ν_3 (in cm^{-1}) in H$_2$O spectral range for reference spectra of monomer and dimer, mixed CH$_3$I/H$_2$O/Ar = 1/24/1500, recorded at 10 K, for H$_2$O (4:1000) at 4K, calculated spectral shifts ($\Delta\nu$) to experimental spectrum for H$_2$O monomer and tentative assignments. ($\Delta\nu = \nu_{calculated} - \nu_{experimental}$).

H$_2$O monomer and dimer	H$_2$O 4:1000	CH$_3$I-H$_2$O	$\Delta\nu$	Tentative assignments
3776	3777	3777		H$_2$O rovibrational band ν_3
3757	3756	3756		H$_2$O rovibrational band ν_3
		3753		H$_2$O rovibrational band ν_3
		3752	16	see text
		3749	13	see text
3739				H$_2$O rovibrational band ν_3
3738	3738	3738		H$_2$O dimer PA
3736	**3736**	**3736**		H$_2$O ν_3 (nrm)
	3731	3731		H$_2$O rovibrational band ν_3
3725	3721	3721		H$_2$O rovibrational band ν_3
		3720	-16	CH$_3$I-3H$_2$O (1 :3c)
3716	3716	3716		H$_2$O dimer PD
3711	3711	3711		H$_2$O rovibrational band ν_3
		3713	-23	CH$_3$I-H$_2$O (1:1a) / CH$_3$I-3H$_2$O (1:3c)
3708	3708			H$_2$O dimer PD
3670	3670	3670		H$_2$O dimer PD / H$_2$O rovibrational band ν_1
	3662	3662		H$_2$O dimer PD
3654	3654	3654		H$_2$O dimer PD / H$_2$O rovibrational band ν_1
	3648	3648		H$_2$O dimer PD
	3647	3647		H$_2$O dimer PD
		3642	4	see text
	3640	3640		H$_2$O dimer PD
3638	**3638**	**3638**		H$_2$O ν_1 (nrm)
3633	3633	3633		H$_2$O dimer PA
	3630	3630		H$_2$O dimer PD
	3628	3628		H$_2$O dimer PD
3623				H$_2$O rovibrational band ν_1
	3617	3617		H$_2$O dimer PD
	3612	3612		H$_2$O dimer PD
		3609	-29	CH$_3$I-H$_2$O (1 :1a)
3607	3607	3607	-31	H$_2$O rovibrational band ν_1 / see text
		3603	-35	see text
		3582	-56	see text

Table 3. 9 continued

H₂O monomer and dimer	H₂O 4:1000	CH₃I-H₂O	Δν	Tentative assignments
3574	3576	3574		H₂O dimer PD
	3567	3567		H₂O trimer
	3564	3564		H₂O trimer
	3553	3553	-85	CH₃I-2H₂O (1:2a) / CH₃I-3H₂O (1:3c)
	3549	3549		H₂O trimer
	3543	3543		H₂O trimer
	3528	3528		H₂O trimer
	3515	3515		H₂O trimer
		3463	-175	CH₃I-3H₂O (1 :3a)
	3445	3445		H₂O tetramer
	3402	3402		H₂O tetramer
	3392	3392		H₂O tetramer
	3373	3373		H₂O tetramer
	3332	3332		H₂O pentamer
	3325	3325		H₂O pentamer
	3209	3209		H₂O High polymer / 2ν₂ harmonic

It is known that methyl iodide is not soluble in water, as a result, it is water self-aggregation which should be favored. However, considering that mixed aggregates and complexes will be trapped in the same matrix cage, we should be able to observe those latter subject to two conditions: they are formed in gas phase prior to sample deposition, and they survive landing on the sample carrier, or they are formed when they land. Indeed, the injection mode is similar to the quenching of a molecular jet when landing on the sample holder. The kinetic energy of translation must then be dissipated which can lead to the dissociation of these complexes. A third way to form those species is to anneal the samples to allow molecules in close neighborhood (few Å to nm) to diffuse through the argon matrix and aggregate. However, methyl iodide concentration is so low that homo-methyl iodide aggregates, by extension hetero complexes with more than one CH₃I molecule, should be formed in the gas phase and survive landing at sample carrier.

Considering the large excess of water we used, it seems more appropriate to start by methyl iodide vibrational regions (Table 3.8). Indeed, CH₃I concentration remains 1/1000 with respect to Ar, which limits homo-methyl iodide aggregation. Therefore, water addition, if there is aggregation with methyl iodide, will lead to less overlapping bands than in the water zone.

Between 930 and 850 cm^{-1} (Figure 3.13, Table 3.8), for pure methyl iodide (spectrum (a)), one observes bands centered at 886, 882, 881 and 879 cm^{-1}. If 882-881 doublet is assignable to the monomer, the band at 886 cm^{-1} and that at 879 cm^{-1} present a blue-shift of ≈ +4 and a red-shift of ≈ -3 cm^{-1} with respect to the 882 cm^{-1} one (the most intense of the doublet). Those shifts match (CH$_3$I)$_2$ HT (+5), and HH (-2). Even it is more unlikely, the blue-shift could also match with THT and TTH trimers. These bands can also be due to Ar sites, what is certainly the case of 882 - 881 doublet. Considering the weak methyl iodide concentration, if the two bands at 886 and 879 cm^{-1} are due to methyl iodide dimers and trimers, it certainly means that those species were formed in the gas phase prior to deposition; indeed at 1/1000 ratio, there is almost no chance that species accrete after deposition. In the case of mixed methyl iodide-water sample (spectrum (b)), one observes the 886 cm^{-1} increase, while 882 and 881 cm^{-1} decrease in intensity, and new bands at 909, 903, 899 and 891 cm^{-1} (Table 3.8). Those latter are blue-shifted by ≈ + 27, +20, +16 and +9 cm^{-1}, with respect to 882 cm^{-1}. These shifts match totally or partially those of the following hetero-complexes and aggregates ((CH$_3$I)$_m$(H$_2$O)$_n$): 1:1a, 1:2a, the 1:3a, 1:3c ones, the whole series 2:1a to 2:1e and the three 2:2f, 2:2g and 2:2h species.

In the ν_2 (bending CH) region (1270-1230 cm^{-1}), one observes, in the case of pure methyl iodide, bands at 1252, 1248, 1246, 1245, 1243 and 1239 cm^{-1} (Table 3.8). If the 1246-1245 cm^{-1} are assigned to two monomer sites, the others are blue-shifted by ≈ +7 and +3 cm^{-1}, while the two latter are red-shifted by ≈ -2 and -6 cm^{-1}. Those shifts allow us to identify almost unambiguously TTH trimer (at 1252 cm^{-1} and tentatively at 1243 and 1239 cm^{-1}), and more tentatively HT dimer and THT trimer (at 1248 cm^{-1}). However, we cannot discard the presence of HH dimer because this latter one presents almost degenerated bands with monomer (see Tables 3.2 and 3.8). In the case of mixed methyl iodide-water sample (spectrum (b)), one observes the 1248 cm^{-1} increase, while 1246-1245 decrease in intensity, and new bands at 1257, 1256, 1254 and 1250 cm^{-1} (Table 3.8). Those latter are blue-shifted by ≈ + 12, 10, 9 and 5 cm^{-1}, with respect to 1245 cm^{-1}. These shifts match totally or partially those of the following hetero-complexes and aggregates ((CH$_3$I)$_m$(H$_2$O)$_n$): 1:1a, 1:2a and 1:2b, the 1:3a and 1:3b, the whole series 2:1a to 2:1e and the three 2:2c, 2:2d, 2:2f and 2:2g species. Concerning the species 1:3b, we can already discard its presence because we did not observe red-shifts of about +44 cm^{-1} in the ν_6 region.

From the analysis of those first regions, we can conveniently discriminate between the first candidates we have found:

CH$_3$I.H$_2$O complex: 1:1a

CH$_3$I.(H$_2$O)$_2$ complexes: 1:2a, 1:2b

CH$_3$I.(H$_2$O)$_3$ complexes: 1:3a, 1:3c

(CH$_3$I)$_2$.H$_2$O complexes: whole series 2:1a to 2:1e

(CH$_3$I)$_2$(H$_2$O)$_2$ complexes: 2:2c, 2:2d, 2:2f, 2:2g and 2:2h.

Water spectral regions should bring decisive clues in the identification of the different isomers, despite the spectral congestion due to water aggregates.

In the ν_2 region (1770-1510 cm^{-1}), in the case of pure water matrix (Figure 3.14(a)), one observes bands at 1663, 1658, 1637, 1627, 1625, 1620, 1616, 1612, 1611, 1608, 1602, 1599, 1593, 1591, and 1590 cm^{-1}. They are due to water monomer and polymers [13]. In the case of methyl iodide-water mixture (trace (b)), one observes only one new band at 1600 cm^{-1} (not shown), blue-shifted by about $\approx$ +11 cm^{-1} with respect to the nrm (non rotating monomer) water bending mode at 1589 cm^{-1}. It is a "poor" area because of strong overlapping between water aggregates signals and those of methyl iodide-water complexes and aggregates, which should be in minority. As a consequence, the only partial matches found are: 1:3a, which should present theoretically three blue-shifts of $\approx$ +32, +16 and +10 cm^{-1} (the +32 and +10 cm^{-1} bands are certainly overlapped by water aggregates ones), and 2:2a, 2:2e and 2:2j species.

In the ν_1 and water polymers region (3695-3100 cm^{-1}) (Figure 3.14(a) and Table 3.9), one observes bands at 3670, 3662, 3654, 3648, 3647, 3640, 3630, 3628, 3617, 3612, 3574 cm^{-1} (Proton Donor, PD, dimer), 3567, 3564, 3549, 3543, 3528, 3515 cm^{-1} (Trimers), 3445, 3409, 3392, 3373 cm^{-1} (Tetramers), 3332-3325 cm^{-1} (Pentamers), and 3209 cm^{-1} (high polymers and $2\nu_2$ harmonic mode of H$_2$O). The first band of interest in the case of mixed samples, is located at 3463 cm^{-1}, *i.e.* between trimers and tetramers. This band is red-shifted with respect to water trimers and blue-shifted with respect to water tetramers, *i.e.* more red-shifted ("perturbed") than a water trimer but less than a water tetramer. This structure is undoubtedly a water trimer perturbed by a methyl iodide partner. In Figure 3.14, there are only two such structures, 1:3a and 1:3d. Considering that we did not find any evidence of 1:3d presence in the other regions, and that in a large excess of water, this is a cyclic conformation that will be adopted by water, we suggest that this band should be assigned to 1:3a. The second band of interest is the one centered at 3553 cm^{-1}, red-shifted by $\approx$ -85 cm^{-1} with respect to ν_1 nrm mode located at 3638 cm^{-1} [13]. This species is located between water dimer Proton Donor (PD) band and those of water trimers. Following the same reasoning, it is thus a water dimer perturbed by a methyl iodide partner. In Figure 3.9, there is only one structure which matches this water dimer type configuration, this is 1:2a. The mode we observe is the ν_1 stretch of water dimer Proton Acceptor (PA) which bridges to iodine atom. This vibrational

assignment is strongly supported by the theoretical $\Delta\nu \approx -97$ cm^{-1} (Table 3.9), found for this species. However, one has to consider also the presence of 1:3c structure which is a "1:2a +1:1a" kind of structure. This last form presents a theoretical red-shift of ≈ -91 cm^{-1} in this region (and also a blue-shift of $\approx +26$ cm^{-1} in ν_6 (CH$_3$I), as already mentioned above). The other bands observed in case of methyl iodide-water mixture are centered at 3582, 3603, 3607, 3609 and 3642 cm^{-1}. The four first bands display red-shifts of ≈ -56, -35, -31 and -29 cm^{-1} against a blue-shift of $\approx +4$ cm^{-1} for the last one. The only forms which could partially or totally match with those shifts are: 1:1a, 1:3c, the whole series 2:1a to 2:1e, and 2:2i.

In the ν_3 region (3950-3700 cm^{-1}) (Figure 3.14 (a) and Table 3.9)), one observes bands at 3777, 3756, 3753, 3738, 3736, 3731, 3721, 3716, 3711, 3708, 3707, 3703, 3700 and 3695 cm^{-1}. Those bands are mainly due to water monomer and polymers, the non rotating monomer (nmr) and rovibrational transitions [13]. Four new bands are observed in the case of mixed sample, at 3752, 3749, 3720 and 3713 cm^{-1}. If the two highest ones are tentatively assigned to $0_{00} \rightarrow 1_{01}$ water monomer rovibronic transition perturbed by methyl iodide proximity, the two lowest ones present red-shift with respect to ν_3 nrm mode of water monomer, located at 3736 cm^{-1} [13] of ≈ -23 and -16 cm^{-1}. Species which present possible matching with those red-shifts are: 1:1a, 1:2b, the whole (1-3) series, 2:1b, 2:1c and 2:1e, 2:2c, 2:2f and 2:2i (2-2) (Tables 3.3-3.7). From the analysis of the three water regions we can conveniently discriminate between the candidates we have found:

CH$_3$I.H$_2$O complex: 1:1a

CH$_3$I.(H$_2$O)$_2$ complexes: 1:2a, 1:2b

CH$_3$I.(H$_2$O)$_3$ complexes: 1:3a, 1:3b, 1:3c, 1:3d

(CH$_3$I)$_2$.H$_2$O complexes: whole series 2:1a to 2:1e

(CH$_3$I)$_2$(H$_2$O)$_2$ complexes: 2:2a, 2:2c, 2:2e, 2:2f, 2:2i and 2:2j.

In summary, comparing the candidates identified from CH$_3$I and H$_2$O regions, we can almost confidently state that we have identified 1:1a, 1:2a and 1:3a, 1:3c species (see Figure 3.6, 3.13 and 3.14), together with CH$_3$I dimers and trimers. Concerning the rest of the possible candidates, either they partially match the observed shifts with no decisive evidence of their presence, or CH$_3$I being the minority product, 2:1 and 2:2 species are hard to see (with some exceptions as 2:2i isomer, which is the only form among all those calculated which present a blue-shift in the ν_1 water region, or 2:1a, 2:1b and 2:1c which could be responsible for the band at 3582 cm^{-1}, while that observed at 3603 cm^{-1} could be assigned to 2:1d and 2:1e species. Finally, in Tables 3.8 and 3.9, we only gathered the 1:1, 1:2 and 1:3 species (with 1, 2 or 3 water molecules, respectively) because they are the only ones for which we have

identified confidently vibrational bands. It may be noted that they present common bands, this is due to their close structures (see theoretical part). It does not mean that the other species (i.e. 2:1 and 2:2) are not present. On the contrary, given the nature of the injected mixtures, and the fact that methyl iodide polymerizes even at low concentrations, there are several vibrational indices of their presence as detailed above.

3.2.3 Preliminary results on the interaction of CH₃I with amorphous ice

Amorphous ice (so called Amorphous Solid Water: ASW) was first produced in laboratory in 1935 [14] and has since been extensively characterized. ASW bulk structure is a four-coordinated tetrahedral arrangement, much like crystalline water ices (see [15-17]) and reference herein). Molecules at the surface present potentially four orientations: a four-coordinated molecule bound in a distorted tetrahedron structure, referred as s4; a tri-coordinated molecule with one lone electron pair exposed at the surface, dO; a tri-coordinated molecule with one OH dangling at the surface, dH; and a bi-coordinated molecule with one lone pair and one OH dangling at the surface, dH (see Figure. 3.15). These surface modes exhibit vibrational frequencies at 3503, 3549, 3698, and 3720 cm^{-1}, respectively, as outlined previously [15-17].
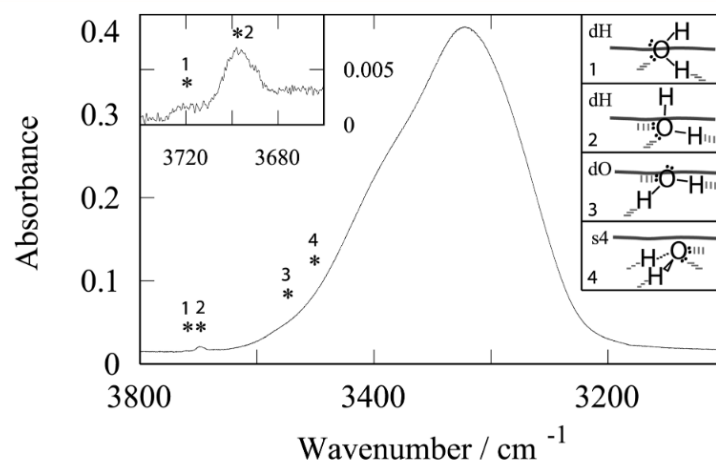
Figure 3. 15 The four surface modes of amorphous ice, dH (3720 and 3698cm^{-1}), dO (3549 cm^{-1}), and s4 (3503 cm^{-1}) [15].

In agreement with previous studies [15-17] and in comparison to Figure 3.16, ASW grown in PIIM laboratory was purely amorphous. Position of the bulk OH stretching and the characteristic dangling modes at 3720 and 3698 cm^{-1} match those of ASW (see Figure 3.16(a)), spectra in black).

After formation of ASW, we carried out a series of CH$_3$I/Ar: 1/1000 injections (3 mbar in 500 ms each time) at 44 K and then cooled to 4 K. The IR spectra in the OH dangling (Figure 3.16(a)) and CH$_3$ deformation regions (Figure 3.16(b)) of the two successive depositions of CH$_3$I on ASW at 4K are marked in red and green in Figure 3.16.
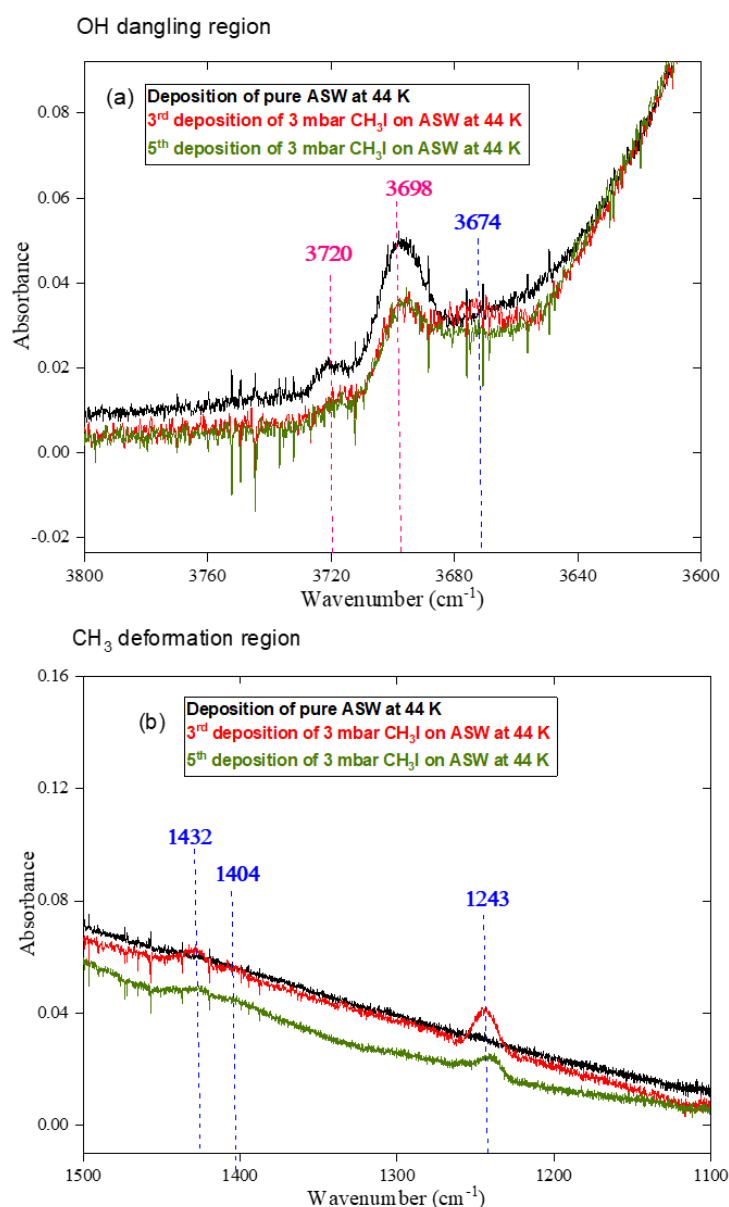
Figure 3. 16 The observed IR spectra in (a) the OH dangling region and (b) the CH$_3$ deformation region. Pure amorphous ice is in black and the successive 3 mbar depositions of CH$_3$I/Ar on pure amorphous ice are in red and green. The OH dangling modes are marked by pink dashed lines. CH$_3$I tentatively assigned bands are marked by blue dashed lines.

The CH$_3$I interaction with ASW can be firstly interpreted based on dangling bonds (dH) of ASW. Any perturbation of the dH bands at 3720 and 3698 cm^{-1} (marked in pink dotted line in Figure 3.16 (a)) or formation of new bands can give insights on the adsorption of CH$_3$I. An observation of a band at 3674 cm^{-1} (marked in blue dotted line in Figure 3.16(a)) shows that

CH$_3$I was adsorbed on the surface of ASW. However, a repetition of CH$_3$I deposition on ASW (spectra marked in green, Figure 3.16(a)) did not indicate any further adsorption of CH$_3$I. On the other hand, one observe new bands at 1432, 1404 and 1243 cm^{-1}, respectively (marked in blue dotted line in Figure 3.16(b)) in all deposition experiments (spectra marked in red and green). However, these observations are only preliminary and more repetition are needed to well interpret these promising results.

Further, we noticed a complete desorption by annealing to 47 K (spectra in dark yellow in Figure 3.17). This preliminary result which indicates a desorbing capability of CH$_3$I above 47 K (complete desorption).
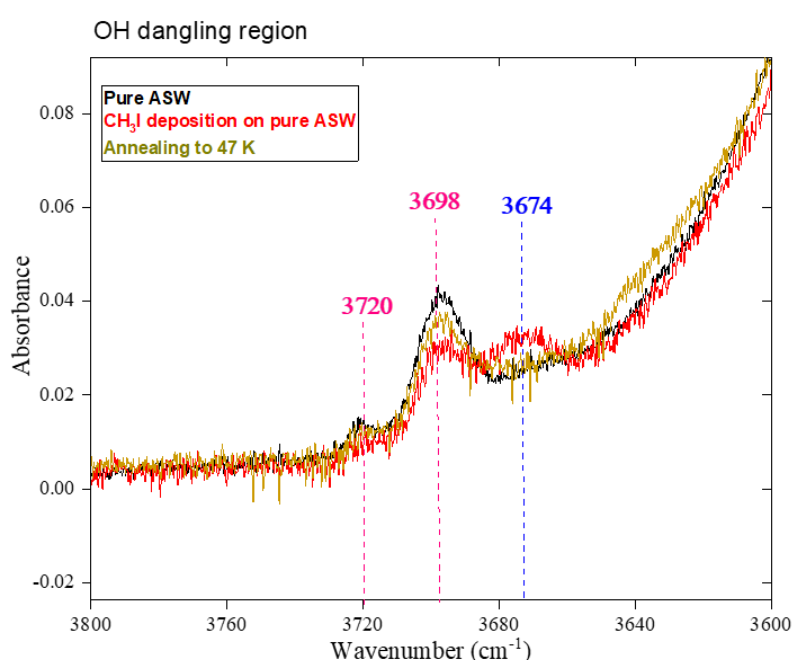
Figure 3. 17 The observed IR spectra in the zone of the OH dangling of amorphous ice for the experiment of desorption of CH$_3$I from pure amorphous ice after CH$_3$I deposition and then annealing up to 47 K. All spectra were recorded at 4K.

It was reported previously [18-20] that the adsorption, diffusion, and desorption of CH$_3$I on ice in the range of 90-100 K depend largely on the morphology of the ice substrate. Where porous ice enhances the trapping of adsorbed CH$_3$I, whereas pore-free ice likely allows monomer adsorption and the formation of CH$_3$I clusters. Moreover, full desorption was observed when adsorbed CH$_3$I molecules on ASW ice by increasing temperature between 100-220 K. These observations were based on monitoring the desorbed species after the adsorption of CH$_3$I on ASW by temperature programmed desorption (TPD) experiment "Indirect measurement of adsorbed CH$_3$I". What is new and interesting with our cryogenic experiments that in the future we will be able to directly investigate well (1) how the ASW

structure is affected (reorganization of ASW surface) when CH_3I is adsorbed on it and (2) how CH_3I is bonded/adsorbed to the surface of ASW.

3.3 Conclusion and perspectives

We have investigated the interaction between CH_3I and water molecules using argon cryogenic matrix experiments. The experimental data were supported by theoretical DFT calculations. The experiments were conducted with a large excess of H_2O molecules compared to CH_3I in order to mimic CH_3I environment in the atmosphere. Cryogenic matrices seem pretty accurate in order to describe inter molecular interactions between atmospherically relevant molecules. Even if working at low temperature and pressure does not mimic atmospheric conditions it brings insights at molecular level. However, working in these conditions allows the study of the ground energy potential of those atmospheric complexes and aggregates. Finally, considering the concentration of methyl iodide used in our experiments, the aggregates are rather formed in the gas phase and not in the matrix cage. Dimers and trimers of CH_3I are observed despite the high water amount in the initial mixture that may be explained by the low affinity of CH_3I with water. The other complexes such as 2:1 and 2:2 cannot be completely excluded but appear as minor species. The inter molecular behavior between CH_3 and H_2O molecules determined for the first time experimentally and supported by DFT calculation highlights that, in the atmosphere, gaseous methyl iodide and water will likely form aggregates of water and methyl iodide polymers instead of $(CH_3I)_m$-$(H_2O)_n$ complexes. This result is consistent with previous theoretical studies, which have predicted the incomplete hydration of CH_3I. Our results have important consequences for the understanding the alkyl halide solvation in primary processes and thus, Cloud Condensation Nuclei (CCN) formation from gaseous phases in the atmosphere and contribute to the understanding of reactive halogen species in tropospheric chemistry. Finally, in the context of the NNP's severe accident, our work is contributing to better understand the fate of nuclear species in the atmosphere and thus, the radionuclide dispersion. In the future, the photochemical behavior of such CH_3I-water aggregates will be investigated as CH_3I is known to be sensitive to the solar radiation.

Further, in this work we have provided a preliminary result on the interaction between CH_3I and amorphous ice. The ensemble of our results shows that surface modes, in particular the dH dangling bonds, can be perturbed upon adsorption of CH_3I. In the future, more experiments will be carried out to improve this first set of experimental results:

(1) How is CH_3I adsorbed on pure amorphous ice surface? is there any $CH_3I…H_2O$ bonding or complex formation? is there any CH_3I polymer formation?

(2) Is it possible to desorb CH₃I using only the kinetic energy of a gas stream?

(3) Is it possible to desorb CH₃I by selectively irradiating dH?

(4) What about photochemical behavior of CH₃I-amorphous ice?

References

[1] S. Seng, Thèse de doctorat : Phototransformation de composés d'intérêt atmosphérique. Etudes spectroscopiques en phase gaz, en matrice cryogénique et à l'échelle des particules individuelles, Université de Lille 2017.

[2] N.E. Lopez, Thèse de doctorat : Etude du transfert de protons dans les systemes moleculaires, Université de Aix-Marseille, (2017).

[3] M.J. Frisch, G. Trucks, H.B. Schlegel, G.E. Scuseria, M.A. Robb, J. Cheeseman, G. Scalmani, V. Barone, B. Mennucci, G.A. Petersson, H. Nakatsuji, M. Caricato, X. Li, H.P. Hratchian, A.F. Izmaylov, J. Bloino, G. Zheng, J. Sonnenberg, M. Hada, D. Fox, Gaussian, E., Gaussian 09 Revision A.1. Gaussian Inc, Gaussian 09 Revis. D.01. Gaussian Inc., Wallingford, CT. (2009).

[4] J. Da Chai, M. Head-Gordon, Long-range corrected hybrid density functionals with damped atom-atom dispersion corrections, Phys. Chem. Chem. Phys. 10 (2008) 6615–6620. https://doi.org/10.1039/b810189b.

[5] K.A. Peterson, B.C. Shepler, D. Figgen, H. Stoll, On the spectroscopic and thermochemical properties of ClO, BrO, IO, and their anions, J. Phys. Chem. A. 110 (2006) 13877–13883. https://doi.org/10.1021/jp065887l.

[6] A. Villard, S. Khanniche, C. Fortin, L. Cantrel, I. Černušák, F. Louis, A theoretical study of the microhydration processes of iodine nitrogen oxides, Int. J. Quantum Chem. 119 (2019) 1–11. https://doi.org/10.1002/qua.25792.

[7] K.K. Irikura, THERMO.PL, National Institute of Standards and Technology, Gaithersburg, MD, USA 2000. Natl. Inst. Stand. Technol. (2002).

[8] D. Khiri, R. Vandeputte, S. Taamalli, L. Cantrel, F. Louis, Microhydration of caesium metaborate: structural and thermochemical properties of CsBO₂ + n H₂O (n = 1–4) aggregates, J. Mol. Model. 25 (2019) 1–8. https://doi.org/10.1007/s00894-019-4094-4.

[9] F. Ito, T. Nakanaga, Y. Futami, S. Kudoh, M. Takayanagi, M. Nakata, Isomeric structures of CH₃I dimers in a supersonic jet studied by matrix-isolation infrared spectroscopy and ab initio calculation, Chem. Phys. Lett. 343 (2001) 185–191. https://doi.org/10.1016/S0009-2614(01)00688-1.

[10] F. Ito, T. Nakanaga, Y. Futami, M. Nakata, Observation of methyl iodide clusters in gas phase by infrared cavity ring-down spectroscopy, Chem. Phys. 286 (2003) 337–345. https://doi.org/10.1016/S0301-0104(02)00919-9.

[11] F. Ito, Infrared studies of the CH3I-H2O complex and large CH3I clusters in Ar matrices, J. Mol. Struct. 1035 (2013) 54–60. https://doi.org/10.1016/j.molstruc.2012.09.027.

[12] A.J. Barnes, M.L. Evans, H.E. Hallam, Infrared cryogenic studies, J. Mol. Struct. 69 (1973) 738–749. https://doi.org/10.1016/0022-2860(83)90026-1.

[13] J.P. Perchard, Anharmonicity and hydrogen bonding. III. Analysis of the near infrared spectrum of water trapped in argon matrix, Chem. Phys. 273 (2001) 217–213. https://doi.org/10.1016/S0301-0104(01)00496-7.

[14] E.F. Burton, W.F. Oliver, The crystal structure of ice at low temperatures, Proc. R. Soc. London. Ser. A - Math. Phys. Sci. 153 (1935) 166–172. https://doi.org/10.1098/rspa.1935.0229.

[15] J.A. Noble, C. Martin, H.J. Fraser, P. Roubin, S. Coussan, Unveiling the surface structure of amorphous solid water via selective infrared irradiation of OH stretching modes, J. Phys. Chem. Lett. 5 (2014) 826–829. https://doi.org/10.1021/jz5000066.

[16] J.A. Noble, C. Martin, H.J. Fraser, P. Roubin, S. Coussan, IR selective irradiations of amorphous solid water dangling modes: Irradiation vs annealing effects, J. Phys. Chem. C. 118 (2014) 20488–20495. https://doi.org/10.1021/jp506943k.

[17] S. Coussan, P. Roubin, J.P. Perchard, Infrared induced isomerizations of water polymers trapped in nitrogen matrix, Chem. Phys. 324 (2006) 527–540. https://doi.org/10.1016/j.chemphys.2005.11.017.

[18] A.J. Desimone, B.O. Olanrewaju, G.A. Grieves, T.M. Orlando, Photodissociation of methyl iodide adsorbed on low-temperature amorphous ice surfaces, Chem. Phys. 138 (2013) 0847031-0847039. https://doi.org/10.1063/1.4790585.

[19] Y. Sohn, J.M. White, Thermal and photochemistry of methyl iodide on ice film grown on Cu(111), Bull. Korean Chem. Soc. 30 (2009) 1470–1474. https://doi.org/10.5012/bkcs.2009.30.7.1470.

[20] E.R. Miller, G.D. Muirhead, E.T. Jensen, Mechanisms for the near-UV photodissociation of CH_3I on D_2O/Cu(110), J. Chem. Phys. 138 (2013) 0847021-08470210. https://doi.org/10.1063/1.477 0225.

Chapter 4: DRIFTS experiments

Chapter 4 focuses on the study of interactions between NaCl solid particles, as model for the atmospheric sea salt aerosols, and gaseous CH$_3$I under controlled conditions.

The experiments were conducted using Diffuse Reflectance Infrared Fourier Transform Spectroscopy (DRIFTS). For our application, this technique will be powerful for following in real time the reactions of alkali halides as NaCl, which are transparent in the infrared, since the formation of infrared absorbing intermediates and products, can be detected with ease. Following the chemical composition evolution of the solid can give quantitative insights on the gaseous molecules taken up by (i.e. spectro kinetics measurements) if coupled with other analytical techniques such as inductively coupled plasma mass spectrometry (ICP-MS).

First, a special attention is devoted to the detailed description of the experimental setup and experimental conditions. In a second step, the spectral characterization of NaCl solid particles surface during CH$_3$I exposure experiments is described. Next, the kinetics and energetics interpretations of the CH$_3$I interaction with NaCl are determined. In particular, we insisted on the interpretation of adsorption/desorption evolution and calculation of the uptake coefficient and global adsorption to exploit the interaction between CH$_3$I and NaCl. Finally, the conclusion and perspectives are given.

4.1. Material and Methods

4.1.1 Reagents

Methyl iodide 1000 ppm (0.1% CH$_3$I, 99.9% Ar) and Argon (99.99% pure) gas bottles were provided from commercial cylinders Air product and Air liquid, respectively. The gases were used without any further purification. Distilled water and Argon (99.99% pure) gas bottles were used to prepare wet Argon as mixture to provide humidity varying between < 10% to 80% inside the DRIFTS cell.

Commercial sodium chloride (NaCl, 99.99%, ALFA AESAR), potassium bromide (KBr, 99+%, SIGMA ALDRICH) and sodium iodide (NaI, 99+%, ACROS) were used as powder for experiments.

Prior to DRIFTS experiments, NaCl was preheated for a minimum of 4 hours at 873 K to remove species adsorbed on the powder surface. NaCl salt is highly hygroscopic, so it has to be kept in a dry and heated environment (oven at 383 K). Same treatment was performed for KBr and NaI powders. The solid samples (145 mg) were manually grinded using an agate mortar and pestle. The granulometry of NaCl powder was estimated in the range of 300 µm -less than 50 µm by sieving on grids ranging between 300 µm and 50 µm. Figure 4.1 shows that the particles with size comprised between 300 and 100 µm, 100 and 60 µm, 60 and 50 µm, and less than 50 µm account for 32%, 26%, 39% and 3% in mass, respectively. The specific surface area measurement of 1g of grinded NaCl was carried out by using Brunauer-Emmett-Teller method "BET" (Nitrogen sorption Micromeritics ASAP 2010 analyzer). The BET surface area of NaCl was found to be low (0.26 m².g^{-1}). This value is close to the BET surface area of NaCl powder mentioned in [1]. The NaCl BET surface area indicates that NaCl surface is non porous and that the available surface area is very low for colliding with trace gas phase species.
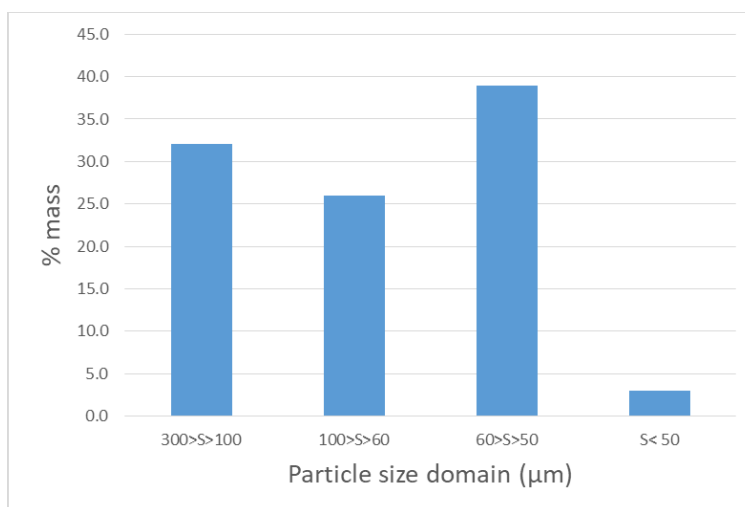
Figure 4. 1 Particle size distribution of the manually grinded NaCl particles by sieving on grids ranging between 300 µm and 50 µm.

4.1.2 DRIFTS Experimental setup

4.1.2.1 DRIFTS Cell and gas supply

Any infrared radiation when in interaction with a solid can, depending on the characteristics of the material, be transmitted, absorbed, externally reflected (specular reflection), internally reflected, or diffused in all directions (see annex 2). The latter effect is of interest in Diffuse Reflectance Infrared Fourier Transform Spectroscopy (DRIFTS). With respect to the conventional transmission FTIR method, DRIFTS is a fast and non-destructive technique.

The continuous, *in situ*, monitoring of NaCl salt was performed in a DRIFTS cell (Harrick, Praying Mantis™ High Temperature Reaction Chambers, 24V, (HVC-DRP-4) with an interior volume of 15.78 ml equipped with Zinc selenide (ZnSe) windows, that was housed by the FTIR-spectrometer (Nicolet 6700 - Thermo Optek). DRIFTS cell wall is composed of black Delrin (116-989), which exhibits low moisture absorption and it is chemically resistant to hydrocarbons, solvents and neutral chemicals. The grinded solid was placed in a crucible of 6.3 mm diameter and 3.175 mm height inside the DRIFTS cell.

The DRIFTS cell was connected to a temperature controller (watlow - Harick) to be able to monitor or adjust the temperature during the experiment from 296 to 623 K. A cooling (water/water) circulation system was connected to the DRIFTS cell to limit temperature fluctuation in case of high temperature. The temperature inside the chamber was recorded using a k-type thermocouple placed on the back of the sample holder.

A scheme of the DRIFTS experimental is shown in Figure 4.2.
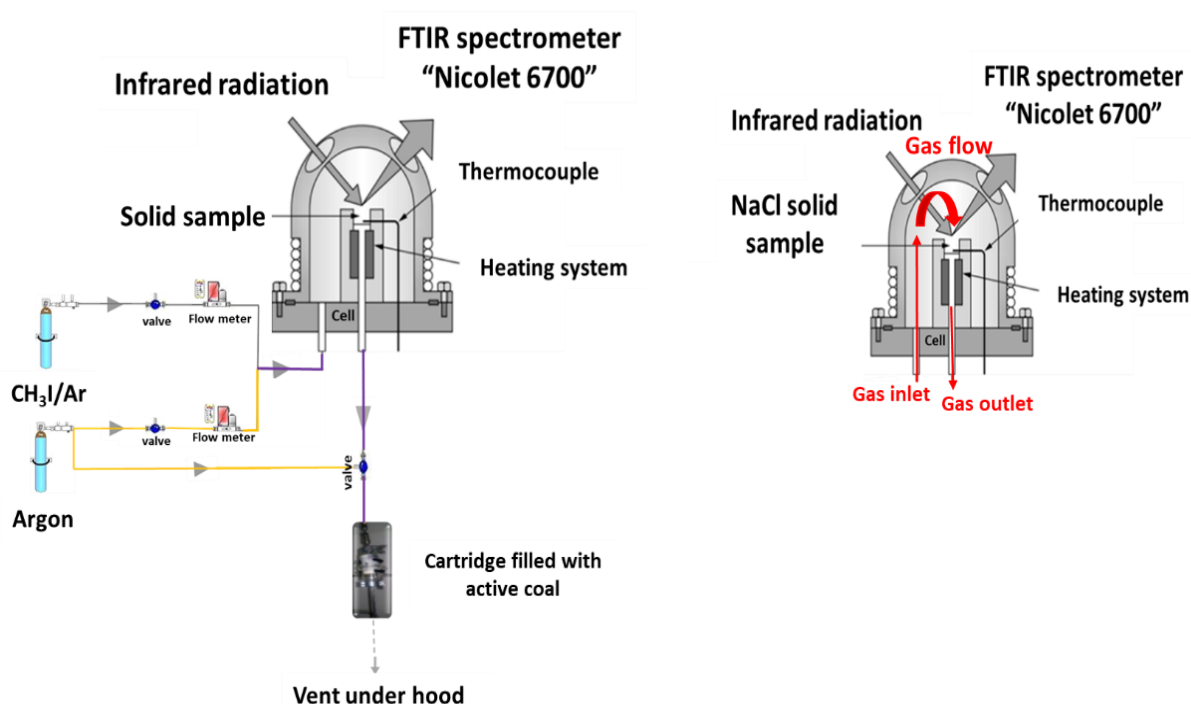
Figure 4. 2 Scheme of DRIFTS experimental setup under dry conditions.

164

The DRIFTS cell was connected to gas supplying lines allowing gas feed into the dome. The gas is passing through the powder sample as shown in Figure 4.2. The flow direction from the bottom to the top of the DRIFTS cell offers the advantage of thermostatically controlling the gases and tracking the surface reactions at the desired temperature. The gas flow was fitted with valves and flow meters type Bronkhorst (F-201CV) to control the flow entering the cell. The total flow rate inside the cell was prepared by controlled mixing of flows from two different lines both allowing a gas feed in the range of 2-108 mL.min^{-1} at 273 K and 1 Bar, carrying each:

- Dry Argon (line in yellow in Figure 4.2);
- Dry CH_3I (line in grey in Figure 4.2).

The exit line was mixed with argon and then connected to a cartridge filled with active coal for CH_3I filtering before exhaust (see Figure 4.2). A suction extractor was placed on top of the chamber to ventilate the released gases in case of leakage. Figure 4.3, shows the DRIFTS experimental setup with all the connections from the gas bottles to the DRIFTS chamber and then to the exit under the hood.
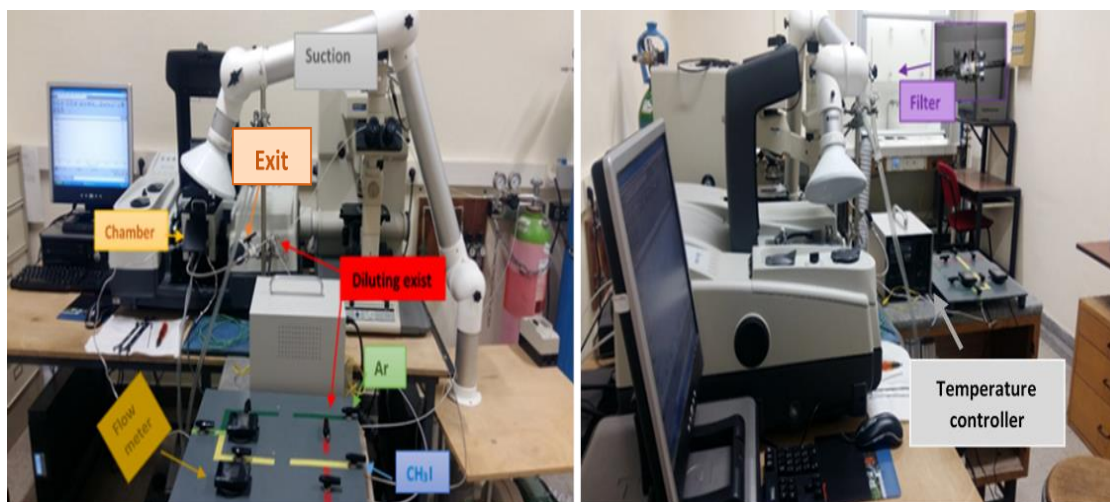
Figure 4. 3 DRIFTS experimental setup from GSM-ISM.

The relative humidity inside the DRIFTS cell was regulated by mixing dry argon with humid Ar after bubbling Ar through glass grits in pure water as shown in Figure 4.4. A relative humidity sensor (SHT75 Sensirion, precision RH= 10-80% ± 10%) was placed at the exit of the mixing line. Humidity control was possible by changing the ratio of dry/saturated Ar flows whilst keeping the total gas flow constant. It should be highlighted that experiments using wet CH_3I cannot be performed due to the fact that H_2O may damage the ZnSe DRIFTS windows.
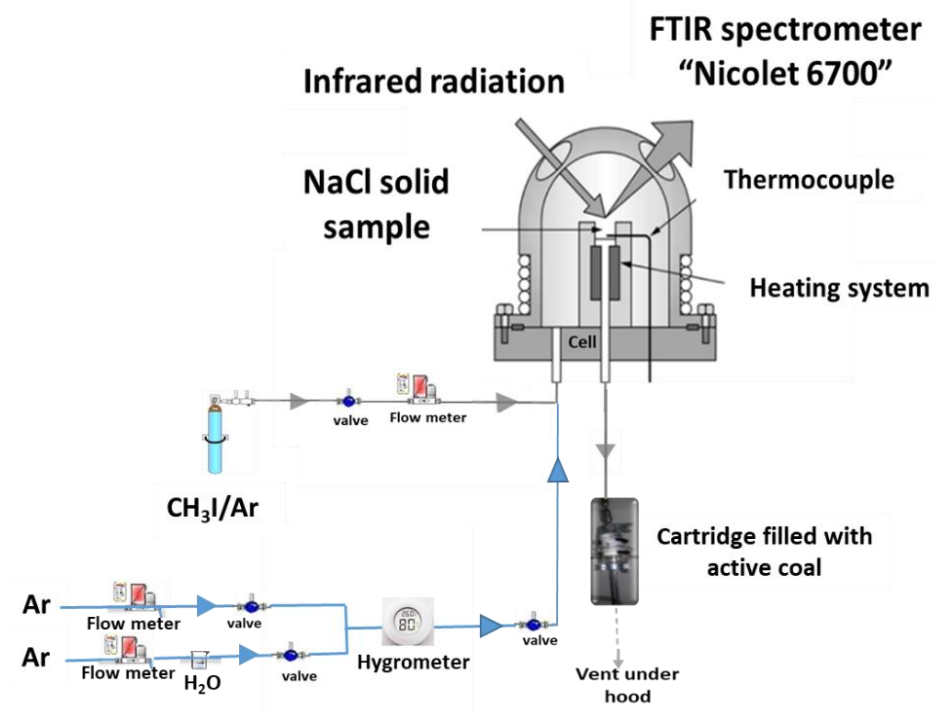
Figure 4. 4 Scheme of DRIFTS experimental setup under humid conditions.

A second set of experiments was performed with the objective to determine quantitatively the amount of CH_3I taken by the solid at the end of the experiment. Such determination is possible by ICP-MS technique after dissolution of the solid in alkaline media (see section 4.1.3). This second set of experiments was conducted without online IR monitoring but under the same conditions as the set of experiments performed initially with IR monitoring.

4.1.2.2 Experimental protocol

Prior to each experiment, we checked that there is no leak from all the system by flowing Ar at 108 mL.min^{-1} forthwith by using a gas leak detector (Jelt, Detect Fuites) and measuring the flow at the outlet.

Background spectrum is usually collected by DRIFTS using IR transparent potassium bromide (KBr) solid. However, in our experiments the background was recorded using preheated NaCl (99.99%) powdered solid.

145 mg of NaCl powder was placed inside the DRIFTS cell at 296 K. Then the chamber was purged with Argon for 10 minutes to ensure the complete removal of H_2O and other pre-adsorbed species. After, NaCl at 296 K was taken as the background spectra under Ar flow 108mL.min^{-1}. It

166

should be noted that the background was verified at the beginning of each experiment with the same procedure. Then, the NaCl salt was exposed continuously to CH_3I with a constant flow rate and spectrum were acquired every 8 minutes till 5 hours of exposure. Both NaCl background and NaCl exposed to CH_3I spectra were recorded under the same spectral conditions.

It should be noted that no major evolution of the spectral region of interest was observed in the spectra recorded after 112 minutes under Ar flow (blank experiment), so that any spectral evolution observed during NaCl exposition to methyl iodide can be owed to CH_3I-NaCl surface interaction.

4.1.2.3 Spectral acquisition using DRIFTS

In DRIFTS system (NICOLET 6700) the scattered IR energy on the surface is collected by a spherical mirror that is focused on to the high sensitivity deuterated triglycine sulfate (DTGS) detector with KBr beam splitter. All infrared spectra were recorded as a function of time in the spectral range from 4000 to 600 cm^{-1} at resolution 8 cm^{-1}. 200 scans were accumulated for each spectrum featuring an overall acquisition duration of 8 minutes. Acquisition of experimental spectra and background spectra were carried out using Omnic software in the same conditions. The background subtraction was achieved by the Omnic software for each spectrum. The baseline was corrected by linear interpolation model using Omnic software. It is highlighted that the C-I stretching mode at 572 cm^{-1} cannot be detected by DRIFTS spectra because ZnSe window cuts the spectrum in the range below 600 cm^{-1}.

4.1.2.4 Spectral data processing for quantification

Regarding the theoretical standpoint of DRIFTS [3] , there is no linear relation between band intensity and concentration so that the Lambert-Beer law, is not applicable for DRIFTS experiments. However, similar expressions were developed: the Kubelka-Munk (K-M) or pseudo absorbance functions corrections as shown in Table 4.1. Complementary informations are displayed in annex 2.

Table 4. 1 Comparison of Kubelka-Munk and Pseudo absorbance theories, which can be adapted for diffuse reflectance [3].

Kubelka-Munk	Pseudo absorbance
For highly absorbing adsorbates	**Poorly absorbing adsorbates**
$$f(R_\infty) = \frac{(1-R_\infty)^2}{2R_\infty} = \frac{K}{s} = \frac{2.303 \cdot \varepsilon(\nu) \cdot C}{s}$$	$$\log(1/R_\infty) = \frac{C}{Constant}$$
R_∞: Diffuse reflected signal K: Absorption coefficient S: Scattering coefficient E: Extinction coefficient C: Concentration	

We have choosen pseudo absorbance to treat our spectral data as we expect to be in the case of poorly absorbing adsorbates (see annex 2) regarding the literature [3]. The quantification was based on the integration of a band intensity within limits defined in a fix spectral range using Fityk software with Levenberg-Marquardt mathematical model [4]. Since one IR bands may results of several overlapped bands, when it was appropriated, a band decomposition was performed by Gaussian function [4] multiple band fit using FityK software.

The band area uncertainty was estimated by the repeat of the three experiments performed under the same conditions (see annex 3). Absolute uncertainty of the band area in the 1400-1000 cm^{-1} was found between ~ 0.03 to 0.37 at 95% confidence level.

4.1.3. Inductively coupled plasma mass spectrometer measurements

The combination between DRIFTS and inductively coupled plasma mass spectrometer (ICP-MS, see annex 4) analysis allowed to quantify the adsorbed gaseous phase. The total concentration of CH_3I taken up by NaCl was determined via ICP-MS measurements (see annex 7) performed after the DRIFTS experiment.

The solid samples were analyzed by ICP-MS (810 MS VARIAN) which is a sensitive technique for the determination of iodine concentration. A detection and quantification limits of 3 $\mu g.L^{-1}$ and 5 $\mu g.L^{-1}$, respectively for iodine were determined previously [5]. The uncertainty of measurement was found to be ± 8% at 95% confidence level [5]– including sample preparation and ICP-MS analysis (see also annex 6). This technique is nevertheless destructive as it requires dissolution of the analyte (the solid sample) in aqueous media.

The NaCl powder samples exposed to CH_3I were prepared as following, instantly after DRIFTS experiment, to avoid ageing process. 100 mg of NaCl samples were dissolved by 10 mL of NaOH (0.1 mol.L^{-1}). The dissolved samples were then diluted in NaOH (0.1 mol.L^{-1}) by a factor of 5, 10 and 20 before ICP-MS analysis.

Then it will be possible to translate the band area of IR bands attributed to methyl iodide adsorption/absorption to the total amount of iodine taken by the solid by a conversion factor [6, 7] that is described later in section 4.3.4.1. Here, it should be highlighted that determination of conversion factor will be based on the hypothesis that CH_3 deformation modes attributed to adsorbed CH_3I represent the total concentration of CH_3I taken up by NaCl.

4.1.4. Experiment grid for DRIFTS experiments and validation
In this work, three types of experimental conditions were explored for exposing NaCl to CH_3I: (1) dry flow of CH_3I, (2) NaCl exposed to humidity varying between 20 and 80 % (at T= 296 K) and then to dry CH_3I, and (3) NaCl exposed to dry CH_3I at temperature comprised between 296 and 423 K. For all experiments, the solid phase evolution was time followed by recording an FTIR spectrum every 8 minutes (200 scans/spectrum). All these experiments were performed under ambient pressure (P=1 atm). A protocol of three phases (CH_3I exposure phase, static condition phase and continuous Ar flow phase) was followed for each experimental condition.

4.1.4.1 Dry Condition
As a first step, a study of the interaction of CH_3I with dry NaCl was carried out at 296 K, 1 atm and estimated RH = 20% conditions. The total flow rate inside the cell was prepared by flowing dry CH_3I at 108 mL.min^{-1}.

The experiments have distinguished three separate phases (1) continuous exposure to CH_3I flow, (2) stopping CH_3I delivery with closed cell as "static condition" and (3) continuous flow of Ar which are described below and summarized in the Table 4.2:

"CH₃I Exposure" phase (1): NaCl salt samples were exposed to continuous flow of CH_3I (1000 ppm) with 108 mL.min^{-1} flow rate corresponding to contact time (T_c) of 55ms in the NaCl solid bed. The contact time (T_c) is defined as the average time that a gas species is put in contact with solid particles. The contact time (T_c) in our DRIFTS configuration is dependent on the solid bed

volume, particles size, packing of particles, surface area and gas flow rate. Herein, we firstly estimated the contact time in the solid bed by the following equation:

$$T_c = \frac{\text{Solid bed volume}}{\text{Total gas flow}} \qquad [\text{E4-1}]$$

The exposure time was for 5 hours as a maximum. The main purpose of the long exposure time is that it can represent more appropriately the presence of CH_3I in the atmosphere due to its long half-life time (~5 days) [8].

"Static condition" phase (2): The flow of CH_3I was stopped i.e. maintaining the system under static conditions. It should be highlighted that two types of static conditions can be maintained either by closing or opening the exit valve. In both cases, the results were the same with a low difference of about 8% (annex 3).

"Continuous Ar flow" phase (3): After static condition, argon was continuously flowed up for 1 hour.

Steps (2) and (3) were performed to check the spontaneous and induced desorption of CH_3I, respectively.

Five scenarii were investigated for exposing dry NaCl to "dry" CH_3I: (i) The capability of CH_3I to be sorbed on NaCl surface (ii) capability of CH_3I to desorb, (iii) the influence of the temperature on the desorption of CH_3I, (iv) the influence of the initial CH_3I gas concentration and (v) variation of the estimated contact time in the solid bed [E4-1]. All these experiments were performed under ambient conditions (RH=20%, P=1 atm and T=296 K) with the same conditions for spectral acquisition.

(i) The capability of CH_3I to be sorbed: was investigated by following the CH_3I on the surface of NaCl over time (Table 4.2).

Experiment with dry NaCl						
Phase 1				Phase 2	Phase 3	Repetition
$[CH_3I]_g$ in ppm	Contact time (Tc) in ms	CH_3I/Ar flow in mL.min^{-1}	CH_3I exposure duration	Static duration	Continuous Ar flow (108 mL.min^{-1}) duration	
1000	55	108/0	5 hours	1 hour	1 hour	3

(ii) The capability of CH₃I to desorb: was conducted by the continuous flow of CH₃I (1000 ppm, 108 mL.min^{-1}) for only two hours on dry NaCl salt (RH= 20% at 296 K) to limit methyl iodide adsorption. Then the static condition and pure argon continuous flow duration were strongly increased to evidence (if any) either spontaneous desorption or induced desorption. In this view, the static conditions were maintained for 24 hours and the phase with pure argon lasted 8 hours. The experimental conditions are listed in Table 4.3.

Table 4. 3 Experimental conditions for CH₃I exposure, static and continuous Ar flow phases of dry experiment with NaCl – scenario (ii).

Experiment with shorter CH₃I exposure time						
Phase 1				Phase 2	Phase 3	
$[CH_3I]_g$ in ppm	Contact time (Tc) in ms	CH_3I/Ar flow in mL.min^{-1}	CH_3I exposure duration	Static duration	Continuous Ar flow (108 mL.min^{-1}) duration	Repetition
1000	55	108/0	2 hours	23 hours	8 hours	1

(iii) Influence of temperature on the CH₃I desorption: As a matter of fact, the reverse process of adsorption can be thermally activated (desorption), that is why one experiment of heating NaCl until 623 K was performed with increasing the temperature during continuous Ar flow (in phase 3). NaCl (RH=20%, at 296 K) was exposed to continuous exposure of CH₃I (108 mL.min^{-1}, 1000 ppm) for 1 hour. After 1 hour of CH₃I continuous flow, the system was maintained under static conditions for 4 hours. After, NaCl was exposed to continuous Ar flow for 1 hour at 296 K. Then after, the temperature was gradually increased from room temperature (296 K) to 373, 473 and finally 623 K with a rate of 3 K.min^{-1} under continuous Ar flow. After reaching each desired

temperature we waited 15 minutes before increasing to the next one. The experimental conditions are listed in Table 4.4.

Table 4. 4 Experimental conditions for CH₃I exposure, static and continuous Ar flow phases of dry experiment with NaCl – scenario (iii).

Influence of temperature				
Phase 1				Phase 2
$[CH_3I]_g$ in ppm	Contact time (T_c) in ms	CH_3I/Ar flow in $mL.min^{-1}$	CH_3I exposure duration	Static duration
1000	55	108/0	**1 hour**	**4 hours**
Phase 3				
Continuous Ar flow (108 $mL.min^{-1}$) duration				
at 296 K	**at 373 K**	**at 473 K**	**at 623 K**	
1 hour	15 minutes	15 minutes	15 minutes	

(iv) Influence of the CH₃I concentration: To investigate the influence of gas phase concentration on the sorption process, dry NaCl (RH= 20% at 296 K) was exposed to a continuous flow of CH_3I of 500 and 200 ppm maintained at 108 $mL.min^{-1}$ for 5 hours. No static or Ar flow phases were applied in this scenario. The experimental conditions are listed in Table 4.5.

Table 4. 5 Experimental conditions for CH₃I exposure, static and continuous Ar flow phases of dry experiment with NaCl – scenario (iv).

Influence of the CH₃I concentration				
Phase 1				
$[CH_3I]_g$ in ppm	Contact time (T_c) in ms	CH_3I/Ar flow in $mL.min^{-1}$	CH_3I exposure duration	Repetition
500	55	54/54	5 hours	2
200	55	21/87	5 hours	1

(v) Variation in contact time: Contact time is considered as main parameters influencing the gas-solid interaction when monitoring the gas phase [7, 8]. However, when renewing the CH₃I flow

all along the exposure phase duration by continuous flow and monitoring the solid phase as in our DRIFTS experiments, this highly suggests that contact time cannot be considered as main parameter influencing the gas-solid interaction. To verify this fact, we intended to perform experiments with different contact times. To investigate the influence of contact time on CH_3I-NaCl interaction, dry NaCl (RH = 20% at 296 K) was exposed to continuous CH_3I flow (500 ppm, 216 mL.min^{-1}) by increasing the total gas CH_3I/Ar flow from 108 mL.min^{-1} to 216 mL.min^{-1}. Thus, the estimated contact time was decreased from 55 ms to 27 ms. Similar to experiment shown in Table 4.2 the duration of the exposure phase was of 5 hours. No static or Ar flow phases were applied in this scenario. The experimental conditions are listed in Table 4.6.

Table 4. 6 Experimental conditions for CH_3I exposure, static and continuous Ar flow phases of dry experiment with NaCl – scenario (v).

Variation in contact time				
Phase 1				
[CH$_3$I]$_g$ in ppm	Contact time (T$_c$) in ms	CH$_3$I/Ar flow in mL.min^{-1}	CH$_3$I exposure duration	Repetition
500	27	108/108	5 hours	1

Additionally, the adsorption of CH_3I on other halide salts (NaI and KBr) was experimented for comparison as the influence of halide atom is questionable. Table 4.7 lists the conditions of experiments performed with NaI and KBr at 1 atm, 296 K and RH= 20%. Only the potential sorption of CH_3I on the halide salt was investigated so no static or Ar flow phases were applied for these experiments.

Table 4. 7 Experimental conditions for CH_3I exposure, static and continuous Ar flow phases of dry experiment with NaI and KBr – scenario (i).

Experiment with dry NaI and KBr					
	Phase 1				
Solid	[CH$_3$I]$_g$ in ppm	Contact time (T$_c$) in ms	CH$_3$I/Ar flow in mL.min^{-1}	CH$_3$I exposure duration	Repetition
NaI	1000	55	108/0	1 hour	1
KBr	1000	55	108/0	1 hour	1

4.1.4.2. Humid conditions

In a second part, the influence of humidity was investigated. The study focused on the interaction between dry gaseous CH_3I and wet solid NaCl. The objective was to compare the behavior of CH_3I when it is exposed to dry and wet NaCl aerosols. Humidity experiments conditions are listed in Table 4.8. At 296 K the protocol was as following:

Humidification of NaCl: NaCl was humidified with a 108 mL.min^{-1} continuous wet Ar flow for 40 minutes with a given %RH of 40, 60 or 80 % at 296 K. It should be noted that the deliquescent point (DRH) of NaCl is obtained when RH reach 75% at 298 K [11]. However, due to the uncertainty on the RH measurement (~10%), the DRH point was not reached to avoid any liquid in the DRIFTS cell.

Dry CH₃I flow: Wet NaCl samples were exposed to continuous dry flow of 1000 ppm of CH_3I at flow rate 108 mL.min^{-1} for 5 hours with a contact time of 55 ms in the solid bed.

Static and continuous Ar flow conditions: The system was maintained under static conditions and then under continuous Ar flow. The DRIFTS cell was maintained at room temperature (296 K).

Table 4. 8 Experimental conditions for CH₃I exposure, static and continuous Ar flow phases of experiment with humid NaCl.

	Experiment with wet NaCl						
	Phase 1				Phase 2	Phase 3	
%RH of NaCl	$[CH_3I]_g$ in ppm	Contact time (Tc) in ms	CH₃I/Ar flow in mL.min^{-1}	CH₃I exposure duration	Static duration	Continuous Ar flow (108 mL.min^{-1}) duration	Repetition
40	1000	55	108/0	**5 hours**	-	**1hour**	1
60	1000	55	108/0	**5 hours**	**1hour**	**1hour**	2
80	1000	55	108/0	**5 hours**	**1hour**	**1hour**	2

In addition to the humidity experiments listed above, an experiment was performed for checking the influence of humidity on desorption of CH_3I. The protocol was the following:

Dry CH₃I flow: Dry NaCl samples (RH=20%, at 296 K) were exposed to continuous dry flow of 100 ppm of CH_3I at flow rate 108 mL.min^{-1} featuring contact time of 55 ms in the solid bed for 5 hours.

Effect of humidity: Then after, wet Ar with RH of 50% (at 296 K) was continuously flowed for 40 minutes.

Conditions of this experiment are listed in Table 4.9.

Table 4. 9 Experimental conditions for CH$_3$I exposure, static and final continuous Ar flow phases of experiment with NaCl featuring humidified argon in the last phase.

Effect of humidity after CH$_3$I was taken up by NaCl						
%RH of NaCl	Contact time (Tc) in ms	[CH$_3$I]$_g$ in ppm	CH$_3$I/Ar flow in mL.min^{-1}	CH$_3$I exposure duration	Continuous flow of 108 mL.min^{-1} wet Ar (RH=50 %)	Repetition
20	55	1000	108/0	5 hours	40 minutes	1

4.1.4.3 Variation of the temperature conditions

NaCl was introduced in the DRIFTS cell and heated from room temperature (RH=20% at 296 K) up to 423 K. Once the target temperature has been reached, NaCl was exposed to CH$_3$I (1000 ppm) in a continuous flow at 108 mL.min^{-1} featuring a contact time of 55 ms in the solid bed. The system was maintained under static conditions and under continuous Ar flow maintaining temperature as during the exposure phase. Experiments under different temperature conditions are listed in Table 4.10.

Table 4. 10 Experimental conditions for CH$_3$I exposure, static and continuous Ar flow phases of experiment with NaCl at different temperatures

Experiment by increasing temperature							
	Phase 1				Phase 2	Phase 3	
Temperature (K)	[CH$_3$I]$_g$ in ppm	Contact time (Tc) in ms	CH$_3$I/Ar flow in mL.min^{-1}	CH$_3$I exposure duration	Static duration	Continuous Ar flow (108 mL.min^{-1}) duration	Repetition
323	1000	55	108/0	5 hours	1hour	1hour	1
348	1000	55	108/0	5 hours	1hour	1hour	1
373	1000	55	108/0	5 hours	1hour	1hour	1
423	1000	55	108/0	5 hours	1hour	1hour	1

4.2. Spectral assignment

4.2.1 Dry conditions

Experiments under dry condition were conducted by the continuous flow of dry CH_3I for 5 hours (108mL.min^{-1}, 1000 ppm) on dry NaCl particles placed in the DRIFTS cell at 296 K and 1 atm (see section 4.1.4.1, Table 4.2). A representative spectrum of NaCl exposed to CH_3I during 5 hours and recorded in the mid IR region (4000-600 cm^{-1}) is shown in Figure 4.5. Further, we observed a good repeatability of the observed IR spectra (i.e. IR band position and band area) for spectra recorded under the same experimental conditions (see annex 3).
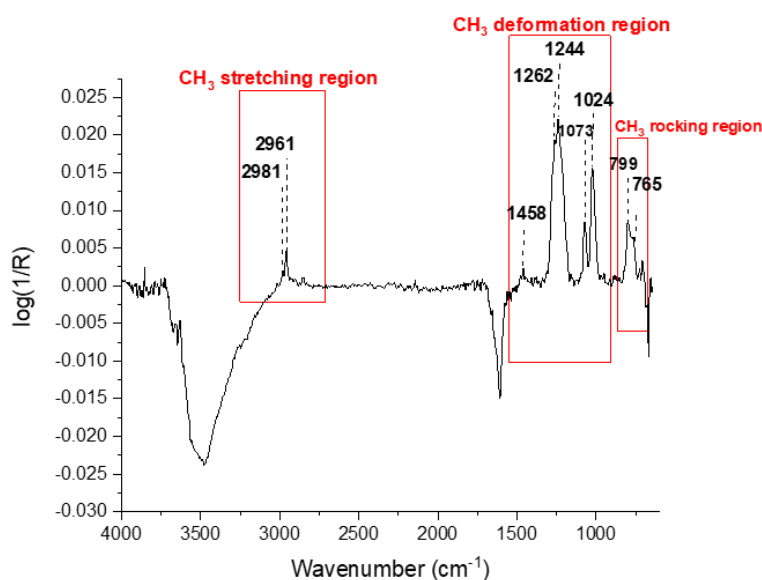
Figure 4. 5 Typical DRIFTS spectra in mid IR spectral range [4000-600 cm^{-1}] of dry NaCl surface exposed to 5 hours of CH$_3$I flow (108mL.min^{-1}, 1000 ppm) at 296 K and 1 atm.

Three typical regions assigned to CH$_3$ stretching, CH$_3$ deformation and CH$_3$ rocking are observed (Figure 4.5). The typical C-I vibration is not seen since the region is below 600 cm^{-1}. The detailed description of the CH$_3$ stretching (3050-2800 cm^{-1}), CH$_3$ deformation (1500-900 cm^{-1}) and CH$_3$ rocking (900-700 cm^{-1}) spectral region for a proper assignment is given below.

4.2.1.1 Band assignment in the CH$_3$ stretching region

The first region of interest is the CH$_3$ stretching region (3050-2800 cm^{-1}) which is shown in Figure 4.6. In the CH$_3$ stretching region bands at 3018, 2993, 2981, 2961, 2953, 2855 and 2847 cm^{-1} are observed.

Overlapped bands in the 2961 cm^{-1} region were decomposed using gaussian function (see procedure described 4.1.2.4) and the two identified bands at 2961 and 2953 cm^{-1} are presented in Figure 4.7.
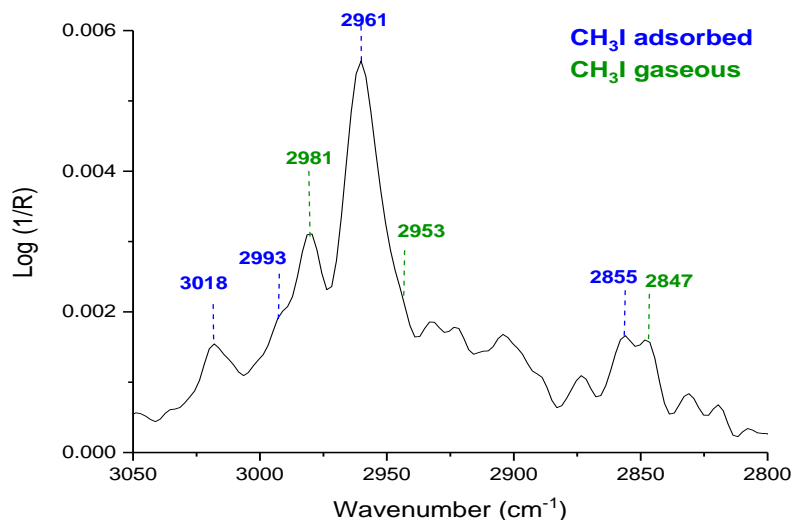
Figure 4. 6 DRIFTS spectra in the 3050-2800 cm^{-1} IR spectral range of NaCl surface exposed to 5 hours of CH$_3$I (108mL.min^{-1}, 1000 ppm) continuous flow at 296 K and 1 atm. Blue bands are CH$_3$I adsorbed on NaCl and green bands are CH$_3$I in gas phase near the surface.
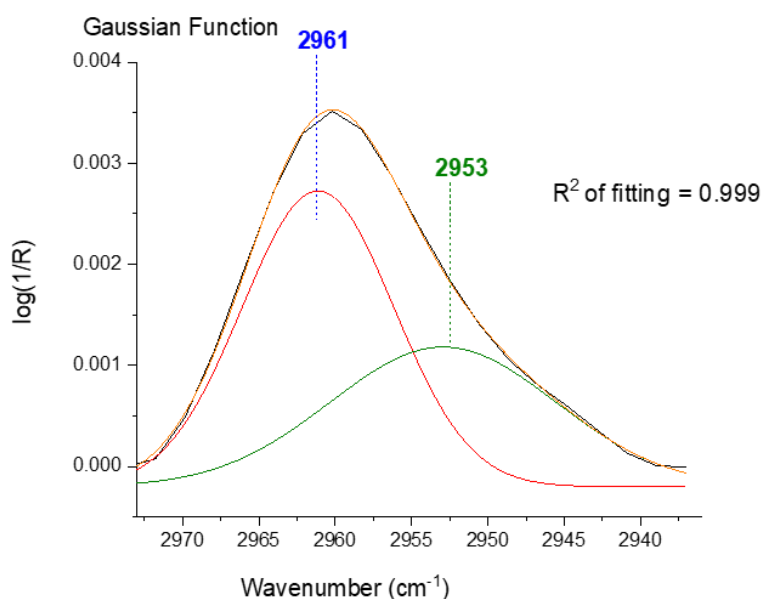
Figure 4. 7 DRIFTS spectra in the 2963-2935 cm^{-1} IR spectral range of NaCl exposed to 5 hours of continuous CH$_3$I flow (108mL.min^{-1},1000 ppm) at 296 K and 1 atm decomposed with Gaussian function using FityK software.

The IR bands observed at 2981, 2953, and 2847 cm^{-1} are assigned to the characteristic bands of CH$_3$I in gas phase (see bands marked in green in the Figure 4.6) as described in the literature [12-14]. The bands at 2981, 2953 and 2847 cm^{-1} are attributed to the CH$_3$ asymmetric stretching, CH$_3$ symmetric stretching and overtone modes of CH$_3$I in gas phase, respectively (Table 4.11). This is explained by the detection of gaseous CH$_3$I which remains near the NaCl surface when using DRIFTS measurement.

Table 4. 11 Identification of IR absorption bands in cm^{-1} of CH$_3$I in gas phase from the literature.

Technique used	FTIR	FTIR	FTIR	This work
Vibrational modes	**CH$_3$I$_{(g)}$** [12]	**CH$_3$I$_{(g)}$** [13]	**CH$_3$I$_{(g)}$** [14]	**CH$_3$I$_{(g)}$**
CH$_3$ rocking			883	
CH$_3$ symmetric deformation	1261	1251	1251	1262
CH$_3$ asymmetric deformation		1445	1435	1477
CH$_3$ overtone		2850	2854	2847
CH$_3$ symmetric stretching	2959	2969	2971	2953
CH$_3$ asymmetric stretching	2980	3065	3018	2981

Based on the IR bands observed for CH$_3$I adsorbed on TiO$_2$ [12] and zeolites [13] (Table 4.12), we have tentativelly assigned the bands observed at 3018, 2961 and 2855 cm^{-1} (marked in blue in Figure 4.6) as characteristic bands for CH$_3$I adsorbed on NaCl. The frequencies are attributed to CH$_3$ asymmetric stretching, symmetric and overtones modes, respectively. Thus, an indicative blue shift of the CH$_3$ asymmetric stretching, symmetric stretching and asymmetric overtone modes of CH$_3$I is observed from gas to adsorbed phase.

Additionally, a low intensity band at 2993 cm^{-1} (Figure 4.6) is observed and also attributed to the interaction with NaCl. Actually, compared to CH$_3$I adsorbed on various surfaces (see Tables 4.12 and 4.13), the symmetric stretching mode of CH$_3$ varies between 3000 and 2909 cm^{-1}. Thus, 2993 cm^{-1} is also tentatively attributed to the CH$_3$ symmetric stretching mode of adsorbed CH$_3$I. The observation of two bands i.e. at 2993 and 2961 cm^{-1} for the same CH$_3$ stretching mode might be explained with different geometrical adsorbed structures of CH$_3$I on NaCl surface.

Table 4. 12 Identification of IR absorption bands in cm^{-1} of CH$_3$I adsorbed on zeolite and catalyst surfaces. FTIR: Fourier Transform Infrared Spectroscopy and DRIFTS: Diffuse Reflectance Infrared Fourier Transform Spectroscopy.

Technique used	DRIFTS	FTIR	
Vibrational modes	**CH$_3$I adsorbed on AgY [13]**	**CH$_3$I adsorbed on TiO$_2$ [12]**	**This work**
CH$_3$ symmetric deformation	1245	1245	1244
CH$_3$ asymmetric deformation	1455	-	1458
CH$_3$ overtone	2855	-	2855
CH$_3$ symmetric stretching	2963	2955	2961
CH$_3$ asymmetric stretching	3020	3050	3018

Table 4. 13 Identification of IR absorption bands in cm^{-1} of CH$_3$I adsorbed on single metallic surfaces. HREELS: High-Resolution Electron Energy Loss Spectroscopy[3]. RAIRS: Reflection-Absorption Infrared Spectroscopy.

Technique used	HREELS	HREELS	HREELS	RAIRS	HREELS	DRIFTS
Vibrational modes	CH$_3$I adsorbed on Si (100) [15]	CH$_3$I adsorbed on Rh (111) [16]	CH$_3$I adsorbed on Cu (111) [17]	CH$_3$I adsorbed on Cu (110) [18]	CH$_3$I adsorbed on Pt (111) [19]	CH$_3$I adsorbed on NaCl This work
CH$_3$ rocking	900	900	830	875	875	
CH$_3$ symmetric deformation	1250	1230	1190	1230	1220	1244, 1183
CH$_3$ asymmetric deformation	1425	1430		1413	1395	
CH$_3$ overtone			2830			
CH$_3$ symmetric stretching	3000			2909		2993
CH$_3$ asymmetric stretching	3080	3044			3025	3018

---

[3] HREELS: is a method used for measuring the vibrational spectra of molecules adsorbed on surfaces. Its resolution is not as high as Infrared, but HREELS possesses the advantage of a wide energy range and good surface sensitivity.

4.2.1.2 Band assignment in the CH₃ deformation region

The second region of interest is the CH_3 deformation region (1500-900 cm^{-1}), where bands at 1477, 1458, 1275, 1262, 1244, 1220, 1183, 1073 and 1024 cm^{-1} are observed (Figure 4.8).

Figure 4. 8 DRIFTS spectra in the 1500-900 cm^{-1} IR spectral range of NaCl surface exposed to 5 hours of CH₃I (108mL.min^{-1}, 1000 ppm) continuous flow at 296 K and 1 atm. Blue bands are CH₃I adsorbed on NaCl, green bands are CH₃I in gas phase near the surface, and red bands are new bands.

Based on the literature (see Table 4.11), the bands at 1477 and 1262 cm^{-1} are assigned to the CH_3 asymmetric and symmetric deformations of gaseous CH₃I.

The band at 1458 cm^{-1} is attributed to the CH_3 asymmetric deformation of adsorbed CH₃I as reported in the literature with a red shift of 18 cm^{-1} compared to the gaseous CH₃I band (see Table 4.12). In this spectral region, the band centered at 1244 cm^{-1} evidenced some shoulders; the decomposition of this band and the fitting procedure allows to extract the additional bands at 1275, 1220 and 1183 cm^{-1} (see Figure 4.9).
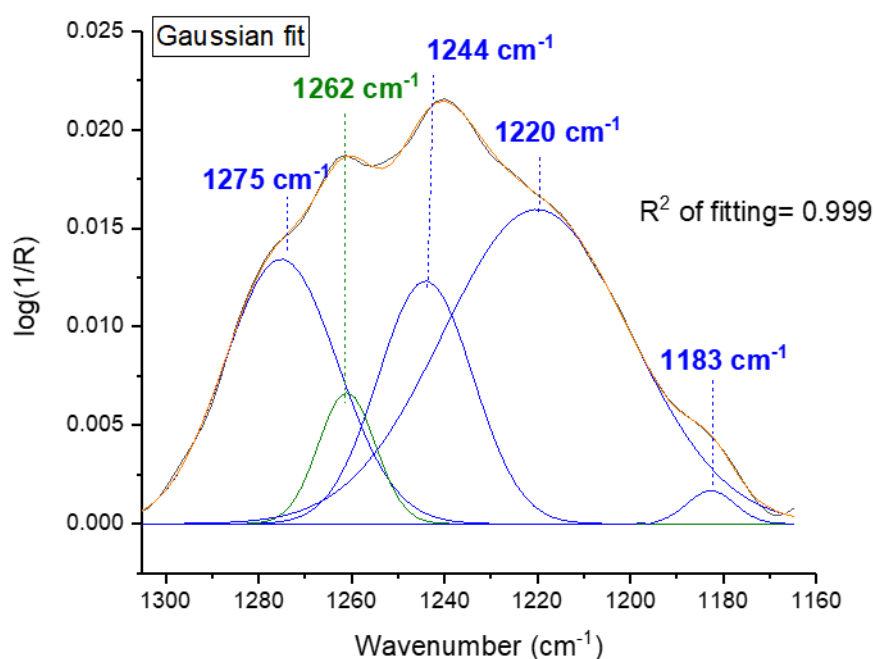
Figure 4. 9 DRIFTS spectra in the 1305-1160 cm⁻¹ IR spectral range of NaCl exposed to 5 hours of continuous CH₃I flow (108mL.min⁻¹,1000 ppm) at 296 K and 1 atm decomposed with Gaussian function using FityK software.

It should be mentioned, that in the published spectra of adsorbed CH_3I on solids, two similar shoulders are clearly observed on the band centered at 1242 cm⁻¹ (see Figure 4.10) although they were not assigned.
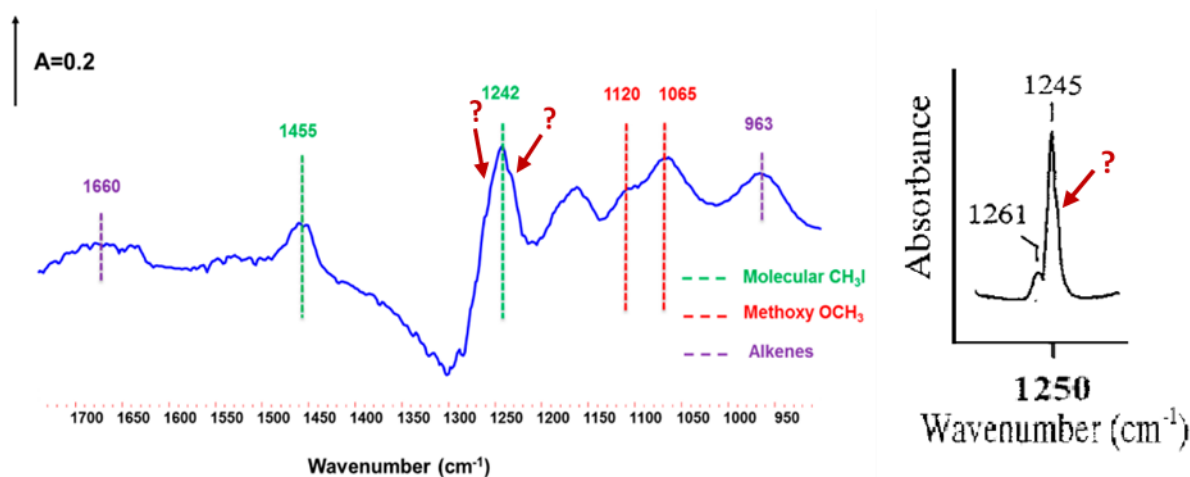
Figure 4. 10 (a) DRIFTS spectrum of 23Ag/Y (2.5) after saturation with CH₃I (1333 ppm/Ar) at 373 K [13] and (b) IR spectrum IR spectrum of the TiO₂ at 308 K in contact with 2 Torr of CH₃I [12].

Similarly, the decomposition of the band centered at 1242 cm⁻¹ of adsorbed CH_3I on zeolites [13] allows to extract IR bands at 1256, 1250, 1242, 1231 and 1216 cm⁻¹ (Figure 4.11). Because the adsorption process is different from zeolites to NaCl, a difference in IR bands shift related to adsorbed CH_3I molecules is expected.
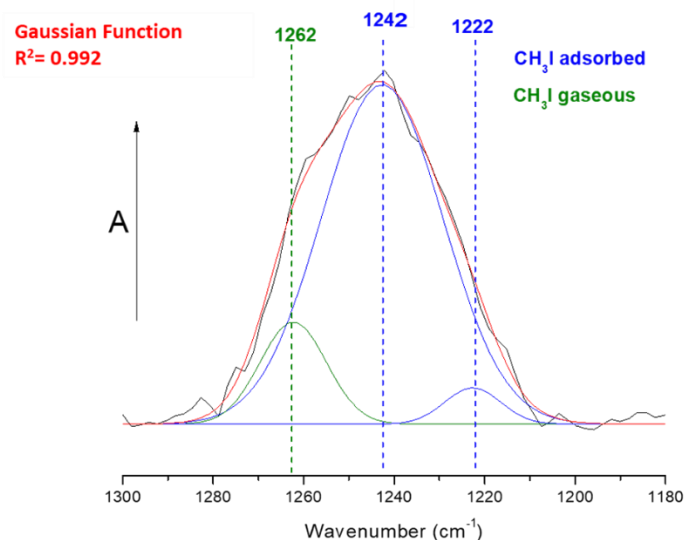
Figure 4. 11 DRIFTS spectrum in the CH$_3$ deformation range of adsorbed CH$_3$I of 23Ag/Y(2.5) after saturation with CH$_3$I (1333 ppm/Ar) at 373 K decomposed using Gaussian fit [13].

In comparison to the experimental studies on the adsorption of CH$_3$I on solids, the band at 1244 cm^{-1} is characteristic to the CH$_3$ symmetric deformation mode of adsorbed CH$_3$I on AgY [13] and TiO$_2$ [12], when the band observed at 1220 cm^{-1} was assigned to the same vibration mode for CH$_3$I adsorbed on Pt [19] (see Figure 4.8). The two additional bands observed at 1275 and 1183 cm^{-1} can be also considered as deformation modes of CH$_3$ of CH$_3$I adsorbed on surface. Actually, regarding the previous work related to the adsorption of CH$_3$I on surfaces [15-19], it was shown that the CH$_3$ symmetric deformation of the CH$_3$I can shift (red and blue shift) from 1190 cm^{-1} to 1250 cm^{-1} depending on the type of metallic surface. We observed a red shift of -18, -42 and -79 cm^{-1} for the bands at 1244, 1220, 1183 cm^{-1}, respectively, and a blue shift of -13 cm-1 for the band at 1275 cm^{-1}. Moreover, it was reported that the band of CH$_3$ symmetric deformation of CH$_3$I on Cu surface can shift based on the orientation of the crystallographic planes such as 1230 cm^{-1} for Cu (110) [18] and 1190 cm^{-1} for Cu (111) [17]. This strongly suggest that the bond geometries of the adsorbed CH$_3$I on the solid surface are a key for understanding the adsorption of CH$_3$I on solid surfaces and their subsequent reactivity which can highly affect the observed vibrational modes. Additionally, it was reported [15-19] that with low coverage, CH$_3$I adsorbed on single metallic surface is of C$_s$ symmetry. However, with higher coverages a geometrical rearrangement occurs until C-I bond becomes aligned with the surface maintaining C$_{3v}$ symmetry and I is in binding to the surface as shown on Figure 4.12. In contrary to powdered sample, a single crystal sample has a continous, unbroken and free of defects lattice. Thus, one would expect that with powdered sample i.e. NaCl, more than one geometrical orientation of adsorbed CH$_3$I are likely to occur. This highly

reflects the observation of more than one band for CH_3 symmetric deformation and symmetric stretching modes of adsorbed CH_3I on NaCl (Figure 4.6 and 4.8).
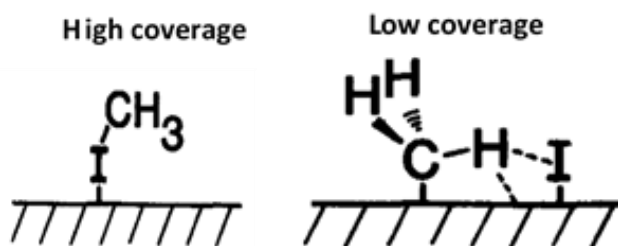
Figure 4. 12 Proposed adsorption geometry of CH₃I to metallic surface [19].

In the CH_3 deformation (Figure 4.8) region we observe two new intense bands at 1073 and 1024 cm^{-1}. These bands are observed in all CH_3I adsorption experiments on halide salts (NaCl, NaI and KBr) (spectra with KBr and NaI are shown later in section 4.2.1.4).

To our knowledge, these bands have never been reported in the literature when CH_3I is adsorbed on the surface, so that, we have scrutinized several hypotheses exposed in details in section 4.2.1.4.

4.2.1.3 Band assignment in the CH_3 rocking region

The CH_3 rocking region (900-700 cm^{-1}) is shown in Figure 4.13. In the CH_3 rocking region bands at 824, 799, 784, 773, 765 and 748 cm^{-1} are observed. The CH_3 rocking mode of gaseous CH_3I was previously observed at 882 cm^{-1} [14]. It should be highlighted that the CH_3 rocking mode of adsorbed CH_3I on AgY zeolite [13] and TiO_2 catalyst [12] were not reported. However, CH_3 rocking mode of adsorbed CH_3I on single particle (see Table 4.13) was between 830-900 cm^{-1}. Thus, the band at 824 cm^{-1} might be assigned to the CH_3 rocking mode of adsorbed CH_3I.

We were not able to well assign the bands in this region due to (1) the lack of attribution of this region with powdered solids in literature, (2) low intensity of these bands and (3) overlap of the bands.
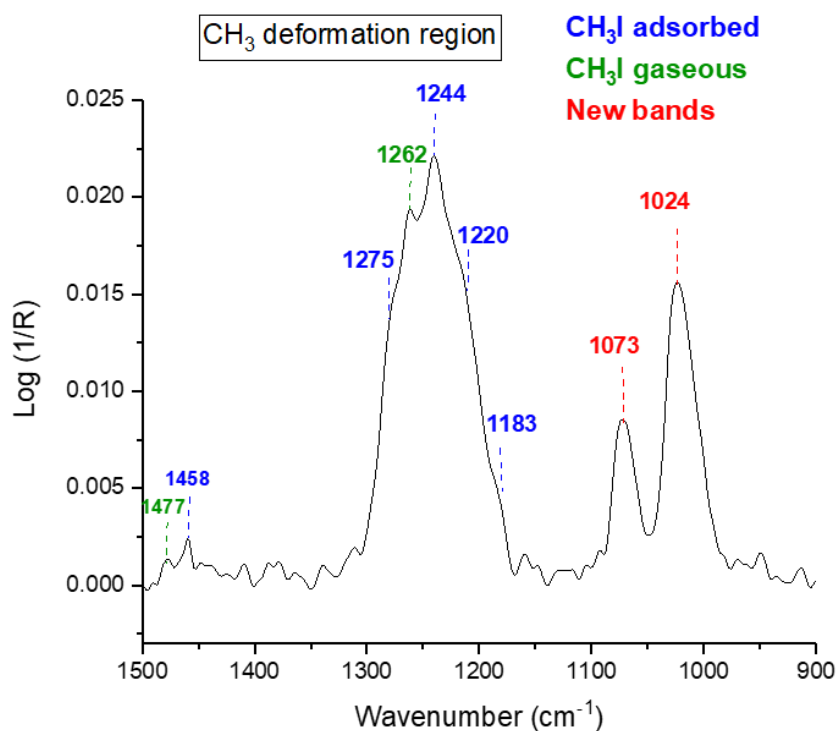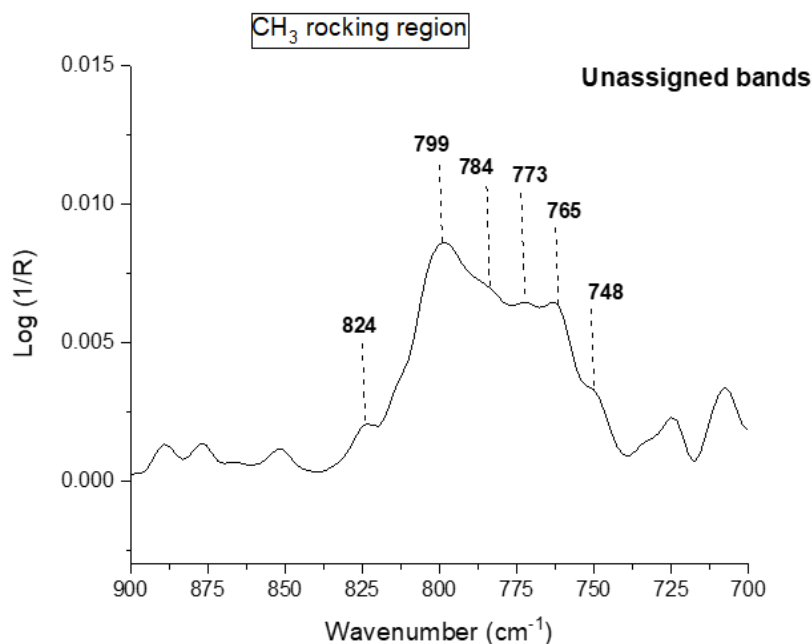
Figure 4. 13 DRIFTS spectra in the 900-700 cm^{-1} IR spectral range of NaCl surface exposed to 5 hours of CH$_3$I (108mL.min^{-1}, 1000 ppm) continuous flow at 296 K and 1 atm. Bands in black are unassigned bands.

4.2.1.4 New bands attribution

As mentioned in the paragraph 4.2.1.2 two intense bands appears systematically at 1073 and 1024 cm^{-1} when NaCl surface was exposed to CH$_3$I. Because these bands were not reported in the literature for CH$_3$I molecules adsorbed on surface, we have first hypothesized the formation of new species.

As it can be seen in Table 4.14, the CH$_2$ bending modes of adsorbed CH$_2$I$_2$ were observed at 1080 cm^{-1} on Rh [20] or 1030 cm^{-1} on Mo [21], but was not observed on Ag [22]. The CH$_2$ symmetric stretching and rocking bands of CH$_2$I$_2$ on Mo [19] were observed at 2960 and 750 cm^{-1}, respectively. Whereas, CH$_2$ symmetric stretching and rocking bands of CH$_2$I$_2$ on Rh [20] were observed at 2940 and 720 cm^{-1}, respectively. Thus, the bands observed at 1073 cm^{-1}, (Figure 4.8), 1024 cm^{-1} (Figure 4.8) and 765 cm^{-1} (Figure 4.13) as well as the band at 2961 cm^{-1} (Figure 4.6) could be assigned to CH$_2$I or CH$_2$I$_2$.

185

Technique used	Theoretical calculation	HREELS	HREELS
Vibrational modes	CH$_2$I$_{2(g)}$ [23]	CH$_2$I$_2$ adsorbed on Mo [21]	CH$_2$I$_2$ adsorbed on Rh [20]
CH$_2$ rocking	714	750	720
CH$_2$ twisting	1028		
CH$_2$ bending	1349	1030	1080
CH$_2$ wagging	1103	1100	
CH$_2$ symmetric deformation		1390	1350
CH$_2$ symmetric stretching	2968	2960	2940
CH$_2$ asymmetric stretching	3047		

However, the formation of such species requires a reaction of CH$_3$I on the surface. The dissociation of CH$_3$I was described on metallic surface only and at 2×10^{-10} mbar and 250-300 K [24 and reference herein]. Therefore, the dissociation of CH$_3$I on NaCl and formation of CH$_2$I$_2$ under ambient conditions (296 K and 1 atm) is unlikely.

On the other hand, in gas phase the experimental study of the micro solvated reaction of OH$^-$ (H$_2$O) with CH$_3$I indicated the formation of CH$_2$I$^-$ by the following proton transfer reaction at 100 K [25]:

$$OH^-(H_2O) + CH_3I \rightarrow CH_2I^-(H_2O) + H_2O \qquad [R4\text{-}1]$$
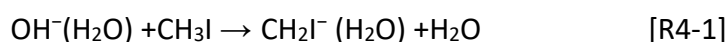
Additionally, the kinetic experimental study of CH$_3$I reactivity in gas phase at high temperature (604 K) showed that CH$_2$I$_2$ could be formed by the following reaction [26]:

$$2CH_3I \rightarrow CH_2I_2 + CH_4 \qquad [R4\text{-}2]$$
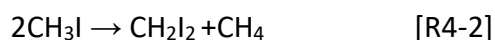
For our experimental conditions the gas phase of CH$_3$I gas flow was under ambient conditions (296 K and 1 atm) and CH$_4$ was not detected in any recorded spectrum. Moreover, there is no possible exitence of OH$^-$ in our experimental conditions. Thus, the formation of CH$_2$I$_2$ or CH$_2$I by the above gas phase mechanisms and then adsorption on NaCl surface is discarded.

The bands at 1073 and 2981 cm^{-1} can also contributes to the CO stretching mode and CH$_3$ symmetric stretching mode of CH$_3$O adsorbed on surface, respectively, as described previously [13] (see Table 4.15).

Table 4. 15 IR absorption bands in cm^{-1} of CH$_3$OH observed from the adsorption of CH$_3$I on Zeolites [13]. DRIFTS: Diffuse Reflectance Infrared Fourier Transform Spectroscopy.

Technique used	DRIFTS
Vibrational modes	CH$_3$O adsorbed on AgY [13]
CO stretching	1065
CH$_3$ rocking	1120
CH$_3$ symmetric stretching	2870
CH$_3$ asymmetric stretching	2967

It has been shown that a fraction of the adsorbed CH$_3$I on zeolites (AgY) may dissociate and yield to the formation of methoxy species at 373 K through the following reaction [13]:

$$CH_3I + Ag^+ + [SiOAl]^- \rightarrow AgI + SiOCH_3Al \qquad [R4\text{-}3]$$

However, halide solids surfaces are not reactive as zeolites or Ag surfaces and the experiments need to be performed at 373 K.

The 2981, 2961, 1458 and 1024 cm^{-1} bands observed might be consistent with the CH$_3$ symmetric stretching and rocking modes, respectively of CH$_3$Cl formed on surface regarding previous results [27-30] (see Table 4.16).

Table 4. 16 IR absorption bands in cm^{-1} of CH$_3$Cl in gas (g) and adsorbed (ads). IRAS: Infrared Reflection Absorption Spectroscopy, FTIR: Fourier Transform Infrared Spectroscopy, RAIRS: Reflection Absorption Infrared Spectroscopy.

Technique used	FTIR	IRAS	FTIR	FTIR	RAIRS
Vibrational modes	CH$_3$Cl$_{(g)}$ [28]	CH$_3$Cl adsorbed on Cu [27]	CH$_3$Cl adsorbed on PdSiO$_2$ [29]	CH$_3$Cl adsorbed on Mo$_2$C [28]	CH$_3$Cl adsorbed on Pt [30]
CH$_3$ rocking	1015	1013			1022
CH$_3$ symmetric deformation	1355	1336	1350	1350	1336
CH$_3$ degenerate deformation	1455	1436	1433	1444	1438
CH$_3$ overtone	2879			2860	
CH$_3$ symmetric stretching	2966	2954	2980	2963	2953

There is a considerable interest in understanding the atomic level of halide substitution reactions [31-33] as following:

$$X^- + CH_3Y \rightarrow CH_3X + Y^- \quad [R4\text{-}4]$$
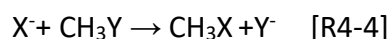
The SN$_2$ halide substition reaction of hydrated chloride with methyl iodide was investigated by simulations and the reaction mechanism is presented in Figure 4.14 [33]. Compared to the unsolvated reaction of Cl$^-$ with CH$_3$I, the addition of water slightly lowers the reaction possibility and the rate constant is correspondingly reduced [33]. Therefore, this substitution reaction obtained with calculations suggests a probable exchange between Cl$^-$ of NaCl and I$^-$ of CH$_3$I, more favored under dry conditions.
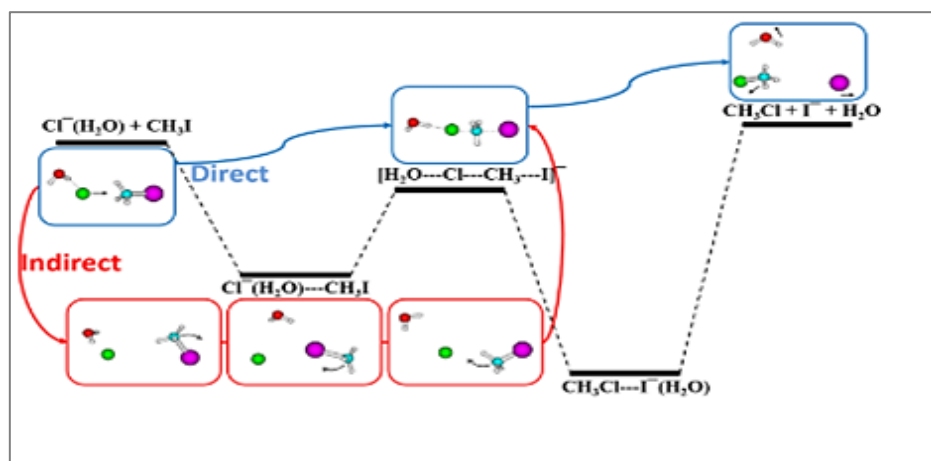
Figure 4. 14 The direct and indirect mechanism of the Cl-(H$_2$O) +CH$_3$I substitution reaction from [33].

However, in our experiment we are in solid phase. Therefore, to prove or not the exchange mechanism between I$^-$ and Cl$^-$ and eventually Br$^-$ in solid phase, experiments were conducted by the continuous flow of CH$_3$I (108mL.min^{-1}, 1000 ppm) for 1 hour on NaI and KBr solid particles at 296 K and 1 atm (section 4.1.4.1, Table 4.7). The zoomed spectrum in the range 1400-900 cm^{-1} are shown in Figure 4.15 and compared with the DRIFTS spectrum of NaCl exposed to CH$_3$I in the same conditions.
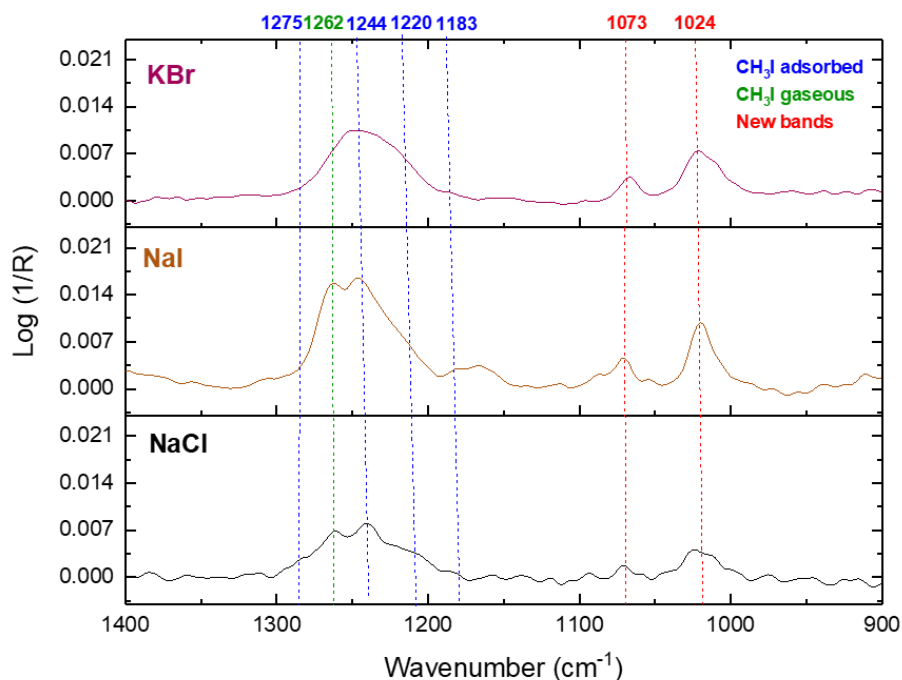
Figure 4. 15 DRIFTS spectra in the 1400-900 cm^{-1} IR spectral range of NaCl surface (in black), NaI (in dark yellow) and KBr (in violet) exposed to 1 hour of CH$_3$I (108mL.min^{-1}, 1000 ppm) continuous flow at 296 K and 1 atm. Bands in blue are adsorbed CH$_3$I, green are gaseous CH$_3$I near the surface and red are new bands.

Figure 4.15 clearly shows the contribution of the new bands (in red) when NaI is exposed to CH$_3$I at the same position as observed in experiments with NaCl. This indicates that exchange between Cl$^-$ of NaCl and I$^-$ of CH$_3$I to form CH$_3$Cl is unlikely since the same new bands are observed with both NaCl and NaI surfaces.

Similar to NaCl, the different orientation of CH$_3$I on NaI surface caused formation of overlapped bands in the CH$_3$ symmetric deformation centered at 1244 cm^{-1}. It is clearly visible from Figure 4.16 that both CH$_3$I and the new bands formation are favored with NaI.

Similarly, Figure 4.15 clearly shows the contribution of the new bands (in red) on KBr at the same position as on NaCl. Both CH$_3$I adsorbed on NaCl and the new bands formation are favored with KBr. This indicates that all halide salts can interact with CH$_3$I.

The strength of the interaction of CH$_3$I with halide salts might be linked to the electronegativity of the halide solid ions. The electro negativity from the highest to the lowest is as follows: Cl$^-$ > Br$^-$ > I$^-$. Thus, this might reveal that the strongest interaction will be with halide solid particles who have the least electronegative ion (weakest ionic bonding) and vice versa.

Therefore, the question that arises here, is how I$^-$ favor the adsorption of CH$_3$I? and does the presence of I$^-$ favors the dissociation of CH$_3$I to form new species?

Additional experiments consisted in exposing 16 g of dry NaCl to CH_3I flow (108 mL.min^{-1}, 1000 ppm) for 1 hour under static conditions in a glass balloon and then to flush the remaining gaseous CH_3I from the glass balloon to the matrix cryogenic chamber. The gas phase analysis was carried out with FTIR spectroscopy as described in the Chapter 3. Then after, the NaCl solid sample was recovered and measured by DRIFTS with the same spectral processing as with DRIFTS experiments (as described in sections 4.1.2.3 and 4.1.2.4). The analysis of the gas phase indicated that seemingly no new gaseous species are detected. The DRIFTS spectra of dry NaCl from the balloon experiment showed same IR bands position as with DRIFTS spectra of dry NaCl from DRIFTS experiment (see Figure 4.16).
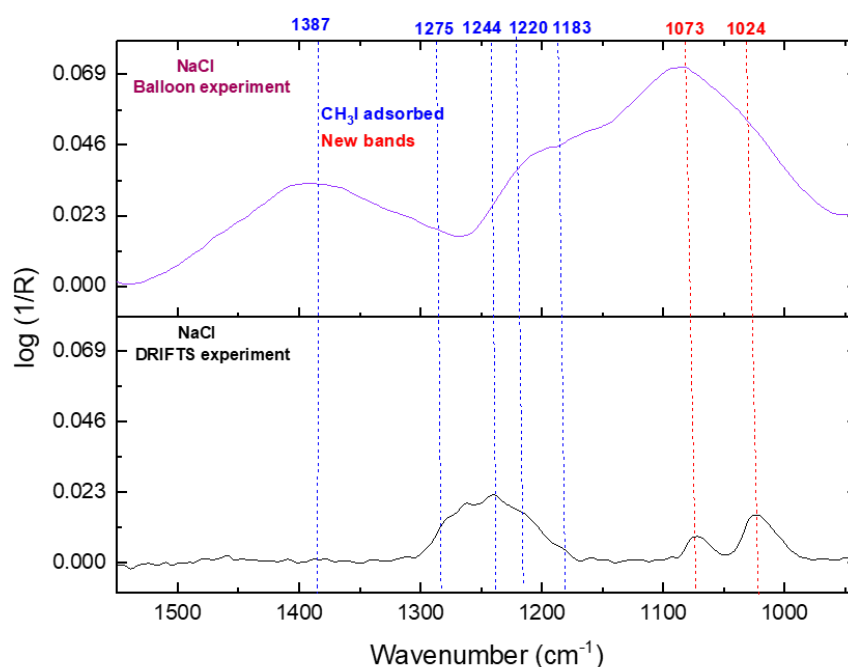
Figure 4. 16 DRIFTS spectra in the 1550-940 cm^{-1} IR spectral range of NaCl surface from dry NaCl of DRIFTS experiment in black and dry NaCl recovered from the balloon experiment at 296 K and 1 atm. Bands in blue are CH_3I adsorbed on NaCl and red are new bands.

Thus, a non-described adsorption geometry of CH_3I at the surface is the last hypothesis. Indeed, the two new bands observed in the CH_3 deformation (Figure 4.8) region at 1073 and 1024 cm^{-1} are intense. These bands are strongly red shifted compared to the CH_3 deformation band of free CH_3 at 1262 cm^{-1} with values at -189 and -238 cm^{-1}, that suggest a strong interaction of CH_3I with NaCl surface. From our DFT calculation of CH_3I monomer (see chapter 3, section 3.1.4), we found that the iodomethane dipole moment is oriented toward carbon atom, which leads to a partial negative Mulliken's charge for iodine atom and partial positive Mulliken's charge for hydrogen atoms (see Figure 4.17) . If we assume that CH_3I is adsorbed on NaCl with a C_{3v} configuration shown in Figure 4.17, then we may expect an attraction of

hydrogen atoms toward chloride atoms at the surface of NaCl due to charge difference. The observation of two bands for this configuration probably reflects the non-equivalent hydrogen atoms attached to the Cl on NaCl surface (see Figure 4.17).

Finally, as stated previously, the electronegativity of chloride atom is higher than iodine atom, which might reveal a strongest interaction of hydrogen atom with iodine ion (weakest ionic bonding).

Mulliken charges from DFT calculation
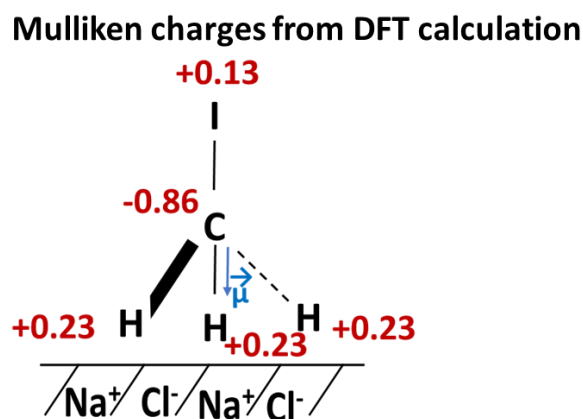
Figure 4. 17 Scheme of the CH$_3$I adsorption on NaCl representing the bands at 1073 and 1024 cm^{-1}. Mulliken charges from DFT calculation perfomed using ωB97XD/aug-cc-pVTZ-PP.

4.2.1.5 Summary of bands assignment

Table 4.17 summarizes the tentative bands assignment observed from the interaction of CH$_3$I on dry NaCl.

Both CH$_3$I gaseous near the surface and adsorbed CH$_3$I are observable. It seems reasonable to hypothesize that CH$_3$I can adsorb on NaCl in different geometrical configuration that can result in apparent frequencies in the CH$_3$ stretching and deformation region. The new intense bands are assigned to the unique C$_3$v geometrical adsorption of CH$_3$I wich occurs specifically with halide salt surfaces. This geometry was not described in the literature.

Table 4. 17 Tentative assignment of the observed IR absorption bands in cm^{-1} of CH$_3$I in gas (g) and adsorbed (ads)on the surface of dry NaCl at 296 K and 1 atm.

Wavenumber (cm^{-1})	Vibrational mode	Possible species
3018	CH$_3$ asymmetric stretching	CH$_3$I$_{(ads)}$
2993	CH$_3$ symmetric stretching	CH$_3$I$_{(ads)}$
2981	CH$_3$ asymmetric stretching	CH$_3$I$_{(g)}$
2961	CH$_3$ symmetric stretching	CH$_3$I$_{(ads)}$
2953	CH$_3$ symmetric stretching	CH$_3$I$_{(g)}$
2855	CH$_3$ overtone	CH$_3$I$_{(ads)}$
2847	CH$_3$ overtone	CH$_3$I$_{(g)}$
1477	CH$_3$ symmetric deformation	CH$_3$I$_{(g)}$
1458	CH$_3$ asymmetric deformation	CH$_3$I$_{(ads)}$
1275	CH$_3$ asymmetric deformation	CH$_3$I$_{(ads)}$
1262	CH$_3$ symmetric deformation	CH$_3$I$_{(g)}$
1244	CH$_3$ symmetric deformation	CH$_3$I$_{(ads)}$
1220	CH$_3$ symmetric deformation	CH$_3$I$_{(ads)}$
1183	CH$_3$ symmetric deformation	CH$_3$I$_{(ads)}$
1073	CH$_3$ symmetric deformation	CH$_3$I$_{(ads)}$
1024	CH$_3$ symmetric deformation	CH$_3$I$_{(ads)}$

4.2.2 Influence of humidity

4.2.2.1 Exposure of wet NaCl to dry CH$_3$I

Humid condition was conducted by the continuous flow of CH$_3$I for 5 hours (108 mL.min^{-1}, 1000 ppm) on humidified NaCl (so called wet NaCl) particles placed in DRIFTS cell at 296 K and 1 atm (see section 4.1.4.2 and Table 4.8). Wet NaCl samples were generated by exposition to an Ar flow of specific relative humidity value (RH=40, 60 and 80% at 296 K) during 40 minutes. The background was recorded under dry Ar flow (108 mL.min^{-1}). The DRIFTS spectra obtained from exposure of dry and humid NaCl at the end of the experiment exhibit similar features as shown in the Figure 4.18.
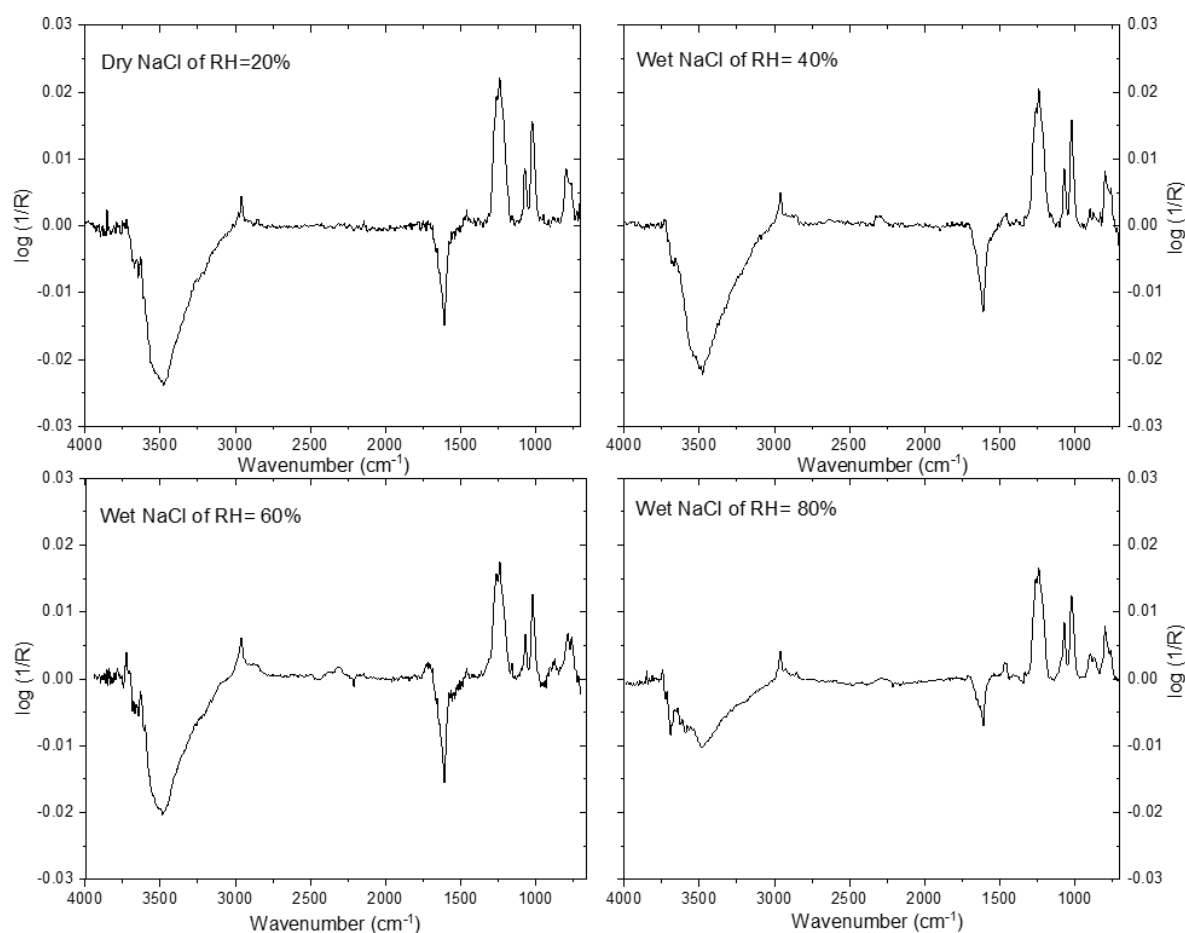
Figure 4. 18 DRIFTS spectra in the 4000-700 cm^{-1} of dry and wet NaCl surface exposed to 5 hours of CH$_3$I (108mL.min^{-1}, 1000 ppm) continuous flow at 296 K and 1 atm.

The DRIFTS spectra in the zoomed CH$_3$ stretching (3100-2800 cm^{-1}), CH$_3$ deformation and rocking (1500-750 cm^{-1}) spectral regions are shown in Figures 4.19 and 4.20, respectively. As stated previously, when comparing the DRIFTS spectra of dry and humid NaCl at the end of the experiment, no major difference is observed (Figure 4.19 and 4.20).
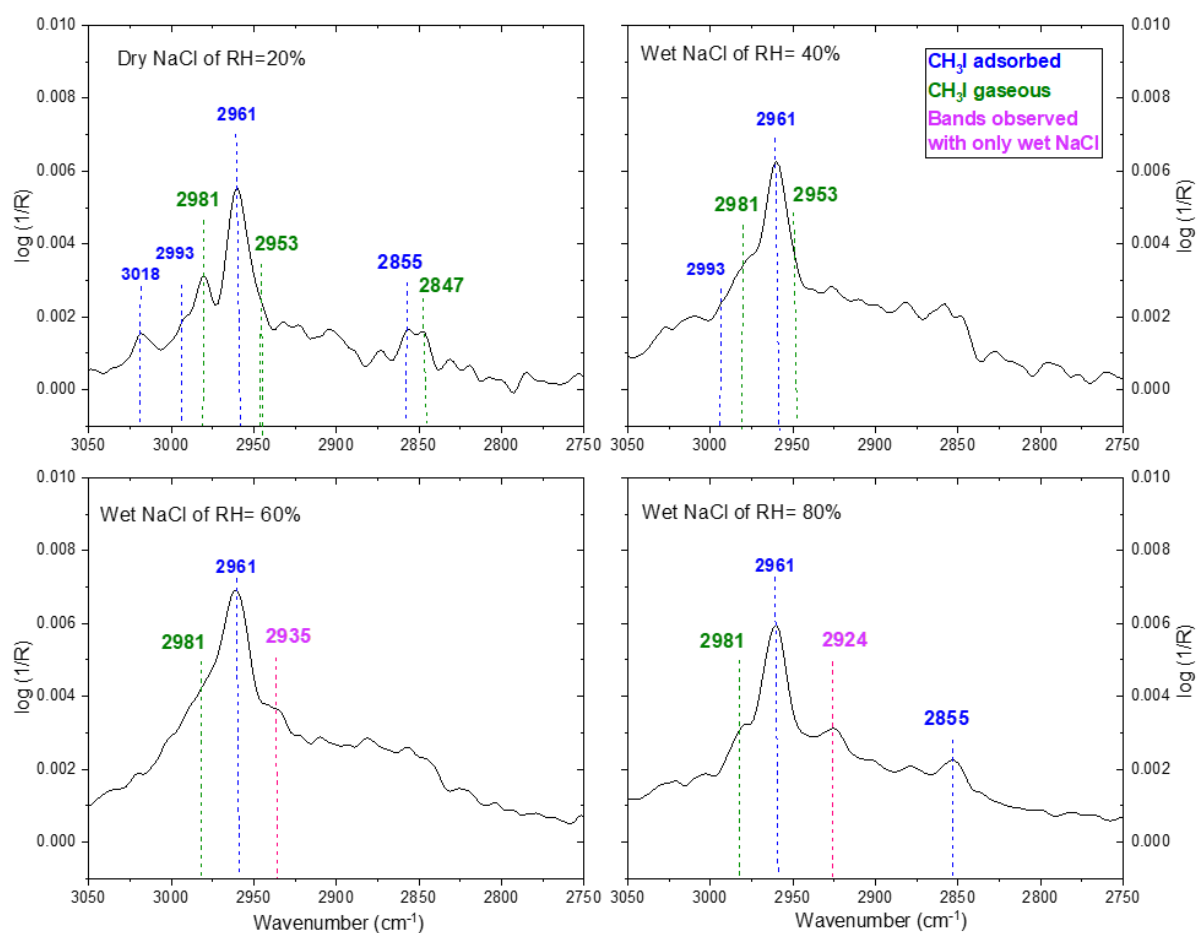
Figure 4. 19 DRIFTS spectra in the 3050-2750 cm^{-1} IR spectral range of dry and wet NaCl surface exposed to 5 hours of CH$_3$I (108mL.min^{-1}, 1000 ppm) continuous flow at 296 K and 1 atm. Bands in blue are adsorbed CH$_3$I on NaCl, green are gaseous CH$_3$I near the surface, black are unassigned bands, red bands are new bands and violet bands are bands observed with only wet NaCl.
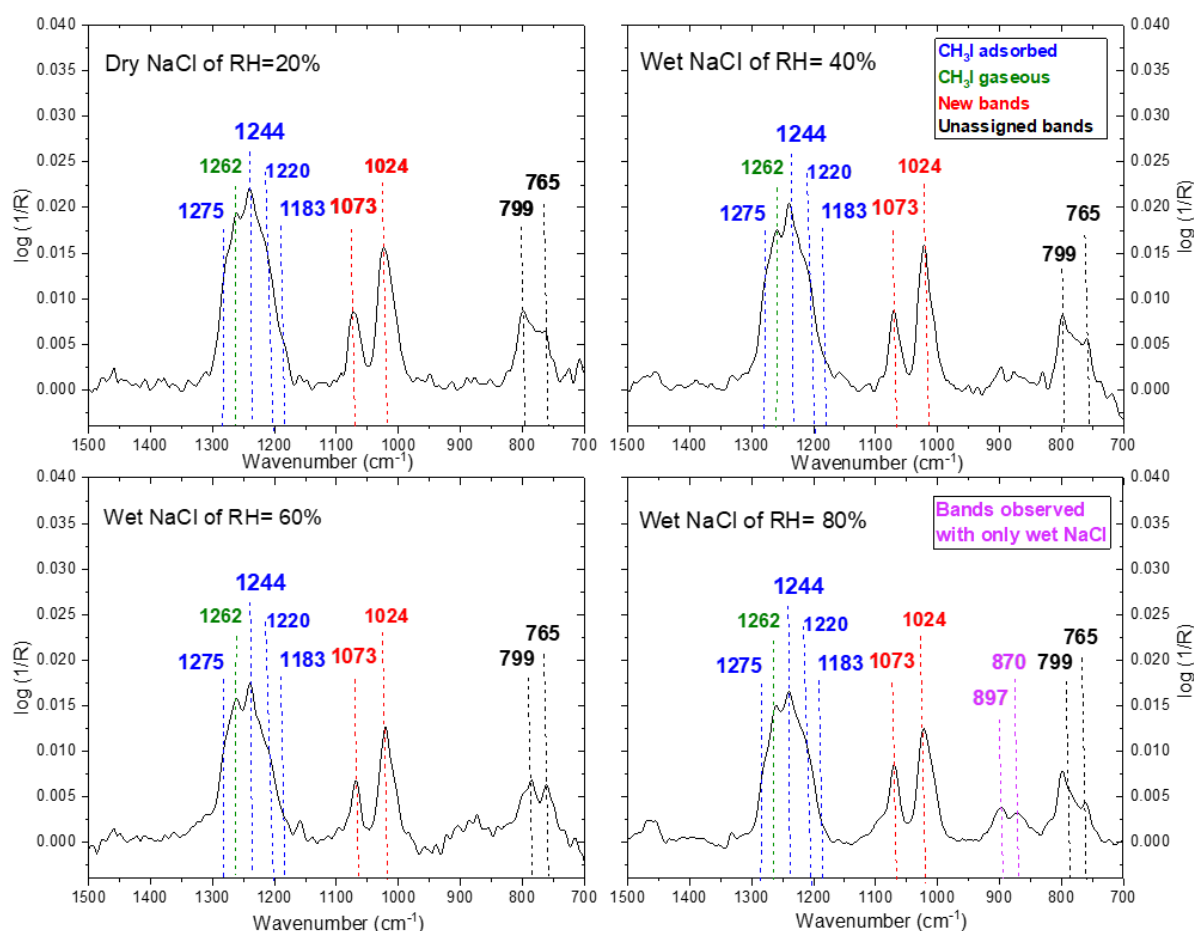
Figure 4. 20 DRIFTS spectra in the 1500-700 cm⁻¹ IR spectral range of dry and wet NaCl surface exposed to 5 hours of CH₃I (108mL.min⁻¹, 1000 ppm) continuous flow at 296 K and 1 atm. Bands in blue are adsorbed CH₃I on NaCl, green are gaseous CH₃I near the surface, black are unassigned bands, red are new bands and violet are bands observed with only wet NaCl.

The main IR bands related to both gaseous CH_3I at the NaCl surface and to the adsorbed CH_3I are observed for the wet NaCl experiments, whatever the RH values (Figure 4.19 and Figure 4.20). The new bands at 1073 and 1024 cm^{-1} are also observable and do not present any major variation with the increasing RH.

Additional bands with a low intensity are observed at 2935 and 2924 cm^{-1} when NaCl is exposed to RH=60% and RH=80%, respectively (see Figure 4.19). Compared to CH_3I adsorbed on various surfaces (see Tables 4.12 and 4.13), both 2924 and 2935 cm^{-1} can be assigned to the CH_3 symmetric stretching mode of adsorbed CH_3I.

Additional bands with a low intensity are observed at 897 and 870 cm^{-1} when NaCl is exposed to RH, the intensity of these bands increase with the RH value and are clearly seen for RH=80%. The bands at 899 and 870 cm^{-1} can be assigned to the CH_3 rocking of adsorbed CH_3I (see Table 4.13), respectively.

4.2.2.2 Influence of water on the CH₃I desorption

To investigate the effect of water on the adsorbed CH_3I, a wet Ar was flowed continuously (108mL.min^{-1}) for 40 minutes under RH=50% after 5 hours of continuous exposure of dry NaCl to CH_3I (1000ppm, 108mL.min^{-1}) (see section 4.1.4.2 and Table 4.9). The DRIFTS spectra in the zoomed CH_3 deformation and rocking (1350-700 cm^{-1}) spectral regions are shown in Figure 4.21.
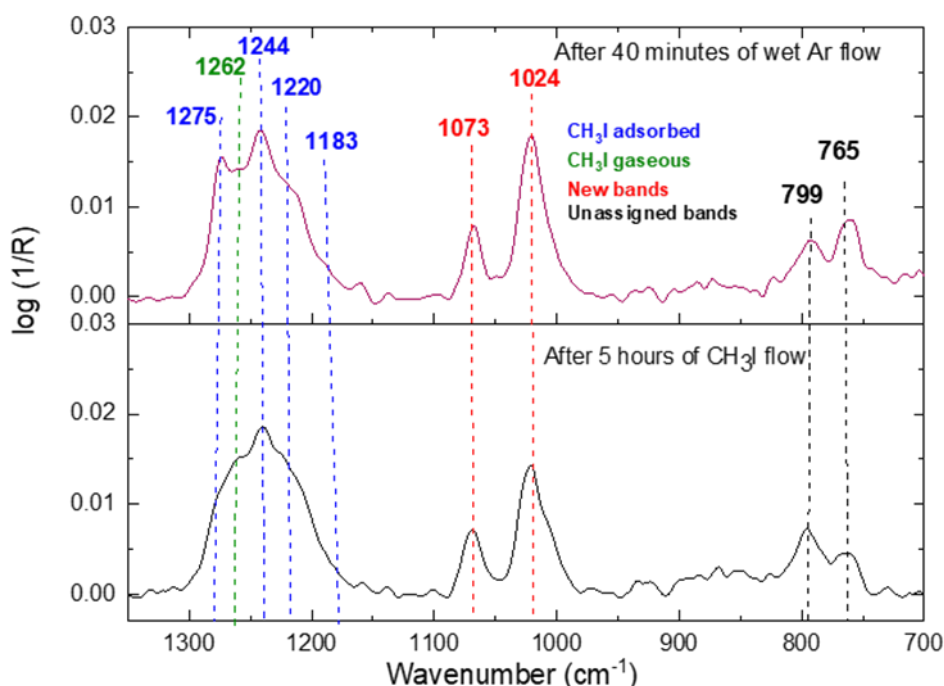
Figure 4. 21 DRIFTS spectra in the 1350-750 cm^{-1} IR spectral range of dry NaCl surface (RH=20%) exposed to 5 hours of continuous CH₃I flow (108mL.min^{-1}, 1000 ppm) and then to 40 minutes of wet Ar continuous flow (RH=50%) at 296 K and 1 atm. Bands in blue are adsorbed CH₃I on NaCl, green are gaseous CH₃I near the surface, black are unassigned bands and red bands are new bands.

We did not observe any major difference under wet Ar flow (RH=50%), except that the band at 1262 cm^{-1} corresponding to CH_3I in gas phase seems to disappear (Figure 4.21).

4.3. Time evolution of CH₃I on NaCl surface during CH₃I exposure, static and Ar flow phases

In this section, the time evolution of adsorbed methyl iodide on NaCl surface is discussed. CH_3I exposure phase, featuring exposure of NaCl to a continuous flow of gaseous CH_3I, static phase featuring static condition and continuous flow of pure argon are considered. Discussion mainly focusses on the CH_3I spectral evolution in deformation region featuring the most intense adsorption bands (1400-900 cm^{-1}). The kinetic parameters of methyl iodide adsorption in dry

conditions are then determined: adsorption rate, uptake coefficient and global energy of adsorption.

4.3.1 Evolution of CH₃I on NaCl surface in dry conditions

4.3.1.1 Experiment with exposure to CH₃I during 5 hours

The experiment was conducted as described in section 4.1.4.1 (Table 4.2) and repeated three times. For each repeat, the spectra showed a similar time evolution. Time evolution in the CH₃I deformation region (1400-900 cm^{-1}) is reported in Figure 4.22 for the CH₃I exposure phase and in Figure 4.23 for the static and dynamic argon flow phases.
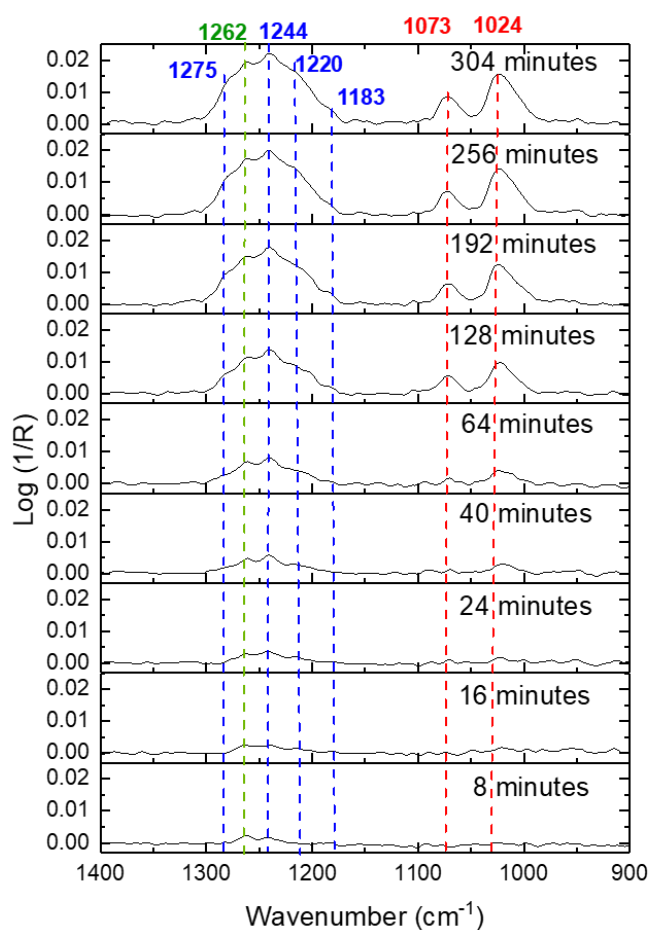
Figure 4. 22 DRIFTS spectra in the deformation (1400-900 cm^{-1}) of NaCl surface as a function of exposure time of the continuous CH₃I (108mL.min^{-1}, 1000 ppm) flow at 296 K and 1 atm. Bands in blue are adsorbed CH₃I on NaCl, green are gaseous CH₃I near the surface and red are new bands.
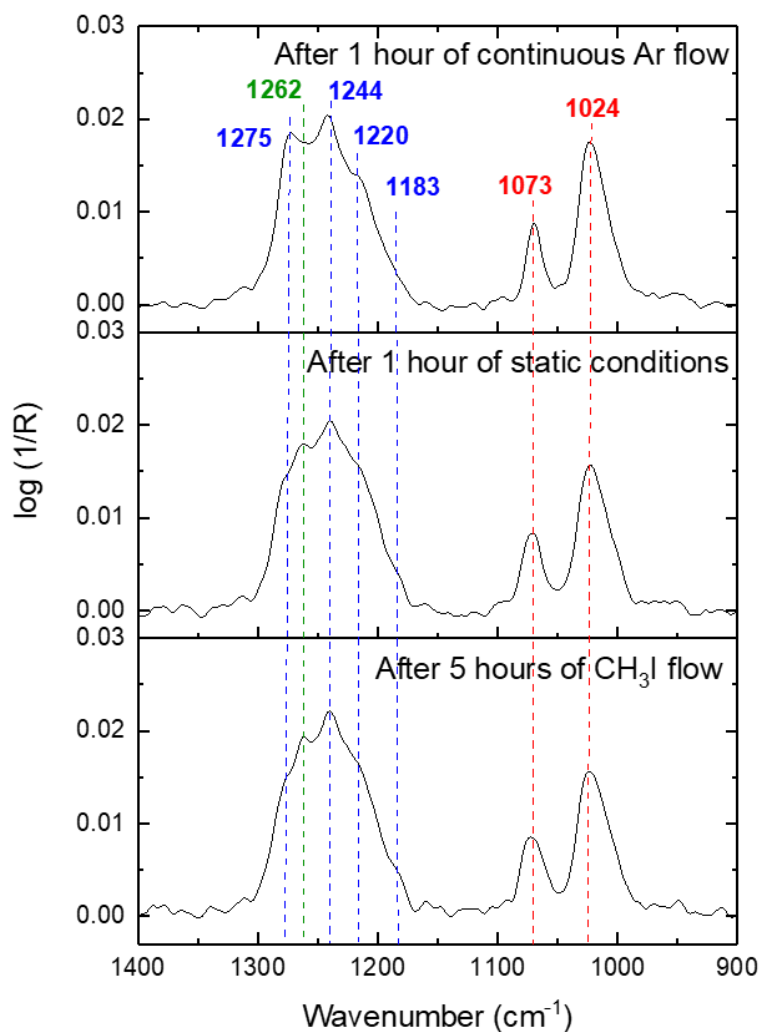
Figure 4. 23 DRIFTS spectra of NaCl after 5 hours of CH₃I continuous flow, then under static conditions for 1 hour and finally under 1 hour of continuous Ar flow in the spectral range 1400-900 cm⁻¹. Bands in blue are CH₃I adsorbed on NaCl, in green are gaseous CH₃I and red are new bands.

The time evolution of band area is reported in Figure 4.24 for the band at 1262 cm^{-1} assigned to gaseous CH$_3$I. The band at 1262 cm^{-1} seems to be stable over time in both CH$_3$I exposure and static phase. Then it seems to disappear under Ar flow as shown in Figure 4.24. The complete disappearance of CH$_3$I gaseous band under Ar flow (see Figure 4.23 and Figure 4.24), agrees with the assignment of the 1262 cm^{-1} band to the gaseous CH$_3$I near the NaCl surface.
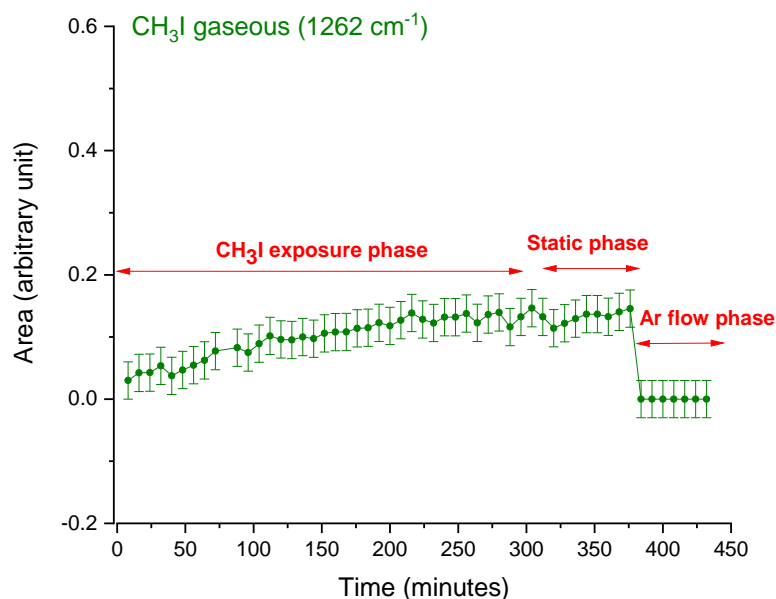
Figure 4. 24 Area of the 1262 cm^{-1} as a function of time during CH$_3$I exposure, static phase and Ar flow phases. The isolated bands are determined using Gaussian fit function. Exposure phase denotes the continuous flow of 108 mL.min^{-1} of CH$_3$I (1000 ppm) on NaCl. The static phase denotes the static conditions after 5 hours of CH$_3$I flow and Ar flow phase denotes the continuous Ar flow after the static conditions.

In Figure 4.22, we observed an increase of the IR bands intensity of the CH$_3$I adsorbed bands with increasing the exposure time. CH$_3$I adsorbed bands at 1244 and 1220 cm^{-1} clearly appeared as soon as the first spectrum is recorded i.e; at 8 minutes. Shoulder bands of adsorbed CH$_3$I at 1275 and 1183 cm^{-1} started to appear after 16 minutes.

Considering that the bands at 1275, 1244, 1220 and 1183 cm^{-1} are markers of CH$_3$I adsorption, thus the evolution of the sum of these band area has been considered in Figure 4.25. No apparent desorption was observed for the adsorbed CH$_3$I bands by stopping the flow of CH$_3$I and keeping the cell under static conditions or by continuous flow of Ar as also seen in Figure 4.23. A slight evolution of the CH$_3$I adsorption band area versus time is observed when the surface is exposed to a continuous Ar flow, that may be explained by the gas phase released.

The new intense bands at 1073 and 1024 cm^{-1} are clearly seen after 40 and 24 minutes, respectively (see Figure 4.22). Figure 4.26 displays the area time evolution of the new bands at 1073 and 1024 cm^{-1} during CH$_3$I exposure, static and Ar flow phases.
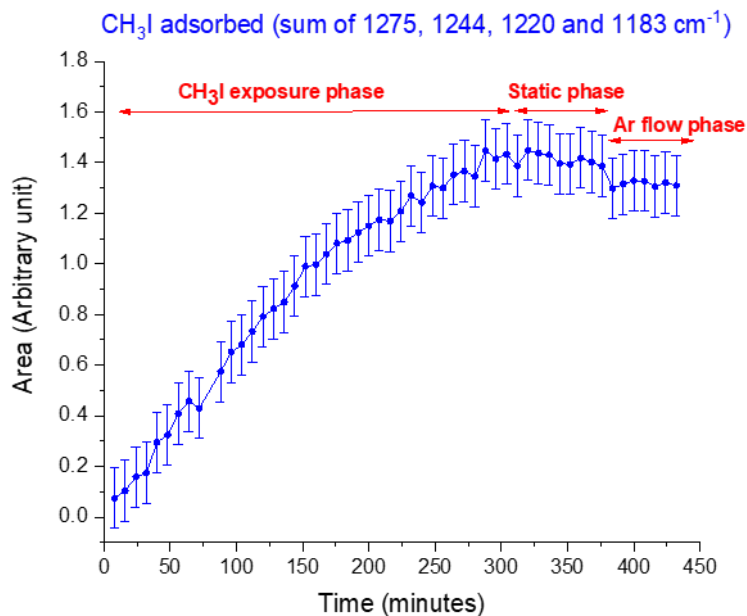
Figure 4. 25 Sum of the area of the 1275, 1244, 1220 and 1183 cm^{-1} bands as a function of time during CH$_3$I exposure, static and Ar flow phases of CH$_3$I on NaCl. The decomposed area is determined using Gaussian fit function. Exposure phase denotes the continuous flow of 108 mL.min^{-1} of CH$_3$I (1000 ppm) on NaCl. The static phase denotes the static conditions after 5 hours of CH$_3$I flow and Ar flow phase denotes continuous Ar flow after the static conditions.
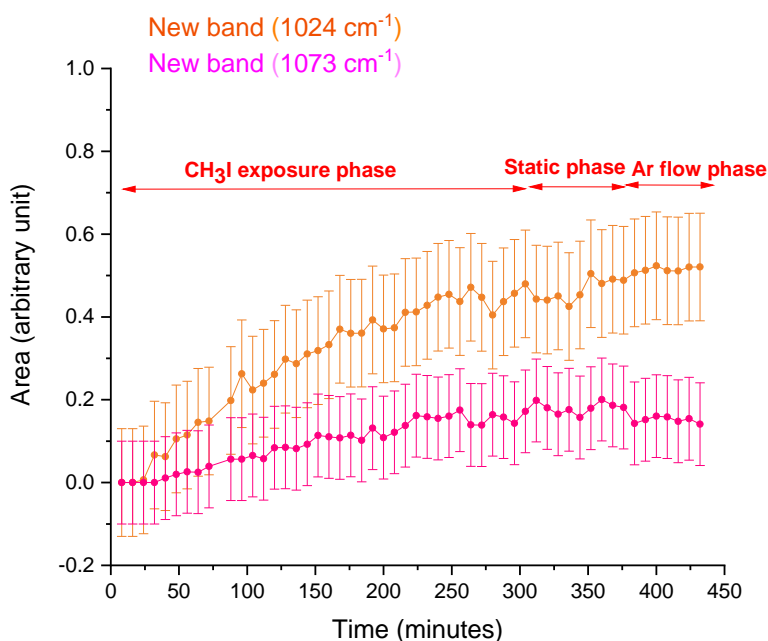
Figure 4. 26 Area of the 1073 and 1024 cm^{-1} bands as a function of time during CH$_3$I exposure, static and Ar flow phases of CH$_3$I on NaCl. The decomposed area is determined using Gaussian fit function. Exposure phase denotes the continuous flow of 108 mL.min^{-1} of CH$_3$I (1000 ppm) on NaCl. The static phase denotes the static conditions after 5 hours of CH$_3$I flow and Ar flow phase denotes continuous Ar flow hour after the static conditions.

The new bands at 1073 and 1024 cm^{-1} increases as function of time in the exposure phase. These new bands remain stable during static and Ar flow phases. (Figure 4.26). The evolution

of these bands is directly correlated with the well identified bands related to CH$_3$I adsorption as seen in Figure 4.27. Thus, in the following sections, the sum of the band areas at 1275, 1244, 1220, 1183, 1073 and 1024 cm^{-1} will be considered to quantify CH$_3$I adsorption on NaCl (i.e. all the bands related to absorbed CH$_3$ in the CH$_3$ spectral deformation region).
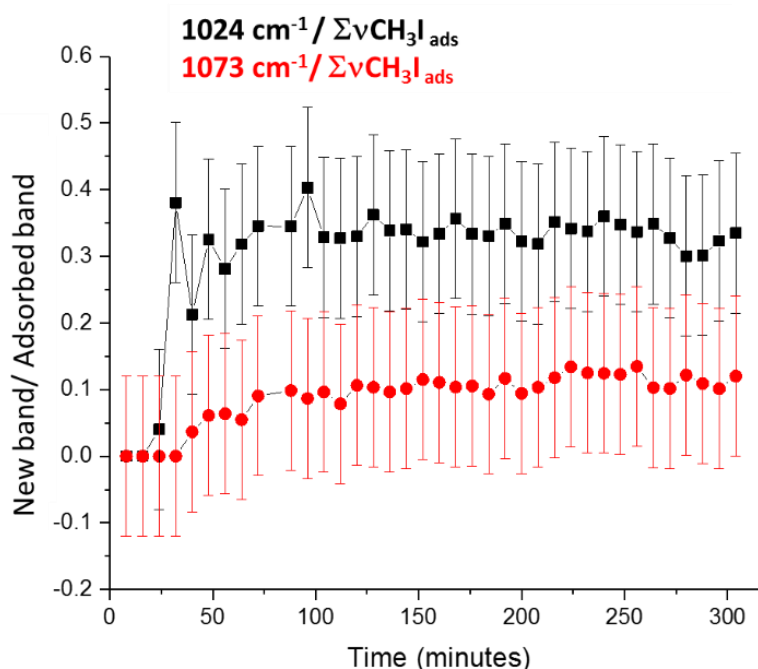
Figure 4. 27 Time evolution of the band area ratio during the CH$_3$I exposure phase: ratio of the Area of the new band (1073 and 1024 cm^{-1} respectively)/ Area of the$\Sigma\nu$CH$_3$I $_{ads}$ (sum of the area 1275, 1244, 1220 and 1183 cm^{-1} bands).

During the CH$_3$I exposure phase, the evolution of the adsorption versus time can be interpolated by a linear function. The rate of methyl iodide adsorption can then be determined from the linear interpolation of the adsorption band area curve versus time as shown in Figure 4.28.
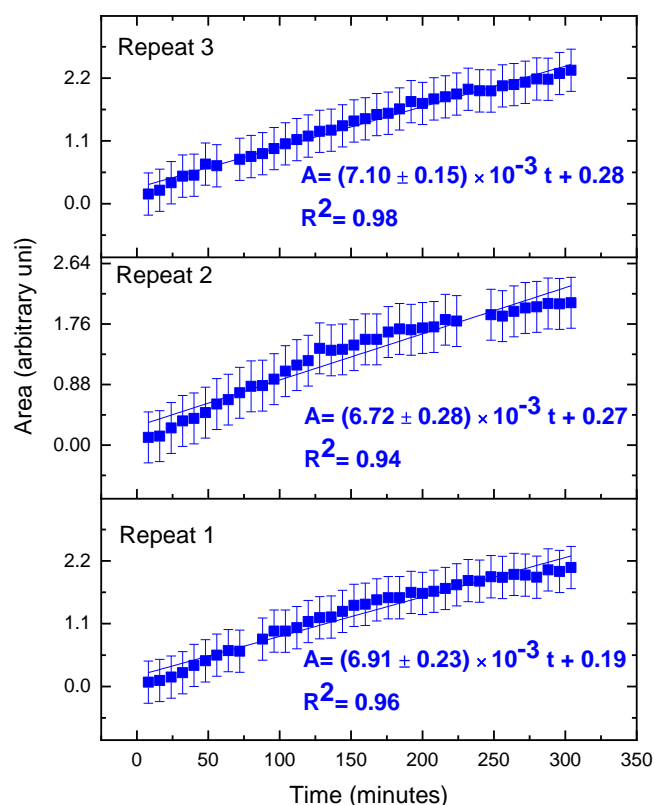
Figure 4. 28 Sum of the area of 1275, 1244, 1220, 1183, 1073 and 1024 cm^{-1} bands as a function of time during exposure phase of CH_3I on NaCl, repeated three times. The decomposed area of 1275, 1244, 1220 and 1183 cm^{-1} is determined using Gaussian fit function. Exposure phase denotes the continuous flow of 108 $mL.min^{-1}$ of CH_3I (1000 ppm) on NaCl. A: area and t= time.

It is observable from Figure 4.28 that the rate of adsorption of CH_3I is repeatable. The average rate of adsorption was found to be $(6.91 ± 0.33) × 10^{-3}$ arbitrary unit.min^{-1}.

During the static and Ar flow phases, the slight decrease which is observed (Figures 4.25 and 4.26) can be interpreted as a desorption of methyl iodide from the NaCl surface. An estimated calculation of the loss have been conducted as following and results are shown in Table 4.18:

1- Determination of CH_3I adsorbed band area of the exposure phase (A_{exp}) after 5 hours of CH_3I continuous flow (end of exposure phase, 304 minutes in Figures 4.25 and 4.26). Area is the sum of the decomposed bands area at 1275, 1244, 1220, 1183, 1073 and 1024 cm^{-1}.

2- Determination of average area of the CH_3I adsorbed band during 1 hour of static conditions (A_{static}) (see Figures 4.25 and 4.26, static phase). Area is the sum of the decomposed bands area at 1275, 1244, 1220, 1183, 1073 and 1024 cm^{-1}.

3- Determination of average area of the CH$_3$I adsorbed band under Ar flow (A$_{Ar}$) over the last 30 minutes of the Ar flow (i.e. last four points in Figures 4.25 and 4.26) of the Ar flow phase. Area is the sum of the decomposed bands area at 1275, 1244, 1220, 1183, 1073 and 1024 cm^{-1}.

4- Calculation of Loss during static phase: (A$_{exp}$ – A$_{static}$) and comparison to the ± uncertainty limit interval of band aera determined in at 95% confidence level (see section 4.1.2.4).

5- Calculation of Loss during Ar flow phase: (A$_{exp}$ – A$_{Ar}$) and comparison to the ± uncertainty limit interval of band aera determined in at 95% confidence level (see section 4.1.2.4).

Table 4. 18 The calculated loss of adsorbed CH$_3$I between exposure phase and static and Ar flow phases. A is the sum of the area of 1275, 1244, 1220, 1183, 1073 and 1024 cm^{-1} bands. A$_{exp}$ denotes the area at the end of exposure phase, A$_{static}$ denotes the average area during static phase and A$_{Ar}$ denotes the average area of the last 32 minutes in Ar flow phase.

Spectral Region	Adsorbed CH$_3$I in CH$_3$ deformation region
Band area uncertainty (section 4.1.2.4)	**0.37**
CH$_3$I exposure phase	
Duration	5 hours
A$_{exp}$: after 5 hours	2.09 ± 0.37
Static phase	
Duration	1 hour
A$_{static}$: average during 1 hour	2.05 ± 0.03
Loss (difference with exposure phase)	0.04 ± 0.37
Ar flow phase	
Duration	1 hour
A$_{Ar}$: average of the last 30 minutes	1.98 ± 0.02
Loss (difference with exposure phase)	0.11 ± 0.37

Thus, the small decrease of adsorbed band area observed under Ar flow was found to be 0.04 (arbitrary unit) which corresponds to the uncertainty limit of band area (see Table 4.18). Therefore, this small decrease can not be accounted for a loss.

4.3.1.2 Experiment with shorter exposure duration and longer desorption phases

Experiments with shorter CH$_3$I exposure phase duration (only 2 hours) and longer static (24 hours) and Ar flow (8 hours) phases were conducted to investigate the capability of adsorbed CH$_3$I to desorb – as described in Table 4.3 (see section 4.1.4.1). Experiments were performed at 296 K.

No desorption is observed for the static and continuous Ar flow conditions as shown in Figure 4.29 and Table 4.19. This indicate that the CH_3I is strongly adsorbed on NaCl.
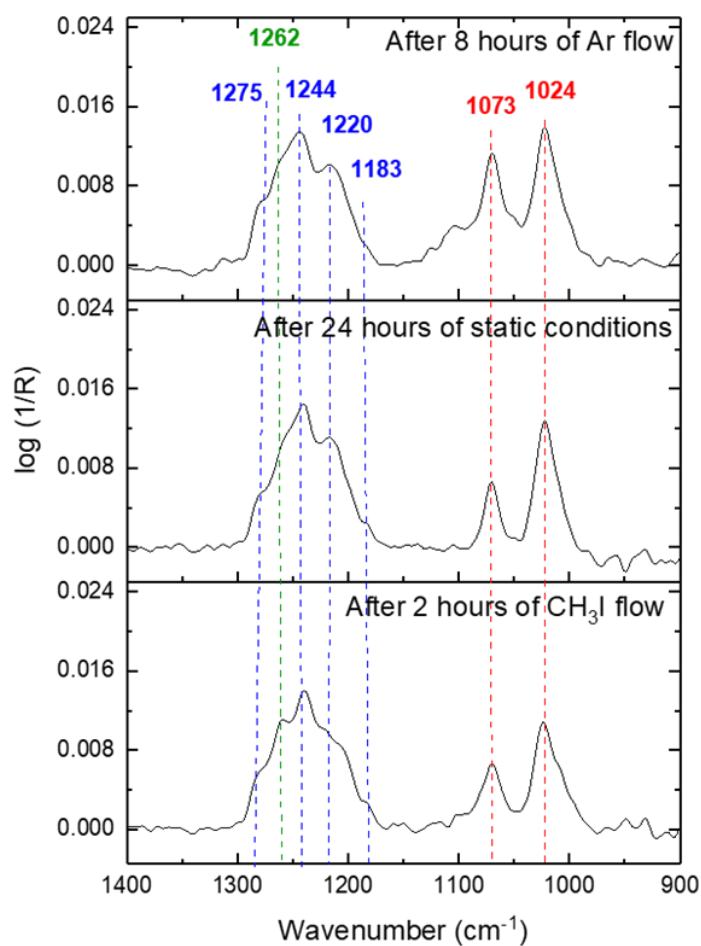
Figure 4. 29 DRIFTS spectra of NaCl after 2 hours of CH_3I continuous flow, then after static conditions for 24 hours and finally after 8 hours of Ar flow in the 1400-700 cm^{-1} spectral region. Bands in blue are adsorbed CH_3I, in green are gaseous CH_3I and red bands are new bands.

Spectral Region	Adsorbed CH₃I in CH₃ deformation region
Band area uncertainty (section 4.1.2.4)	**0.37**
CH₃I exposure phase	
Duration	2 hours
A$_{exp}$: after 2 hours	1.30 ± 0.37
Static phase	
Duration	24 hours
A$_{static}$: average of the last 30 minutes	1.30 ± 0.02
Loss (difference with exposure phase)	0
Ar flow phase	
Duration	8 hours
A$_{Ar}$: average of the last 30 minutes	1.34 ± 0.02
Loss (difference with exposure phase)	0

4.3.1.3 Experiment by increasing temperature during the Ar flow phase

Experiment conditions are reported in Table 4.4 (section 4.1.4.1). Firstly, the duration of the exposure phase was shorten to one hour, then the static phase lasted 4 hours. These two phases were performed at 296K. The dynamic argon phase lasted for one hour at 296K and then the NaCl sample was heated at a rate of 3K/min until 623K – still under argon flow in order to activate the desorption process (if any). Spectra recording was performed at 373 K, 473 K and 623K. Spectra are displayed in Figure 4.30 (deformation spectral zone). Compared to the spectrum recorded at the end of the exposure phase, no significant changes are observed at the end of the static phase nor at the end of the Ar flow phase at 296 K – consistently with previous tests. At 373 K and 473 K, the spectrum shows a small decrease in the bands intensity (Figure 4.30). However, this decrease is unmeasurable as shown in Table 4.20. Whereas, at 623 K the spectrum is too perturbed for a reliable interpretation (Figure 4.30).

Therefore, the non-desorbing capability of CH₃I under different static, Ar flow and temperature conditions suggests that CH₃I is strongly bonded to NaCl and that the CH₃I uptake by NaCl is occurring via chemisorption process.
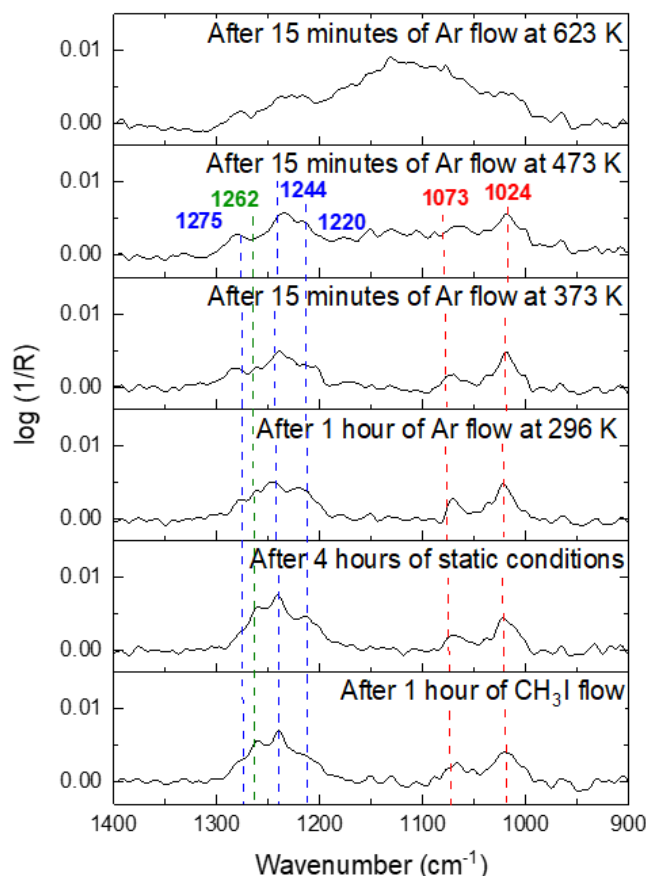
Figure 4. 30 DRIFTS spectra of NaCl in the spectral range 1400-900 cm^{-1} after 1 hour of CH$_3$I continuous flow, then under static conditions for 4 hours and finally under Ar flow at 296 K for 1 hour, at 373 K for 15 minutes , 473 K for 15 minutes and 623 K for 15 minutes. Bands in blue are CH$_3$I adsorbed on NaCl, green are gaseous CH$_3$I and red bands are new unidentified bands.

Table 4. 20 The calculated loss of adsorbed CH$_3$I between exposure phase and static and Ar flow phases. A is the sum of the area of 1275, 1244, 1220, 1183, 1073 and 1024 cm^{-1} bands. A$_{exp}$ denotes the area at the end of exposure phase, A$_{static}$ denotes the average area of the last 32 minutes in static phase and A$_{Ar}$ denotes the area at different temperature in Ar flow phase

Spectral Region	Adsorbed CH$_3$I in CH$_3$ deformation region
Band area uncertainty (section 4.1.2.4)	0.37
CH$_3$I exposure phase	
Duration	1 hour
A$_{exp}$: after 1 hour	0.46 ± 0.37
Static phase	
Duration	1 hour
A$_{static}$: after 4 hour	0.48 ± 0.37
Ar flow phase	
Duration	2 hours
A$_{Ar}$: Area at 296 K	0.42 ± 0.37
A$_{Ar}$: Area at 373 K	0.48 ± 0.37
A$_{Ar}$: Area at 473 K	0.39 ± 0.37

4.3.1.4 Experiments featuring different CH₃I concentrations in the gas phase

Figure 4.31 shows the time evolution of the adsorbed CH_3I on NaCl with CH_3I gaseous concentration of 1000, 500 and 200 ppm (see section 4.1.4.1 and Table 4.5).

Figure 4. 31 Sum of the area of 1275, 1244, 1220, 1183, 1073 and 1024 cm⁻¹ bands as a function of time during exposure phase of CH₃I on NaCl. The decomposed area of 1275, 1244, 1200 and 1183 cm⁻¹ is determined using Gaussian fit function. Exposure phase denotes the continuous flow of 108 mL.min⁻¹ of 1000 (first repeat), 500 ppm (first repeat) and 200 ppm of CH₃I in gas phase. A: area and t= time.

It is observable from Figure 4.31 that by decreasing the gaseous CH_3I concentration by factor 2, the rate of CH_3I adsorption diminished by ~ 2 i.e. $(6.91\pm0.23) \times 10^{-3}$ arbitrary unit.min⁻¹ for 1000 ppm to $(3.91\pm0.05) \times 10^{-3}$ arbitrary unit.min⁻¹ for 500 ppm. Similarly, when decreasing the gaseous CH_3I concentration by 5, the rate of CH_3I adsorption diminished by ~ 5 i.e. $(6.91\pm0.23) \times 10^{-3}$ arbitrary unit.min⁻¹ for 1000 ppm to $(1.54\pm0.06) \times 10^{-4}$ arbitrary unit.min⁻¹ for 200 ppm. This signify that the adsorption rate depends on the concentration of gaseous CH_3I. Assuming that this relation can be extrapolated to the low CH_3I concentrations of the atmosphere (atmospheric $[CH_3I]_g$ maximum is 2000 ppt, see chapter 2, section 2.1), then we would expect very low CH_3I adsorption bands (even below the detection limit of our spectrometer) if we consider the case of NaCl exposed to CH_3I gaseous concentration close to its atmospheric range. Indeed, in this case, the adsorption rate will be diminished by a factor 5×10^5 (as the ratio of CH_3I concentration in our experiments relative to the atmospheric maximum concentration).

Table 4.21 summarizes the rate of CH_3I adsorption bands in arbitrary unit.min⁻¹.

Table 4. 21 Summary of the rate in arbitrary unit.min^{-1} versus CH$_3$I concentration in gas phase. The sum of the area of the bands at 1275, 1244, 1220 and 1183 cm^{-1} represent the adsorbed CH$_3$I referenced in the literature. The bands at 1073 and 1024 cm^{-1} represent the adsorbed C$_{3v}$ CH$_3$I (new adsorption geometry). The last column (sum of the area of all CH$_3$ bands in the deformation region related to adsorbed CH$_3$I) represent the total CH$_3$I adsorbed on NaCl. The rate is determined from the slope of Area (arbitrary units) versus time (minutes).

Band	Adsorption bands			
	Sum of (1275 ,1244, 1220, 1183 cm^{-1})	1024 cm^{-1}	1073 cm^{-1}	Sum of (1275 ,1244, 1220, 1183, 1073, 1024 cm^{-1})
[CH$_3$I]$_{gaseous}$ (ppm)	Rate in arbitrary unit.min^{-1} (slope of area versus time)			
1000	(4.69±0.30) ×10^{-3}	(1.60±0.08) ×10^{-3}	(6.16±0.27) ×10^{-4}	(6.91±0.23) ×10^{-3}
500	(2.39 ±0.06) ×10^{-3}	(1.07±0.03) ×10^{-3}	(4.27±0.14) ×10^{-4}	(3.91 ±0.05) ×10^{-3}
200	(9.80±0.86) ×10^{-4}	(3.92±0.18) ×10^{-4}	(1.76±0.14) ×10^{-4}	(1.54±0.06) ×10^{-3}

Further, the rate order of adsorbed CH$_3$I on NaCl can be determined from the slope of the bi-logarithmic plot of rate versus the concentration of CH$_3$I in gas phase [6, 8, 34]. Slope of the bi-logarithmic plot of the rate of the sum of 1275, 1244, 1220 and 1183 cm^{-1} bands is (9.34±0.31) ×10^{-1} as shown in Figure 4.32. To recall 1073 and 1024 cm^{-1} represent the CH$_3$I C$_{3v}$ geometrical configuration on NaCl. The bi-logarithmic plot of rate of adsorption bands at 1073 and 1024 cm^{-1} versus CH$_3$I concentration gives a slope of (8.26±1.41) ×10^{-1} and (8.89±1.46) ×10^{-1}, respectively (see Figure 4.32). Finally, the slope of the bi-logarithmic plot of the rate of the sum of 1275, 1244, 1220, 1183, 1073 and 1024 cm^{-1} bands is (8.41±0.54) ×10^{-1} as shown in Figure 4.32. This indicate that the different geometrical configuration of adsorbed CH$_3$I on NaCl follows first order rate.
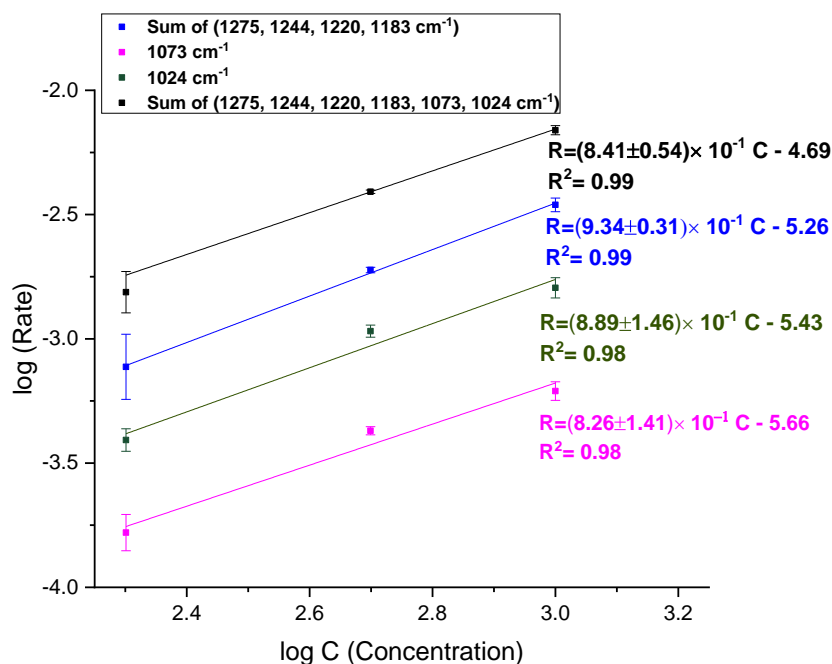
Figure 4. 32 Double log curve of rate of adsorbed CH₃I (sum of band aera at 1275, 1244, 1220, 1183 cm⁻¹), new band area at 1073 cm⁻¹ and 1024 cm⁻¹, and sum of all CH₃ adsorption related bands in the CH₃ spectral deformation region (sum of band area at 1275, 1244, 1220, 1183, 1073 and 1024 cm⁻¹) versus CH₃I gaseous concentration at 1000, 500, 200 ppm.

4.3.1.5 Experiment featuring variation in contact time

The influence of the contact time on the adsorption rate was investigated. The experiments featured a CH_3I gas phase concentration of 500 ppm and contact time between the gas flow and the solid bed of 55 ms and 27 ms respectively (see section 4.1.4.1, Table 4.6).

A similar adsorption rate is observed as shown in Figure 4.33: (3.21 ±0.25) ×10⁻³ arbitrary unit.min⁻¹ for a contact time of 27 ms and (3.90 ±0.05) ×10⁻³ arbitrary unit.min⁻¹ for a contact time of 55 ms. This shows that the contact time has no effect on the evolution of the adsorbed CH_3I as expected.
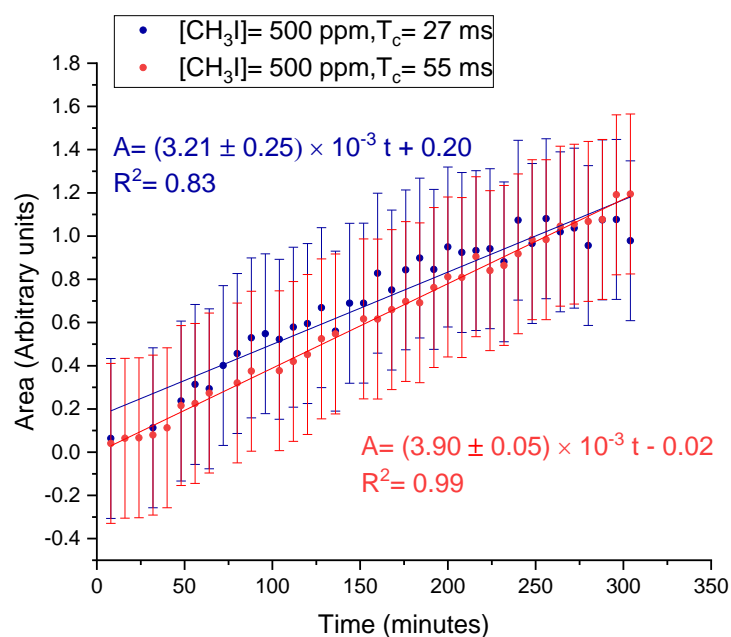
Figure 4. 33 Sum of the area of 1275, 1244, 1220, 1183, 1073 and 1024 cm^{-1} bands as a function of time during exposure phase. The decomposed area is determined using Gaussian fit. Exposure phase denotes the continuous flow of 108 mL.min^{-1} and 216 mL.min^{-1} of CH$_3$I (500 ppm) on NaCl. A: area and t= time.

4.3.2 CH$_3$I exposure on dry NaI and KBr

The experiments were conducted by the continuous flow of CH$_3$I (108mL.min^{-1}, 1000 ppm) for 1 hour on dry NaI and KBr salts (section 4.1.4.1, Table 4.7) and compared to the adsorption on NaCl salt (Test conditions displayed in Table 4.2).

Figure 4.34 shows the adsorption rate of CH$_3$I on NaI, KBr and NaCl as a function of time.
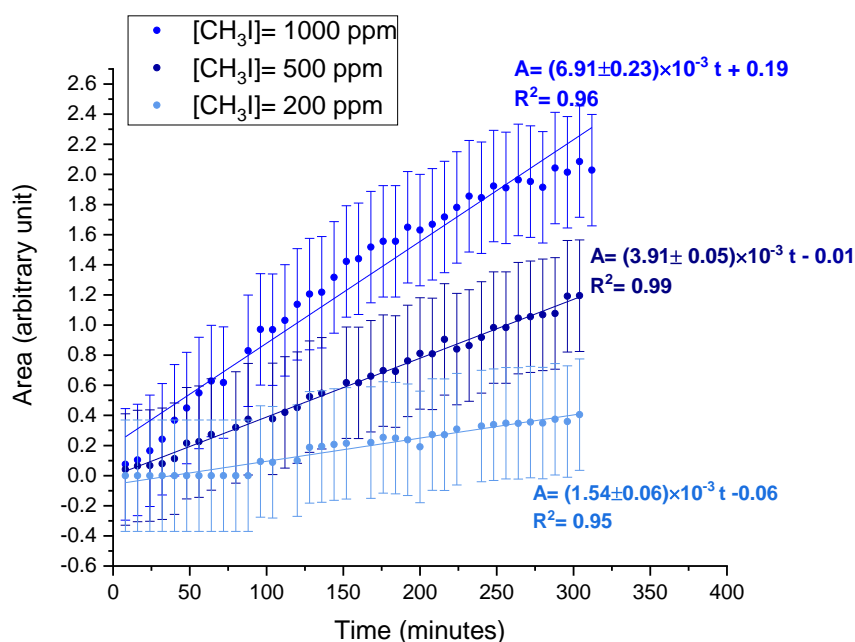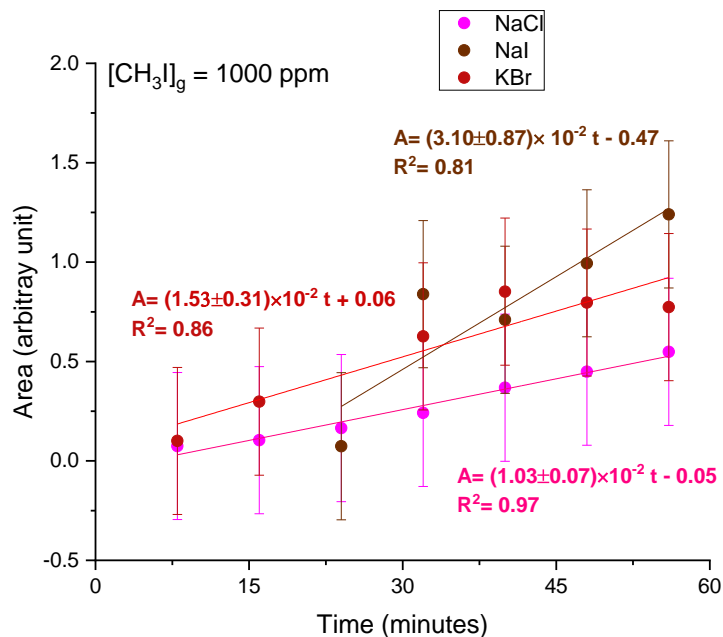
Figure 4. 34 Sum of the area of the 1275, 1244, 1220, 1183, 1073 and 1024 cm^{-1} bands as a function of time during exposure phase of CH$_3$I on NaCl, NaI and KBr. The decomposed area of 1275, 1244, 1220, 1183 cm^{-1} is determined using Gaussian fit function. Exposure phase denotes the continuous flow of 108 mL.min^{-1} of CH$_3$I (1000 ppm). A: area and t= time.

Adsorption rate are determined for one hour test duration for all conditions. In the case of NaCl experiment (Repeat 1), the initial adsorption rate determined for the first hour of exposure phase is slightly higher than that determined for the total exposure phase duration (5 hours, see Figure 4.25). For 1000 ppm of gaseous CH$_3$I the initial adsorption rate of methyl iodide on NaI is strongly enhanced with a rate of $(3.10\pm0.87) \times 10^{-2}$ arbitrary unit.min^{-1} compared to KBr and NaCl of $(1.53\pm0.31) \times 10^{-3}$ and $(1.03\pm0.07) \times 10^{-2}$ arbitrary unit.min^{-1}, respectively. Seemingly, the adsorption rate increases in the following order: NaCl < KBr < NaI. The change of adsorption rate with halide solid type indicates the influence of electronegativity on the adsorption of CH$_3$I on halide particles as stated previously in section 4.2.1.4.

4.3.3 Evolution of CH$_3$I on wet NaCl

Humid condition was conducted as described in see section 4.1.4.2 and Table 4.8. Wet NaCl samples were generated by exposition to an Ar flow of specific relative humidity value (RH=40, 60 and 80% at 296 K) during 40 minutes.

It is noticed that the CH$_3$I adsorption bands and new bands are observed only after 25 minutes of CH$_3$I flow, when the NaCl surface starts to dry (see Figure 4.35). The evolution of the adsorbed bands on wet NaCl is shown in Figure 4.35 and seems similar to the one observed on dry NaCl. For 1000 ppm of gaseous CH$_3$I the adsorption rate of CH$_3$I on wet NaCl $((7.12\pm0.09) \times 10^{-3}$ arbitrary unit.min$^{-1})$ is very close to the rate on dry NaCl $((6.91 \pm 0.23) \times 10^{-}$

arbitrary unit.min^{-1}). This indicate that wet NaCl seems to have no effect on the adsorption of CH$_3$I under continuous flow in our conditions. This result agrees with our previous observations showing that CH$_3$I has a low affinity for water.
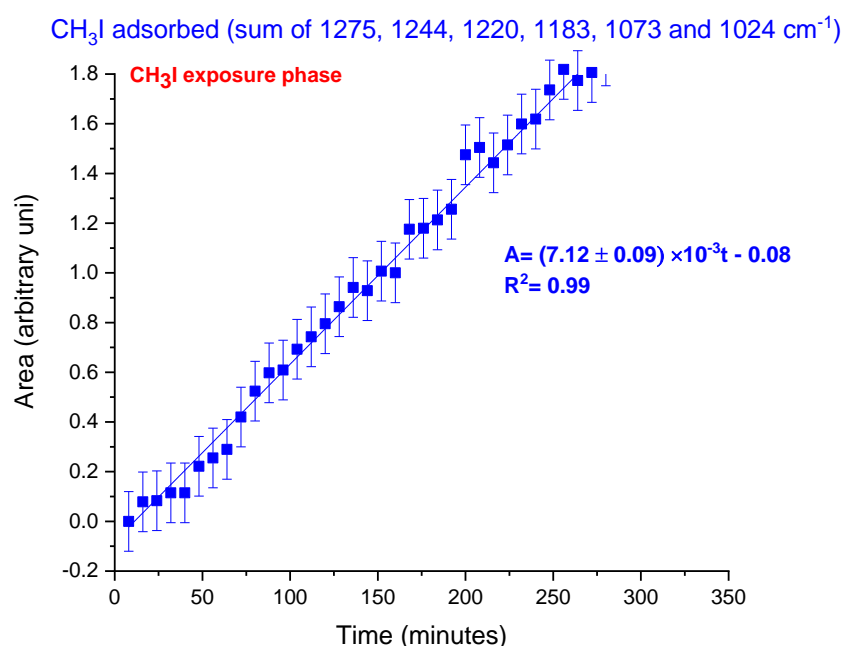
Figure 4. 35 Sum of the area of 1275, 1244, 1220, 1183, 1073 and 1024 cm^{-1} bands as a function of time during exposure phase. The decomposed area is determined using Gaussian fit. Exposure phase denotes the continuous flow of 108 mL.min^{-1} of CH$_3$I (1000 ppm) on wet NaCl (RH=60%). A: area and t= time.

4.3.4 Determination of uptake coefficient of CH$_3$I adsorption by NaCl surface

4.3.4.1 Quantification of iodine on NaCl

For a quantitative interpretation of the observed IR bands in terms of amount of methyl iodide taken up by NaCl, we assumed that the area of the bands assigned to adsorbed methyl iodide is proportional to the total amount of iodine taken up by NaCl (see pseudo absorbance equation in Table 4.1). This amount is determined by ICP MS analysis after NaCl dissolution in a given volume of alkaline solution (see section 4.1.3). Post test iodine quantification by ICP-MS was applied after tests performed in conditions corresponding to scenario i/ as reported in Table 4.2. For those tests (3 repeat), NaCl powder was recovered immediatelly after CH$_3$I exposure phase.

By applying the calculation shown in annex 7, the total amount of iodine taken up by NaCl was determined to be 521 ± 254 ppb at 95% confidence level after 5 hours of CH$_3$I continuous flow (1000 ppm, 108 mL.min^{-1}) on dry NaCl at 296 K and 1 atm. By converting, the concentration from ppb to iodine atoms.mg$_{NaCl}^{-1}$, we found a {CH$_3$I}$_{ads}$ of (1.68± 0.85) × 10^{14} molecule. mg$_{NaCl}^{-1}$.

Comparing the total amount of injected $[CH_3I]_g$ during the exposition phase to the total amount of adsorbed $[CH_3I]_{ads}$ on NaCl, we found that only 3.10^{-3} % of initially injected methyl iodide was found adsorbed on NaCl (see Table 4.22), indicating a very low residual amount of CH_3I on NaCl.

Table 4. 22 Calculation of %{CH₃I} residual on NaCl.

Total amount of injected gaseous CH_3I_g in molecules	Total amount of adsorbed CH_3I {CH_3I_{ads}} in molecules	% of CH_3I residual on NaCl = {CH_3I_{ads}} / CH_3I_g X 100
8.03×10^{20}	$(2.47 \pm 1.21) \times 10^{16}$	3×10^{-3} %

4.3.4.2 Conversion factor

The average total amount of iodine taken up by NaCl was found to be $(2.47 \pm 1.21) \times 10^{16}$ iodine atoms (average of the three tests) (see annex 7). The large uncertainty observed here is not unusual – as already mentioned in previous studies concerning gas solid interaction quantification [1]:

 (1) The consistent variation in manually solid grinding.
 (2) The consistent variation in packing of solid particles in the DRIFTS sample holder.
 (3) The very low gas-solid interaction.

Conversion of band area into quantity of adsorbed methyl iodide is then determined by the following relation:

$$F = \frac{Total\ amount\ of\ iodine\ taken\ by\ total\ solid}{Band\ area} \quad \text{[E4-6]}$$

The conversion factor (F) of $(1.14 \pm 0.37) \times 10^{16}$ at 95% confidence level is calculated (average of the three tests) for the sum of bands at 1275, 1244, 1220, 1183, 1073 and 1024 cm^{-1} (adsorbed CH_3I).

The adsorption of methyl iodide can be therefore converted from band area in arbitrary unit to the total number of iodine atoms by this conversion factor.

4.3.4.3 Uptake coefficient

The uptake coefficient, ɣ, is defined as the ratio of the gas-surface collision rate to the total gas-surface collision rate (see section 2.3.2, chapter 2). Saturation effect phase have been hardly reached after 5 hours of continuous CH_3I exposure time (see Figure 4.27). Thus, the

uptake in this work can be assumed as an average uptake during the 5 hours of CH_3I exposure. The uptake coefficient of CH_3I by the surface of the NaCl particles is [4, 35-37]:

$$\gamma = \frac{d\{CH_3I\}}{dt} \times \frac{1}{Z} \qquad\qquad \text{[E4-7]}$$

Where,

$$\text{Z: Rate of collision} = \frac{1}{4} \times \omega \times A \times [CH_3I]_g \qquad \text{[E4-8]}$$

$$\omega = [8RT/(\pi M)]^{1/2} \qquad\qquad \text{[E4-9]}$$

d{CH_3I}/dt is the surface adsorption rate of CH_3I on NaCl, $[CH_3I]_g$ denotes the concentration of CH_3I (molecule.m^{-3}) in the gas phase under 5 hours of constant flow, ω is the mean thermal velocity of CH_3I (210 m.s^{-1}) and A is the effective surface area (BET surface area × mass of NaCl).

BET surface area of NaCl was found to be 0.26 m^2/g typical of a non-porous material. It should be highlighted that two extreme cases of effective sample surface can be considered for calculating the uptake coefficient [36, 37]. If the interaction probability is high, the reactants would have no time to diffuse into the sample before reacting and the effective surface area will be the geometric surface area of the sample. If the interaction probability is low, the reactants may have enough time for diffusion into the entire sample and thus the BET surface area and geometrical surface are very close [37, 38]. The adsorption rate of CH_3I can be expressed as the slope of the integrated absorbance area against the time and multiplied by the conversion factor. Substituting the parameters into the formula, the average uptake coefficient is calculated for different experiment conditions as listed in Tables 4.23 and 4.24.

Table 4.23 summarize the average uptake coefficient values determined for the experiments featuring gaseous methyl iodide concentrations of 1000 ppm, 500 ppm and 200 ppm. Approximately close uptake values in the range of 10^{-11} are obtained under these different CH_3I gaseous concentrations. This feature is consistent with first order dependence of adsorption rate with gas phase concentration.

Assuming that the uptake is independent of gaseous methyl iodide concentration even outside the concentration range experimentally investigated, thus we can expect a very low methyl iodide uptake (~10^{-11}) on NaCl in environmental conditions i.e $[CH_3I]_g$ = 2000 ppt.

[CH$_3$I] in molecule.m^{-3}	T$_c$ in ms	Rate of collision in molecule. s^{-1}	Adsorption rate in molecule. s^{-1}	ɣ$_{ss}$
2.48 × 10^{22}	55	4.74 × 10^{22}	1.31 × 10^{12}	(2.76 ± 0.93) × 10^{-11}
1.24 × 10^{22}	55	2.37 × 10^{22}	7.40 × 10^{11}	(3.17 ± 1.05) × 10^{-11}
4.96 × 10^{21}	55	9.49× 10^{21}	2.92 × 10^{11}	(3.07 ± 1.04) × 10^{-11}

Even if the contact time is decreased by factor 2 (55 ms to 27 ms for 500 ppm of CH$_3$I gas phase concentration) (see Table 4.24), the average uptake (2.52 ± 0.89) × 10^{-11} remains close to the average uptake observed with 55 ms (2.76 ± 0.93) × 10^{-11}. This is consistent with the fact that contact time has no significant influence on adsorption rate as already discussed. Therefore, this result agrees with our expectation mentioned on section 4.1.4.1, where in contrary to gas phase monitoring, experiments based on surface monitoring are independent of contact time with surface.

Table 4. 24 Average uptake coefficient of CH$_3$I on NaCl particles for an exposure phase duration of 5 hours and under dry conditions and at 296K and 1 atm, 500 ppm= 1.24 × 10^{22} molecule.m^{-3}. T$_c$= contact time

[CH$_3$I] in molecule.m^{-3}	T$_c$ in ms	Rate of collision in molecule. s^{-1}	Rate of adsorption in molecule. s^{-1}	ɣ$_{ss}$
1.24 × 10^{22}	55	2.37 × 10^{22}	7.40 × 10^{11}	(2.76 ± 0.93) × 10^{-11}
1.24 × 10^{22}	27	2.37 × 10^{22}	5.97 × 10^{11}	(2.52 ± 0.89) × 10^{-11}

As seen in section 4.3.2 that the initial adsorption rate of CH$_3$I is highly enhanced with NaI. The initial uptake coefficient of CH$_3$I on KBr and NaI were estimated assuming i/ the same BET surface for KBr and NaI as for NaCl (powder grinded in the same manner) ii/ the same conversion factor of band area into methyl iodide mass taken up at the halide solid surface. On NaI, the initial uptake coefficient (calculated after one-hour exposure time) is strongly enhanced (1.24 ± 0.81) × 10^{-10} in comparison to NaCl (4.12 ± 1.48) × 10^{-11} and KBr (6.13 ± 3.18) × 10^{-11} (see Table 4.25). Thus, uptake coefficient can strongly varies based on the anion of the halide solid (i.e. Cl$^-$ for NaCl and I$^-$ for NaI). This highlights the influence of electronegativity on the adsorption of CH$_3$I on halide particles as stated previously in section 4.2.1.4.

Table 4. 25 Initial uptake coefficient of CH₃I (1000 ppm) on NaCl, NaI and KBr particles for an exposure phase duration of 1 hour and under dry conditions, 55 ms contact time and at 296 K and 1 atm. 1000 ppm= 2.48 × 10²² molecule. m⁻³.

Salt	[CH$_3$I] in molecule.m^{-3}	Rate of collision in molecule.s^{-1}	Rate of adsorption in molecule.s^{-1}	γ_0
NaCl	2.48×10^{22}	4.74×10^{22}	1.96×10^{12}	$(4.12 \pm 1.48) \times 10^{-11}$
NaI	2.48×10^{22}	4.74×10^{22}	5.89×10^{12}	$(1.24 \pm 0.81) \times 10^{-10}$
KBr	2.48×10^{22}	4.74×10^{22}	2.91×10^{12}	$(6.13 \pm 3.18) \times 10^{-11}$

The steady state uptake coefficient of Cl_2 on synthetic sea salt aerosols and both steady state and initial uptake of HOI, HOI/IONO$_2$, ICl on halide salts (see chapter 2, section 2.4.1) was found to be in the order of 10^{-2}. Similarly, the initial and steady state uptake of HOI, HI, IBr, ICl on amorphous ice, crystalline thin film ice or doped ice was found in the order of 10^{-2} (see chapter 2, section 2.4.2.1). On the other hand, the initial uptake of CH$_3$I and C$_2$H$_5$I on soot film or black carbon was also determined in the 10^{-2} order (see chapter 2, section 2.4.3). Therefore, it is clear that the uptake coefficient of CH$_3$I on NaCl of the order 2-3 10^{-11} is very low in comparison to the uptake previously found with other iodinated species. This indicates that the interaction of CH$_3$I with NaCl is very weak. This high difference in uptake coefficient can be due for instance to the high affinity of methyl iodide to soot particles and porosity of soot particles (BET surface area of soot particles is of 740 m^2/g [39]). To best of our knowledge the uptake coefficient of methyl halides (CH$_3$Br, CH$_3$Cl, CH$_3$I) with atmospheric aerosols was not investigated yet.

4.3.5 Rate evolution with temperature

With increasing the temperature during the exposure phase from 296 K up to 423 K (other experiment conditions being that of the dry experiments reported in Table 4.10 in section 4.1.4.3). All the observed bands are highly reduced as shown in Figure 4.36.

In Figure 4.36, the overlapped bands at 1275, 1262, 1244, 1220 and 1183 cm^{-1} become significantly more separated at 323 K and 348 K. The new bands at 1073 and 1024 cm^{-1} are less visible. Above 373 K the bands at 1220 and 1183 cm^{-1} disappear. The band at 1024 cm^{-1} is hardly observed. At 423 K, the new bands are no more observed. Only the strongest bands of the deformation region of CH$_3$ are still detectable at 1244 and 1262 cm^{-1}. On a whole, the overall interaction of CH$_3$I with NaCl decreases with the increase in temperature, indicating that temperature above room temperature hinders the adsorption of CH$_3$I on NaCl.
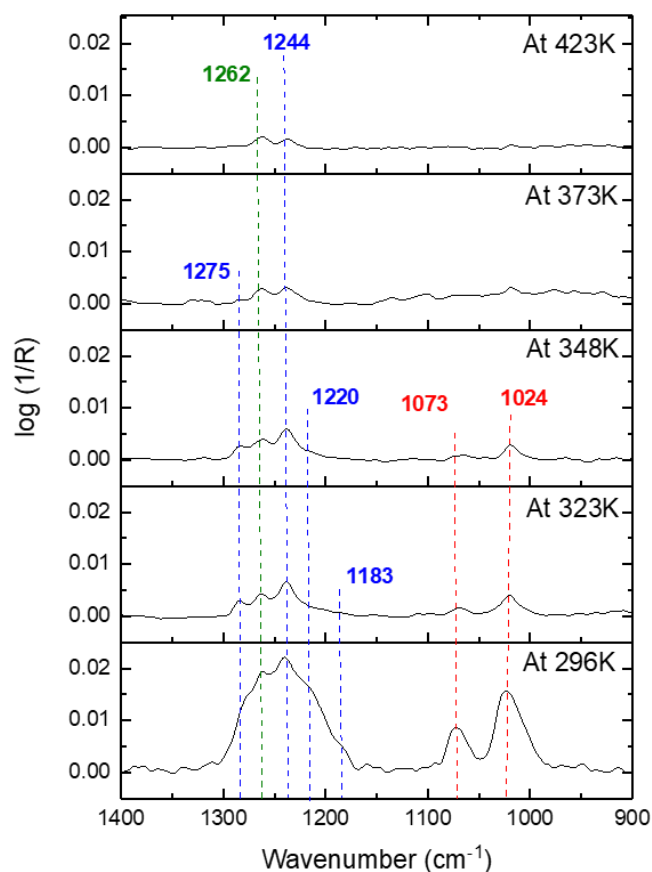
Figure 4. 36 DRIFTS spectra in the 1400-900 cm^{-1} IR spectral range of dry NaCl surface exposed for 5 hours to CH$_3$I continuous flow (108mL.min^{-1}, 1000 ppm) as a function of temperature at 1 atm. Bands in blue are CH$_3$I adsorbed by NaCl, green are the gaseous CH$_3$I and red are new bands.

The rate of the adsorption of CH$_3$I on NaCl were determined at a number of temperatures (296 K, 323 K, 348 K, 373 K and 423 K) as given in Table 4.26. The rate becomes slower and dispersed for temperatures above 296 K as shown in Table 4.26. Therefore, it is obvious that the temperature remarkably influences the uptake of CH$_3$I by NaCl.

This observation can be explained by the fact that the rate of reaction or adsorption increase as the temperature increase. When the temperature becomes high enough, the observed rate is no longer limited by the chemical details of the process, but rather by insufficient transport – gaseous species can no longer interact with the surface to match the adsorption kinetics.

Table 4. 26 Summary of observed rate of the area of the sum of 1275, 1244, 1220, 1183, 1073 and 1024 cm^{-1} bands at different temperature (in kelvin) during 5 hours of CH$_3$I flow (1000 ppm, 108 mL.min^{-1}). Rate is determined from the slope of area of the sum of 1275, 1244, 1220, 1183, 1073 and 1024 cm^{-1} bands versus time. R^2 is the coefficient of the linear fit.

Temperature (K)	1/T	Rate of the area versus time			
		Rate of CH$_3$I adsorption	R^2	Confidence interval on rate +/- at 95 % level	ln(Rate)
296	3.38×10^{-3}	6.91×10^{-3}	0.96	4.67×10^{-4}	-4.97
323	3.10×10^{-3}	1.24×10^{-3}	0.95	9.70×10^{-5}	-6.69
348	2.87×10^{-3}	1.01×10^{-3}	0.90	1.12×10^{-4}	-6.90
373	2.68×10^{-3}	2.15×10^{-4}	0.41	8.54×10^{-5}	-8.44
423	2.38×10^{-3}	-2.36×10^{-5}	0.04	3.97×10^{-2}	Negative, not included

Arrhenius equation is usually used to estimate the activation energy of adsorption for an elementary process [40]. However, as we were not able to determine the reactional pathway of CH$_3$I uptake on NaCl, therefore we are not sure if the observed rate at different temperature corresponds to an elementary process or not.

Therefore, we estimated a global adsorption energy (*E)* of the adsorption of CH$_3$I on NaCl (macro process) using Arrhenius equation [E4-10]

$$k= Ae^{-E/RT} \qquad (E4\text{-}10)$$

Where R is the gas constant (8.31 J.mol^{-1}) and the temperature (T) is in Kelvin. k is the rate constant; A is the pre-exponential factor and E is the global adsorption energy (KJ/mole).

As shown in section 4.3.1.4 the adsorption of CH$_3$I on NaCl is of 1st order. Thus, the adsorption rate is proportional to the slope of the linear interpolation and dependent on the CH$_3$I gaseous concentration. Forthwith, the rate constant (k) is given by the following equation:

$$\ln(k) = \ln(Rate)\text{-}\ln([CH_3I]) \qquad [E4\text{-}11]$$

However, since the gas phase concentration is constant over time (experiment performed under continuous flow) and the interaction is very low. Therefore, the adsorption rate (Rate) is assumed to be equal to the rate constant (k).

From the rate of CH$_3$I adsorption given in Table 4.26 and by plotting Ln(Rate) versus 1/*T* (Figure 4.37) it is possible to determine *E* from the slope of the linear interpolation of the plot. The value of *E* was found to be -38.07 ± 1.69 KJ.mol^{-1} at 95% confidence level.
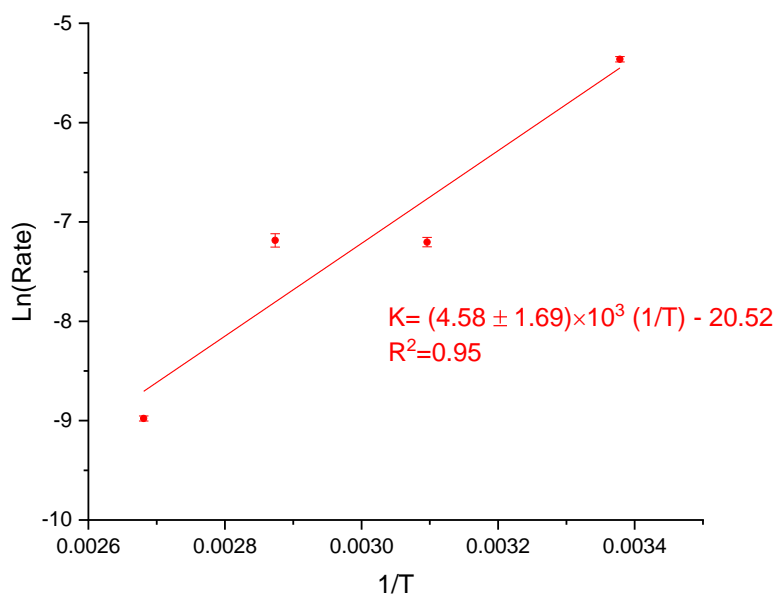
Figure 4. 37 Plot of ln (Rate) versus 1/T. Rate is the rate of the time evolution of the sum of the area of the 1275, 1244, 1220, 1183, 1073 and 1024 cm^{-1} bands and T is the temperature in kelvin.

A negative value of the global adsorption energy is generally a good indication that there is (1) a reduction in the probability of colliding CH_3I molecules with NaCl surface and (2) an overstep to the diffusion limits of CH_3I on NaCl. Therefore, this suggests that we were not more measuring the adsorption of CH_3I on NaCl [41, 42].

Therefore, it seems that the chemisorption process of methyl iodide interaction with NaCl surface occur at room temperature.

4.4. Conclusion

The heterogeneous interaction of CH_3I on wet and dry NaCl salt was investigated using DRIFTS technique. CH_3I adsorption is clearly observed on dry NaCl at 296 K and 1 atm. In addition to the adsorbed CH_3I bands in the CH_3 stretching region at 3018, 2993, 2962, and 2855 cm^{-1} and in the CH_3 deformation region at 1275, 1244, 1220 and 1183 cm^{-1}, the DRIFTS spectra revealed the presence of new strong vibrational bands at 1073 and 1024 cm^{-1} which are not referenced in the literature. Theses bands seems to be linked to the methyl iodide interaction with halide salt surface, but to the best of our knowledge, no previous studies have considered such chemical systems featuring organic halogenated gaseous species (i.e. CH_3Cl, CH_3Br,...) and halide salts. Owing to the inhomogeneity of the NaCl surface, we hypothesize that these new bands are attributable to different geometrical form of CH_3I (C_3v) adsorbed on NaCl.

The adsorption of CH_3I is likely chemisorption since no desorption was observed even after heating the system. Consistently to the cryogenic study in gas phase, the study of the interaction between CH_3I and wet NaCl showed the low affinity of CH_3I towards water.

The $\{CH_3I\}_{residual}$ on NaCl was found to be very low 0.003% and the average uptake coefficients were determined to be very low in the order of 10^{-11}. This indicates that the interaction between NaCl and CH_3I is very weak. The uptake by NaCl was found to be independent of contact time and CH_3I gaseous concentration (in the ppm range). Though atmospheric CH_3I concentrations, are 10^{-5}-10^{-6} lower than the concentrations used in our experiments, we can still expect a very low uptake on NaCl- at least of the same order (10^{-11}). The global energy of adsorption was found to be -38 $KJ.mol^{-1}$, and which suggests that there is a reduction in the probability of colliding CH_3I with NaCl above atmospheric temperature (> 296 K).

Although the uptake of CH_3I on NaCl is very weak, its irreversible character makes it of particular importance for the dispersion of CH_3I in the atmosphere. Because such irreversible uptake may occur on surfaces of aerosols particles that are known to be transported and play a role in the chemistry of the troposphere, which would further affect or participate in different atmospheric mechanisms.

Finally, it seems challenging to confirm if the new bands are characteristics of different geometrical configuration C_3v of CH_3I or not, which would require an additional spectroscopy analysis using deuterium instead of hydrogen atom (CD_3I, CD_2HI, etc) and theoretical calculation taking into consideration different geometrical configuration of adsorbed CH_3I.

References

[1] R. Vogt, B.J. Finlayson-Pitts, A Diffuse Reflectance Infrared Fourier Transform Spectroscopic (DRIFTS) study of the surface reaction of NaCl with gaseous NO2 and HN03, J. Phys. Chem. 98 (1994) 3747–3755. https://doi.org/10.1021/j100065a033.

[2] T. Armaroli, T. Bécue, S. Gautier, Diffuse Reflection Infrared Spectroscopy (DRIFTS): Application to the in Situ Analysis of Catalysts, Oil Gas Sci. Technol. 59 (2004) 215–237. https://doi.org/10.2516/ogst:2004016.

[3] J. Sirita, S. Phanichphant, F.C. Meunier, Quantitative analysis of adsorbate concentrations by diffuse reflectance FT-IR, Anal. Chem. 79 (2007) 3912–3918. https://doi.org/10.1021/ac0702802.

[4] C.Lentz, S.Panahian Jand, J.Melke, C.Roth, P.Kaghazch, DRIFTS study of CO adsorption on Pt nanoparticles supported by DFTcalculations, J. Mol. Catal. A : Chemical, 426 (2017) 1-9. https://doi.org/10.1016/j.molcata.2016.10.002

[5] M. Gouello, Thése de doctorat, Chimie de l'iode et composition des aérosols dans le circuit primaire d'un réacteur nucléaire en situation d'accident grave, Université de Grenoble, 2013.

[6] L.D. Kong, X. Zhao, Z.Y. Sun, Y.W. Yang, H.B. Fu, S.C. Zhang, T.T. Cheng, X. Yang, L. Wang, J.M. Chen, The effects of nitrate on the heterogeneous uptake of sulfur dioxide on hematite, Atmos. Chem. Phys. 14 (2014) 9451–9467. https://doi.org/10.5194/acp-14-9451-2014.

[7] H.J. Li, T. Zhu, D.F. Zhao, Z.F. Zhang, Z.M. Chen, Kinetics and mechanisms of heterogeneous reaction of NO_2 on $CaCO_3$ surfaces under dry and wet conditions, Atmos. Chem. Phys. 10 (2010) 463–474. https://doi.org/10.5194/acp-10-463-2010.

[8] A. Saiz-Lopez, J.M.C. Plane, A.R. Baker, L.J. Carpenter, R. Von Glasow, C.G. Juan, G. Mcfiggans, R.W. Saunders, Atmospheric Chemistry of Iodine, Chem. Rev. 112 (2012) 1773–1804. https://doi.org//10.1021/cr200029u.

[9] A. Allanic, M.J. Rossi, Heterogeneous reactions of HOI on substrates of atmospheric importance, Geophys. Res. Lett. 104 (1999) 18689–18696. https://doi.org/10.1029/1999JD900285.

[10] C.J. Percival, J.C. Mo, R.A. Cox, The uptake of HI and HBr on ice, Phys. Chem. Chem. Phys. 1 (1999) 4565–4570. https://doi.org/10.1039/A904651H.

[11] A. Alshawa, O. Dopfer, S.A.N. Christopher W. Harmon, J.S. Underwood, Hygroscopic growth and deliquescence of NaCl nanoparticles mixed with surfactant SDS, J. Phys. Chem. B. 114 (2010) 2435–2449. https://doi.org/10.1021/jp909661q.

[12] C. Su, J.C. Yeh, C.C. Chen, J.C. Lin, J.L. Lin, Study of adsorption and reactions of methyl iodide on TiO2, J. Catal. 194 (2000) 45–54. https://doi.org/10.1006/jcat.2000.2909.

[13] M. Chebbi, B. Azambre, L. Cantrel, A. Koch, A Combined DRIFTS and DR-UV-Vis Spectroscopic in Situ Study on the Trapping of CH_3I by Silver-Exchanged Faujasite Zeolite, J. Phys. Chem. C. 120 (2016) 18694–18706. https://doi.org/10.1021/acs.jpcc.6b07112.

[14] J.L. Duncan, A.M. Ferguson, S. Mathews, Vibrational anharmonicity in CH_3I: A joint local and normal mode study, J. Chem. Phys. 91 (1989) 783–790. https://doi.org/10.1063/1.457131.

[15] M.L. Colaianni, P.J. Chen, H. Gutleben, J.T. Yates, Vibrational studies of CH_3I on Si(100)-(2×1): adsorption and decomposition of the methyl species, Chem. Phys. Lett. 191 (1992) 561–568. https://doi.org/10.1016/0009-2614(92)85589-3.

[16] F. Solymosi, G. Klivényi, HREELS study of CH_3I and CH_3 adsorbed on Rh(111) surface, J. Electron Spectros. Relat. Phenomena. 64/65 (1993) 499–506. https://doi.org/10.1016/0368-2048(93)80115-3.

[17] J. Lin, B.E. Bent, Iodomethane dissociation on Cu(111): Bonding and chemistry of adsorbed methyl groups, J. Vac. Sci. Technol. A Vacuum, Surfaces, Film. 10 (1992) 2202–2209. https://doi.org/10.1116/1.578005.

[18] C.J. Jenks, B.E. Bent, N. Bernstein, F. Zaera, The Chemistry of Alkyl Iodides on Copper Surfaces. Adsorption Geometry, Phys. Chem. B. 104 (2000) 3008–3016. https://doi.org/10.1021/jp993021s.

[19] M.A. Henderson, G.E. Mitchell, J.M. White, The chemisorption of methyl halides (Cl, Br and I) on Pt(111), Surf. Sci. Lett. 184 (1987) 325–331. https://doi.org/10.1016/0167-2584(87)90754-7.

[20] G. Klivényi, F. Solymosi, Generation of CH2 species: thermal and photo-induced dissociation of CH_2I_2 on Rh(111) surface, Surf. Sci. 342 (1995) 168–184.https://doi.org/10.1016/0039-6028(95)00767-9.

[21] M.K. Weldon, C.M. Friend, Spectroscopic characterization of surface methylene on Mo (110), Surf. Sci. 321 (1994) L202-L208. https://doi.org/10.1016/0039-6028(94)90175-9.

[22] K.C. Scheer, A. Kis, J. Kiss, J.M. White, Adsorption and reactions of CH_2I_2 on clean and oxygen-modified Ag (111): a RAIRS and TPD study, Top. Catal. 20 (2002) 43–51. https://doi.org/10.1023/A:1016395214602.

[23] T. Shimanouchi, Tables of Molecular Vibrational Frequences Consolidated, volume I, washington, D.C: National Bureau of Standards, NSRDS-NBS3, 1972. https://doi.org/10.1063/1.555560.

[24] E.M. Karp, T.L. Silbaugh, C.T. Campbell, Energetics of Adsorbed CH_3 and CH on Pt(111) by Calorimetry: Dissociative Adsorption of CH_3I, J. Phys. Chem. C. 117 (2013) 6325–6336. https://doi.org/10.1021/jp400902f.

[25] R. Otto, Thesis on Dynamics of a Microsolvated Ion-Molecule Reaction, Univ. Freibg. (2011).

[26] S. Furuyama, D.M. Goldex, S.W. Bekson, Kinetic Studies of the Reactions CH_2I_2 + HI =CH_3I +I_2 and CH_3I =CH_4+CH_2I_2 The Heat of Formation of the Iodomethyl Radical *, Int. J. Chem. Kinet. I (1969) 283–296. https://doi.org/10.1002/kin.550010302.

[27] T. Makino, S. Zulaehah, J.S. Gueriba, W.A. Diño, M. Okada, CH_3Cl/Cu (410): Interaction and Adsorption Geometry, J. Phys. Chem. C. 122 (2018) 11825–11831.https://doi.org/10.1021/acs.jpcc.8b01296.

[28] F.S. J. Cserenyi , L. Ovari, T. Bansagi, Adsorption and reactions of CH_3Cl on MoC based catalyst, J. Mol. Catal. A Chem. 162 (2000) 335–352. https://doi.org/10.1021/acscatal.5b02424.

[29] J.Rakso, J.Bontovics, F.Solymosi, Infrared Spectroscopic Study of the Adsorption and Dissociation of Methyl Halides on Silica-Supported Pd, J. Catal. 143 (1993) 138–148. https://doi.org/10.1006/jcat.1993.1260.

[30] F. Zaera, H. Hoffmann, P.R. Griffiths, Determination of molecular chemisorption geometries using reflection-absorption infrared spectroscopy: alkyl halides on Pt(111), J. Electron Spectros. Relat. Phenomena. 54–55 (1990) 705–715. https://doi.org/10.1016/0368-2048(90)80263-A.

[31] J. Zhang, U. Lourderaj, S. V. Addepalli, W.A. de Jong, W.L. Hase, Quantum Chemical Calculations of the Cl^- + CH_3I → CH_3Cl + I- Potential Energy Surface, J.Phys. Chem. A. 113 (2009) 1976–1984. https://doi.org/10.1039/c6cp06195h.

[32] I. Szabó, G. Czakó, Benchmark ab Initio Characterization of the Complex Potential Energy Surface of the Cl- + CH3I Reaction, J. Phys. Chem. A. 121 (2017) 5748–5757. https://doi.org/10.1021/acs.jpca.7b05503.

[33] M. Gu, X. Liu, L. Yang, S. Sun, J. Zhang, Dynamics of $Cl^-(H_2O)$ + CH_3I Substitution Reaction: The Influences of Solvent and Nucleophile, J. Phys. Chem. A. (2019) acs.jpca.9b00348. https://doi.org/10.1021/acs.jpca.9b00348.

[34] M. Ullerstam, M.S. Johnson, R. Vogt, E. Ljungström, DRIFTS and Knudsen cell study of the heterogeneous reactivity of SO_2 and NO_2 on mineral dust, Atmos. Chem. Phys. Discuss. 3 (2003) 4069–4096. https://doi.org/10.5194/acp-3-2043-2003.

[35] H.J. Li, T. Zhu, D.F. Zhao, Z.F. Zhang, Z.M. Chen, Kinetics and mechanisms of heterogeneous reaction of NO_2 on $CaCO_3$ surfaces under dry and wet conditions, Atmos. Chem. Phys. 10 (2010) 463–474. https://doi.org/10.5194/acp-10-463-2010.

[36] H. Li, T. Zhu, J. Ding, Q. Chen, B. Xu, Heterogeneous reaction of NO_2 on the surface of NaCl particles, Sci. China, Ser. B Chem. 49 (2006) 371–378. https://doi.org/10.1007/s11426-006-0371-z.

[37] L. Li, Z.M. Chen, Y.H. Zhang, T. Zhu, S. Li, H.J. Li, L.H. Zhu, B.Y. Xu, Heterogeneous oxidation of sulfur dioxide by ozone on the surface of sodium chloride and its mixtures with other components, J. Geophys. Res. Atmos. 112 (2007) 1–13. https://doi.org/10.1029/2006JD008207.

[38] P. Li, H.A. Al-Abadleh, V.H. Grassian, Measuring heterogeneous uptake coefficients of gases on solid particle surfaces with a Knudsen cell reactor: Complications due to surface saturation and gas diffusion into underlying layers, J. Phys. Chem. A. 106 (2002) 1210–1219. https://doi.org/10.1021/jp011828q.

[39] W. Wang, M. Ge, Y. Tian, L. Yao, A flow tube study of methyl iodine uptake on soot surface, Chem. Phys. Lett. 440 (2007) 348–351. https://doi.org/10.1016/j.cplett.2007.04.053.

[40] B.J. Finlayson-Pitts, J. James N. Pitts, Chemistry of the Upper and Lower Atmosphere: Theory, Experiments, and Applications, Academic Press, California, ISBN: 978-0-12-257060-5, 2000. https://doi.org/10.1016/B978-0-12-257060-5.X5000-X.

[41] R. Kobiraj, N. Gupta, A.K. Kushwaha, M.C. Chattopadhyaya, Determination of equilibrium, kinetic and thermodynamic parameters for the adsorption of Brilliant Green dye from aqueous solutions onto eggshell powder, Indian J. Chem. Technol. 19 (2012) 26–31. Corpus ID: 9344586.

[42] P.A. Parikh, N. Subrahmanyam, Y.S. Bhat, A.B. Halgeri, Kinetics of zeolite-catalysed toluene isopropylation, Chem. Eng. J. Biochem. Eng. J. 54 (1994) 79–85. https://doi.org/10.1016/0923-0467(93)02818-H.

Chapter 5: Static reactor experiments

Chapter 5 focuses on determining CH$_3$I reactivity with organic and inorganic solids as models of atmospheric aerosols by monitoring methyl iodide concentration in the gas phase. This chapter completes the study performed using DRIFTS technique with halide salts (chapter 4). The DRIFTS technique is not suitable for other compounds chosen as proxy of primary and secondary atmospheric aerosols (i.e. Na$_2$SO$_4$, Na$_2$CO$_3$, glutaric acid, malonic acid…). Indeed, the model species own a huge IR absorption, which cannot be attenuated using dilution within halide solids since these later may directly interfere with CH$_3$I as seen in the chapter 4. Additionally, the evolution of the CH$_3$I interaction with NaCl determined by following the solid phase, can be completed using technique following the gaseous phase.

In this chapter, we studied the evolution of CH$_3$I concentration in the gas phase when exposed to inorganic and organic compounds under dry conditions (RH~20%, at 296 K) using static solid phase reactor coupled with gas chromatography technique. The static reactors used were breakthrough type reactor and were only adapted to continuous gas flow conditions. Gas chromatography coupled to an electron capture detector was adapted to our intentions with methyl iodide determination in the gas phase in the 1 ppb- 100 ppb concentration range.

The experimental setup featuring a small reactor and a larger one coupled with gas chromatography is described. The experimental conditions under continuous gas flow conditions for the study of the interaction of gaseous CH$_3$I with inorganic and organic solids is listed and justified. Results on the breakthrough curves are then discussed and finally, the conclusion and perspectives are stated.

5.1 Materials and methods

5.1.1 Reagents

Diluted CH$_3$I in air or argon (0.1% CH$_3$I, 99.9% Ar or Air) bottles were provided by Air products in a concentration ranging from ppb up to 1000 ppm. Argon (99.99% purity) and Air (80% N$_2$, 20%O$_2$) gas bottles were provided from commercial cylinders Air liquid. The gases were used without any further purification.

Commercial sodium chloride (NaCl, 99.99% purity, ALFA AESAR), sodium sulphate (Na$_2$SO$_4$, 99% purity, ALFA AESAR), sodium carbonate (Na$_2$CO$_3$, 99+% purity, ACROS), ammonium nitrate (NH$_4$NO$_3$, 99+% purity, SIGMA ALDRICH) and, malonic acid (99+% purity, ACROS), sodium stearate (ALFA AESAR, no data on purity), palmitic acid (99+% purity, ACROS), sodium

oxalate (99+%, ALFA AESAR), glutaric acid (99+% purity, ALFA AESAR), oxalic acid (AnalaR NORMAPUR, no data on purity), trisodium citrate diyhdrate (AnalaR NORMAPUR, no data on purity), trisodium citrate anhydrous (99% purity, AnalaR NORMAPUR), citric acid (AnalaR NORMAPUR, no data on purity), succinic acid (AnalaR NORMAPUR, no data on purity), citric acid monohydrate (AnalaR NORMAPUR, no data on purity) were used as powder for experiments.

All inorganic and organic solid samples were manually grinded using an agate mortar and pestle. NaCl was preheated for a minimum of 4 hours at 873 K to remove species adsorbed on the powder surface. NaCl salt is highly hygroscopic, so it was kept in a dry desiccator. Sodium carbonate and ammonium nitrate were preheated at 473 K, whereas sodium sulphate was preheated to 323 K. No preheating was performed for organic solids due to the possibility of solid destruction and safety consideration. Up to 1 g and 14-18 g of powder was used for the experiments depending on reactor size.

5.1.2 Experimental setup

Two types of static reactors were developed: a small stainless reactor and a large glass reactor (see Figures 5.1(a) and 5.1(b), respectively).
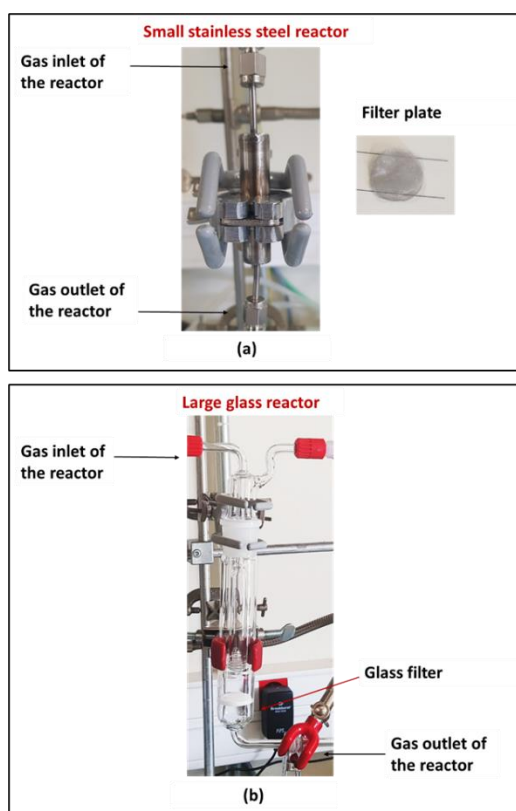
Figure 5. 1 Photo of the (a) small stainless reactor and (b) large glass reactor.

The reactors were designed with a gas inlet placed on the top and a gas outlet on the bottom of the reactor (see Figure 5.1). The solid samples were placed on a metallic filter inside the small stainless steel reactor or glass filter inside the large glass reactor allowing the gases to pass through.

One of the main parameters that must be taken into account when monitoring the gas phase is the contact time (T_c) between gas phase and solid phase [1]. With our reactor configuration, the contact time (T_c) depends on the solid bed volume, particles size, packing of particles, surface area and gas flow rate. However, in this work, the contact time (in sec) was firstly estimated by considering only the geometrical volume of the solid bed with the following equation:

$$T_c = \frac{\text{Solid bed volume}}{\text{Total gas flow}} \qquad \text{(E5-1)}$$

The small stainless steel reactor (Figure 5.1(a)) was developed in order to get conditions close to that of DRIFTS cell (i.e. contact time, dark conditions, mass of solid sample and gas flow). The small reactor overall volume was of 5 cm^3. The measured geometrical volume of 1 g of solid bed (powdered compounds) was 2 cm^3. Contact time of the gas phase with the solid bed was thus ~844 milliseconds - 1 second. The characteristics of the small stainless steel reactor are listed in Table 5.1

Table 5. 1 Characteristics and featured conditions of the small stainless reactor.

Reactor Volume	5 cm^3
Mass of solid	1 g
Volume of solid bed	2 cm^3
Gas: Total gas flow	Ar: 108 mL.min^{-1} Air: 77 mL.min^{-1}
Gas: Contact time	Ar: 844 ms Air: 1 sec

The large glass reactor developed an inner volume of 180 cm^3. The solid bed volume (corresponding to 14-18 g of powdered compound) was estimated on average to 30 cm^3. The resulting calculated contact time was 16-24 seconds depending on the overall gas flow. The characteristics of the large glass reactor are listed in Table 5.2.

Reactor Volume	180 cm^3
Mass of solids	14-18 g
Volume of solid bed	30 cm^3
Gas: Total gas flow	Ar: 108 mL.min^{-1}
	Air: 77 mL.min^{-1}
Gas: Residence time	Ar: 16 sec
	Air : 24 sec

For both reactors, the reactor inlet was connected to a gas supply network allowing a controlled mixing of dry CH_3I and argon or dry air flows from two different lines (Figure 5.2) in order to achieve a wide range of CH_3I concentrations from 1 ppb up to 100 ppb. Each line was equipped with a mass flow regulator (Bronkhorst, (F-201CV), 2-108 mL.min^{-1}) allowing controlled mixing of CH_3I with Ar or Air. The exit line was connected to a cartridge filled with active coal for CH_3I. Gas sampling were performed at the reactor inlet and reactor outlet as shown on Figures 5.2. The gas sampling lines were provided with isolation valve that allowed to connect gas sampling bags. The whole device (gas supply lines and reactor) was placed in a ventilated fume hood.
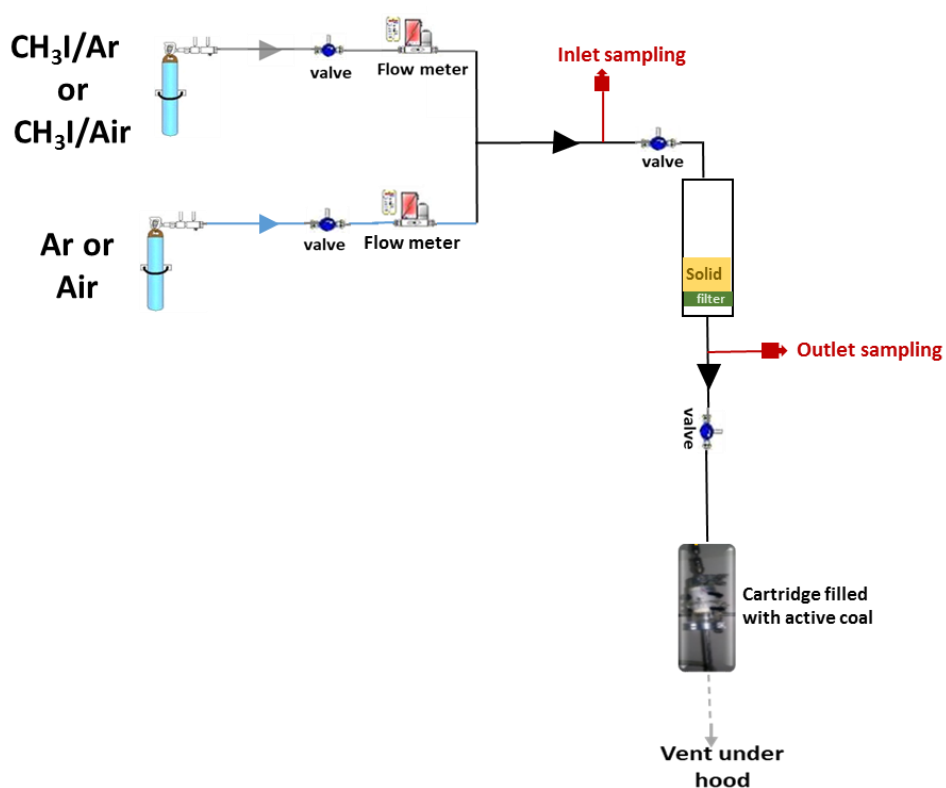
Figure 5. 2 Scheme of the static reactor setup.

The mixed flows as a function of CH$_3$I concentration are listed in Table 5.3, with a total flow rate of 108 mL.min^{-1} diluted in Ar or 77 mL.min^{-1} diluted in Air.

Table 5. 3 Prepared [CH$_3$I] in ppb as function of CH$_3$I concentration (ppb) and Ar or Air flow (mL.min^{-1}) at 1 atm and 296 K. Q: mass flow rate in mL.min^{-1}.

Initial [CH$_3$I] in the reactor (ppb)	QAr or QAir (mL.min^{-1})	QCH$_3$I (mL.min^{-1})	[CH$_3$I] supply
100	106 (Ar)	2	5 ppm in Ar
50	107 (Ar)	1	5 ppm in Ar
1	76 (Air)	1	100 ppb in Air

Gas chromatography (GC) coupled with an Electron Capture Detector was used to follow methyl iodide concentration evolution.

5.1.3 Gas phase CH$_3$I sampling and GC analyses

In continuous flow, the sampling of gaseous CH$_3$I/Ar mixtures at the inlet or outlet (see Figure 5.2) was done by filling a 0.6 L gas bag for 5 minutes.

Analysis of gaseous methyl iodide (CH$_3$I) concentration in the gas phase was performed by gas chromatography (Agilent7820A) provided with a capillary column of 0.32 mm internal diameter and 30 mm length and an ECD detector following the methods developed in the L2EC Laboratory (see annex 5).

Analysis of gas phase in the filled gas bag using GC-ECD can be performed by both manual and automated injection. The type of injection was dependent on the CH$_3$I concentration range. Manual injection was applied for the methyl iodide concentration of 100 ppb. Injection through automated thermodesorption (TD) is retained for the low concentration levels (1 ppb). Under our experimental conditions, methyl iodide concentration were determined with an uncertainty interval at 95% confidence level of ± 8 % with TD injection. For manual injection, the uncertainty interval at 95% confidence level was of ± 14 %. The uncertainty values were determined previously at L2EC laboratory. The calculation of uncertainty was based on the combination of accuracy and precision data analysis (annex 6).

5.1.4 Protocol description for experiments performed in continuous gas conditions

Under continuous conditions, gas phase monitoring allows the access to the break through curves [2]. Contrarily to static conditions, where the total amount of gas taken up by the solid can be determined [1, 3].

Indeed, if CH_3I capture on the selected solid particles is low as for NaCl, we expect a rapid outlet gas phase depletion at the experiment beginning which then increases rapidly until observing a breakthrough which correspond to saturation of the solid bed. However, if the residence time in the solid bed is increased, the initial outlet CH_3I concentration depletion will be amplified as shown in Figure 5.3. Then, a relation between the outlet gas phase depletion and residence time in the solid bed can give an access to the initial gas uptake by solid (γ_0).

At the beginning of the experiment

$1 < T_c < 5$

$5 < T_c < 10$

$15 < T_c < 20$

$20 < T_c < 25$

$[CH_3I]_g$

Contact time (seconds)
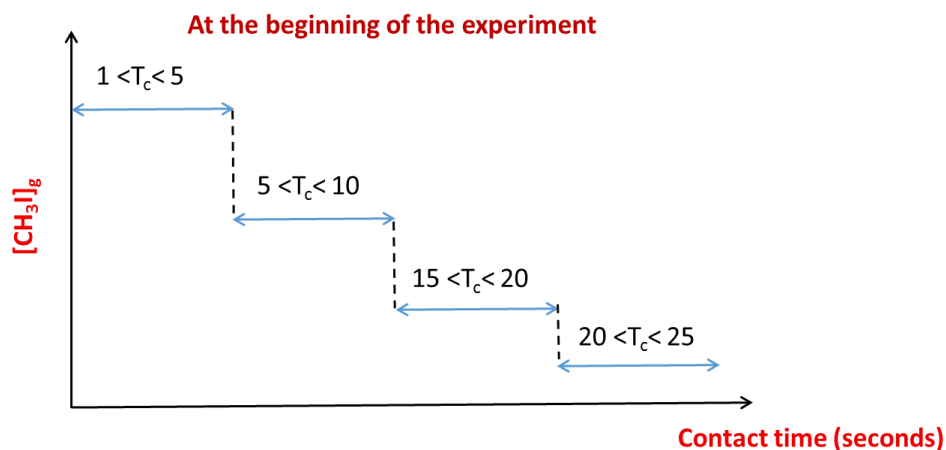
Figure 5. 3 [CH₃I]outlet as function of contact time.

All experiments were performed at RH=20%, 296K and 1 atm. Small reactor was as DRIFTS experiments under dark conditions. We assume that the large reactor was also close to dark conditions since (1) the experiments were performed inside a laboratory with the presence of only artificial light (2) the UV-Vis light did not penetrate into the solid bed.

Before each experiment, a blank test with a pure Ar flow at 108 mL.min^{-1} was conducted and gas phase analyses at both inlet and outlet were performed to check that the experimental setup was clean. Before injecting the methyl iodide mixed with Ar or Air into the reactor, we verified the initial CH_3I concentration. For this purpose, the gas mixture (CH_3I/Ar or CH_3I/Air) was sampled at the inlet of the experimental set up and analyzed by GC. After validating the methyl iodide concentration at the inlet (inlet sampling in Figure 5.2), the gas mixture was injected into the reactor. After 1 minute of gas flow through the solid sample, a gas bag of 0.6 L was placed at the reactor outlet (outlet sampling in Figure 5.2) and filled for 6 minutes. Successive gas bag fillings were performed during the experiment (gas sampling was performed every 6 minutes). The experiment duration varied between 36 and 300 minutes. At the end of the test, the overall gas flow was stopped (CH_3I and dilution lines), and the solid was recovered. The reactor was cleaned and then argon was flowed at 108 mL.min^{-1} all night.

5.1.5 Experiment grid for continuous conditions

As a low reactivity between methyl iodide and the inorganic and organic solid is expected, the static reactor experiments will feature conditions suited to a low gas phase depletion: we choose to operate with low methyl iodide gas phase concentration (1-100 ppb) and high amount of solid particles (1-15 g). Such conditions are opposite to that retained for the DRIFTS experiments - featuring high methyl iodide gas phase concentration (1000 ppm) and low salt mass (150 mg) in order to allow measurable salt surface structural changes.

The first series of experiments was conducted with the small reactor. The CH_3I wall loss was firstly determined with empty reactor under continuous flow of 100 ppb and 1 ppb of CH_3I (blank experiments). In the small reactor, we firstly aimed to globally investigate the interaction with different solid models of atmospheric aerosols. Inorganic solids (i.e $NaCl$, Na_2CO_3, NH_4NO_3 and Na_2SO_4) and organic solids (i.e glutaric acid, malonic acid, oxalic acid, succinic acid, palmitic acid, citric acid, citric acid monohydrate, sodium stearate, sodium oxalate, trisodium citrate dihydrate and anhydrous trisodium citrate) placed inside the small reactor were exposed successively to a 100 ppb CH_3I/Ar continuous flow. Secondly, we chose to expose CH_3I at trace level (1 ppb) to selected inorganic solids ($NaCl$ and Na_2CO_3) and organic solids (trisodium citrate dihydrate and glutaric acid). As shown in Table 5.4, the organic solids featured all carboxylic acid functional groups (i.e. glutaric acid, malonic acid, oxalic acid, succinic acid, palmitic acid, citric acid and citric acid monohydrate) or were the solids of the corresponding conjugated bases (i.e. sodium stearate, sodium oxalate, trisodium citrate dihydrate and anhydrous trisodium citrate). Therefore, we selected one organic solid with carboxylic acid group (glutaric acid) and one sodium salt of the conjugated base (trisodium citrate dihydrate).
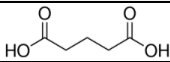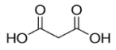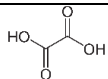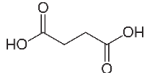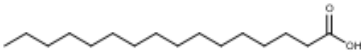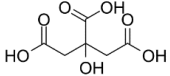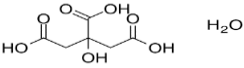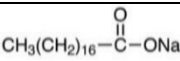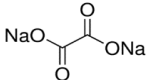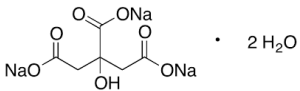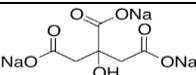
The second series of experiments was conducted with the large glass reactor. First, blank experiments were performed with empty reactor under continuous flow of 100 ppb and 1 ppb of CH_3I. Secondly, CH_3I (100 ppb)/Ar was exposed to selected three inorganic solids ($NaCl$, Na_2CO_3, NH_4NO_3), and three organic solids with carboxylic acid group (glutaric acid, malonic acid, oxalic acid) and one sodium salt of the conjugated base (trisodium citrate dihydrate). Later, CH_3I (1ppb)/Air was subjected to $NaCl$, Na_2CO_3, NH_4NO_3, trisodium citrate dihydrate and glutaric acid.

Our selection of organic solids was generally based on: (1) Oxalic acid is generally the dominant organic species in atmospheric aerosols followed by malonic, (2) glutaric acid can

act as cloud condensation nuclei (CCN) and (3) trisodium citrate dihydrate conjugate base of citric acid which can play a role in ice nucleation [4, 5].

The evolution of the gaseous CH_3I concentration was monitored over all the experiment duration.

Table 5. 4 Formula and structure of organic solids.

Solid name	Formula	Structure
Glutaric acid	$C_5H_8O_4$	
Malonic acid	$C_3H_4O_4$	
Oxalic acid	$C_2H_2O_4$	
Succinic acid	$C_4H_6O_4$	
Palmitic acid	$C_{16}H_{32}O_2$	
Citric acid	$C_6H_8O_7$	
Citric acid monohydrate	$C_6H_8O_7.H_2O$	
Sodium stearate	$C_{18}H_{35}NaO_2$	$CH_3(CH_2)_{16}-C-ONa$
Sodium oxalate	$Na_2C_2O_4$	
Trisodium citrate dihydrate	$Na_3C_6H_5O_7.2H_2O$	
Anhydrous trisodium citrate	$Na_3C_6H_5O_7$	

5.2. Results and discussion

5.2.1 Empty reactors

- **$[CH_3I]_g$=100 ppb:**

Figure 5.4 and 5.5 shows the time evolution of CH_3I outlet concentration under CH_3I/Ar continuous flow (100 ppb, 108 mL.min^{-1}) with the small reactor and large reactor respectively. Experiment with large reactor was repeated 5 times.

In Figure 5.4, the outlet concentration remained in general close to the range of the expected one (given the uncertainty range (± 14%) of the GC analyses).

As seen from Figure 5.5, even if the outlet CH$_3$I concentration remained in general close to the range of the expected one (given the uncertainty range (± 14%) of the GC analyses), a slow and constant decrease of this concentration of about 12% (marked in dashed box in Figure 5.5) is observed at the beginning of two experiments (experiments 1 and 5). Therefore, this series of experiments points out the difficulties to obtain a stable CH$_3$I concentration with empty large glass reactor and will make interpretation of experiments with solids not easy if low interaction is expected.
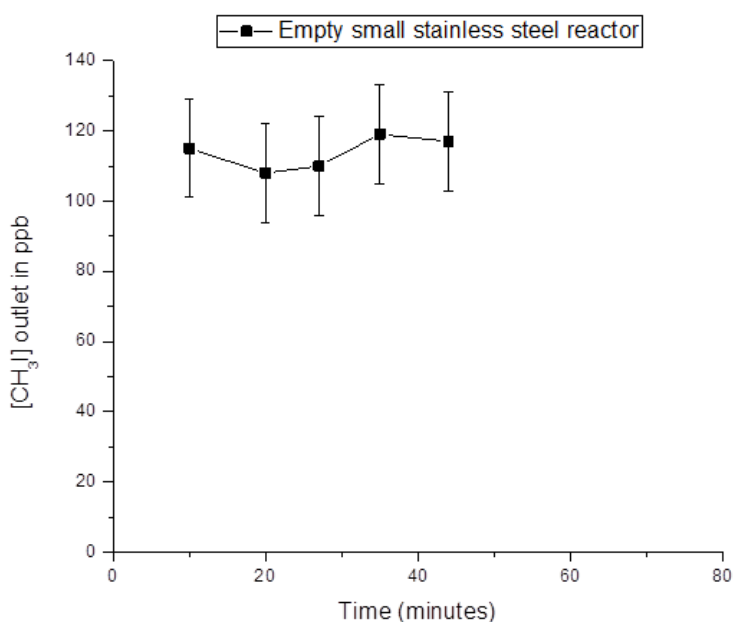
Figure 5. 4 The evolution of [CH$_3$I] outlet as function of time in the empty small reactor for an injected CH$_3$I concentration of 100 ppb and 108 mL.min^{-1} continuous gas flow under RH=20% at 296 K and 1 atm.
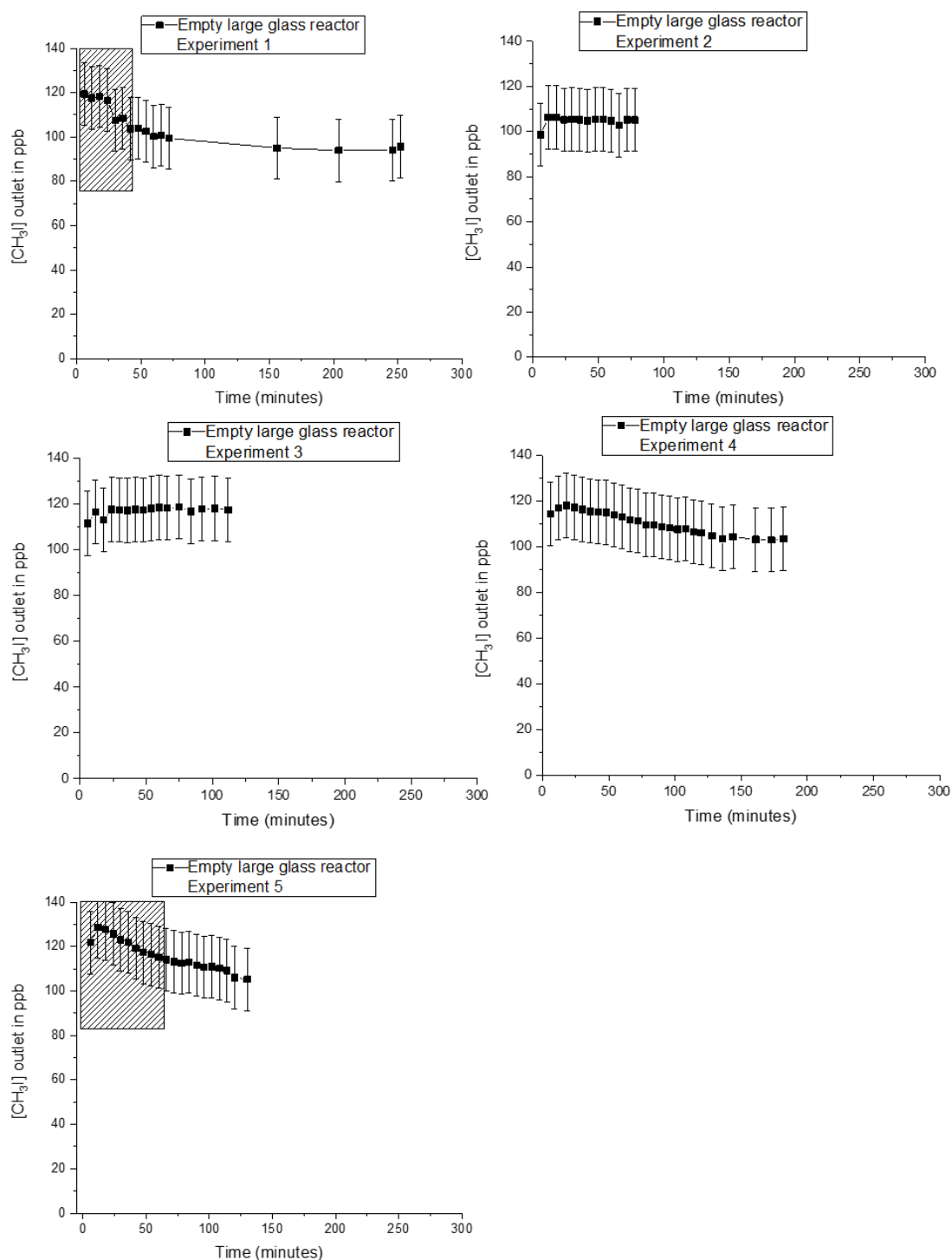
Figure 5. 5 The evolution of [CH₃I] outlet as function of time in the empty large reactor for an injected CH₃I concentration of 100 ppb and 108 mL.min⁻¹ continuous gas flow under RH=20% at 296 K and 1 atm.

[CH₃I]$_g$=1 ppb:

Figure 5.6 and 5.7 shows the time evolution of CH₃I outlet concentration under CH₃I/Ar continuous flow (1 ppb, 77 mL.min⁻¹) with the small reactor and large reactor respectively. Experiments with both reactors were repeated 2 times.

In both reactors, the CH_3I outlet concentration as well as the inlet concentration in general were up to 30% higher than the range of the expected one (given the uncertainty range ($\pm$ 8%) of the GC analyses). This underlines the problem of achieving low stable concentrations in the inlet line by mixing low gaseous flows: i.e. for 1 ppb of CH_3I a mixing of 76 mL.min^{-1} of Air with 1 mL.min^{-1} of CH_3I was needed (see Table 5.3). Nevertheless, during the experiment, the outlet concentration remained stable and within the uncertainty ($\pm$ 8%) range of the GC analyses as shown in Figure 5.6 and 5.7.
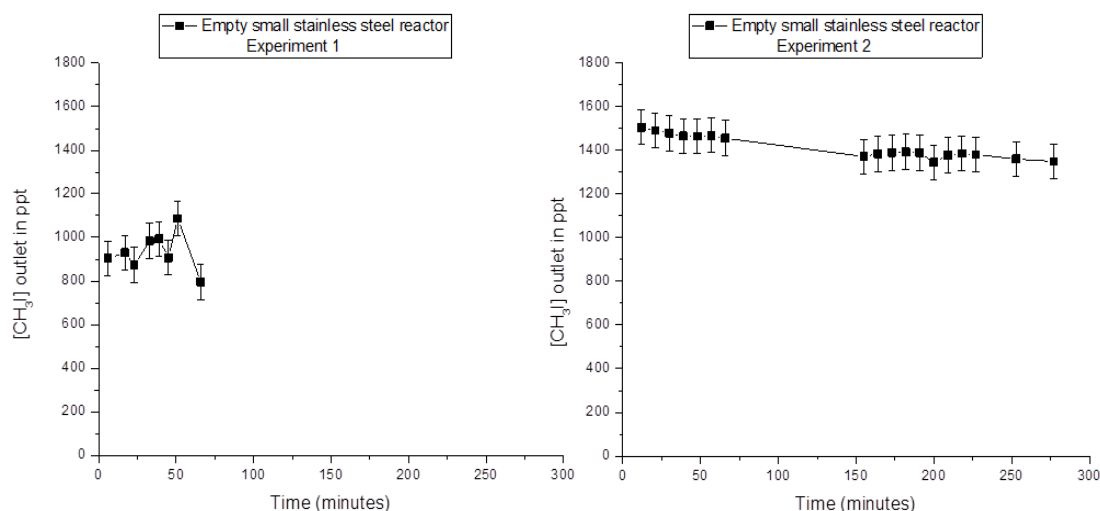
Figure 5. 6 The evolution of [CH₃I] outlet as function of time in the empty small reactor for an injected CH₃I concentration of 1 ppb and 77 mL.min^{-1} continuous gas flow under RH=20% at 296 K and 1 atm. 1 ppb= 1000 ppt.
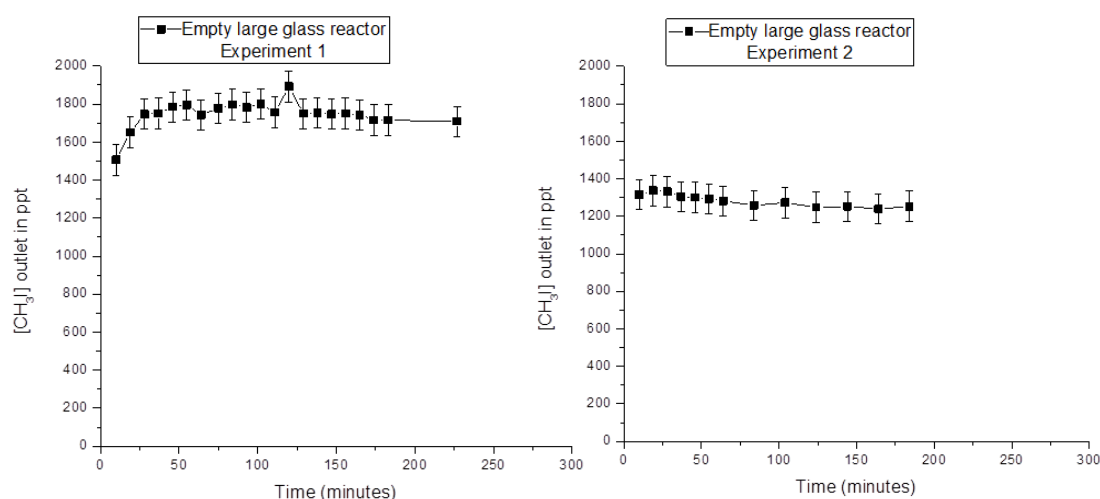
Figure 5. 7 The evolution of [CH₃I] outlet as function of time in the empty large reactor for an injected CH₃I of 1 ppb and 77 mL.min^{-1} continuous gas flow under RH=20% at 296 K and 1 atm. 1 ppb= 1000 ppt.

234

5.2.2 Reactor filled with inorganic solids

Experiments were performed with both small and large reactors filled with 1 g (844 ms -1 sec) and 18 g (16-24 sec) of inorganic solids, respectively.

[CH₃I]$_g$= 100 ppb:

The evolution of the CH_3I outlet concentration over time was stable in comparison to blank experiment when CH_3I was exposed to all the selected inorganic solids in both reactors. As an example, Figure 5.8 and Figure 5.9 shows the time profile of CH_3I outlet concentration when CH_3I was exposed to NaCl and NH_4NO_3. Indeed, the CH_3I outlet concentration presented a similar pattern to that observed with tests performed in the empty reactors (see section 5.2.1). Similar trends were also observed with Na_2CO_3 and Na_2SO_4 (annex 8).
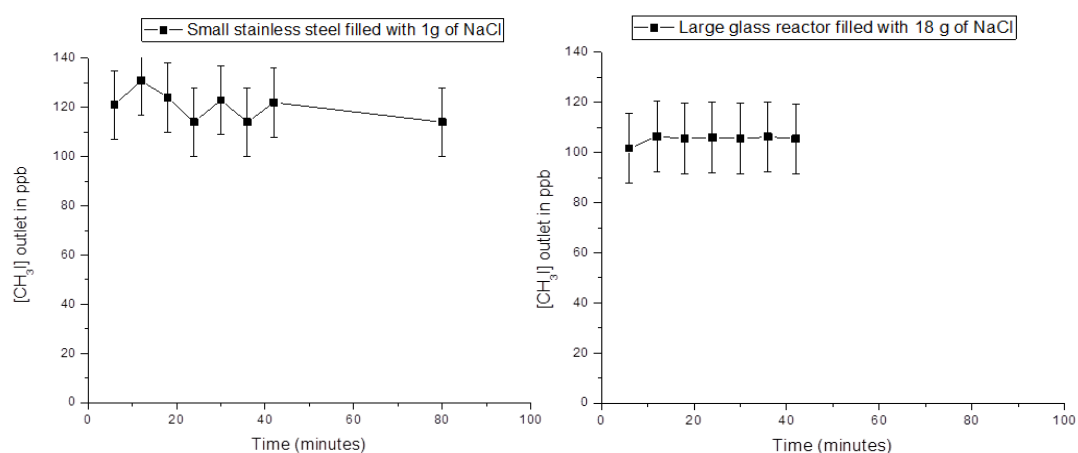
Figure 5. 8 The evolution of [CH₃I] outlet as function of time in the small and large glass reactor filled with 1g and 18g of NaCl, respectively for an injected CH₃I concentration of 100 ppb and 108 mL.min⁻¹ continuous gas flow under RH=20% at 296 K and 1 atm.
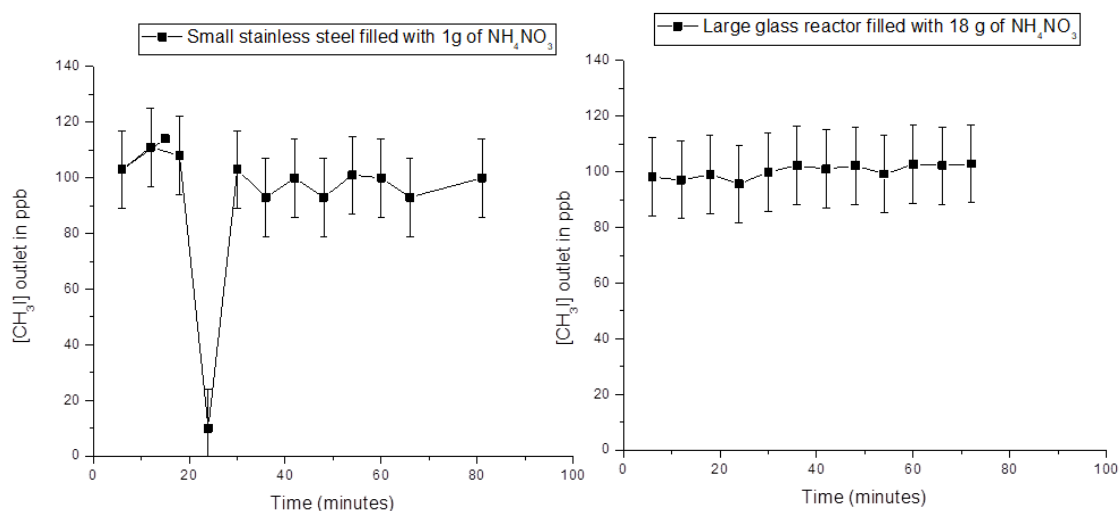
Figure 5. 9 The evolution of [CH₃I] outlet as function of time in the small and large reactor filled with 1g and 18g of NH₄NO₃, respectively for an injected CH₃I concentration of 100 ppb and 108 mL.min⁻¹ continuous gas flow under RH=20% at 296 K and 1 atm.

[CH₃I]ₘ =1 ppb:

The evolution of the CH₃I outlet concentration over time was stable in comparison to blank experiments even with low initial CH₃I concentration in the gas phase – for both reactors. As an example, Figure 5.10 and Figure 5.11 shows the evolution of CH₃I outlet concentration when CH₃I was exposed to NaCl and Na₂CO₃. Similar trend was observed with NH₄NO₃ in the large reactor (annex 8).
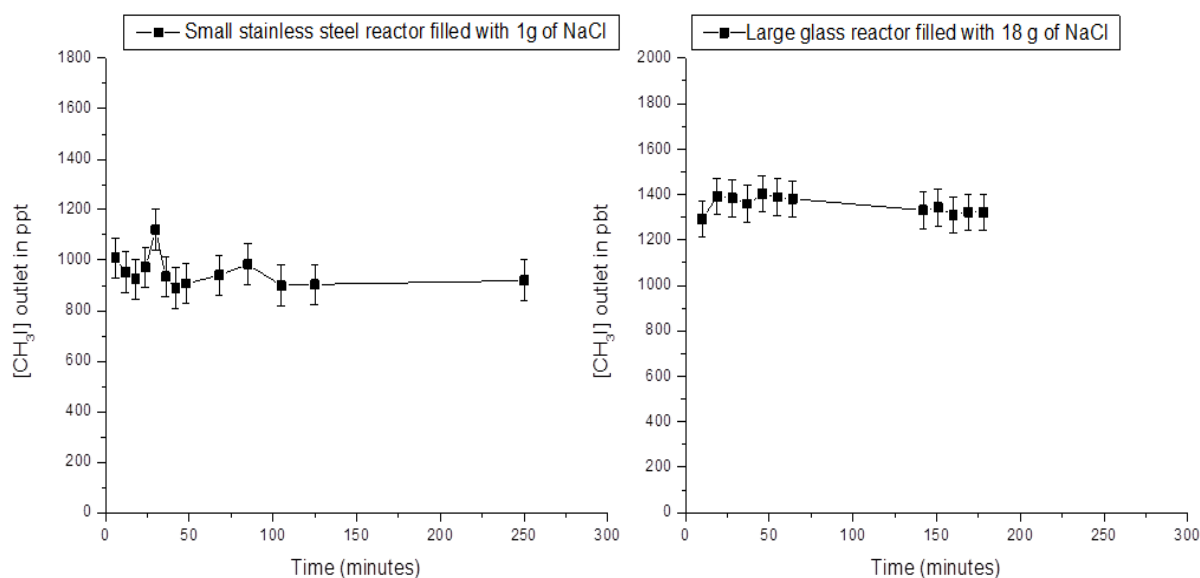
Figure 5. 10 The evolution of [CH₃I] outlet as function of time in the small and large reactor filled with 1g and 18g of NaCl, respectively for an injected CH₃I concentration of 1 ppb and 77 mL.min⁻¹ continuous gas flow under RH=20% at 296 K and 1 atm. 1 ppb=1000 ppt.
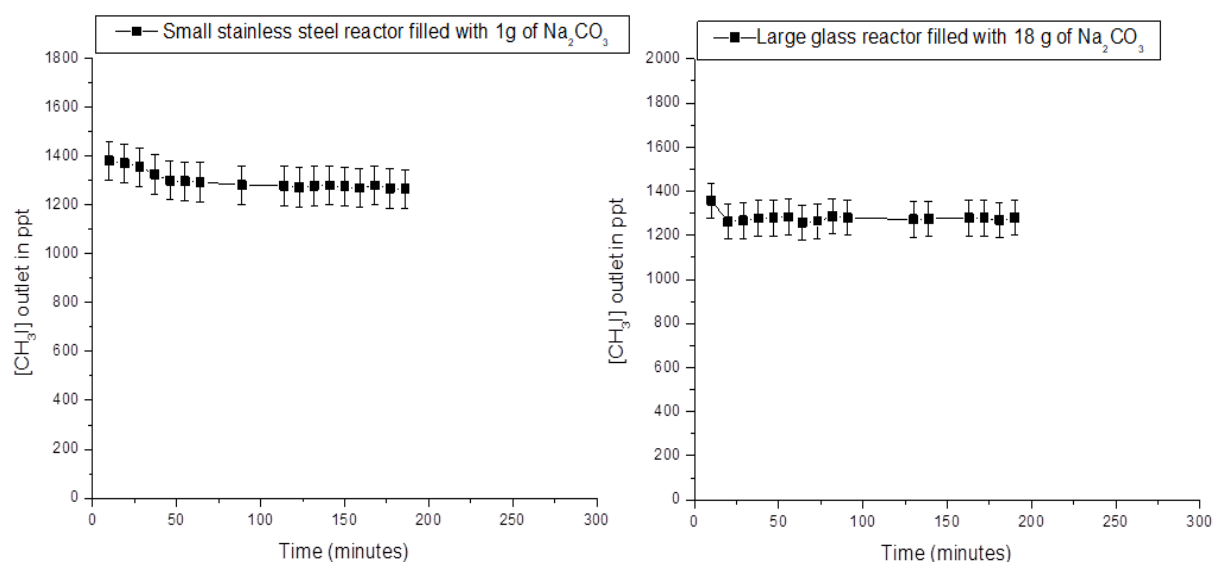
Figure 5. 11 The evolution of [CH₃I] outlet as function of time in the small and large reactor filled with 1g and 18g of Na₂ CO₃, respectively for an injected CH₃I concentration of 1 ppb and 77 mL.min⁻¹ continuous gas flow under RH=20% at 296 K and 1 atm. 1 ppb=1000 ppt

5.2.3 Reactor filled with organic solids

Experiments were performed with both small and large reactors filled with 1 g and 14 to 18 g of inorganic solids, respectively. The contact time was 844 ms- 1sec and 16-23 sec in the small and large reactors, respectively.

[CH$_3$I]$_g$ = 100 ppb:

The time profile of CH$_3$I outlet concentration in presence of organic solids did not show any significant evolution. As observed in Figure 5.12 and Figure 5.13 with glutaric acid and trisodium citrate dehydrate respectively, CH$_3$I outlet concentration was stable over time in comparison to blank experiment. Similar trend was observed with all the other organic solids (palmitic acid, malonic acid, oxalic acid, succinic acid, citric acid, citric acid monohydrate, sodium stearate, trisodium citrate anhydrous, sodium oxalate) in the small reactor (annex 8). Similarly, in the large reactor, no significant evolution of outlet CH$_3$I concentration was observed with oxalic acid (annex 8).
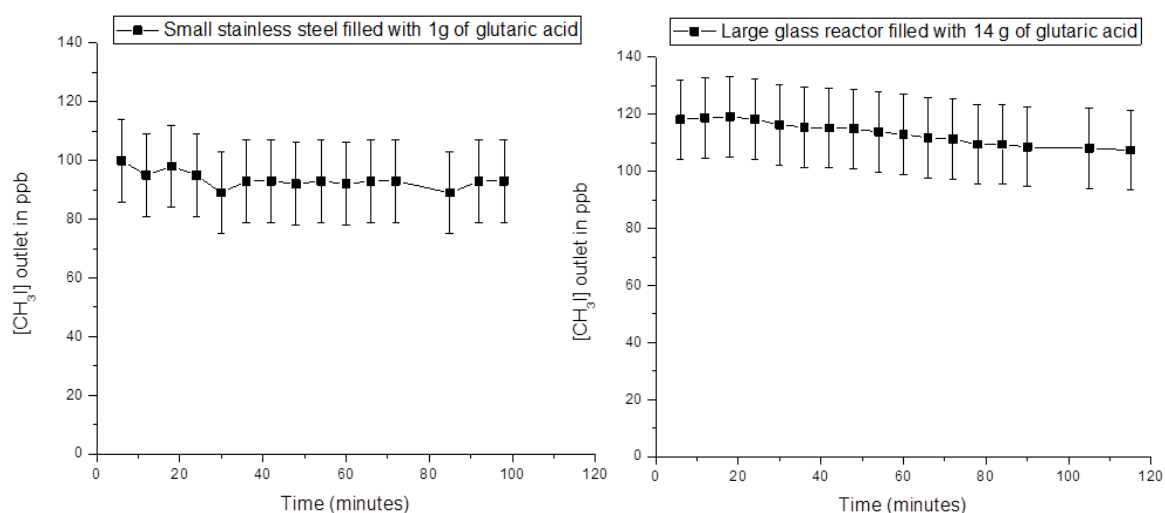
Figure 5. 12 The evolution of [CH$_3$I] outlet as function of time in the small and large reactor filled with 1g and 14g of glutaric acid, respectively for an injected CH$_3$I concentration of 100 ppb and 108 mL.min^{-1} continuous gas flow under RH=20% at 296 K and 1 atm.
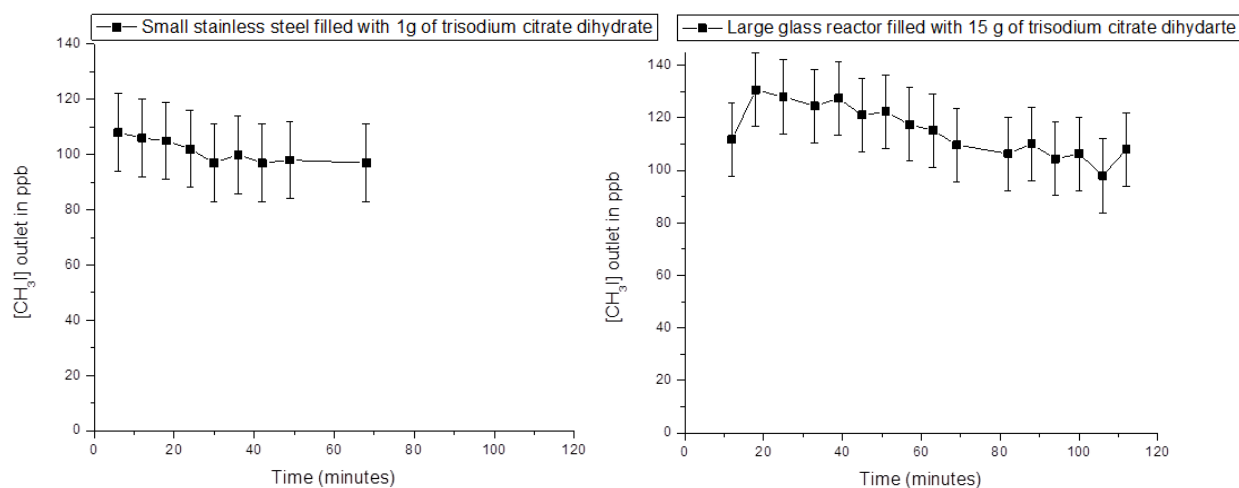
Figure 5. 13 The evolution of [CH₃I] outlet as function of time in the small stainless and large glass reactor filled with 1g and 15g of trisodium citrate dihydrate, respectively for an injected CH₃I concentration of 100 ppb and 108 mL.min⁻¹ continuous gas flow under RH=20% at 296 K and 1 atm.

CH₃I]$_g$=1 ppb:

The evolution of CH₃I outlet concentration as function of time in presence of organic solids did not show any significant evolution in comparison to blank experiment (see section 5.2.1). As an example, Figure 5.14 and Figure 5.15 shows the evolution of CH₃I outlet concentration when CH₃I was exposed to glutaric acid and trisodium citrate dihydrate.
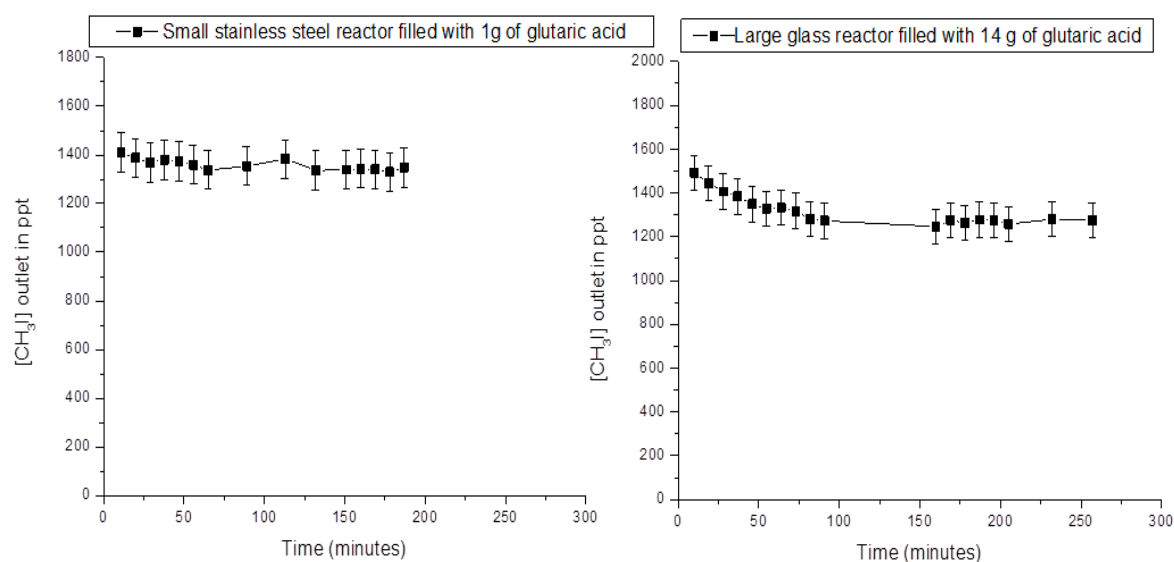
Figure 5. 14 The evolution of [CH₃I] outlet as function of time in the small and large reactor filled with 1g and 14g of glutaric acid, respectively for an injected CH₃I concentration of 1 ppb and 77 mL.min⁻¹ continuous gas flow under RH=20% at 296 K and 1 atm. 1 ppb=1000 ppt.
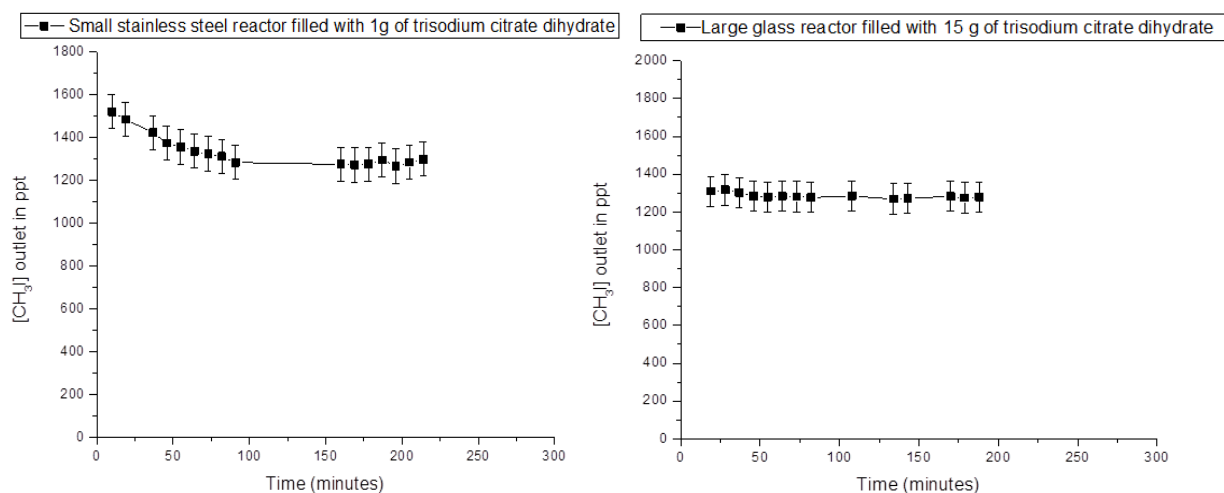
Figure 5. 15 The evolution of [CH₃I] outlet as function of time in the small and large reactor filled with 1g and 15g of trisodium citrate dehydrate, respectively for an injected CH₃I concentration of 1 ppb and 77 mL.min⁻¹ continuous gas flow under RH=20% at 296 K and 1 atm. 1 ppb=1ppt.

To sum up, we did not observe any significant evolution of CH_3I when exposed to the selected inorganic and organic solids by varying the contact time from 844 ms -1 sec (small reactor, 1 g of solid) to 16-23 sec (large glass reactor, 14-18 g of solid).

5.3 Conclusion and perspectives

The interaction of CH_3I with inorganic and organic models of primary and secondary atmospheric aerosols seems to be very weak and hardly detectable in our experimental conditions.

Further, it was not worth to consider humid conditions as methyl iodide has low affinity to water as shown in chapter 3 and chapter 4.

As the interaction of CH_3I with different solid aerosols is found to be very weak, a second step will be to evaluate the interaction of I_2 with the same compounds as models of atmospheric aerosols. With this purpose, a glass static reactor coupled with UV-Visible and ICP-MS has been built up to access the interaction of I_2 with inorganic and organic solids. This technique will allow to monitor the gas phase of I_2 when it is exposed to solids under both dry and humid conditions.

References

[1] C.J. Percival, J.C. Mo, R.A. Cox, The uptake of HI and HBr on ice, Phys. Chem. Chem. Phys. 1 (1999) 4565–4570. https://doi.org/10.1039/A904651H.

[2] M.N. Romanías, H. Ourrad, F. Thévenet, V. Riffault, Investigating the Heterogeneous Interaction of VOCs with Natural Atmospheric Particles: Adsorption of Limonene and Toluene on Saharan Mineral Dusts, J. Phys. Chem. A. 120 (2016) 1197–1212. https://doi.org/10.1021/acs.jpca.5b10323.

[3] S. Scolaro, Ph.D. thesis: Effects of humidity and fatty acid surfactants on the uptake of NO_2 to NaCl : Combined study of kinetics and surface analysis, Lille University, France (2009).

[4] K. Kawamura, L.L. Ng, I.R. Kaplan, Determination of Organic Acids (C1-C10) in the Atmosphere, Motor Exhausts, and Engine Oils, Environ. Sci. Technol. 19 (1985) 1082–1086. https://doi.org/10.1021/es00141a010.

[5] T.W. Wilson, B.J. Murray, R. Wagner, O. Möhler, H. Saathoff, M. Schnaiter, J. Skrotzki, H.C. Price, T.L. Malkin, S. Dobbie, S.M.R.K. Al-Jumur, Glassy aerosols with a range of compositions nucleate ice heterogeneously at cirrus temperatures, Atmos. Chem. Phys. 12 (2012) 8611–8632. https://doi.org/10.5194/acp-12-8611-2012.

This page is left empty

General conclusion and perspectives

Following a severe accident on a nuclear reactor, radio-iodine species (as ^{131}I) produced by the fuel fission, may be released into the atmosphere mainly under molecular iodine or methyl iodide gaseous forms. Radioiodine (^{131}I) species are highly toxic at short term and can affect both human health and environment. Besides, these iodine products are highly reactive and may interact with the other species present in the atmosphere (gas or particles) to evolve in gaseous or particulate form which play an important role on the dispersion of iodine in the atmosphere. The reactivity of iodine during its dispersion in the atmosphere is up to now not fully accounted in the IRSN (Institut de Radioprotection et de Sûreté Nucléaire) atmospheric operational dispersion tools. This is worrisome because the simulated atmospheric dispersion of radio-iodine may be quite different from the actual one due to the different possible fates of iodine within the Earth's atmosphere. Forthwith, the radiological consequences (thyroid equivalent dose) are predicted without considering the derived actual forms of the dispersed iodine. This prediction is indeed dependent on the chemical form of iodine released i.e. gaseous, liquid or solid phase and could be improved by assuming the iodine physical/ chemical evolution of radio-iodine in the atmosphere.

Gaseous organic iodine species (CH_3I) are naturally emitted at trace level (with a maximum at 2000 ppt) into the atmosphere over oceans through the algae and phytoplankton activities. Over the last four decades, the fate of emitted iodine species has a great atmospheric interest because of the oxidizing properties of iodine compounds in the atmosphere and its impact on the catalytic destruction of the ozone layer. More recently, interest was brought on gaseous iodine species interaction with atmospheric aerosols, which may affect the physico chemical form of iodine in the atmosphere and thus, their atmospheric fate. Finally, interactions between iodine species and water may enhance the iodine role in atmospheric aerosol nucleation and thus, the cloud condensation nuclei process (CCN).

In this context, the objective of this Ph.D. work was to better enhance the actual state of knowledge of atmospheric iodine chemistry focusing on the gaseous iodine - atmospheric aerosols interaction. Understanding the iodine-aerosols or iodine-water interactions can help in acknowledging the atmospheric iodine dispersion following a severe accident.

To meet the objectives of this Ph.D. work, studies have been performed via the following experimental approaches:

- Cryogenic isolation technique supported by Density Functional Theory (DFT) calculation to study the molecular interaction between CH_3I and water and in a preliminary investigation, the uptake of CH_3I on amorphous water ice. Cryogenic matrices experiments is accurate for describing intermolecular interactions between atmospherically relevant molecules. Even if working at low temperature and pressure does not mimic atmospheric conditions, such technique brings insights at molecular level for the first steps of the process and may help at understanding the mechanisms. The experiments were conducted with a large excess of H_2O molecules compared to CH_3I ($CH_3I/Ar/H_2O$: 1/24/1500) in order to mimic CH_3I environment in the atmosphere. This approach allowed the characterization of the product species that may results from the interaction between CH_3I-H_2O molecules and CH_3I-amorphous ice surface (chapter 3).

- Diffuse Reflectance Infrared Fourier Transformed Spectroscopy (DRIFTS) is useful to investigate the heterogeneous interaction between CH_3I with dry or wet NaCl solid as surrogate of sea salt aerosols. The experiments were performed under 1 atm at 296 K. This technique allowed a time monitoring of the evolution of the NaCl powder under continuous CH_3I flow (1000 ppm); and gave information about the adsorption of CH_3I and its reactivity on NaCl. By increasing the temperature of the system, the global energy of adsorption was determined. Besides, by coupling DRIFTS with ICP-MS results, the uptake coefficient of CH_3I by NaCl was estimated (chapter 4).

- Static reactor coupled with gas chromatography (GC) was used to inspect the interactions of CH_3I with different inorganic and organic solids as model of primary and secondary atmospheric aerosols. Gas chromatography allowed quantitaive analysis of CH_3I in the gas phase at the ppb level. The experiments were conducted with dry solids under 1 atm at 296 K. Forthwith, the evolution of CH_3I concentration in the gas phase and the global uptake of this gaseous species on a given solid phase was determined without any concern on the reaction mechanism with the solid (chapter 5).

The main original outputs obtained from this work are summarized below:

(1) The intermolecular behavior between CH_3I and excess of H_2O molecules trapped in Ar matrix was determined experimentally at a molecular scale and supported by DFT calculations. The results highlight that, with excess of water, gaseous methyl iodide and water molecules will likely form aggregates of water and methyl iodide polymers instead of $(CH_3I)_n$-$(H_2O)_m$ complexes. This result is consistent with previous theoretical

studies, which have predicted the low hydration of CH$_3$I. Therefore, CH$_3$I will stay in the gaseous phase as homo or hetero water-CH$_3$I aggregates with low influence on nucleation process.

(2) Preliminary results show that amorphous ice surface modes, in particular the dH dangling bonds, can be perturbed upon adsorption of CH$_3$I. The appearance of CH$_3$ modes in stretching, deformation and rocking region confirms the adsorption of CH$_3$I on amorphous ice. However, the adsorption and desorption processes are not clearly identified.

(3) The DRIFTS experiments clearly evidenced adsorption of CH$_3$I on the NaCl particles. The DRIFTS spectra showed two new and intense bands at 1024 and 1073 cm^{-1} which are typical of the CH$_3$ deformation. These bands are probably assigned to new geometrical orientation of CH$_3$I adsorbed on halide solids. Theoretical calculations as well as experimental studies using isotopic products (CD$_3$I, CD$_2$HI, etc) would confirm the assignment.

(4) The adsorption of CH$_3$I on NaCl is likely chemisorption since no desorption was observed even after the heating of the system. The presence of water on the surface of NaCl seems to hinder the interaction between CH$_3$I and NaCl, which can be explained by the fact that CH$_3$I is insoluble in water. However, further experiments and/or theoretical studies are necessary for fully unravel the molecular processes.

(5) The adsorption curves featuring the area of the IR band related to the adsorbed CH$_3$I versus time, show that the adsorption of CH$_3$I on NaCl did not reach any saturation even after 5 hours of continuous flow of CH$_3$I (1000 ppm). The % {CH$_3$I}$_{residual}$ on NaCl was found to be low of 0.003%. CH$_3$I adsorption at the NaCl surface follows a pseudo 1st order kinetic law regarding CH$_3$I gas phase concentration. Although the high concentration of CH$_3$I considered in our experiments, the calculated uptake coefficients are of low values in the order of 10^{-11}. Indeed, the % {CH$_3$I}$_{residual}$ and the uptake coefficient values indicate a very weak macroscopic interaction between CH$_3$I and NaCl in our experimental conditions. Thus, regarding the CH$_3$I atmospheric concentration, which is in the order of ppt, the influence of aerosols on the behavior of gaseous CH$_3$I can be considered negligible. The rate of methyl iodide adsorption at the surface decreases with increasing temperature, which suggests a low probability

of the colliding molecules with NaCl when temperature is above 323 K. A global adsorption energy of -38 KJ/mol was determined.

(6) It was found that CH$_3$I interact with halide salts surface (NaCl, NaI, KBr) in an original geometrical configuration which has never been described.

(7) The interactions of CH$_3$I with organic and inorganic solids (sodium chloride, sodium sulphate, sodium carbonate, ammonium nitrate, sodium bicarbonate, malonic acid, sodium stearate, palmitic acid, sodium oxalate, glutaric acid, oxalic acid, trisodium citrate diyhdrate, trisodium citrate anhydrous, citric acid, succinic acid and citric acid monohydrate) were investigated using static reactors in various conditions of exposure. We have found very weak and hardly detectable interactions by monitoring the gas phase, even for CH$_3$I concentration at the ppb level.

Finally, considering that our experimental conditions can be transposed to atmospheric conditions, we hypothesis that CH$_3$I when released will interact very little with the solid aerosols and will mainly remain in the gaseous phase probably as homo or hetero-aggregates. Therefore, the photochemical processes occurring in the gaseous phase are likely the main processes of CH$_3$I reactivity in the atmosphere.

In case of severe nuclear accident such as Fukushima daiichi nuclear power plant accident, a maximum total ^{131}I iodine concentration reported on site was about 10 MBq.m^{-3} representing thus less than one ppt (~ 0.4 ppt) which is in the lower concentration range of naturally occurring iodine. So, even if our study at laboratory scale is far from representing atmospheric conditions, we can expect still a very low uptake in the environemental conditions featuring methyl iodide concentrations below the ppb range. Thus, a minimal uptake in the 10^{-10} -10^{-11} range can be still reasonably considered for environmental conditions.

Although CH$_3$I capture by halide-containing aerosols is weak, the irreversible nature of this process is not without consequences on the dispersion of atmospheric iodine. This point should be implement in the radioactive iodine dispersion model to evaluate any influence on the thyroid equivalent dose, in case of accidental radioactive iodine releases.

Certainly, the uptake coefficient given in this work will give insights for the IRSN modeling tools to better understand and model radioactive organic iodine atmospheric interactions and deposits.

This work opens new perspectives in the field of the atmospheric organic iodine species. Actually, up to now, the homogeneous reactivity is investigated, especially the photoreactivity of CH₃I where the influence of water or the potential catalytic effect of aerosols on these photochemical processes are poorly considered.

It is important to investigate the photochemical behavior of CH$_3$I-water aggregates, which are known to be sensitive to the solar radiation and representative of atmospheric condition. Additional experiments are required to explain the interaction of CH$_3$I with amorphous ice at molecular scale. These studies may be investigated using cryogenic experimental set up that would improve our understanding on the interaction between CH$_3$I-H$_2$O and CH$_3$I-amorphous ice exposed to various radiations by responding to the following questions:

- How do CH$_3$I-water aggregates behave under solar radiation?
- How the adsorption of CH$_3$I does affect the surface structure and reorganization of the amorphous ice?
- Upon adsorption of CH$_3$I on ice, is there any CH$_3$I-H$_2$O bonding or complex formation? Is there any polymer formation?
- Under which conditions can CH$_3$I migrate to the bulk of amorphous ice?
- Is it possible to desorb CH$_3$I using only the kinetic energy of a gas stream?
- Is it possible to desorb CH$_3$I by selectively irradiating dH?
- How does the adsorbed CH$_3$I on amorphous ice behave under solar radiation?

An improved understanding of the adsorption process of CH$_3$I on NaCl surface and confirmation of the attribution of the new IR bands observed in DRIFTS (Chapter 4) may be achieved with the help of theoretical calculation and experiments with deutered species of CH$_3$I. The organisation of the CH$_3$I molecules at the solid surface as well as their dynamic, the influence of water on these organization and/or reorganization and finally the potential reactivity are the key questions that can be investigated using theoretical calculations.

Finally, to completely update the radio-iodine atmospheric dispersion modelling, the interaction of molecular iodine (I$_2$) with water and dry/humid atmospheric aerosols have to be investigated. Molecular iodine is indeed the other key iodine gaseous compound believed to be released into the troposphere in case of an accident on a nuclear power plant.

The data gained from these studies will help in the mid-term to improve the capabilities of the IRSN dispersion tool to better predict radio-iodine dispersion following an accidental release and be at the state of the art.

Annex 1: CH₃I chemical properties

Table A 1 Chemical properties of CH₃I [1].

Names	Iodomethane Methyl iodide
Molecular Weight	141.94 g.mol^{-1}
Boiling point	42.5 °C
Melting point	-66.5°C
Relative density	2.28 g.cm^{-3} at 25 °C
Henry's law constant	0.01 atm.m^3.mole^{-1}
Vapor pressure	50 kPa at 20°C
Atmospheric OH rate	7.20×10^{-14} cm^3.molecule^{-1}.sec^{-1}
Heat of Combustion	194.7 kg.cal.g^{-1}.mole^{-1}
Heat of Vaporization	27.97 kJ.mol^{-1} at 25 °C
Index of refraction	1.5380 at 20 °C

Annex 2: Infrared Spectroscopy techniques

1-Principle of Infrared spectroscopy [2, 3]

Spectroscopy deals with the interaction of atoms and molecules with electromagnetic radiation. These interactions can be absorption, emission or scattering. Electromagnetic radiation is described by Maxwell's law consists of two oscillating fields perpendicular to each other on a unique plane. These components are represented by simple sinusoidal functions at a constant velocity (c), the speed of light. The energy (E) and the frequency (v) associated to the radiation is given by the following equations where h is the Planck's constant

$$E = \frac{h.c}{\lambda} \quad \text{[EA-1]}$$

The IR radiation corresponds to the less energetic (10^{-3}-1 eV) domain and to the range of vibrational and rotational transitions. The absorption of IR radiation is dictated by a selection rule that requests a change in the dipole moment of the molecule. For non-linear molecules of N atoms, the number of vibrational modes is 3N-6, whereas a linear molecule has 3N-5 normal vibrational modes as rotation about its molecular axis cannot be observed. The coordinate of a normal vibration is a combination of changes in the position of atoms in the molecule. It is usual to describe molecular vibrations by the change of internal

coordinates: stretching, bending, rocking, etc and normal coordinate (Q). Q can be constructed and described as a combination of internal coordinates.

In classical mechanics, the simplest description of the chemical bond formed between two atoms, A and B with corresponding masses in vibration is the harmonic oscillator (Figure A.1). For the stretching mode, d represents the displacement of the spring (cm), k is the force constant (N.cm^{-1}) and F is the force required for the spring to get back in its initial state (N) (EA-2). The reduced mass μ of the two atoms is used [EA-3].

A   B
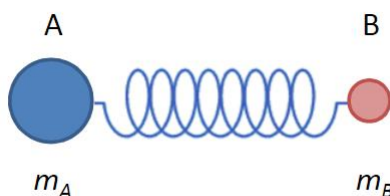
m_A m_B

Figure A. 1 Simplified spring ball model to represent the harmonic oscillator [2].

$$F = k.d \quad \text{[EA-2]}$$

$$\mu = \frac{m_A \times m_B}{m_A + m_B} \quad \text{[EA-3]}$$

The system possesses both kinetic and potential energies (E_k and E_p respectively).

$$E_k = \frac{1}{2}(m_1 d_1^2 + m_2 d_2^2) \quad \text{[EA-4]}$$

$$E_p = \frac{1}{2}(k d_1^2 - k d_2^2) \quad \text{[EA-5]}$$

Using the Lagrange's set of equations to solve the energy of this vibration, a simple equation relating the frequency to the reduced mass and the force constant of the spring is obtained [EA-6]:

$$v = \frac{1}{2\pi}\sqrt{\frac{k}{\mu}} \quad \text{[EA-6]}$$

From this equation, we can see that the observed vibrational mode frequency is correlated with the reduced mass of the molecules.

Solving the Shroedinger wave equation, the energy states of each normal coordinate are given by:

$$E_v = \left(v + \frac{1}{2}\right)\frac{h}{2\pi}\sqrt{\frac{k}{\mu}} \quad \text{[EA-7]}$$

Where n is a quantum number that can take values of 0, 1, 2, … and h the Planck constant. The difference in energy when n changes by 1 is therefore equal to the energy derived using classical mechanics. For a harmonic oscillator, transitions are allowed only when the quantum number n changes by one (Δn = ± 1). The observation of overtones Δn > ± 1 is only possible because the vibrations are anharmonic.

A vibrational mode is active in infrared absorption spectroscopy if the derivative of the molecular dipole moment $(\vec{\mu})$ with respect to the normal coordinate, $\frac{d\vec{\mu}}{dQ} \neq 0$.

2-Principle of Fourier Transform Infrared spectroscopy [3]

Fourier-transform infrared spectroscopy (FTIR) is a method of exploring the physical properties of solids, liquids, and gases. More specifically, it allows the study of the absorptive and emissive properties of materials. The choice of IR wavelengths in FTIR method is particularly useful for studying chemical bonds that connect atoms.

Fourier transform infrared (FTIR) spectroscopy is a measurement technique for collecting infrared spectra and its principle is shown in the scheme A.2. Instead of recording the amount of energy absorbed when the frequency of the infra-red light is varied (monochromator), the IR light is guided through a Michelson's interferometer. The principle is the measurement of the temporal coherence of the light, using the time-domain measurements of the electromagnetic radiation. After passing through the sample, the interferogram is measured.
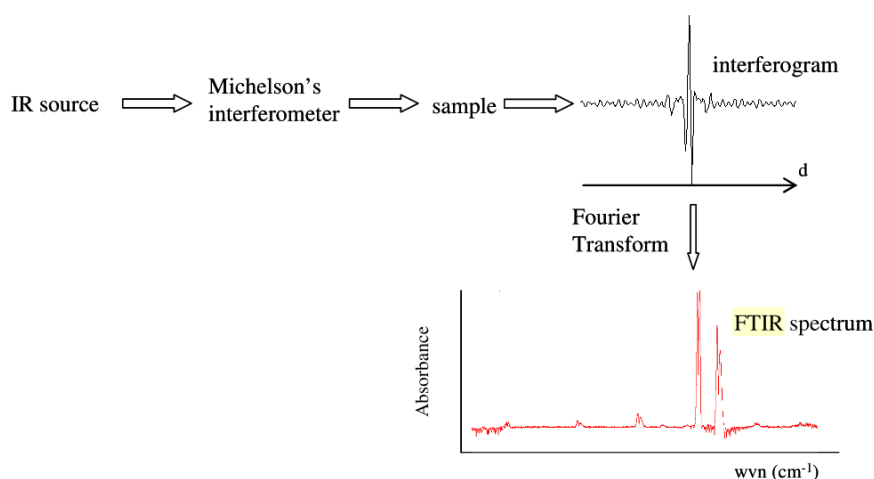
Figure A. 2 Measurement principle of a FTIR spectrometer [3].

Performing a mathematical Fourier transform on this interferogram results in a spectrum identical to that from conventional (dispersive) infrared spectroscopy. Measurement of a

single spectrum is faster with the FTIR technique because information at all frequencies is collected simultaneously. This allows multiple samples to be collected and averaged together resulting in an improvement in sensitivity.

3-Diffuse Reflectance Fourier Transform Infrared Spectroscopy [4-6]

The principle of Diffuse Reflection Infrared Fourier Transform Spectroscopy (DRIFTS) is based on the penetration of incident radiation into a sample of fine particles. In contrast to specular reflection experiments where light reflected from a polished surface (mirror) is analyzed at a particular angle, in diffuse reflection, the radiation penetrates the diffusing solid sample, undergoes reflection, refraction, absorption and scattering effects, and is then re-emitted in all directions of a surrounding hemisphere (see Figure A.3).
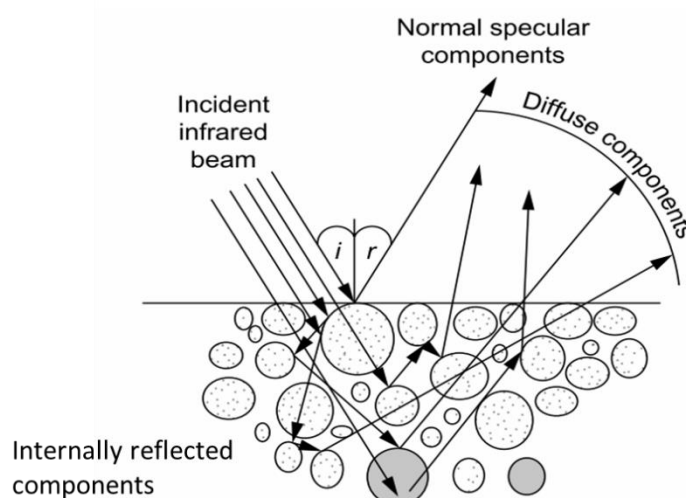
Figure A. 3 Mechanisms generating the infrared spectrum of a powder [4].

When the specular reflection component is low, diffuse reflection spectra will be very similar to transmittance spectra. The samples are in the form of powders divided and dispersed in a non-absorbent matrix. However, the quantitative relationship between the absorbed light and the concentration of the absorbing species will differ in diffuse reflection from the Beer-Lambert law used in absorption.

➢ **Kubelka Munck theory**

To interpret the diffuse reflection spectra, it is necessary to know the attenuation suffered by the incident wave during its propagation in the sample, due to absorption and scattering phenomena. Kubelka-Munck's theory makes it possible to account for this effect.

As a rule, the specific properties of the material liable to influence the quality of the DRIFTS spectrum are as follows:

– Refractive index of the sample;

– Particle dimensions;

– Packing density;

– Homogeneity;

– Concentration;

– Absorption coefficients

Let us consider a sample diluted in an infrared transparent matrix (KBr for example), of thickness d, subjected to an incident flux I_o in the x direction and reflecting a flux J_o in the same direction (Figure A3).
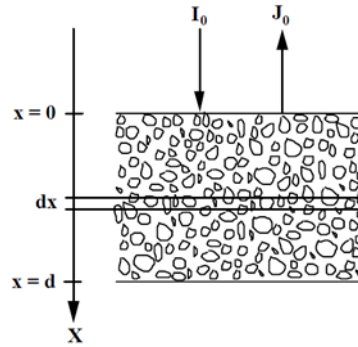
Figure A. 4 Scheme of a layer of particles that absorb and diffuse light [5].

In Kubelka-Munk's theory, it is admitted, to simplify, that photons will move only in the 0x direction. Thus, it is possible to describe the radiation field in the sample thanks to the fluxes I and J corresponding respectively to the energy propagating in the direction x>0 and x<0. Considering an element of thickness dx in the sample, it is possible to write the energy conservation balance in the volume between the planes of thickness x and x+dx. The flux I passing through the element will be on the one hand attenuated due to absorption and scattering, and on the other hand amplified by the fraction of photons of the flux J which is backscattered in the direction of I. In the same way, a balance on J can be written. To write these balances, two phenomenological coefficients K and s are introduced, respectively characterizing the absorption and scattering per unit length in the sample. It then becomes possible to formalize the energy balance previously described in the form of a differential system of the first order, linking I and J. The boundary conditions (in the case of a totally reflective substrate I=I_0 for x=0 and J=0 for x=d) make it possible to obtain the explicit values of I and J, and thus the transmittance and diffuse reflectance as a function of the parameters K and s.

Using this simple model, we can show that the transmittance (ratio of the intensity of the exiting light to the entering light crossing the sample) can be expressed by:

$$T = \frac{I_{x=d}}{I_0} = \frac{2\beta}{(1+\beta^2)\sinh(\kappa d)+2\beta\cosh(\kappa d)} \quad \text{[EA-8]}$$

and diffuse reflection:

$$R = \frac{J_{x=0}}{I_0} = \frac{(1-\beta^2)\sinh(\kappa d)}{(1+\beta^2)\sinh(\kappa d)+2\beta\cosh(\kappa d)} \quad \text{[EA-9]}$$

In these expressions : $\kappa = \sqrt{K(K + 2s)}$ and $\beta = \sqrt{\dfrac{K}{K+2s}}$

While k, the absorption coefficient, is easily known from the Lambert-Beer law, parameter s is difficult to determine. To circumvent this problem, Kubelka and Munk considered the limiting case of a sample of infinite thickness (2 or 3 mm of powder satisfies this condition). This accordingly gives:

$$T_\infty = 0 \text{ and } R_\infty = \frac{1-\beta}{1+\beta} \quad \text{[EA-10]}$$

Which can also be placed in the form: $f(R_\infty) = \dfrac{(1-R_\infty)^2}{2R_\infty} = \dfrac{K}{s} \quad \text{[EA-11]}$

f(R∞) is called the re-emission function or Kubelka-Munk function. A comparison with a standard sample consisting of a nonabsorbent powder, i.e. KCl, KBr, etc. (such that k $\cong$ 0 and R∞ $\cong$ 1) helps to determine the ratio:

$$r_\infty = \frac{(R_\infty)\text{sample}}{(R_\infty)\text{standard}} \quad \text{[EA-12]}$$

to which we apply the expression:

$$f(r_\infty) = \frac{(1-r_\infty)^2}{2r_\infty} = \frac{K}{s} \quad \text{[EA-13]}$$

by replacing k by $2.303.\varepsilon(\nu).C$, where: ε = extinction coefficient (function of the wavenumber v); c = sample concentration; this gives:

$$f(r_\infty) = \frac{2.303 \cdot \varepsilon(\nu) \cdot C}{s} \quad \text{[EA-14]}$$

and if s is a constant, i.e. an intrinsic property of the material which depends on the grain size, f(r∞), at a given frequency, varies directly with the sample concentration c. This produces a similar expression to the absorbance expression that enables us to obtain a spectrum resembling the transmission spectrum.

> ➢ **Quantitative analyses of DRIFTS spectra**

DRIFTS technique can bring many invaluable insights into the mechanism of heterogeneous reactions. The qualitative analysis of the DRIFTS spectra is sufficient to assess the nature of the adsorbates present. However, a fully quantitative analysis of DRIFTS data is required when the surface concentrations and the specific rate constants of reaction (or desorption) of adsorbates are needed to carry out complete spectro-kinetic studies.

The Kubelka-Munk and pseudo-absorbance data treatement are the most commonly used functions when data collected by DRIFTS. The basis of the diffuse reflectance theory used to quantify the concentration of an adsorbate was developed by Kubelka and Munk and widely applied to the mid-IR regionsand sometimes to the UV-vis and near-IR regions. The Kubelka-Munk formula [EA-13, EA-14] relates the diffuse reflectance radiation to the sample absorption and scattering coefficients k and s, respectively. In practice, many of the conditions required for the Kubelka-Munk theory to apply are not often met, e.g., because of the presence of Fresnel (i.e., specular, mirror-like) reflection, matrix absorption, and nonuniform optical properties of the sample. Signal corrections can be made, even for nondiluted samples, but the data treatment is complex and the effect of the sample micro- or nanostructure will also affect the scattering coefficient, making the comparison difficult between differently prepared samples. In many cases, simple calibration curves have shown that the Kubelka-Munk equation is not linear with respect to the concentration of the solute, displaying a curved or brokenline shape. In this case, pseudo absorbance (log (1/R∞)) can be used to linearly represent the adsorbate concentration given by:

$$\log (1/R_\infty) = \frac{\text{Concentration}}{\text{Constant}} \quad [\text{EA-15}]$$

It has been previously shown [5] that the intensity of adsorbates should be reported in the form of the Kubelka-Munk function for the case of highly absorbing adsorbates to obtain DRIFTS data proportional to the adsorbate surface concentrations. Whereas, the intensity of adsorbates should be reported in the form of pseudo absorbance for the case of poorly absorbing adsorbates to obtain DRIFTS data proportional to the adsorbate surface concentrations.

Annex 3: Uncertainty estimation of the band area observed in DRIFTS spectra and effect of closing or opening valves on static conditions

The uncertainty of band area for the bands observed in the deformation region (1400-900 cm^{-1}) are estimated using t distribution (Student's t-distribution) and results are reported in Table A.1.

Student's t-distribution is a probability distribution that is used to estimate population parameters when the sample size is small and/or when the population variance is unknown. The confidence interval was constructed as follow:

Step 1: Find the mean, μ and standard deviation, σ for the data.

Step 2: Subtract 1 from your sample size to find the degrees of freedom (df).

Step 3: Subtract the confidence level from 1, then divide by two. This is the alpha (α) level.

Step 4: Look for df (Step 2) and α (Step 3) in the t-distribution table.

Step 5: Divide standard deviation (step 1) by the square root of your sample size (Standard error).

Step 6: Multiply step 4 by step 5. This value is the confidence interval (at 95%) +/- in absolute.
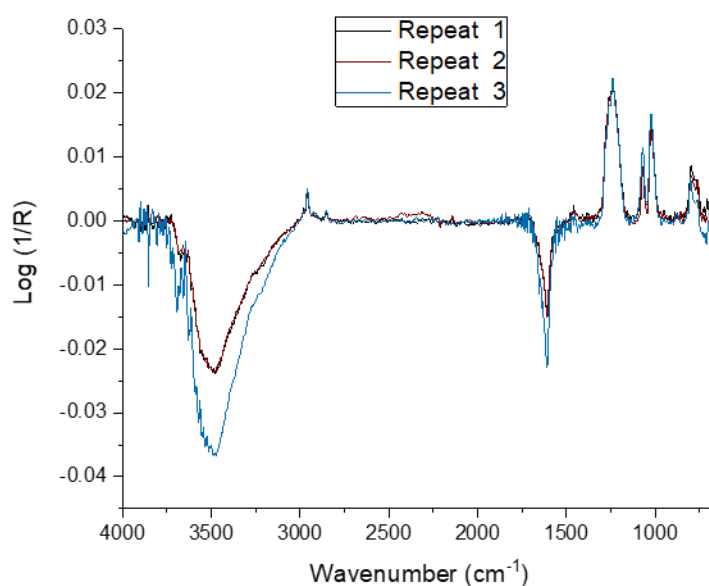
Figure A. 5 Typcial DRIFTS spectra in the 4000-650 cm^{-1} spectral range expressed in pseudo-absorbance for NaCl exposed to 5 hours of CH$_3$I (108mL.min^{-1},1000 ppm) flow at 296 K and 1 atm. The spectra are from dry experiments repeat 1, repeat 2 and repeat 3.

Table A.2 Calculation of the the uncertainity of band using student's t-distribution law.

Experiment	Band (cm⁻¹)	Band area (arbitrary unit)	Mean of band area	Standard deviation	Relative standrad deviation	Standard error	Confidence interval (at 95%) +/- in absolute
Repeat 1	1275+1244+1220+1183+ 1073+1024	2.34	2.16	0.15	6.97	0.09	0.37
Repeat 2		2.09					
Repeat 3		2.07					
Repeat 1	1275+1244+1220+1183	1.48	1.43	0.05	3.31	0.03	0.12
Repeat 2		1.43					
Repeat 3		1.39					
Repeat 1	1073	0.24	0.20	0.04	19.46	0.02	0.10
Repeat 2		0.18					
Repeat 3		0.17					
Repeat 1	1024	0.59	0.53	0.05	10.03	0.03	0.13
Repeat 2		0.51					
Repeat 3		0.49					
Repeat 1	1262	0.12	0.13	0.01	9.90	0.01	0.03
Repeat 2		0.15					
Repeat 3		0.14					

Table A.3 Effect of closing or opening valve on static conditions.

	Sum of the band area of 1275, 1244, 1220 and 1183 cm^{-1} in arbitrary units		
	After 5 hours of CH$_3$I flow	After 1 hour of static conditions (closed valve)	% difference $(A_{CH3I} - A_{Istatic})/A_{CH3I}$
Experiment 1	1.43	1.39	2.9%
	After 5 hours of CH$_3$I flow	After 1 hour of static conditions (open valve)	% difference $(A_{CH3I} - A_{Istatic})/A_{CH3I}$
Experiment 2	1.48	1.45	2.1%

Annex 4: Principle of Inductively coupled plasma mass spectroscopy (ICP-MS) [7]

Inductively Coupled Plasma (ICP), coupled with a mass spectrometer (MS), is an analytical technique based on the separation, identification and quantification of the constituent elements of a sample according to their mass. It is based on the coupling of an ion generating plasma torch and a mass spectrometer (quadrupole) allowing the separation of ions according to their mass-to-charge ratios. The ICP-MS technique allows multi-element trace determinations (1µg/g) in solution.

The ICP-MS analysis of the samples can be divided into four stages: introduction-atomizing, ionization, separation in mass, detection as shown in Figure A6:

- The liquid sample is injected into the system through a capillary tube and driven by a peristaltic pump to the nebulizer. It is then nebulized in the nebulizer chamber and pumped into the plasma torch as an aerosol. Thus, the aerosol formed is sent in an argon plasma torch at very high temperature (from 5000 to 10000K), which is sufficient to allow the liquid aerosol to vaporize, dissociate, atomize and ionize completely the majority of the elements.

- The generated ions are then extracted through the interface region and into a set of electrostatic lenses called the ion optics. The ion optics focuses and guides the ion beam into the quadrupole mass analyzer.

- A quadrupole (mass analyzer) is based on the separation of the ions according to their mass to charge ratio and the ions having the desired ratio m/z (mass/charge) will be transmitted to the detector.

- The ion detector can thus generate a measurable signal pulse (counts) from the impact of a single ion, which is proportional to the concentration.
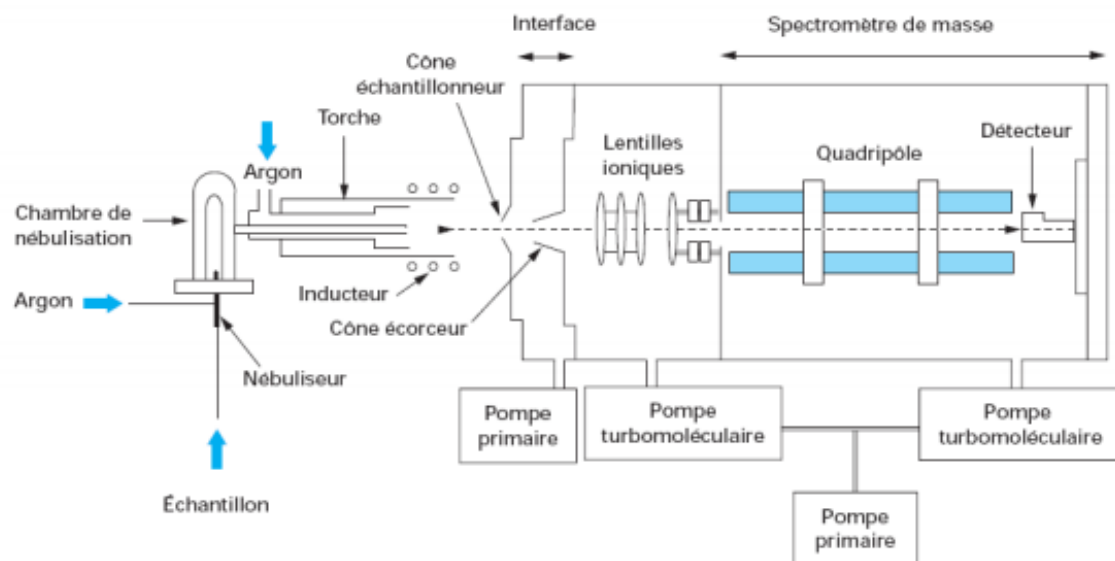
Figure A. 6 ICP-MS scheme. Q-pole: Quadrupole [7].

Annex 5: Gas chromatography (GC) [8]

Gas chromatography (GC) is a widely used analytical technique. It is a separation technique applicable to gaseous compounds or compounds that can be volatilized by raising temperature without decomposition (with a molecular weight of less than 300 atomic mass units). The mobile phase is a gas (helium), so it allows the advancement of analytes in the column which are in the gaseous state. The mobile phase behaves like an inert carrier gas, it does not cause any interaction with the analytes to be separated.
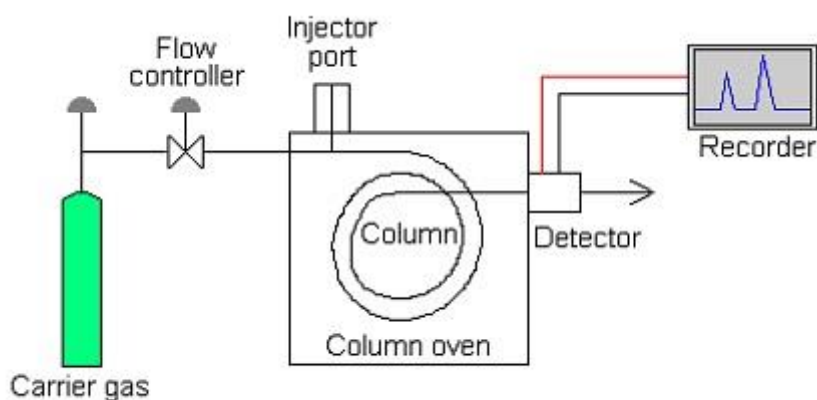
Figure A. 7 GC scheme [8].

Injection: The CPG present at the L2EC [8] allows the use of two different injection modes: manual injection and injection through the thermo-desorber.

258

- Manual injector: The sample to be analyzed is introduced into the chromatograph using a gas sampling syringe (10 or 25 mL) or Tedlar® bag (500mL or 1L). Manual injection includes an injection loop. The choice of the loop volume is based on the size of the column and the assumed concentration of the products to be analyzed. The injection loop system avoids dead volume and ensures a constant injection volume, which is important for quantitative analysis.

- Injection through the thermo-desorber: The sample to be analyzed is not introduced directly into the chromatograph. This technique is used when the analyte is not concentrated enough to be detected or quantified. A pre-concentration step is required. This technique uses the possibility for the analyte to adsorb on a solid phase (cold-trap), and conversely to desorb in the injector under the effect of heat. Several modes of injection in the cold-trap are possible: Tedlar® gas bag or sample tube.

The GC has a split/splitless injector that allows the fraction of the sample sent to the column to be adjusted in relation to the total quantity introduced into the chromatograph. In split mode, a stream of carrier gas arrives in the injection chamber where it mixes with the injected sample. A leakage valve divides into two fractions, the smaller of which is the only one to enter the column. The fraction of the sample entering the column is equal to the split ratio, which can vary between 1 and 165.

In splitless mode, the entire sample is injected and then entrained into the first turns of the capillary column. The injector is then swept by the carrier gas which removes the excess solvent. This procedure is reserved for highly diluted samples. When injecting via the thermo-desorber, the injection method on the GC must be in splitless mode (because the TD has its own split).

Column: The gas chromatographic column may be considered the heart of the GC system, where the separation of sample components takes place. Columns are classified as either packed or capillary columns.

Packed columns are stainless steel or glass tube filled with particulate packing material (an adsorbent material, or a support material coated or impregnated with a solid phase). Packed columns produce broad band shapes and have low separation performance, but can also handle large sample volumes and are not susceptible to contamination.

The capillary columns usually consist of a fused silica (quartz, SiO_2) capillary that is coated with a polyimide layer. The polyimide layer provides the capillary with flexibility and stability, as well as its characteristic brownish color. Capillary columns produce sharp band shapes, achieve excellent separation performance, and are suited to high-sensitivity analysis. The

column used in our experiments is a GASPRO capillary (open tube) column. The internal diameter of the column is 0.32 mm and is 30 m long (twice 15 m). The maximum operating temperature of this column is 350°C.

Detector: The detector senses a physicochemical property of the analyte and provides a response which is amplified and converted into an electronic signal to produce a chromatogram. In L2EC laboratory the GC has two detectors: Thermal Conductivity Detector (TCD) and Electron Capture Detector (ECD).

The TCD is a universal response detector but is relatively insensitive (of the order of ppb). This detector is based on a continuous comparison between the heat flux carried by the pure carrier gas and the heat flux carried by the carrier gas loaded with the molecules to be analyzed. These heat fluxes are produced by thermistors, through which a direct current of fixed voltage flows, in a thermostatically controlled enclosure. The thermistors are mounted in a Wheastone bridge, which allows the evolution of the current to be monitored as a function of the variation in resistance due to temperature variations around the filaments.

The ECD is a more selective detector and sensitive to halocarbon compounds such as iodomethane. It is a very sensitive detector that can analyze samples with concentrations of the order of ppt. ECD has a low-energy radioactive source that allows free electrons to be sent into the detector. When substances with an affinity for free electrons pass through the detector, ions are produced which are collected in the existing electrostatic field by an anode and form an ionization current.

Annex 6: Method of calculating the uncertainty of GC and ICP-MS measurements [9]

An estimate of the expanded measurement uncertainty for manual injection and via the thermodesorber was determined based on IRSN internal report [8] for GC and Melany's work [7] for ICP-MS. These determinations were based on EURACHEM/CITAC Guide [9]. The estimation of an uncertainty involves a number of successive steps: Specification of the measurand; Identification of the sources of uncertainty; Quantification of the uncertainty components; Calculation of the combined uncertainty; Final expression of the measurement result.

Definition of the measurand: In GC the measurand corresponds to the volume concentration of methyl iodide (CH_3I) in gaseous form (expressed in ppt, ppb or ppm). It is calculated from a sampling flow rate (Nl/min) and the initial concentration of the standard cylinder. In ICP-MS the measurand corresponds to the number of moles of the elements $^{127}1$ present in the solutions analyzed after testing in the bench (samples in bubblers, filter solutions, rinsing solutions).

Sources of uncertainty: The sources of uncertainty are identified (1) for GC the dilution factor and the analytical method (GC) (2) for ICP-MS the weighing volume of the solution, dilution factor and the analytical method.

Quantifying the uncertainty components: Determining the accuracy and precision were conducted to quantify uncertainty of each component volume, analysis and dilution method. The accuracy used to evaluate the difference between a certified value and a measured result. The precision takes into account the effects of random factors that influence the measurement of samples (temperature, pressure, storage conditions, reliability of the method over time, preparation of solutions, etc).

Calculation of the combined and expanded uncertainty: The compound uncertainty is associated with the determination of the combination of uncertainty contributions (analysis, volume and dilution).

The final stage is to multiply the combined standard uncertainty by the chosen coverage factor in order to obtain an expanded uncertainty. The expanded uncertainty is required to provide an interval which may be expected to encompass a large fraction of the distribution of values which could reasonably be attributed to the measurand.

Therefore, the expanded uncertainty for GC measuremnets was found to be 8% and 14 % at 95 % confidence level, for thermos-desorber and manual injection, respectively. For ICP-MS measurements, the uncertainity was found to be 8% at 95 % confidence level.

Annex 7: ICP-MS data and conversion factor calculation

Using ICP-MS, we were able to determine the total number of iodine taken up by salt in mg using [EA-16]:

$$m_t \text{ (I) in the solution} = \text{[I] in ppb} \times \text{Volume of NaOH (mL)} \quad \textbf{[EA-16]}$$

Then total mass of iodine taken up by dissolved salt in number of atoms /mg was determined by [EA-17]:

$$m_t \text{ (I) in dissolved salt} = \frac{m_t\text{(I) in the solution (mg)}}{\text{mNaCl dissolved (mg)}} \times 10^{-3} \times \frac{\text{Avogadros number}}{\text{Molar mass of Iodine}} \quad \textbf{[EA-17]}$$

The total amount of iodine taken up **total salt (number of atoms)** is then [EA-18]:

$$m_t \text{ (I) in total salt} = m_t \text{ (I) in dissolved salt (number of atoms /mg)} \times \text{Total } m_{NaCl} \text{ (mg)} \quad \textbf{[EA-18]}$$

Table A.3 summarize the determination of total number of iodine taken up by salt.

The conversion factor was then determined from the combination of ICP-MS and DRIFTS results by [EA-19]   (see Table A.4):

$$F = \frac{Total\ amount\ of\ iodine\ uptaken\ by\ solid\ (ICP-MS)}{\textbf{Band area at the end of exposure phase (DRIFTS)}} \text{[EA-19]}$$

Table A.4 Determination of the total amount of iodine taken up by NaCl using ICP-MS technique.

Experiment	1: NaCl exposed to 1000 ppm CH_3I for 5 hours	2: NaCl exposed to 1000 ppm CH_3I for 5 hours	3: NaCl exposed to 1000 ppm CH_3I for 5 hours
Mass of salt in the reactor for exposure to methyl iodide (mg)	150.0	144.2	146.2
Mass of salt dissolved in NaOH (mg)	100.1	100.6	100.3
Mass / volume of NaOH (ml)	10	10	10
ICP MS results and determination of total number of I taken up by the salt :			
Analyse 1 (dilution factor=5)	**293.679**	**348.004**	**432.914**
Analyse2 (diulution factor=10)	$\mathbf{2.918 \times 10^2}$	$\mathbf{3.522 \times 10^2}$	$\mathbf{4.464 \times 10^2}$
Analyse 3 (dilution factor= 20)	$\mathbf{2.799 \times 10^2}$	$\mathbf{3.421 \times 10^2}$	$\mathbf{4.250 \times 10^2}$
Retained [CH_3I] in ppb in initial 10 mL NaOH	$\mathbf{2.884 \times 10^2}$	$\mathbf{3.474 \times 10^2}$	$\mathbf{4.345 \times 10^2}$
Total mass of iodine in the solution (mg)	$\mathbf{2.884 \times 10^{-3}}$	$\mathbf{3.474 \times 10^{-3}}$	$\mathbf{4.345 \times 10^{-3}}$
Total mass of iodine taken up (mg/mg of salt)	$\mathbf{2.881 \times 10^{-5}}$	$\mathbf{3.455 \times 10^{-5}}$	$\mathbf{4.330 \times 10^{-5}}$
Total amount of iodine taken up (number of atoms/ mg of salt)	$\mathbf{1.366 \times 10^{14}}$	$\mathbf{1.638 \times 10^{14}}$	$\mathbf{2.053 \times 10^{14}}$
Total mass of iodine taken up by total mass of salt (mg)	$\mathbf{4.322 \times 10^{-3}}$	$\mathbf{4.982 \times 10^{-3}}$	$\mathbf{6.331 \times 10^{-3}}$
Total amount of iodine taken up by salt (number of atoms)	$\mathbf{2.050 \times 10^{16}}$	$\mathbf{2.362 \times 10^{16}}$	$\mathbf{3.002 \times 10^{16}}$
Absolute uncertertainty interval (+/- number of atoms)	$\mathbf{1.640 \times 10^{15}}$	$\mathbf{1.890 \times 10^{15}}$	$\mathbf{2.402 \times 10^{15}}$
Mean of total amount of iodine taken up by salt (number of atoms)	$\mathbf{2.471 \times 10^{16}}$		
Absolute uncertertainty interval at 95% confidence level(+/- number of atoms)	$\mathbf{1.206 \times 10^{16}}$		

Table A.5 Determination of the conversion factor

IR data : [CH₃I]= 1000 ppm, contact time in sample holder = 55 ms , continous flow for 5 hours			
Experiment	Repeat 1	Repeat 2	Repeat 3
Band (cm^{-1})	1275+1244+1220+1183+1074+1023	1275+1244+1220+1183+1074+1023	1275+1244+1220+1183+1074+1023
Area (a.u) - pseudo absorbance **Absolute area uncertainty (+/- surface unit of integrate area)**	2.085 0.374	2.069 0.374	2.338 0.374
Conversion factor (number of I atoms/ surface unit of integrated band area) **Conversion factor absolute uncertainty (+/-)**	9.829×10^{15} 1.913×10^{15}	1.142×10^{16} 2.236×10^{15}	1.284×10^{16} 2.277×10^{15}
Mean conversion factor	**1.136×10^{16}**		
Mean conversion factor uncertainty (+/-)	**3.740×10^{15}**		

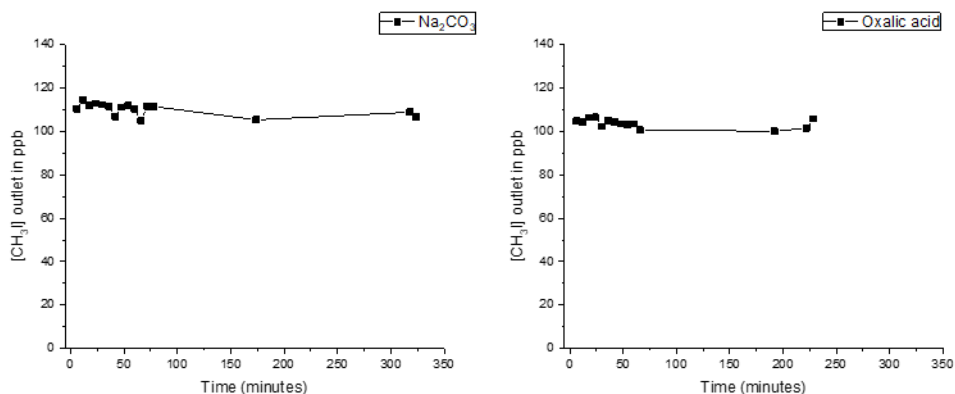# Annex 8: Time evolution of CH₃I outlet concentration in static reactors filled with solids

Figure A. 8 The evolution of [CH₃I] outlet as function of time in the large reactor filled with 14-18g of oxalic and Na₂CO₃ solids for an injected CH₃I concentration of 100 ppb and 108 mL.min⁻¹ continuous gas flow under RH=20% at 296 K and 1 atm.
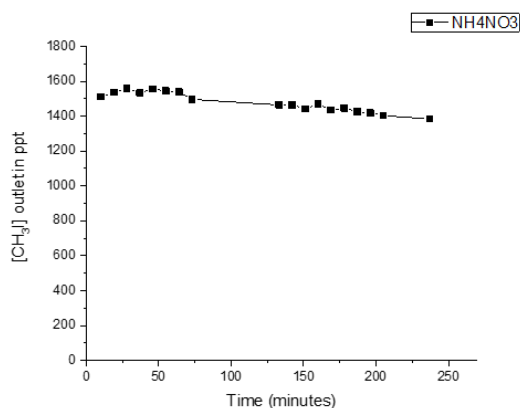
Figure A. 9 The evolution of [CH₃I] outlet as function of time in the large reactor filled with 18g of NH₄NO₃ solid for an injected CH₃I concentration of 1 ppb and 77 mL.min⁻¹ continuous gas flow under RH=20% at 296 K and 1 atm.
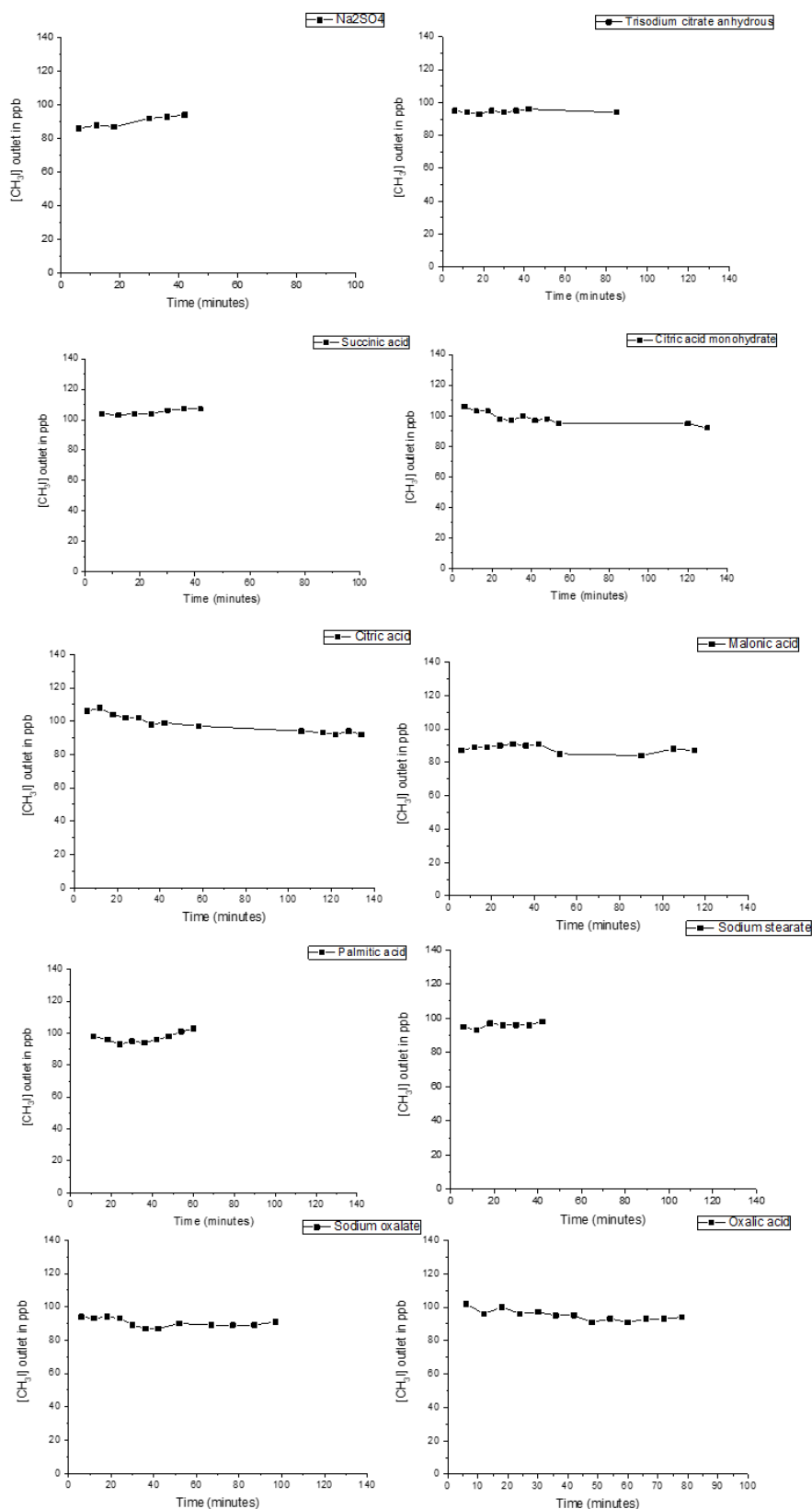
Figure A. 10 The evolution of [CH₃I] outlet as function of time in the small reactor filled with 1g of different organic and inorganic solids for an injected CH₃I concentration of 100 ppb and of 108 mL.min⁻¹ continuous gas flow under RH=20% at 296 K and 1 atm.

Reference

[1] https://pubchem.ncbi.nlm.nih.gov/compound/Iodomethane

[2] Y.Neehaul, Ph.D. thesis Study of protein interactions in the respiratory chain by IR spectroscopy and electrochemistry, Strasbourg University, 2012.

[3] S. Scolaro, Ph.D. thesis on effects of humidity and fatty acid surfactants on the uptake of NO_2 to NaCl : Combined study of kinetics and surface analysis, Lille University, 2009.

[4] T. Armaroli, T. Bécue, S. Gautier, Diffuse Reflection Infrared Spectroscopy (DRIFTS): Application to the in Situ Analysis of Catalysts, Oil Gas Sci. Technol. 59 (2004) 215–237. https://doi.org/10.2516/ogst:2004016.

[5] J. Sirita, S. Phanichphant, F.C. Meunier, Quantitative analysis of adsorbate concentrations by diffuse reflectance FT-IR, Anal. Chem. 79 (2007) 3912–3918. https://doi.org/10.1021 /ac0702802.

[6] E.Siurdyban, Thése de doctorat, Immobilisation de dérivés du cryptophane-A sur des surfaces planes SiO_2/or et OR ainsi que sur des nanoparticules magnétiques, Université de Bordeaux, 2015.

[7] M. Gouello, Thése de doctorat, Chimie de l'iode et composition des aérosols dans le circuit primaire d'un réacteur nucléaire en situation d'accident grave, Université de Grenoble, 2013.

[8] C. Alvarez, J.Nguyen-sadassivame «Conduite de l'analyse d'ICH_3 par CPG, validation de méthode d'analyse et calcul d'incertitude,» Rapport interne IRSN - IRSN/2020-00341, 2020.

[9] EuraChem guide, Quantifying Uncertainty in Analytical Measurement, 3rd Edition (2012). https://www.eurachem.org/index.php/publications/guides/quam

Titre : Etude expérimentale des réactions de capture/désorption des iodes gazeux (I$_2$, CH$_3$I) sur des aérosols environnementaux

L'iode gazeux est émis dans l'atmosphère soit par l'activité biologique des océans soit, pour l'iode radioactif, lors de situations d'accident nucléaire. Mieux modéliser le transport/réactivité de ces composés halogénés est essentiel du fait de leur implication dans la formation/disparition de l'ozone atmosphérique ainsi que des conséquences radiologiques lors de la dispersion d'iode radioactif. Dans ce contexte, ce travail a concerné les interactions entre un composé gazeux de l'iode et l'eau ou des aérosols atmosphériques par des techniques de spectroscopie.

Ce composé gazeux interagit très peu avec les aérosols atmosphériques de sels marins. Avec l'eau atmosphérique, il se forme des agrégats interagissant avec des polymères d'eau plutôt que des nouveaux composés. Aux températures typiques de l'atmosphère, l'adsorption de l'iode gazeux sur la glace amorphe est très peu probable. Ces résultats vont permettre d'implémenter les connaissances sur le devenir atmosphérique de l'iode.

Title: Experimental study on the Capture/Desorption of gaseous iodine (I$_2$, CH$_3$I) on environmental aerosols

Iodine is emitted into the atmosphere either by biological activity in the oceans or more specifically, for radioactive iodine, during a severe nuclear accident. Improving the modelling of the transport/reactivity of these so-called halogenated compounds in the atmosphere is important since they are strongly linked to the cycle of ozone formation/depletion and since the dispersion of radioactive iodine may have radiological consequences. In this context, the interactions between a gaseous organic iodine compound and water or atmospheric aerosols, such as sea salts, was studied by using spectroscopic approach.

We have shown very weak interactions with sea salt atmospheric aerosols. With water, it forms aggregates interacting with water polymers rather than forming new compounds. At atmospheric temperatures, adsorption of this gaseous organic iodine compound on amorphous ice is unlikely to occur. These results will allow the implementation of knowledge on iodine fate in the atmosphere.